N73-31577
NASA CR-2304

NASA CONTRACTOR REPORT

NASA CR-2304

A COMPILATION OF STUDIES FROM ATMOSPHERIC VARIABILITY EXPERIMENT (AVE)

by J. R. Scoggins, H. E. Fuelberg, R. D. Carlson, R. W. Phelps, and D. G. Bellue

Prepared by
TEXAS A&M UNIVERSITY
College Station, Texas 77843
for George C. Marshall Space Flight Center

NATIONAL AERONAUTICS AND SPACE ADMINISTRATION • WASHINGTON, D. C. • AUGUST 1973

TECHNICAL REPORT STANDARD TITLE PAGE

1. REPORT NO.	2. GOVERNMENT ACCESSION NO.	3. RECIPIENT'S CATALOG NO.
NASA CR-2304		

4. TITLE AND SUBTITLE	5. REPORT DATE
A Compilation of Studies From Atmospheric Variability Experiment (AVE)	August 1973
	6. PERFORMING ORGANIZATION CODE M114
7. AUTHOR(S) J. R. Scoggins, H. E. Fuelberg, R. D. Carlson, R. W. Phelps, and D. G. Bellue	8. PERFORMING ORGANIZATION REPORT #
9. PERFORMING ORGANIZATION NAME AND ADDRESS Texas A&M University College Station, Texas 77843	10. WORK UNIT NO.
	11. CONTRACT OR GRANT NO. NAS8-26751
12. SPONSORING AGENCY NAME AND ADDRESS National Aeronautics and Space Administration Washington, D.C. 20546	13. TYPE OF REPORT & PERIOD COVERED CONTRACTOR
	14. SPONSORING AGENCY CODE

15. SUPPLEMENTARY NOTES

Prepared under the sponsorship of the Aerospace Environment Division, Aero-Astrodynamics Laboratory, Marshall Space Flight Center, Alabama.

16. ABSTRACT

Five methods for obtaining the sign of vertical motion at various levels in the atmosphere were investigated to determine which gave the best explanation for areas of rain and no-rain in the southeastern United States during the period February 19-22, 1964. The methods used were the terrain-induced vertical motion, the kinematic method including the terrain effect, the adiabatic method, the omega equation, and the vorticity equation combined with Dines' Compensation Principle. Stability and moisture availability were considered but not as extensively as vertical motion.

Orographic lifting was found to be an important factor in producing the observed precipitation; 63% of the occurrence of rain and no rain at 130 data collection points was explained by terrain-induced vertical motion alone. Values of vertical motion obtained by the kinematic method, including orographic lifting at 850 mb, produced the best agreement with observed areas; 80.8% of the data collection points was explained correctly. Various forms of the adiabatic method gave results for the 700-500-mb layer that explained about 72% of the points. The vorticity equation produced results at all levels that verified only about 50% of the time. When terms in the omega equation were added through use of constant multipliers, results comparable to the adiabatic method were obtained. Without this addition large uncertainties occurred. Maps showing areas where terms of the omega equation would indicate positive vertical motion did not correlate well with the observed rainfall patterns.

17. KEY WORDS	18. DISTRIBUTION STATEMENT
Vertical Motion Orographic Lifting Omega Equation Vorticity Equation Atmospheric Variability	20

19. SECURITY CLASSIF. (of this report)	20. SECURITY CLASSIF. (of this page)	21. NO. OF PAGES	22. PRICE
Unclassified	Unclassified	197	3.00

For sale by National Technical Information Service, Springfield, Virginia 22151

FOREWORD

This report is one of several to be published from research conducted under, or supported in part by, NASA Contract No. NAS8-26751, entitled "A Compilation of Studies From AVE I." This effort is sponsored by the NASA Office of Applications and Office of Manned Space Flight under the direction of Marshall Space Flight Center's Aerospace Environment Division. A number of approaches have been and continue to be followed in the conduct of the research. The results presented in this report represent only a portion of the total research effort. Other reports will be published as the research progresses. Previously published research results appear in NASA CR 2030-An Investigation of Relationships Between Meso- and Synoptic-Scale Phenomena, NASA CR 2189-Atmospheric Energetics As Related to Cyclogenesis Over the Eastern United States and NASA CR 2192-An Investigation of the Sutcliffe Development Theory.

TABLE OF CONTENTS

TABLE OF CONTENTS (Continued)

TABLE OF CONTENTS (Continued)

A COMPILATION OF STUDIES FROM ATMOSPHERIC VARIABILITY EXPERIMENT (AVE)

INTRODUCTION

by

James R. Scoggins
Henry E. Fuelberg
Ronald D. Carlson
Ronald W. Phelps
and
Dan G. Bellue

Department of Meteorology
Texas A&M University
College Station, Texas

The importance of meteorological systems of a scale too small to be detected and analyzed from upper-air synoptic data taken at 12-hr intervals in local weather forecasts and variability of parameters such as wind, temperature, and stability, has long been recognized. Because of the importance of subsynoptic-scale phenomena in the design and operation of space vehicles and the need for a better understanding of these phenomena, the Aerospace Environment Division of NASA's Marshall Space Flight Center carried out a measurement program during the period February 19-22, 1964. Rawinsonde soundings were made at 30 stations over the eastern part of the United States south of the Great Lakes. Soundings were made at intervals of 3 hours at all stations except Huntsville, Alabama and Mississippi Test Facility (near New Orleans) where soundings were made at intervals of 1.5 hours. This is known as the Atmospheric Variability Experiment I (AVE I).

Four studies conducted at Texas A&M University under NASA Contract NAS8-26751 entitled, "Atmospheric Variability and Vertical Motion," using the AVE I data are contained in this document. Three of these are masters degree theses. Each report was prepared independently of the others and is complete within itself. While this led to some redundancy in the data sections of the reports, they may be read in any order or separately without loss of reference or perspective.

Research continues on AVE I, and preliminary plans are being formulated for other AVE-type experiments. Subsequent reports will be printed when significant milestones are reached.

ACKNOWLEDGMENTS

The authors of this composite report wish to acknowledge the support and encouragement of all who participated in the research. They are too numerous to mention by name, but without their help and dedication our work would have been more difficult and less rewarding. We especially wish to thank Mr. William W. Vaughan and other personnel of the Aerospace Environment Division of NASA's Marshall Space Flight Center for providing the AVE I data, and for numerous stimulating and helpful discussions regarding the research.

CHAPTER I. A STUDY OF WINTER PRECIPITATION AREAS IN RELATION TO SEVERAL INDICATORS OF VERTICAL MOTION

by

Henry Ernest Fuelberg
Department of Meteorology
Texas A&M University, College Station, Texas

A. ABSTRACT

Five methods for obtaining the sign of vertical motion at various levels in the atmosphere were investigated to determine which gave the best explanation for areas of rain and no-rain in the southeastern United States during the period February 19-22, 1964. The methods used were the terrain-induced vertical motion, the kinematic method including the terrain effect, the adiabatic method, the omega equation, and the vorticity equation combined with Dines' Compensation Principle. Stability and moisture availability were considered but not as extensively as vertical motion.

Orographic lifting was found to be an important factor in producing the observed precipitation; 63% of the occurrence of rain and no rain at 130 data collection points was explained by terrain-induced vertical motion alone. Values of vertical motion obtained by the kinematic method, including orographic lifting at 850 mb, produced the best agreement with observed areas; 80.8% of the data collection points was explained correctly. Various forms of the adiabatic method gave results for the 700-500-mb layer that explained about 72% of the points. The vorticity equation produced results at all levels that verified only about 50% of the time. When terms in the omega equation were added through use of constant multipliers, results comparable to the adiabatic method were obtained. Without this addition large uncertainties occurred. Maps showing areas where terms of the omega equation would indicate positive vertical motion did not correlate well with the observed rainfall patterns.

B. INTRODUCTION

1. General

The occurrence, type, and amount of precipitation are related to moisture availability, vertical motion, and stability. Vertical motion is a critical factor in the occurrence of precipitation because as air rises and cools its ability to retain water vapor decreases. With upward vertical motion, the formation of clouds and precipitation may result. Downward vertical motion usually leads to a decrease in the relative humidity and a

decrease in cloudiness. Thus, a knowledge of vertical motion often is required to explain the presence of clouds and precipitation as well as to forecast their occurrence.

2. Statement of problem

The purpose of this investigation is to explain the rainfall patterns observed in the southeastern United States during the period February 19-22, 1964. Synoptic-scale processes were considered at 3-hr intervals. The edge of the area considered was at least 325 km from the Great Lakes so that effects due to these large bodies of water were excluded. Five methods of determining vertical motion were investigated to determine which gave the best correlation with the rainfall patterns during this wintertime period. The presence of clouds was not used as verification. If particular terms in the equations were difficult to evaluate, the relative importance of each term to the overall method was investigated. A simple, yet accurate, method of determining areas of positive vertical motion associated with precipitation for the time and area in question was the desired outcome.

Moisture availability and stability were not considered to be deciding factors in precipitation occurrence. Since these factors were favorable for precipitation in areas where it actually took place, it was not necessary that they be considered. If positive vertical motion was present in areas where precipitation was not observed, additional moisture and different stability conditions might have led to precipitation. Without positive vertical motion increased moisture or changes in stability would have little effect on the occurrence of precipitation. If these additional factors had been included in this study, some improvement in results would have been expected.

C. METHODS OF DETERMINING VERTICAL MOTION

1. Orographic lifting

Air which is moving over sloping terrain obtains an induced vertical component of velocity. The magnitude of the vertical component is directly related to the wind speed near the ground and to the angle of inclination of the slope in the direction of flow. Atmospheric stability and frictional effects due to the nature of the terrain also have an influence on this induced vertical motion (Jarvis and Agnew, 1970; Elliot and Shaffer, 1962). Terrain-induced vertical motions can, by themselves, produce heavy rainfall. Sawyer (1952) has shown that the intensity of already existing rain areas is affected by terrain, and Vederman (1961) showed that over 1.5 in. of rain per day could be expected under certain conditions in portions of the Pacific Northwest due only to terrain effects. The orographic effect decays rapidly with height, usually completely by 500 mb (Haltiner *et al.*, 1963), but dynamic effects also must be considered. For example, the ratio between amounts of mountain and valley precipitation in northwest Utah was found to

decrease for precipitation associated with "cold" lows as compared to frontally-produced rainfall, since the large-scale vertical motion in these lows was able to counteract the terrain-induced negative vertical motion in the valley (Williams and Peck, 1962). Myers (1964) has shown that topography can influence convective activity in central Pennsylvania through the formation of gravity waves and thermally produced circulations.

Precipitation anomalies resulting from terrain-induced vertical motion are especially evident in the mountainous regions of the western United States where heavy rainfall occurs on the windward side of the mountains (induced positive vertical motion), but much smaller amounts occur on the leeward side (induced negative vertical motion). The terrain effect also is noticeable along the Appalachians where Schwarz (1970) observed that it was related to rainfall anomalies associated with the heavy precipitation occurring in Virginia due to hurricane Camille.

2. Kinematic method

The equation of continuity may be written

$$-\frac{\partial w}{\partial z} = \vec{\nabla}\cdot\vec{V} + \frac{1}{\rho}\frac{d\rho}{dt} \tag{1}$$

where w is the vertical component of the wind in the positive z direction, $\vec{V}$ is the horizontal wind velocity, ρ is the density of the air, and t is time. Panofsky (1958) states that the magnitude of the term $\frac{1}{\rho}\frac{d\rho}{dt}$ usually is only about 10% as large as the other terms in Eq. (1). A good approximation to the continuity equation is then

$$-\frac{\partial w}{\partial z} = \vec{\nabla}\cdot\vec{V} \,. \tag{2}$$

With the assumption $\frac{\partial w}{\partial z} = \frac{dw}{dz}$, integration from the surface S to some level L gives

$$w_L = w_S - \int_S^L \vec{\nabla}\cdot\vec{V}\, dz. \tag{3}$$

The hydrostatic equation may be written

$$\frac{dp}{dz} = -\rho g \tag{4}$$

where p is atmospheric pressure and g is the acceleration due to gravity. Substitution for dz into Eq. (3) gives

$$w_L = w_s + \int_{p_s}^{p_L} \frac{1}{\rho g} \vec{\nabla}\cdot\vec{V}\, dp. \tag{5}$$

Vertical motion at any level L in the atmosphere may be determined from Eqs. (3) or (5) if adequate data are available. Data from constant-pressure maps may be used to solve for w_L from Eq. (5).

An advantage to use of the kinematic method is that instantaneous values can be obtained because no time derivatives are involved. A disadvantage is that the method is highly sensitive to errors in wind measurement.

Hansen and Thompson (1965) used the kinematic method in western and central areas of the United States to obtain the sign of vertical motion at 700 mb and to compare this sign with satellite pictures of cloud cover. The terrain effect was not included in their study, but 59% of the area of broken-to-overcast clouds was found to have positive vertical motion at 700 mb during a 3-day period in August 1961. In areas of clear to scattered clouds, 56% of the area experienced negative vertical motion at 700 mb. From divergence values computed in 50-mb increments from the surface to 300 mb, Thompson and Collins (1953) used the kinematic method together with a moisture parameter to forecast precipitation amounts in the Mississippi River Valley where orographic lifting could be neglected. Rainfall in four categories was forecast correctly 70% of the time for a 5-day period in January.

3. Vorticity equation combined with Dines' Compensation Principle

The simplified vorticity equation is (Haltiner and Martin, 1957)

$$\frac{d\eta}{dt} = -\eta\, \vec{\nabla}\cdot\vec{V} \tag{6}$$

where η, the absolute vorticity, equals the relative vorticity (ζ) plus the coriolis parameter (f). After expanding the left-hand side of Eq. (6), one obtains

$$-\frac{\partial\eta}{\partial t} - \vec{V}\cdot\vec{\nabla}\eta = \eta\vec{\nabla}\cdot\vec{V} \tag{7}$$

which may be solved for velocity divergence. Frequently, only the signs of the terms are required. By computing the sign of divergence at several levels, one can determine the sign of vertical motion in many cases in the mid-troposphere by use of Dines' Compensation Principle (Petterssen, 1956).

This principle states that divergence in the upper troposphere and stratosphere above convergence in the lower troposphere indicates positive vertical motion in intermediate layers, while the opposite case indicates negative vertical motion. Positive vertical motion is indicated by positive values of the terms on the left-hand side of Eq. (7) above the level of non-divergence, and negative values below the level of non-divergence. The opposite is true for negative vertical motion. The level of non-divergence usually is assumed to be near 600 mb.

A disadvantage to this method is that the sign of vertical motion cannot be computed instantaneously because of the term $\frac{\partial \eta}{\partial t}$. This term is often neglected although it can be quite important. If the term is computed, data usually are available at 12-hr intervals so that only average values can be obtained.

Williams (1963) found a strong relationship between positive advection of vorticity at 500 mb and precipitation at Salt Lake City. Values greater than 5×10^{-5} sec^{-1} indicated precipitation 57% of the time. Much poorer agreement was found for lower values of vorticity advection. A stronger agreement was found between initial vorticity plus vorticity advection and precipitation occurrence. The term $\frac{\partial \eta}{\partial t}$ was not computed. Jenrette (1960), using vorticity and moisture parameters, explained summer precipitation with high accuracy in central Illinois. Collins and Kuhn (1954) used a graphical procedure for computing vorticity advection, the local change term, and a moisture parameter to explain precipitation. Their method, which included the terrain effect, was 76% accurate. Younkin (1968) found that snowfall in the western United States usually occurred ahead of maximum vorticity values at 500 mb; this indicated that $\left(-\frac{\partial \eta}{\partial t} - \vec{V}\cdot\vec{\nabla}\eta\right)$ was usually positive at 500 mb during heavy snowfall if the level of non-divergence was below 500 mb. Heavy snowfall in the central and eastern United States was found to lie ahead and slightly to the left of the position of the storm at 850 mb (Browne and Younkin, 1970).

4. Adiabatic method

The equation for adiabatic motion is

$$\frac{d\theta}{dt} = 0 \tag{8}$$

where θ is the potential temperature. In dealing with a layer, we may replace θ by $\bar{\theta}$. After making this substitution and expanding, we see that Eq. (8) becomes

$$\frac{\partial \bar{\theta}}{\partial t} + \vec{V}\cdot\vec{\nabla}\,\bar{\theta} + w\frac{\partial \bar{\theta}}{\partial z} = 0 \tag{9}$$

or

$$w = \left(\frac{\partial\bar{\theta}}{\partial z}\right)^{-1}\left(-\frac{\partial\bar{\theta}}{\partial t} - \vec{V}\cdot\vec{\nabla}\,\bar{\theta}\right). \qquad (10)$$

The term $\frac{\partial\bar{\theta}}{\partial z}$ is a measure of static stability. Under stable conditions $\left(\frac{\partial\bar{\theta}}{\partial z} > 0\right)$, warm advection and a decrease in $\bar{\theta}$ with time will lead to positive (upward) vertical motion. With unstable conditions $\left(\frac{\partial\bar{\theta}}{\partial z} < 0\right)$, these circumstances lead to negative (downward) vertical motion.

There are several disadvantages to the adiabatic method. When saturation is reached, θ is not conserved, and Eq. (8) is no longer valid. Near the ground where diabatic processes have a pronounced effect on temperature, serious errors would occur also through the use of this method (Panofsky, 1946). The term $\frac{\partial\bar{\theta}}{\partial t}$ frequently is neglected, but it may be important, especially in some mesoscale systems. The adiabatic method is not as sensitive to errors in wind measurement as the previous methods since wind speed and not the derivative of wind speed is used.

Hansen and Thompson (1965) used the adiabatic method at the 700-mb level only to estimate vertical motion. They found that 38% of broken-to-overcast cloud regions had $w > 0$ when they assumed the air was not saturated.

5. Omega equation

The omega equation is derived from the adiabatic assumption given by Eq. (8), Poisson's equation, the equation of state, the vorticity equation, and the hydrostatic equation. Thompson (1961) gives the result as

$$-\left(-\sigma\nabla^2\omega + \frac{f^2}{g^2}\frac{\partial^2\omega}{\partial p^2}\right) = \frac{f}{g}\frac{\partial}{\partial p}\left(-\vec{V}\cdot\vec{\nabla}\eta\right) + \frac{R}{\rho g}\left(\frac{p_L}{p_o}\right)^k \nabla^2\left(-\vec{V}\cdot\vec{\nabla}\theta\right) \qquad (11)$$

where σ $\left(=\frac{\partial\theta}{\partial p}\right)$ is a stability parameter, ω $\left(=\frac{dp}{dt}\right)$ is approximately proportional to vertical velocity but of opposite sign, R is the gas constant, p_L and p_o are the atmospheric pressures at level L and the surface, respectively, and $k = \frac{R}{c_p}$, where c_p is the specific heat capacity at constant pressure.

Djuric (1969) simplified the omega equation so that it can be used to obtain qualitative estimates of the sign of vertical motion. The simplified form of the equation is

$$w\alpha - \vec{V}.\vec{\nabla}\eta - \nabla^2\left(-\vec{V}\cdot\vec{\nabla}\,\bar{\theta}\right) \qquad (12)$$

where the bar represents an average through a thick layer below the level of maximum wind. Djuric states that upward motion in the mid-troposphere is associated with positive vorticity advection above the level in question and

maximum warm advection below. Negative vertical motion is associated with the opposite conditions. If the two terms differ in sign, an estimate of the sign of vertical motion cannot be made. He further states that $-\vec{V}\cdot\vec{\nabla}\,\bar{\theta}$ usually can be substituted for its Laplacian in areas of maximum or minimum value. With this further simplication, Eq. (12) becomes

$$w\alpha - \vec{V}\cdot\vec{\nabla}\eta - \vec{V}\cdot\vec{\nabla}\,\bar{\theta}. \tag{13}$$

Djuric found that the sign of vertical motion determined from Eq. (13) was associated with heavy snowfall in the western United States. In addition, Booth (1970) found that areas of positive vertical motion delineated by the omega equation were related to areas of convective activity over Texas.

6. Combined studies

While many investigators have estimated vertical motion by several methods, little has been published on the intercomparison of the methods in a particular synoptic situation. Miller and Panofsky (1958) computed vertical motion at 700 mb using the kinematic method, the adiabatic method, and a numerical model. If the three methods gave similar values of vertical motion, the value was correlated with precipitation and moisture availability. If the values were dissimilar, no correlation was made. They found that the probability of clear skies at a station varied from 5% for moist ascending air to 93% for dry descending air. For precipitation, the corresponding values ranged from 67% to 0%. Topography was not considered in the study. In their investigation, Hansen and Thompson (1965) used the adiabatic method, the kinematic method, and a numerical model to compute vertical motion at 700 mb. They found that the kinematic method gave the best results although it seemed little better than some of the other methods; the adiabatic method gave the poorest results. Topography was not considered in their study.

D. DATA

1. Description

For four days in February 1964, the Marshall Space Flight Center of the National Aeronautics and Space Administration (NASA) supported an observational program whereby 30 stations in the southeastern United States (see Fig. 1) made rawinsonde observations every 3 hr instead of the customary 12 hr. The program was called Project AVE (Atmospheric Variability Experiment) and began at 00 GMT on February 19, 1964 and ended at 00 GMT on the 22nd, although some stations took additional observations on the 22nd. Special procedures were used to process the readout, and a great deal of time was spend in checking the data for errors, most of which were corrected subsequently. The final product was recorded on magnetic tape and supplied to

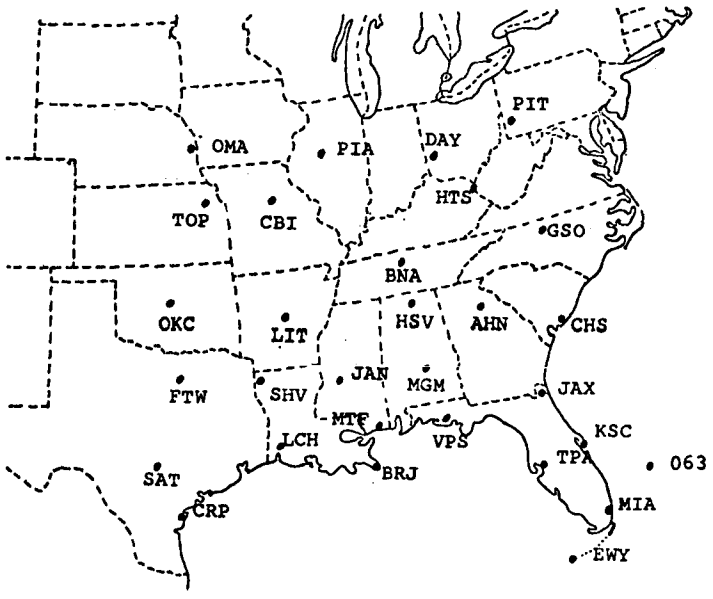

Fig. 1. Location of rawinsonde stations. Station identifiers are given in Appendix B (p. 78).

Texas A&M University by personnel of the Aerospace Environment Division, Marshall Space Flight Center, NASA, under NASA contract NAS8-26751, "Study of Atmospheric Variability and Vertical Motions."

2. Accuracy

Information provided by NASA personnel* gives the accuracies of the data used in this study as follows:

1) Height: Values were obtained at each contact point on the radiosonde's baroswitch by integrating the hypsometric equation over layers of one pressure interval in thickness. The mean virtual temperature used in the equation was obtained by averaging the values at the top and bottom of each pressure interval. Height values at 25-mb intervals then were obtained by interpolation between values at the contact points. Based on a temperature error of 1C with consistently the same sign, height errors range from 3 gpm (geopotential meters) at 900 mb, to 20 gpm at 500 mb and 87 gpm at 50 mb. This is an improvement over routine measurements. Actually, height errors probably are smaller inasmuch as errors in temperature are likely to be of both signs.

---

*Personal communication with Mr. William W. Vaughan, Chief, Aerospace Environment Division, NASA Marshall Space Flight Center, Huntsville, Alabama 35812.

2) Pressure: Values at contact points were obtained from the calibration curve for each radiosonde. Interpolation between contact points produced values at 25-mb intervals. The rms error is 1.3 mb at pressures greater than 400 mb, 1.1 mb between 400 and 100 mb, and 0.7 mb between 100 and 10 mb.

3) Temperature: Values at 25-mb intervals were obtained by interpolation of data given at the contact points. The values have an uncertainty of ±1C.

4) Relative Humidity: Values at 25-mb intervals were obtained by interpolation of data given at the contact points. A 10% rms error is likely in the data. The error would appear also in dew point temperatures which were provided on the tape.

5) Wind: Special procedures were used to determine wind direction and speed. The angles of elevation and azimuth used in the computations were recorded at 6-sec intervals to the nearest 0.01 deg. This is the best resolution available from the standard equipment used. Angles corresponding to the pressure contacts were obtained by averaging over the number of time points between contacts. The points were centered about the time corresponding to the contact with between four and six points being averaged in the levels used in this study. Velocity (vector) values below 7 km then were computed at each pressure contact by using centered finite differences with a one-contact overlap. Interpolation was used to obtain the values at 25-mb intervals. The wind speed has an approximate rms error of 1.5 m sec^{-1} at 700 mb, 2.5 m sec^{-1} at 500 mb, and 4 m sec^{-1} at 300 mb. Direction errors (rms) based on speeds of 10 m sec^{-1} are 2° at 700 mb, 3° at 500 mb, and 5° at 300 mb. The rms errors in direction are inversely proportional to the wind speed.

E. COMPUTATIONAL PROCEDURES

1. Selection of data points

Microfilm copies of surface facsimile maps and surface data were provided by NASA for use in this study. From these maps and data, 6-hr rainfall totals were plotted for all reporting stations in the area of interest onto new maps of scale and projection that were not varied throughout the investigation. The maps were of conformal conic projection with a scale of 1:12,500,000. Rainfall data were available for stations about 150 km apart for the 6-hr periods ending at 00, 06, 12, and 18 GMT. Areas where rainfall occurred within each 6-hr period were outlined.

Points at which data would be collected were selected from the analyzed rainfall maps; an example is shown in Fig. 2.

Four criteria were used in the selection of these points, called data points:

1) each point was located at least 325 km from the Great Lakes,

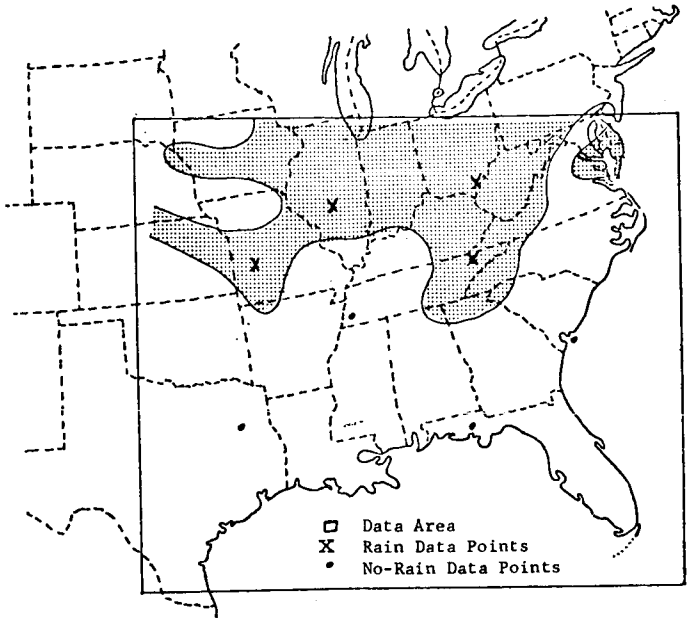

Fig. 2. An example of data points used in the study.

2) each point was located at least 75 km from the boundary separating rain areas from no-rain areas,

3) all points were selected at least 300 km from each other, and

4) points were selected in regions of good data density.

An average of four points was selected in rain areas and four points in no-rain areas for each of the 16 time periods, but the location of the points changed at each period. A total of 65 points in each category was selected. Information from the 130 points was taken by overlaying them onto fields of the particular parameter involved at the given time period, and then reading off the value at each point. Except for absolute vorticity (η) which was computed every 3 hrs, all parameters were computed for the time in the middle of the 6-hr rainfall reporting period. This was made possible by the AVE data. For example, parameters computed at 03 GMT were used with the data points selected at the 06 GMT rainfall report (total rainfall between 00 and 06 GMT).

2. The grid system

To facilitate the computation of parameters needed in the investigation, a grid system was set up to envelop the area covered by the rawinsonde network. The system is shown in Fig. 3. The grid points were placed 158.75 km apart; this corresponded to a distance of 0.5 in. on the maps used. The grid area was 15 by 13 points.

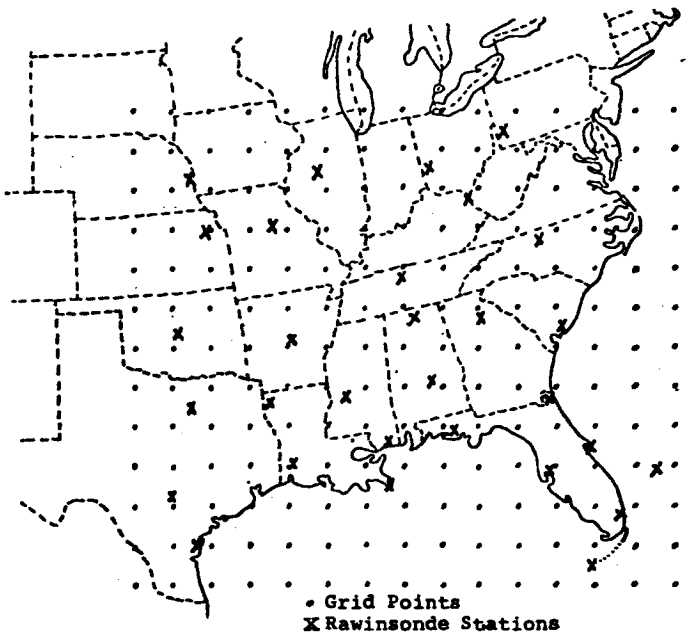

Fig. 3. The grid system.

To place the data on the grid points, a technique developed by Barnes (1964) was used to interpolate between rawinsonde stations. Barnes describes the technique as a "convergent weighted-averaging interpolation scheme." He states that, "The scheme is based on the supposition that the two-dimensional distribution of an atmospheric variable can be represented by the summation of an infinite number of independent waves, i.e., a Fourier integral representation." He showed that the technique gave results which were comparable to careful hand analysis. Smoothing was performed on the interior points, the borders, and the corners. No resolution is available for wavelengths less than 300 km (the smoothing filters these out), but near complete resolution is obtained for wavelengths of 500 km and longer.

3. Quantities computed

From data taken directly from the magnetic tapes provided by NASA, the potential temperature (θ) was averaged at each station by using values every 25 mb to give $\bar{\theta}$ between 1000-850 mb, 850-700 mb, and 700-500 mb, hereafter called the levels of Set 1. The interpolation scheme then placed these values onto the 15x13 grid system. The same technique was used to compute the average relative humidity between 1000-850 mb and 850-700 mb.

The u- and v-components of wind (zonal and meridional, respectively) were computed at each grid point from the wind velocity values available on tape. These quantities were obtained at the 925-, 850-, 700-, and 500-mb levels, hereafter called the levels of Set 2.

The equivalent potential temperature (θ_ε) was obtained at each rawinsonde station using the equation

$$\theta_\varepsilon = \theta e^{\frac{LC_s}{C_p T}} \tag{14}$$

where L is the latent heat of condensation, e is the base of natural logarithms, C_s is the saturation mixing ratio, T is temperature, and C_p is as given previously. Values of θ_ε were computed at the 1000-, 850-, 700-, and 500-mb levels so that $\frac{\partial \theta_\varepsilon}{\partial z}$ could be determined for each grid point by use of the interpolation scheme. By use of the preceding parameters computed at each grid point, the following terms were evaluated by computer:

1) η : The absolute vorticity was determined at the levels in Set 2. Since centered finite differences were used to obtain values of $\frac{\partial v}{\partial x}$ and $\frac{\partial u}{\partial y}$, the grid area was reduced to 13x11, i.e., values were not computed for the perimeter points.

2) $-\vec{V}\cdot\vec{\nabla}\eta$: Values were computed for the levels listed in Set 2. The grid area then was reduced to 11x9 because centered finite differences were used to compute $\vec{\nabla}\eta$.

3) $\frac{\partial \eta}{\partial t}$: Values were computed for the levels listed in Set 2 at each grid point.

4) $\vec{\nabla}\cdot\vec{V}$: Values were computed for the levels listed in Set 2 by use of the equation

$$\vec{\nabla}\cdot\vec{V} = \frac{\partial u}{\partial x} + \frac{\partial v}{\partial y} . \tag{15}$$

5) $-\vec{V}\cdot\vec{\nabla}T$: Values were computed at each grid point by the use of centered finite differences at the levels listed in Set 1. The grid was reduced to 13x11.

6) $-\vec{V}\cdot\vec{\nabla}\bar{\theta}$: Values were determined on the 13x11 grid system for 1000-850 mb by using the wind values reported at 925 mb. For the layers 850-700 mb, and 700-500 mb, the average of the wind reported at the top and bottom of the layer was used.

7) $\nabla^2\left(-\vec{V}\cdot\vec{\nabla}\bar{\theta}\right)$: Values were computed at each grid point for the layers in Set 1. They were obtainable only for a grid of 11x9 since an additional finite difference procedure was needed to determine the Laplacian.

8) $\frac{\partial \bar{\theta}}{\partial t}$: Values were determined by hand at each data point; values of $\bar{\theta}$ at 12-hr intervals were used. Values of $\bar{\theta}$ at 6-hr intervals may have produced better results, but this possible improvement was not thought to be worth the additional computer time needed.

The terrain-induced vertical motion, w_s, was computed by hand at each of the 130 data points. Wind velocities at 925 mb were used, and the assumption was made that these winds followed the relief of the terrain. From relief maps, w_s was determined with the equation

$$w_s = \left| \vec{V} \right| \frac{\Delta z}{\Delta x} \tag{16}$$

where $\frac{\Delta z}{\Delta x}$ was taken parallel to the 925-mb streamlines. This method was used by Collins and Kuhn (1954) to determine w_{1000} for use in their forecasting scheme, and a somewhat similar technique was used by Harley (1965) at the 1000- or 850-mb levels, depending on the heights of the nearby mountains. Individual peaks were not considered in the determination of Δz; only average terrain heights were used. A maximum elevation of 6000 ft was used in western North Carolina. A distance of approximately 300 km was used for Δx. Although many assumptions were made, the values of w_s are thought to be good approximations to the true average values. Some of these values were obtained on a smaller scale than for other parameters and may not be strictly compatible with those that are more coarsely obtained.

The kinematic method, Eq. (5), was used by solving the equation

$$w_L = w_s + \frac{1}{g} \sum_{i=1}^{N} \frac{1}{\rho_i} \left(\vec{\nabla} \cdot \vec{V} \right)_i \left(-\Delta p \right)_i \tag{17}$$

where ρ_i, the density at level i, and $(\vec{\nabla} \cdot \vec{V})_i$, the divergence at level i, are assumed to describe conditions throughout $(\Delta p)_i$, the pressure increment used. The vertical motion at 850 mb is given by Eq. (18), where $(\Delta p)_i$ is negative. The equation is

$$w_{850} = w_s - \frac{1}{g} \left[\frac{1}{\rho_{925}} \left(\vec{\nabla} \cdot \vec{V} \right)_{925} (35\text{mb}) + \frac{1}{\rho_{850}} \left(\vec{\nabla} \cdot \vec{V} \right)_{850} (40\text{mb}) \right] \tag{18}$$

where ρ_{925} and $(\vec{\nabla} \cdot \vec{V})_{925}$ are assumed to describe the 35-mb layer between 925 mb and 890 mb, and ρ_{850} and $(\vec{\nabla} \cdot \vec{V})_{850}$ are assumed to describe the 40-mb layer between 890 mb and 850 mb. The procedure is illustrated in Fig. 4. Likewise, vertical motions at 700 mb and 400 mb are given by the

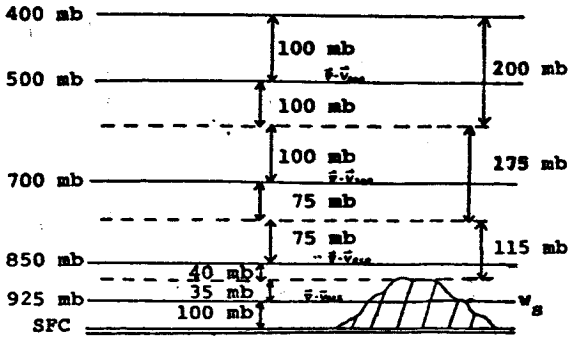

Fig. 4. Layers used in the computation of vertical velocity by the kinematic method.

equations ($(\Delta p)_i$ is negative as in Eq. (18).)

$$w_{100} = w_s - \frac{1}{g}\left[\frac{1}{\rho_{925}}(\vec{\nabla}\cdot\vec{V})_{925}(35\text{mb}) + \frac{1}{\rho_{850}}(\vec{\nabla}\cdot\vec{V})_{850}(115\text{mb}) + \frac{1}{\rho_{700}}(\vec{\nabla}\cdot\vec{V})_{700}(75\text{mb})\right] \tag{19}$$

$$w_{400} = w_s - \frac{1}{g}\left[\frac{1}{\rho_{925}}(\vec{\nabla}\cdot\vec{V})_{925}(35\text{mb}) + \frac{1}{\rho_{850}}(\vec{\nabla}\cdot\vec{V})_{850}(115\text{mb}) + \frac{1}{\rho_{700}}(\vec{\nabla}\cdot\vec{V})_{700}(175\text{mb}) + \frac{1}{\rho_{500}}(\vec{\nabla}\cdot\vec{V})_{500}(200\text{mb})\right] \tag{20}$$

These values of vertical motion were computed by hand.

Values of divergence below 925 mb were not used in the computation of vertical motion. It was assumed that all vertical motions below 925 mb were explained by orographic effects.

F. SYNOPTIC CONDITIONS

The synoptic conditions at the beginning of the time period studied, 00 GMT, February 19, are shown in Fig. 5. An occluded front in eastern North Carolina dominated the surface map. The system developed during the previous day in the western Gulf of Mexico, moved toward the east crossing the coastline near Mobile, Alabama, and then took a more northeasterly course. Widespread cloudiness and precipitation in the form of rain and snow were associated with the system; 24-hr totals of 1 in. were common. The center of the cyclone was east of Maine at 12 GMT on the 21st and continued to move toward the northeast so that it was barely noticeable in the area of interest by 21 GMT, February 21 (Fig. 6). A "bent-back occlusion" was present through most of the period with the axis of the trough shifting from an east-west to a northeast-southwest orientation by the middle of the period. Precipitation at the beginning of the period occurred along the axis of the east-west trough; but as the trough moved, the rainfall pattern did not follow. It continued to be located along the Appalachian Mountains and in the Ohio River Valley.

Cyclogenesis occurred in the Gulf of Mexico on the 21st and produced a large rain shield to the northeast of the system along the Gulf States. The center passed to the south of Miami and became disorganized by the end of the period (00 GMT, February 22).

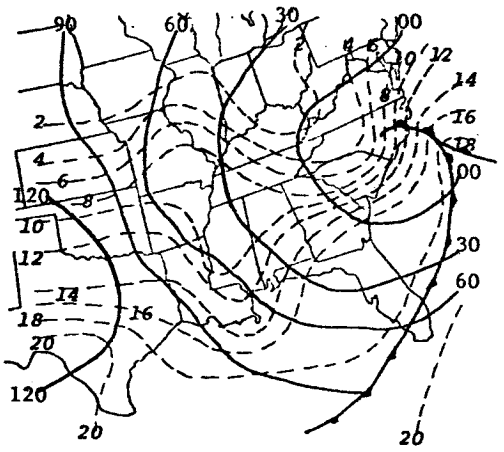

1000 mb

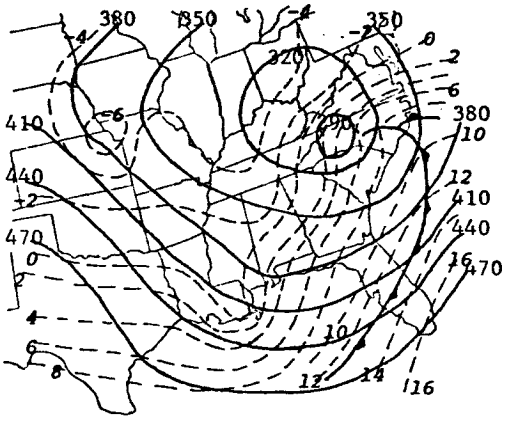

850 mb

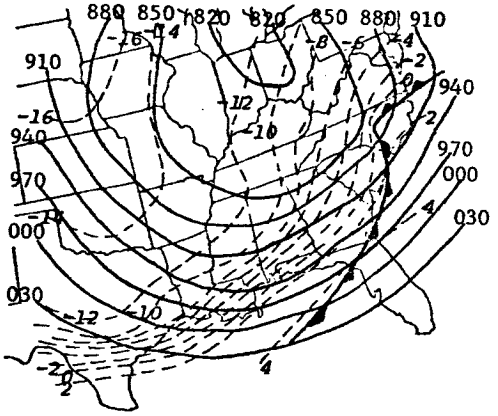

700 mb

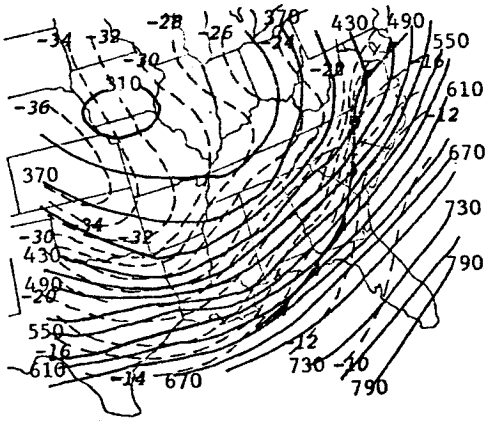

500 mb

Fig. 5. Synoptic conditions at 00 GMT, February 19.

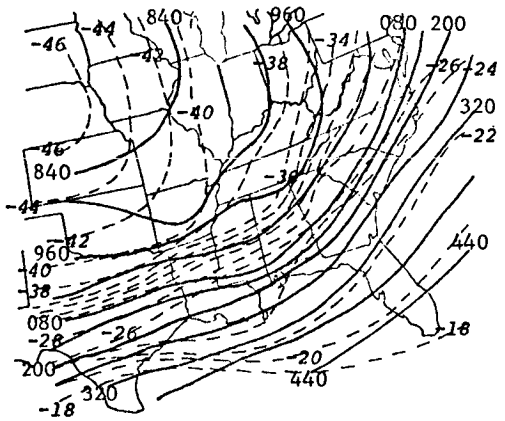

400 mb

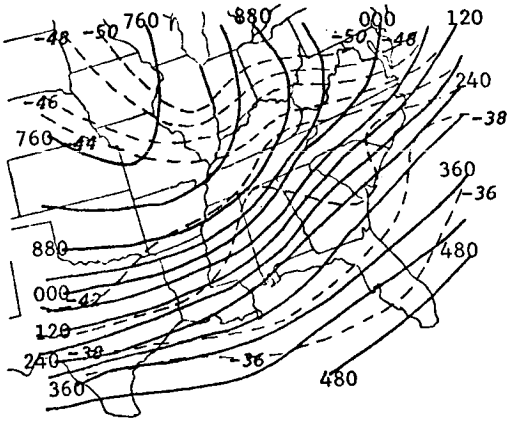

300 mb

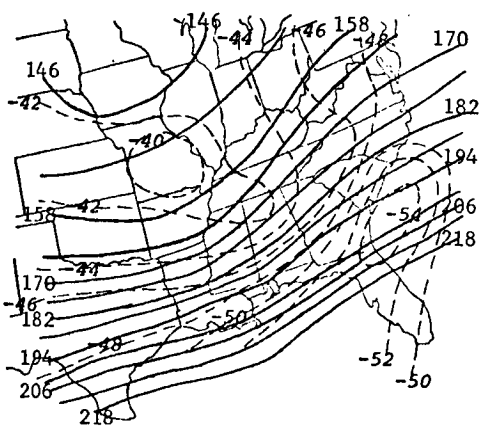

200 mb

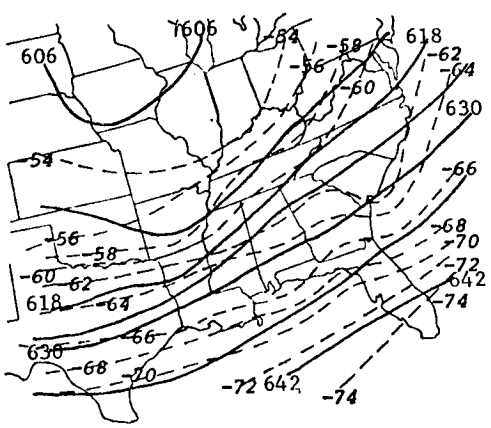

100 mb

Fig. 5. (Continued)

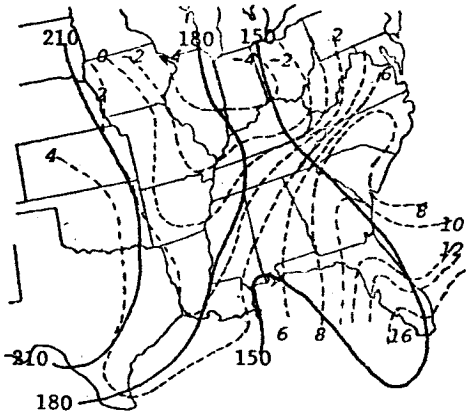

1000 mb

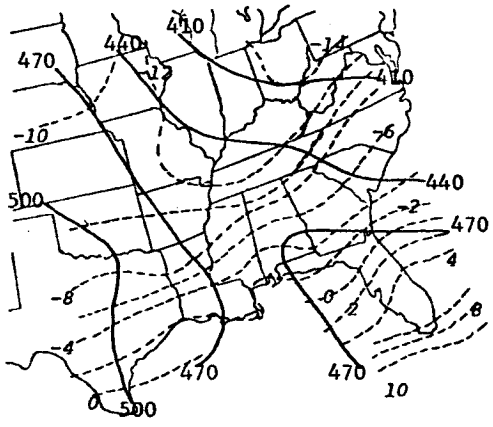

850 mb

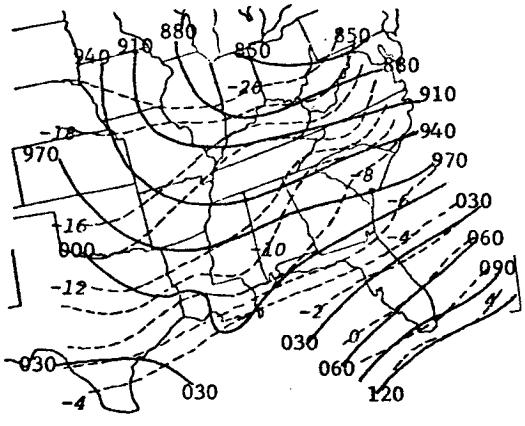

700 mb

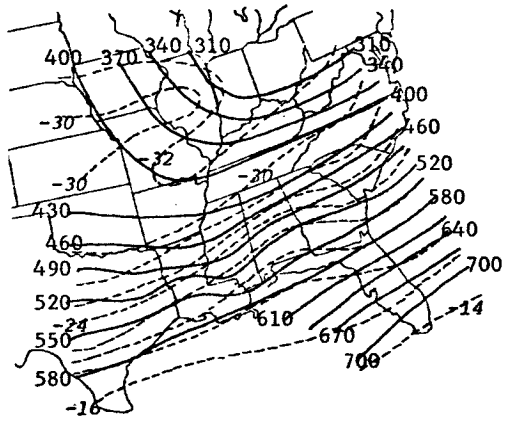

500 mb

Fig. 6. Synoptic conditions at 21 GMT, February 21.

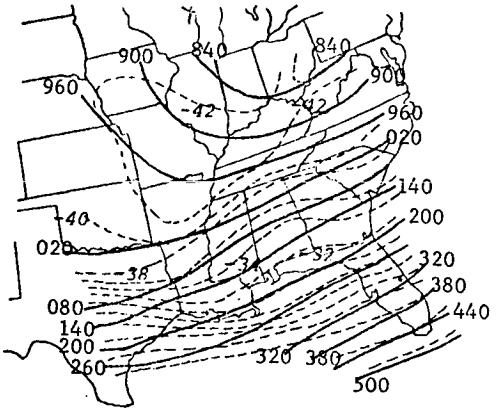

400 mb

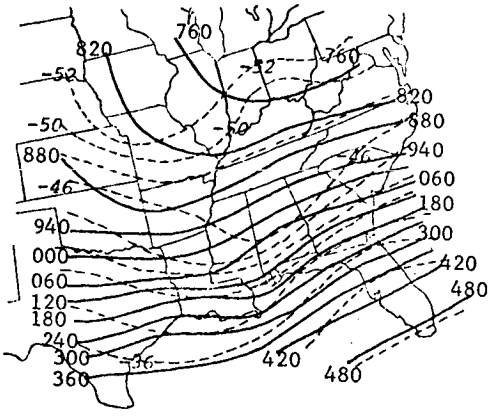

300 mb

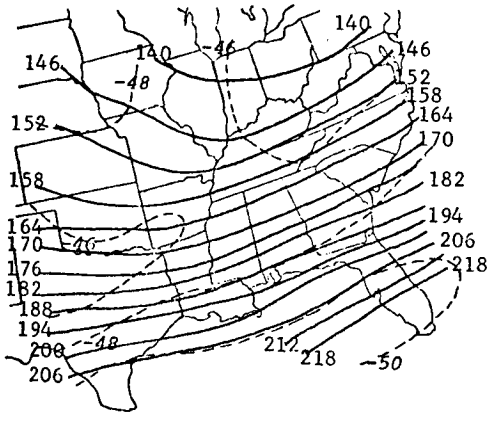

200 mb

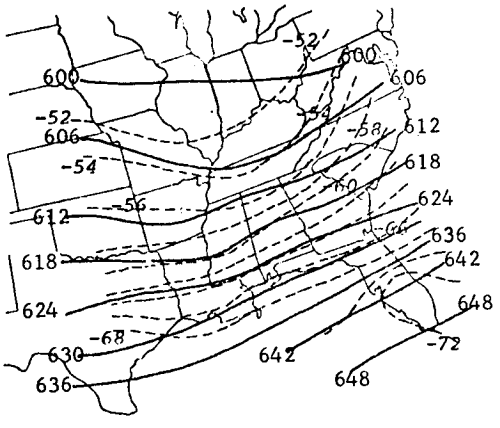

100 mb

Fig. 6. (Continued)

Conditions at 850 mb were similar to those occurring at the surface. At the beginning of the period (00 GMT, February 19), the front extended from central Florida, over the Atlantic, and then into central North Carolina. By February 20 the front had moved to the south of the area outlined by the data.

The frontal system at 700 mb was along the East Coast and the panhandle of Florida at the beginning of the time period, and moved to southern Florida where it became diffuse by the 22nd. A pronounced trough stretching from Ohio to Louisiana was present on the 19th and continued throughout the period with several short-wave troughs moving through the system. The cyclogenesis in the Gulf showed up well at the 700-mb level in the form of a short wave.

The flow at 500 mb in the southeastern United States was dominated by a long-wave trough which moved slowly from the westward edge of the region delineated by the data to the Atlantic Coast by the 22nd. The short-wave troughs at 700 mb were present also at 500 mb and could be followed easily using the AVE data. The frontal system at 500 mb stretched from central Virginia to Western Florida at the beginning of the period, and had moved to the Florida peninsula by 18 GMT, February 19. The front became difficult to locate in Florida by the 20th.

A long-wave trough dominated the 200-mb level. Short-wave troughs were traveling through the system as in the lower levels. Similar conditions were observed at 100 mb.

G. RESULTS

1. Orographic lifting

Values of terrain-induced vertical motion, collected at the 130 data points, indicate that this was an important factor in explaining the rain and no-rain areas. Table 1 gives the results where values of $w_s = 0$ were counted as indicating no rain. No-rain areas were explained correctly 77%

Table 1. Contingency table of sign of terrain-induced vertical motion.

Expected / Observed	Rain $w_s > 0$	No Rain $w_s \leq 0$
Rain	32	33
No Rain	15	50

Percent Explained: Rain 49.3%, No Rain 77.0%, Overall 63.0%

of the time by $w_s \leq 0$, but rain areas were explained correctly only about half of the time. The explanation of rain areas was computed by dividing the number of points which were expected to have rain and where it was actually observed (32) by the total of points where rain was observed (65). The explanation of no-rain areas was computed by dividing the number of points where no rain was expected and none was observed (50) by the total number of points where no rain was observed (65). The overall explanation was computed by dividing the sum of the number of correctly explained rain and no-rain cases (82) by the total number of cases (130). The cumulative frequency distribution (CFD) in Fig. 7 shows the tendency for rain cases to be explained by $w_s > 0$ and no-rain cases by $w_s \leq 0$. All of the no-rain cases occurred for $w_s \leq 1$ cm sec^{-1} as compared with only 77% of the rain cases.

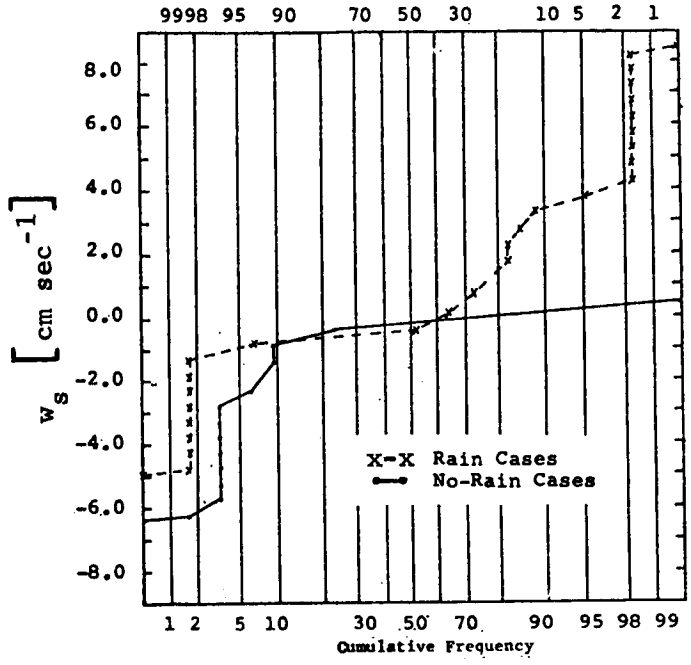

Fig. 7. Cumulative frequency distributions for terrain-induced vertical motions.

Precipitation maps show a striking relationship between terrain-induced vertical motion and 6-hr rainfall. Beginning at 12 GMT, February 20, the eastward extent of rainfall in the Tennessee and Ohio River Valleys roughly coincided with the ridge line of the Appalachian Mountains. Three examples of this effect which continued for 11 time periods until the end of the study are given in Fig. 8; convergence patterns at 850 mb also are outlined. Westerly winds at the 925-mb level were occurring throughout the time periods mentioned. These rainfall patterns were observed in spite of the fact that there was predominant convergence to the east of the mountains at 700 mb and below, while predominant divergence occurred to the west of the

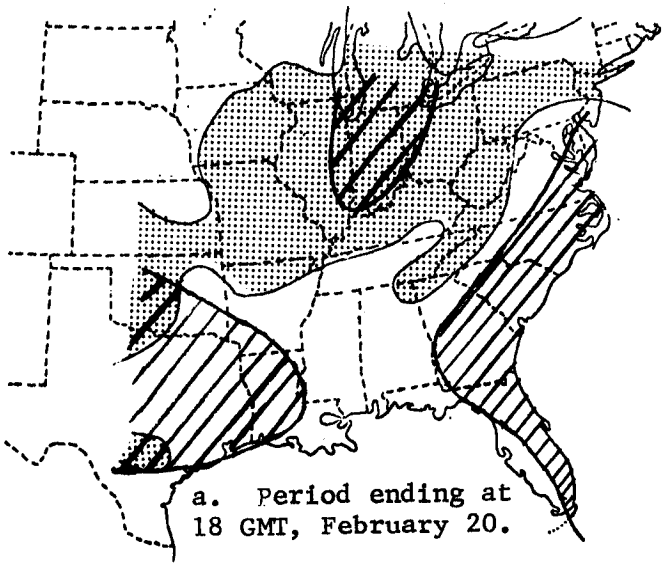

a. Period ending at 18 GMT, February 20.

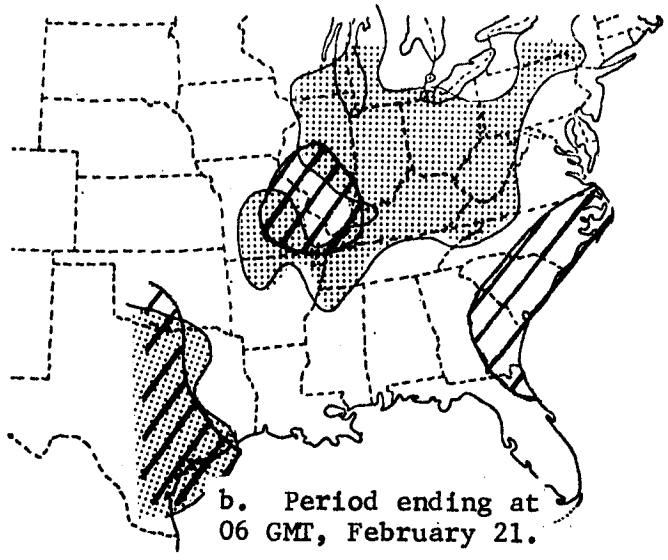

b. Period ending at 06 GMT, February 21.

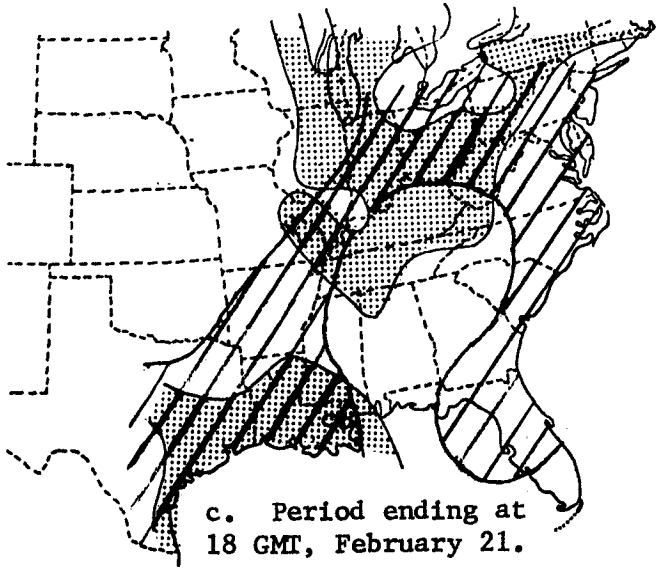

c. Period ending at 18 GMT, February 21.

Rain Area

$\vec{\nabla}\cdot\vec{V} < 0.0$ at 850 mb

Fig. 8. Maps showing the relationship between terrain-induced vertical motion and 6-hr precipitation.

Appalachians. The terrain effect dominated that of convergence and divergence in these areas. In some of the earlier time periods, the low-level convergence to the east of the mountains outweighed the negative terrain-induced vertical motion so that rainfall did occur. An example of this is given in the next section.

Based on these results, terrain-induced vertical motion should always be considered in explaining and predicting precipitation, although it is frequently neglected.

2. Kinematic method

The kinematic method considers terrain-induced vertical motion already found to be important in this synoptic situation, and adds the effects of divergence at various levels above the station.

850-mb level. Values of vertical motion at 850 mb obtained by the kinematic method produced agreement with areas of precipitation which were superior to that of any other method. Results were much better than those obtained by Hansen and Thompson (1965), who did not include terrain effects and who used vertical motion at 700 mb for verification. Table 2 shows that the combination of rain and no-rain cases was correctly explained 80.8% of the time. There was no appreciable difference in the accuracy of the

Table 2. Contingency table of sign of vertical motion at 850 mb determined by the kinematic method.

Expected / Observed	Rain $w > 0$	No Rain $w \leq 0$
Rain	51	14
No Rain	11	54

Percent Explained: Rain 78.5%, No Rain 83.2%, Overall 80.8%

method between rain and no-rain categories. The CFD, shown in Fig. 9, indicates that the median value of vertical motion for rain cases is 0.25 cm sec^{-1} while for the no-rain cases it is -0.75 cm sec^{-1}. For values less than 1.0 cm sec^{-1}, only 70% of the rain cases occurred while 97.5% of the no-rain cases occurred. Only 8% of the rain cases occurred for values less

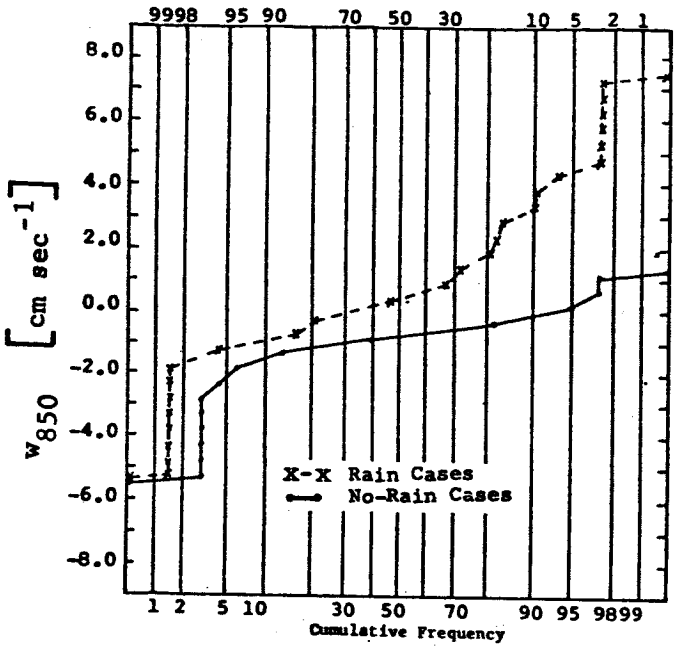

Fig. 9. Cumulative frequency distributions of vertical motion at 850 mb determined by the kinematic method.

than -1.0 cm sec^{-1} as compared with 30% of the no-rain cases. Although 9.0% of the no-rain cases occurred for values between 0.0 and 2.0 cm sec^{-1}, 48.0% of the rain occurred in that interval. A good horizontal displacement is noted between the two curves, especially for $w > 0$.

700-mb level. The kinematic method produced slightly poorer results at the 700-mb level. Table 3 indicates that the percent of rain and no rain explained dropped 16.3% compared to the values at 850 mb, but there is a

Table 3. Contingency table of sign of vertical motion at 700 mb determined by the kinematic method.

Expected / Observed	Rain $w > 0$	No Rain $w \leq 0$
Rain	41	24
No Rain	22	43

Percent Explained: Rain 63.1%, No Rain 66.4%, Overall 64.5%

greater spread between the lines of rain and no-rain cases on the CFD at 700 mb than at 850 mb (see Fig. 10). The median value of vertical motion for rain cases is 0.8 cm sec^{-1} while for no-rain cases it is -0.9 cm sec^{-1}. At values less than 1.0 cm sec^{-1}, only 51% of the rain cases occurred as compared with 95.5% of the no-rain cases. At values less than -1.0 cm sec^{-1}, 20% of the rain cases occurred as compared with 48% of the no-rain cases.

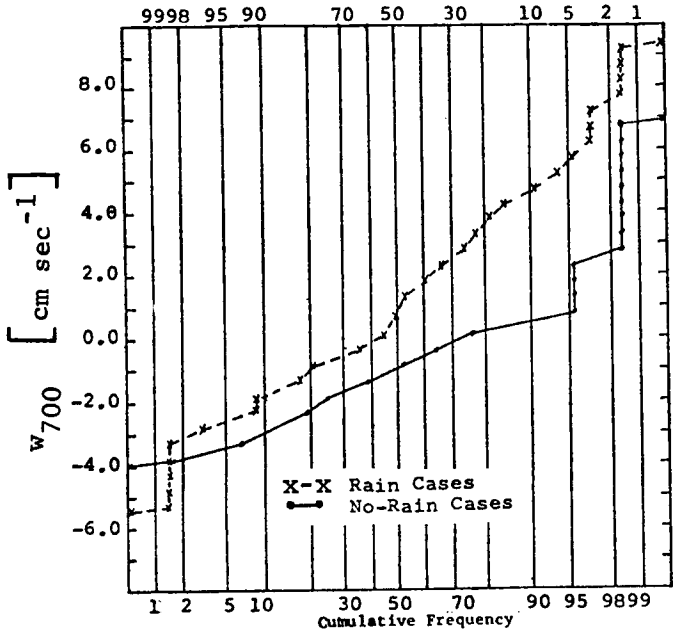

Fig. 10. Cumulative frequency distributions of vertical motion at 700 mb determined by the kinematic method.

Between -1.0 cm sec^{-1} and 1.0 cm sec^{-1}, 22% of the rain cases, and 24.5% of the no-rain cases occurred. As more values of vertical motion deviated significantly from zero, some of them obtained a sign which was different from that expected in the particular rain or no-rain situation. Lower values of the percent explained resulted but the greater spread between curves is a desireable feature since it better distinguishes between rain and no-rain areas.

400-mb level. Values of vertical motion at 400 mb obtained by the kinematic method explained a lower percentage than those at lower levels, thus indicating that the processes producing rainfall were occurring primarily in the lower troposphere. The assumptions made in the computational procedures may have contributed to errors as well. Table 4 shows that while rain areas continued to be explained with 63.1% accuracy, no-rain areas were explained with only 46.2% accuracy, a drop of about 20% compared to the 700-mb level. The frequency distributions of vertical motion at 400 mb in Fig. 11 indicate little difference between values for rain and no-rain

Table 4. Contingency table of sign of vertical motion at 400 mb determined by the kinematic method.

Expected / Observed	Rain $w > 0$	No Rain $w \leq 0$
Rain	41	24
No Rain	35	30

Percent Explained: Rain 63.1%, No Rain 46.2%, Overall 54.5%

cases. At the 700-mb level, decreased explanation compared to the 850-mb level was accompanied by a better distinction between values of the two cases (rain and no-rain); this did not occur at 400 mb.

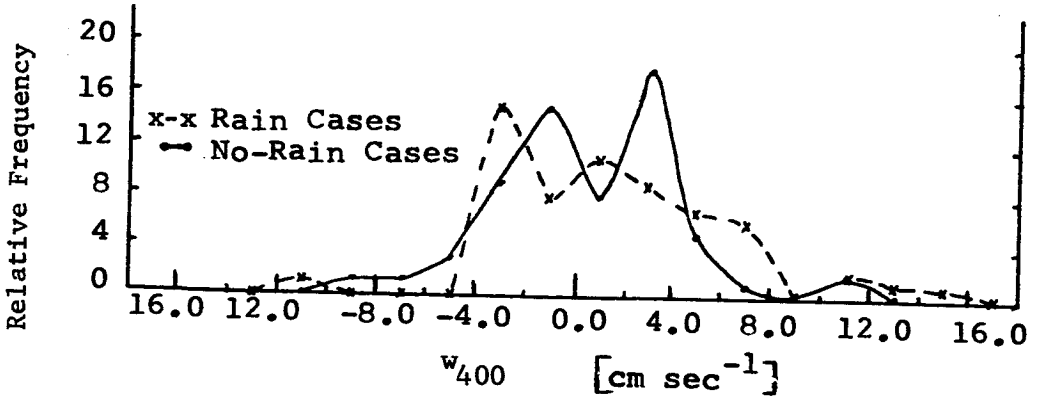

Fig. 11. Frequency distributions of vertical motion at 400 mb determined by the kinematic method.

The effect of moisture. If insufficient moisture is present in areas of positive vertical motion, rainfall will not occur. Figure 12 shows the relation between average relative humidity between 850-700 mb, vertical motion at 850 mb, and rainfall occurrence. As expected, rainfall was accompanied by increased average relative humidity. Some points which had positive vertical motion also had low humidity values so that precipitation probably would not have occurred even though the point was counted as indicating precipitation.

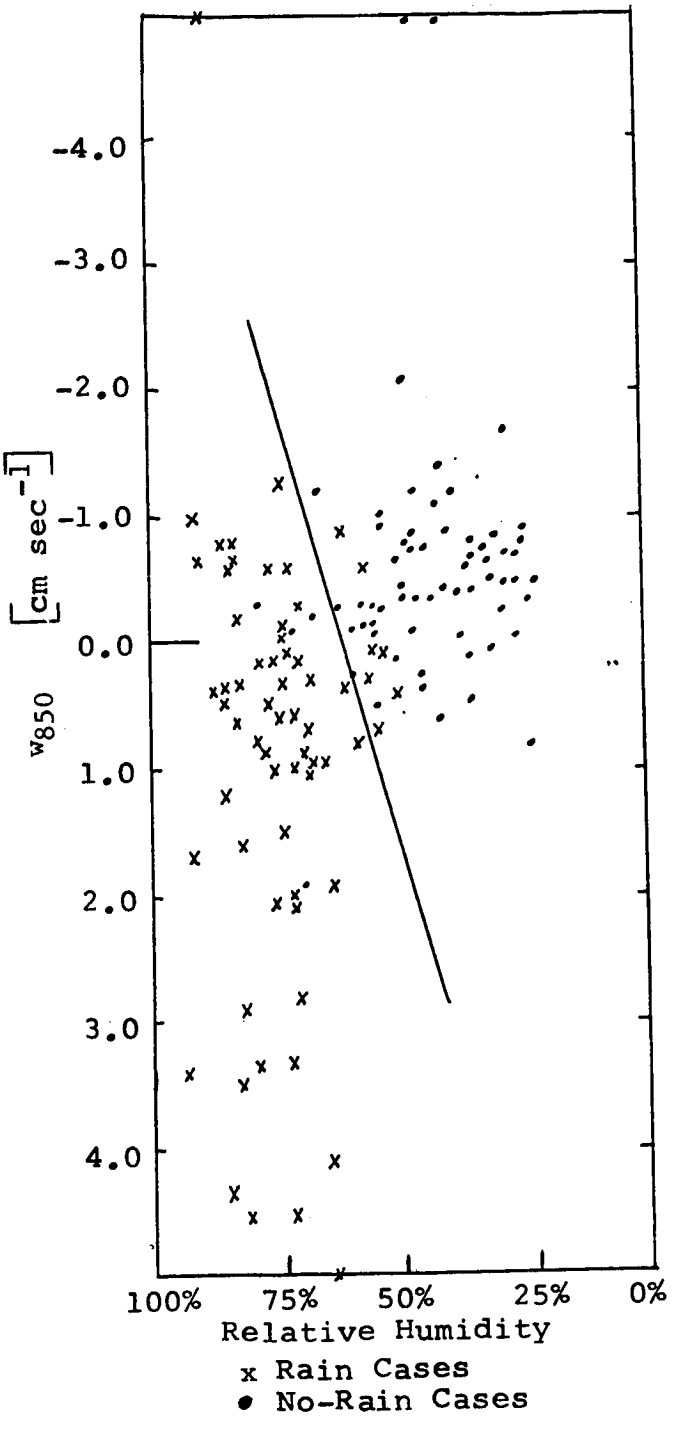

Fig. 12. Scatter diagram of average relative humidity between 850 and 700 mb and vertical motion at 850 mb vs rain and no rain.

To separate the rain and no-rain cases, a line was drawn from the upper-left corner to the lower-right corner of the diagram. This orientation of the line was expected since large values of positive vertical motion would require less moisture to produce rainfall than would smaller values of vertical motion (Miller and Panofsky, 1958). A somewhat similar result was obtained for vertical motion at 850 mb, and for different combinations of vertical motion and average relative humidity.

The case of 00 GMT, February 20. The rainfall pattern for the 6-hr period ending at 00 GMT, February 20 (Fig. 13) illustrates the delicate balance between terrain-induced vertical motion and vertical motion produced by divergence. Divergence and moisture patterns indicate that there should be no break between the rain area east of the Appalachians and the area in

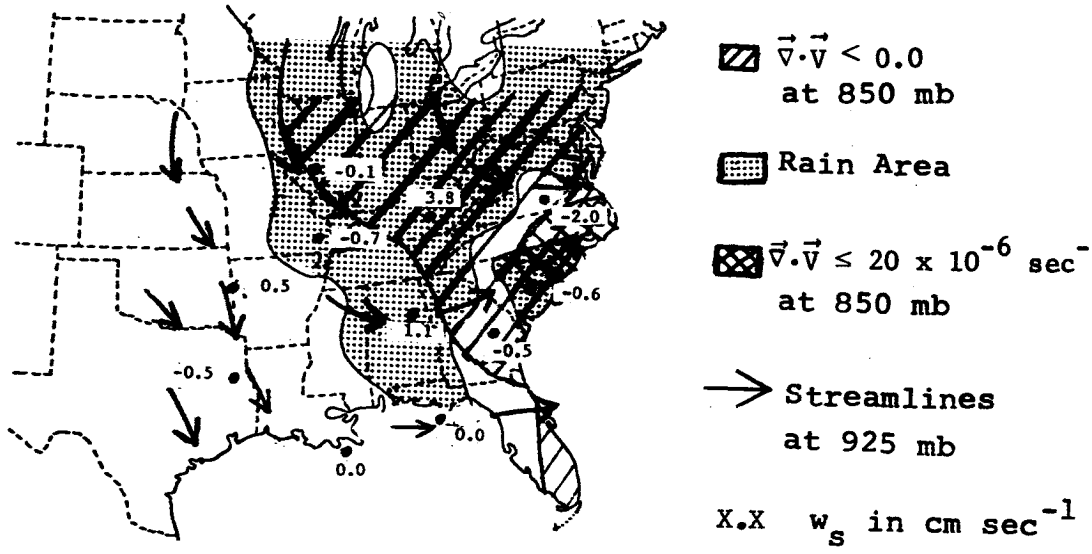

Fig. 13. Map showing the relationship between terrain-induced vertical motion and 6-hr precipitation for the period ending at 00 GMT, February 20.

southern North Carolina and coastal sections of South Carolina. The separation can be explained on the basis of orographic lifting. Streamlines at 925 mb are shown in Fig. 13 along with several values of the terrain-induced vertical motion. The areas of convergence and values greater than 20×10^{-6} sec^{-1} are indicated. Positive terrain-induced vertical motion occurred west of the mountains while downslope flow occurred to the east. The downslope flow cancelled the effect due to convergence directly east of the mountains. The location of the area of largest convergence, coupled with the rapid decrease in downslope flow, caused the rainfall to begin again in the Carolinas where downslope flow became too weak to counteract the positive vertical motion produced by low-level convergence.

3. Vorticity equation combined with Dines' Compensation Principle

Use of the vorticity equation, Eq. (7), to obtain the sign of divergence from which vertical motion could be inferred gave poor results in this situation. Terrain-induced vertical motion was not considered. More sophisticated techniques and the inclusion of moisture may have produced results comparable to those of the other methods.

The advective term. Meteorologists often use a rule which states that positive vorticity advection above the level of non-divergence, here assumed to be 600 mb, and/or negative vorticity advection below it, is an indicator of positive vertical motion in the mid-troposphere. The term $\frac{\partial \eta}{\partial t}$ is assumed to be small in comparison to the advection term. This rule gave poor results for the synoptic situation examined in this study. Tables 5-8 show that the sign of vertical motion inferred from the sign of vorticity advection explained only about 50% of the rain and no-rain areas at each of

Table 5. Contingency table of sign of $-\vec{V}\cdot\vec{\nabla}\eta$ at 925 mb.

Expected / Observed	Rain $-\vec{V}\cdot\vec{\nabla}\eta < 0$	No Rain $-\vec{V}\cdot\vec{\nabla}\eta > 0$
Rain	13	52
No Rain	14	51

Percent Explained: Rain 20.0%, No Rain 78.5%, Overall 49.3%

Table 6. Contingency table of sign of $-\vec{V}\cdot\vec{\nabla}\eta$ at 850 mb.

Expected / Observed	Rain $-\vec{V}\cdot\vec{\nabla}\eta < 0$	No Rain $-\vec{V}\cdot\vec{\nabla}\eta > 0$
Rain	16	49
No Rain	23	42

Percent Explained: Rain 24.6%, No Rain 64.6%, Overall 44.6%

Table 7. Contingency table of sign of $-\vec{V}\cdot\vec{\nabla}\eta$ at 700 mb.

Expected / Observed	Rain $-\vec{V}\cdot\vec{\nabla}\eta < 0$	No Rain $-\vec{V}\cdot\vec{\nabla}\eta > 0$
Rain	33	32
No Rain	27	38

Percent Explained: Rain 50.8%, No Rain 58.5%, Overall 54.6%

Table 8. Contingency table of sign of $-\vec{V}\cdot\vec{\nabla}\eta$ at 500 mb.

Expected / Observed	Rain $-\vec{V}\cdot\vec{\nabla}\eta > 0$	No Rain $-\vec{V}\cdot\vec{\nabla}\eta < 0$
Rain	32	33
No Rain	33	32

Percent Explained: Rain 49.3%, No Rain 49.3%, Overall 49.3%

the levels in Set 2. No-rain cases were explained best by conditions existing in the lower levels where positive vorticity advection was occurring primarily. The accuracy of the method for the no-rain cases increased from 49.3% at 500 mb to 78.5% at 925 mb. Values of the advective term, however, failed to distinguish rain areas from no-rain areas in the large regions of positive vorticity advection on the back side of the east coast cyclone. Rain cases were explained better by conditions in high levels (700 and 500 mb). The explanation of the rain cases increased from 20.0% at 925 mb to 49.3% at 500 mb. The trough was more nearly in the center of the study area at upper levels than at lower levels thereby giving more negative values of vorticity advection. Frequency distributions for values of vorticity advection indicate no significant difference between values occurring in rainfall and no-rainfall cases (see Figs. 14 and 15).

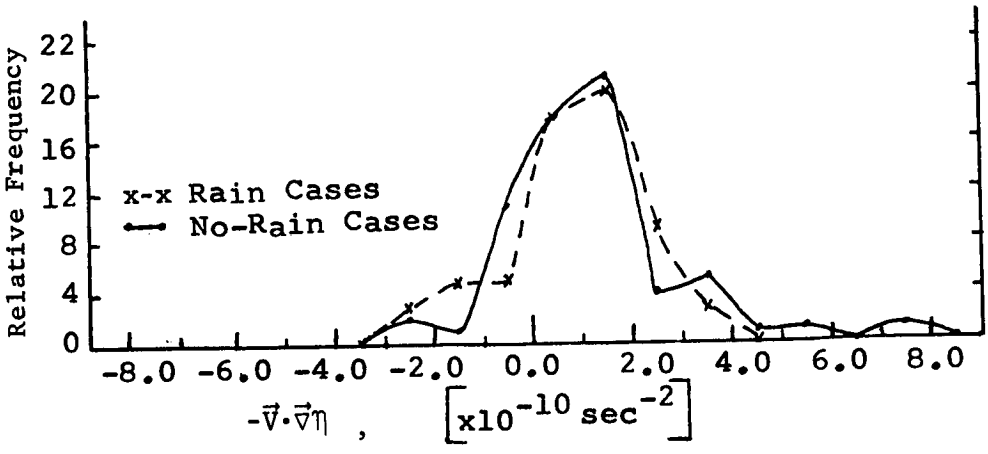

Fig. 14. Frequency distributions of $-\vec{V}\cdot\vec{\nabla}\eta$ at 925 mb.

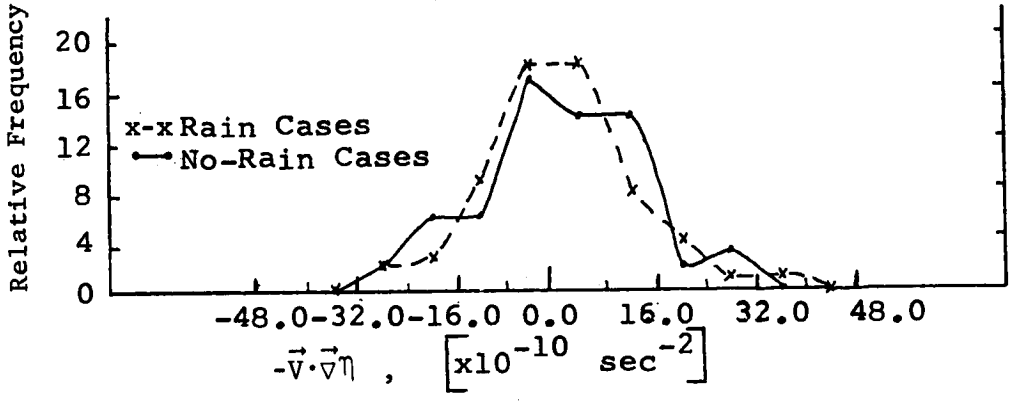

Fig. 15. Frequency distributions of $-\vec{V}\cdot\vec{\nabla}\eta$ at 500 mb.

Inclusion of the local term. The local rate-of-change term, $\frac{\partial \eta}{\partial t}$, was included in the vorticity equation in an attempt to determine its importance to the method and to improve results (see Tables 9-12). The addition of the term caused the left-hand side of Eq. (7) to be negative

Table 9. Contingency table of sign of $\left(-\frac{\partial \eta}{\partial t} - \vec{V}\cdot\vec{\nabla}\eta\right)$ at 925 mb.

Observed \ Expected	Rain $(-\frac{\partial \eta}{\partial t} - \vec{V}\cdot\vec{\nabla}\eta)<0$	No Rain $(-\frac{\partial \eta}{\partial t} - \vec{V}\cdot\vec{\nabla}\eta)>0$
Rain	23	42
No Rain	17	44

Percent Explained: Rain 36.0%, No Rain 72.3%, Overall 53.6%

Table 10. Contingency table of sign of $(-\frac{\partial \eta}{\partial t} - \vec{V}\cdot\vec{\nabla}\eta)$ at 850 mb.

Observed \ Expected	Rain $(-\frac{\partial \eta}{\partial t} - \vec{V}\cdot\vec{\nabla}\eta)<0$	No Rain $(-\frac{\partial \eta}{\partial t} - \vec{V}\cdot\vec{\nabla}\eta)>0$
Rain	22	43
No Rain	25	36

Percent Explained: Rain 34.4%, No Rain 59.0%, Overall 46.4%

Table 11. Contingency table of sign of $(-\frac{\partial \eta}{\partial t} - \vec{V}\cdot\vec{\nabla}\eta)$ at 700 mb.

Observed \ Expected	Rain $(-\frac{\partial \eta}{\partial t} - \vec{V}\cdot\vec{\nabla}\eta)<0$	No Rain $(-\frac{\partial \eta}{\partial t} - \vec{V}\cdot\vec{\nabla}\eta)>0$
Rain	32	33
No Rain	26	35

Percent Explained: Rain 49.2%, No Rain 57.4%, Overall 53.6%

Table 12. Contingency table of sign of $(-\frac{\partial \eta}{\partial t} - \vec{V}\cdot\vec{\nabla}\eta)$ at 500 mb.

Observed \ Expected	Rain $(-\frac{\partial \eta}{\partial t} - \vec{V}\cdot\vec{\nabla}\eta)>0$	No Rain $(-\frac{\partial \eta}{\partial t} - \vec{V}\cdot\vec{\nabla}\eta)<0$
Rain	30	34
No Rain	32	29

Percent Explained: Rain 46.9%, No Rain 47.6%, Overall 47.2%

more often than previously in the lower levels. (Note that one rain case and four no-rain cases were lost because $\frac{\partial \eta}{\partial t}$ could not be computed at the last time period because of the lack of data). Improved explanation of rain cases and poorer explanation of no-rain cases was obtained at all levels producing a slight overall improvement at 925 mb and 850 mb. At the 700- and 500-mb levels, a slight overall decrease in the explanation of rain and no-rain cases was obtained. Frequency distributions of $(-\frac{\partial \eta}{\partial t} - \vec{V}\cdot\vec{\nabla}\eta)$ given in Figs. 16 and 17 for 925 and 500 mb

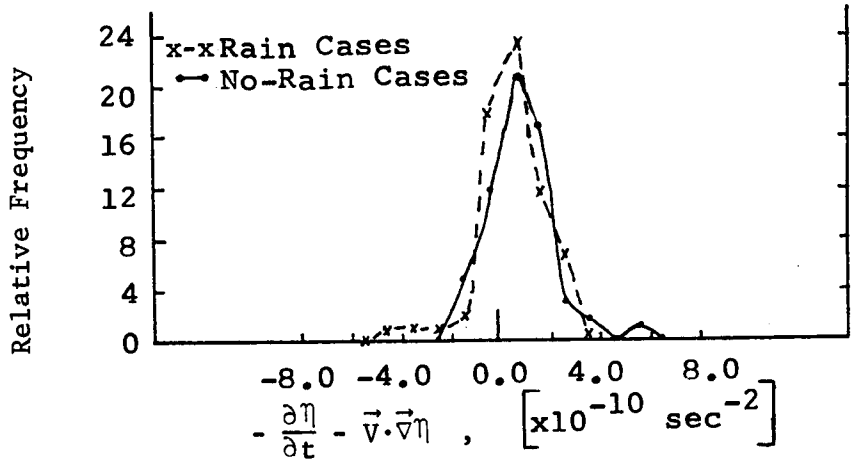

Fig. 16. Frequency distributions of $(-\frac{\partial \eta}{\partial t} - \vec{V}\cdot\vec{\nabla}\eta)$ at 925 mb.

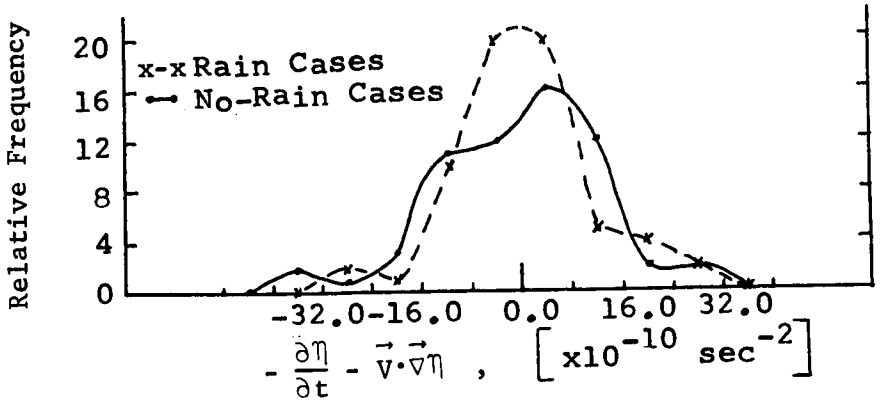

Fig. 17. Frequency distributions of $(-\frac{\partial \eta}{\partial t} - \vec{V}\cdot\vec{\nabla}\eta)$ at 500 mb.

show no significant difference between values for rain and no-rain cases. Also, there was no significant improvement between these curves and those which excluded the local rate-of-change term (Fig. 14 and 15). With respect to all levels, the inclusion of the local rate-of-change term did not significantly improve results.

4. Adiabatic Method

The adiabatic method gave results which at upper levels were superior to those obtained from the vorticity equation and the kinematic method which included orographic effects. At low levels, the results were about the same as those from the vorticity equation, but were much less accurate than those from the kinematic method.

The advective term. If the local rate-of-change of average potential temperature is assumed to be much smaller than the advective term and the atmosphere is statically stable, positive vertical motion is directly proportional to the advection of average potential temperature (Eq. 10). Results using the adiabatic method were poor in the 1000-850-mb layer. Table 13 indicates that 50.8% of all areas were correctly explained. Rainfall not associated with the Gulf cyclone was occurring on the back side of the system off the east coast -- a region of cold advection. The adiabatic method did not distinguish between rain and no-rain areas in this large region. Little difference was noted between the CFD of rain and no-rain cases (Fig. 18).

Table 13. Contingency table of sign of $-\vec{V}\cdot\vec{\nabla}\bar{\theta}$ in the 1000-850-mb layer.

Expected / Observed	Rain $-\vec{V}\cdot\vec{\nabla}\bar{\theta} > 0$	No Rain $-\vec{V}\cdot\vec{\nabla}\bar{\theta} < 0$
Rain	4	61
No Rain	3	62

Percent Explained: Rain 6.2%, No Rain 95.5%, Overall 50.8%

The adiabatic method, for this situation, produced better results with increasing height since a larger number of values of warm advection occurred in the 700-500-mb layer than in the 1000-850-mb layer. The effect of latent heat release became smaller with height, thus causing

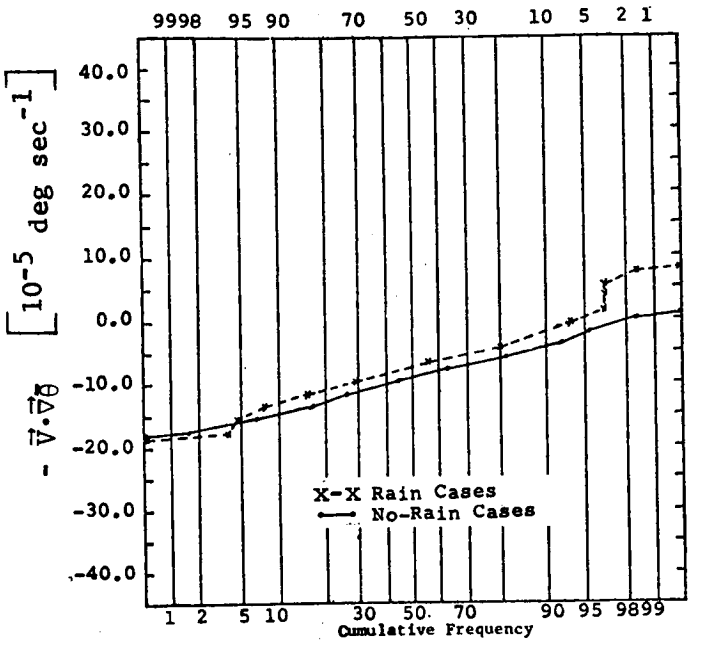

Fig. 18. Cumulative frequency distributions of $-\vec{V}\cdot\vec{\nabla}\bar{\theta}$ from 1000-850-mb.

fewer errors compared to lower levels since clouds were located mostly in the lower few thousand meters of the atmosphere. Table 14 indicates a 20% increase in the explanation of rain cases for the 850-700-mb layer compared to the 1000-850-mb layer; a 1.5% increase compared to the

Table 14. Contingency table of sign of $-\vec{V}\cdot\vec{\nabla}\bar{\theta}$ in the 850-700-mb layer.

Observed \ Expected	Rain $-\vec{V}\cdot\vec{\nabla}\bar{\theta} > 0$	No Rain $-\vec{V}\cdot\vec{\nabla}\bar{\theta} < 0$
Rain	17	48
No Rain	2	63

Percent Explained: Rain 26.2%, No Rain 97.0%, Overall 61.5%

1000-850-mb layer occurred for no-rain cases. An overall explanation of 61.5% was obtained. Figure 19 shows that in spite of poor explanation, there is good separation between the curves of rain and no-rain on the CFD. The median advection value for rain cases is $-4.5\text{x}10^{-5}$ deg sec^{-1} while for no-rain cases it is $-10.5\text{x}10^{-5}$ deg sec^{-1}. The slopes of the curves are similar for advection values below $-3.0\text{x}10^{-5}$ deg sec^{-1} but differ for larger values. Although 51% of the rain cases were associated with advection values greater than $-5.0\text{x}10^{-5}$ deg sec^{-1}, only 17% of the no-rain cases were associated with values greater than this amount.

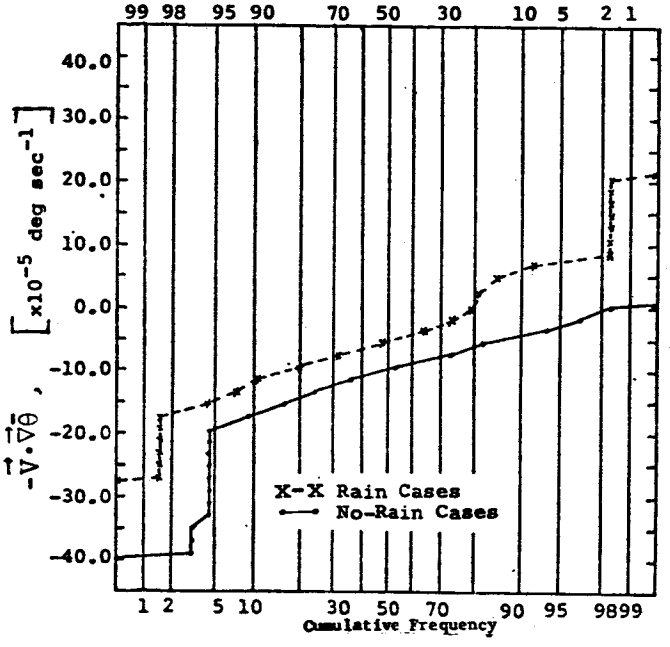

Fig. 19. Cumulative frequency distributions of $-\vec{V}\cdot\vec{\nabla}\bar{\theta}$ from 850-700 mb.

A significant improvement compared to lower levels occurred in the 700-500-mb layer (Table 15). The explanation of rain areas doubled, but a small decrease occurred in the no-rain category. An even better separation occurred between curves of the CFD. Median advection values of $-0.5\text{x}10^{-5}$ deg sec^{-1} and $-10.0\text{x}10^{-5}$ deg sec^{-1} are indicated, respectively, for rain and no-rain areas according to Fig. 20. For advection values greater than $-5.0\text{x}10^{-5}$ deg sec^{-1}, 66% of the rain cases occurred while only 23% of the no-rain cases occurred.

Inclusion of the local term. The local rate-of-change of average potential temperature was computed at each level in Set 1 to test the importance of the term and to attempt to improve results. The atmosphere was assumed to be stable, i.e., $\frac{\partial\bar{\theta}}{\partial z} > 0$. (Because $\frac{\partial\bar{\theta}}{\partial t}$ could not be computed

Table 15. Contingency table of sign of $-\vec{V}\cdot\nabla\vec{\theta}$ in the 700-500-mb layer.

Observed \ Expected	Rain $-\vec{V}\cdot\nabla\vec{\theta} > 0$	No Rain $-\vec{V}\cdot\nabla\vec{\theta} < 0$
Rain	35	30
No Rain	6	59

Percent Explained: Rain 53.8%, No Rain 91.0%, Overall 72.5%

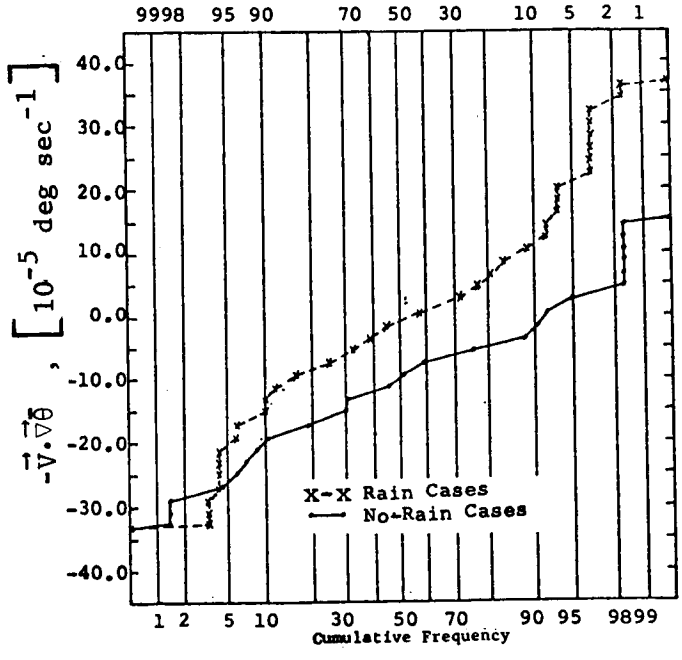

Fig. 20. Cumulative frequency distributions of $-\vec{V}\cdot\nabla\vec{\theta}$ from 700-500 mb.

at the first and last time periods, values for 9 rain cases and 9 no-rain cases were excluded.) Tables 16-18 show that rain areas were explained more accurately with the inclusion of the local term. The accuracy of the lowest level in explaining rainfall areas increased by 26% but was still only 32.2% accurate; rain areas at other levels also were forecast

Table 16. Contingency table of sign of $(-\frac{\partial\bar{\theta}}{\partial t} - \vec{V}\cdot\vec{\nabla}\bar{\theta})$ in the 1000-850-mb layer.

Observed \ Expected	Rain $(-\frac{\partial\bar{\theta}}{\partial t} - \vec{V}\cdot\vec{\nabla}\bar{\theta}) > 0$	No Rain $(-\frac{\partial\bar{\theta}}{\partial t} - \vec{V}\cdot\vec{\nabla}\bar{\theta}) < 0$
Rain	18	38
No Rain	13	43

Percent Explained: Rain 32.2%, No Rain 76.8%, Overall 54.4%

Table 17. Contingency table of sign of $(-\frac{\partial\bar{\theta}}{\partial t} - \vec{V}\cdot\vec{\nabla}\bar{\theta})$ in the 850-700-mb layer.

Observed \ Expected	Rain $(-\frac{\partial\bar{\theta}}{\partial t} - \vec{V}\cdot\vec{\nabla}\bar{\theta}) > 0$	No Rain $(-\frac{\partial\bar{\theta}}{\partial t} - \vec{V}\cdot\vec{\nabla}\bar{\theta}) < 0$
Rain	26	30
No Rain	7	49

Percent Explained: Rain 46.5%, No Rain 87.5%, Overall 67.0%

Table 18. Contingency table of sign of $(-\frac{\partial\bar{\theta}}{\partial t} - \vec{V}\cdot\vec{\nabla}\bar{\theta})$ in the 700-500-mb layer.

Observed \ Expected	Rain $(-\frac{\partial\bar{\theta}}{\partial t} - \vec{V}\cdot\vec{\nabla}\bar{\theta}) > 0$	No Rain $(-\frac{\partial\bar{\theta}}{\partial t} - \vec{V}\cdot\vec{\nabla}\bar{\theta}) < 0$
Rain	32	24
No Rain	8	48

Percent Explained: Rain 57.1%, No Rain 85.9%, Overall 71.4%

more accurately. Decreases in accuracy were noted for explanations of the no-rain cases at each level. An overall increase in accuracy resulted for the 1000-850-mb layer and the 850-700-mb layer, but a slight decrease occurred in the 700-500-mb layer. Overall accuracy continued to increase with height when the local term was included.

Although only slight overall improvements in explanation were obtained with the inclusion of the local term, more significant differences occurred between the CFD of the rain and no-rain cases at low levels (Figs. 21-23). Figure 21, for the 1000-850-mb layer, indicates that there is the tendency for rain cases to be explained by more positive

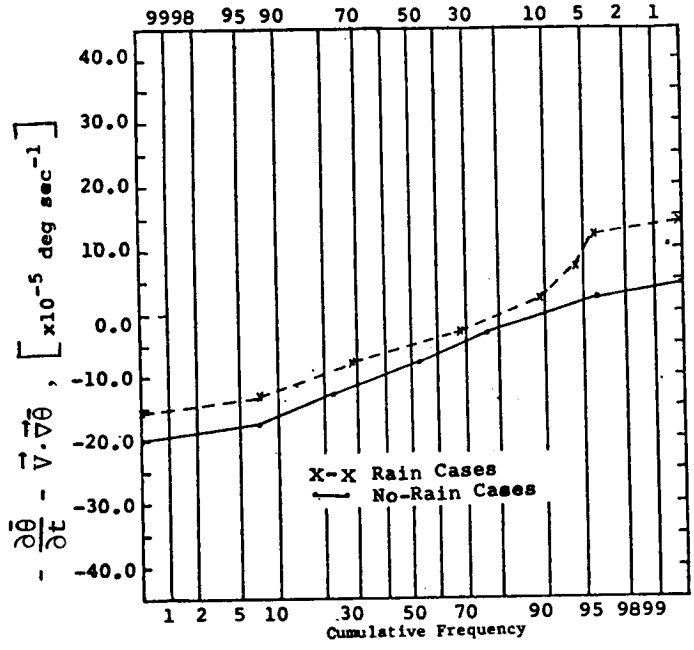

Fig. 21. Cumulative frequency distributions of $(-\frac{\partial\bar{\theta}}{\partial t} - \vec{V}\cdot\nabla\bar{\theta})$ from 1000-850 mb.

values of the term than no-rain cases. The median value for rain cases is $-5.0\text{x}10^{-5}$ deg sec^{-1} and is $-8.0\text{x}10^{-5}$ deg sec^{-1} for no-rain cases; 50% of the rain cases, but only 32% of the no-rain cases, occurred with $(-\frac{\partial\bar{\theta}}{\partial t} - \vec{V}\cdot\nabla\bar{\theta}) \geq 5.0$ deg sec^{-1}.

The separation between rain and no-rain curves on the cumulative frequency distribution (CFD) increased from the 1000-850-mb layer to the 850-700-mb layer. The 850-700-mb layer (Fig. 22) has median values of $3.0\text{x}10^{-5}$ deg sec^{-1} and $-9.0\text{x}10^{-5}$ deg sec^{-1} for rain and no-rain cases, respectively. The same spread of $6.0\text{x}10^{-5}$ deg sec^{-1} occurred without the inclusion of the local term. While 70% of the rain cases occurred for values greater than $-5.0\text{x}10^{-5}$ deg sec^{-1}, only 24% of the no-rain values occurred in this range. This is a spread of 46% compared to a spread of 34% without the local term.

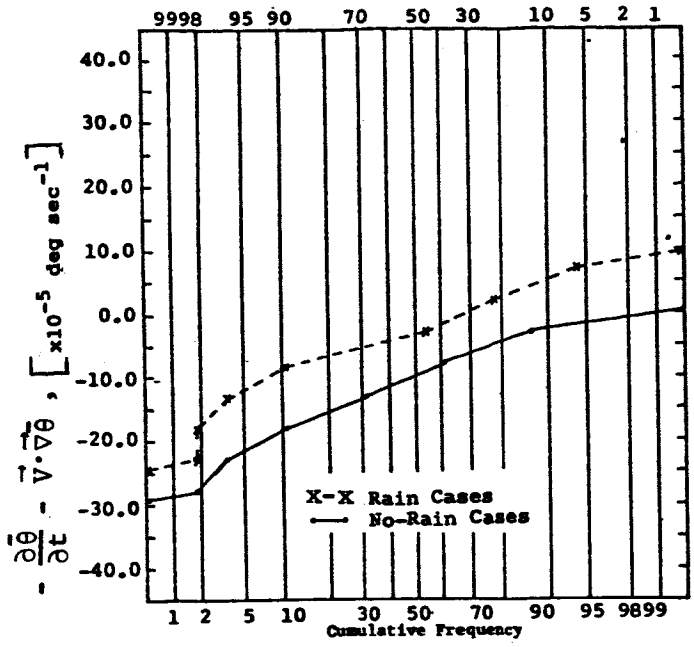

Fig. 22. Cumulative frequency distributions of $(-\frac{\partial\theta}{\partial t} - \vec{V}\cdot\vec{\nabla}\theta)$ for 850-700 mb.

The addition of the local term did not improve results in the 700-500-mb layer. Figure 23 indicates median values of $-1.0\text{x}10^{-5}$ deg sec^{-1} and $-9.5\text{x}10^{-5}$ deg sec^{-1} for rain and no-rain cases, respectively. The spread between median values was $8.5\text{x}10^{-5}$ deg sec^{-1} compared to $9.5\text{x}10^{-5}$

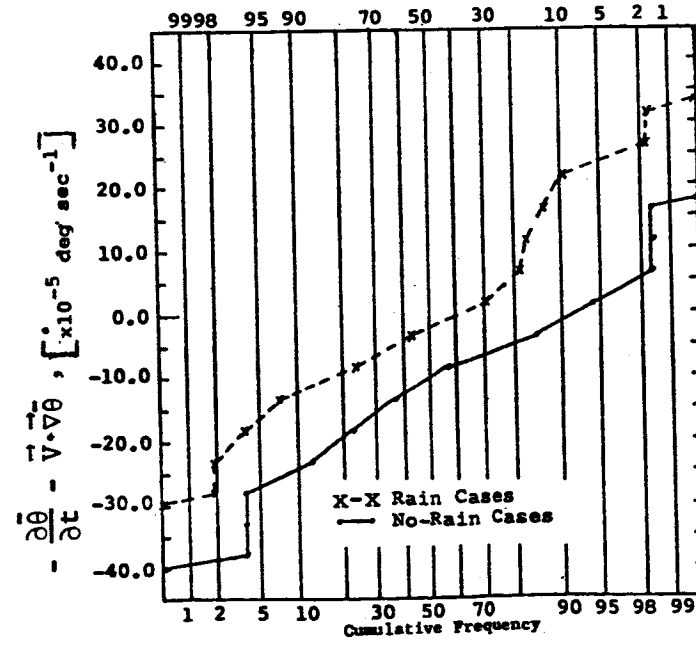

Fig. 23. Cumulative frequency distributions of $(-\frac{\partial\theta}{\partial t} - \vec{V}\cdot\vec{\nabla}\theta)$ for 700-500 mb.

deg sec^{-1} without the local term. For values greater than -5.0×10^{-5} deg sec^{-1}, 66% of the rain cases and 26% of the no-rain cases occurred; the spread of 40% is 3% smaller than that occurring without the local term.

The effect of moisture. Scatter diagrams were prepared with average relative humidity in a layer as one variable and the advective term or the sum of the advective term and local-change term as the second variable. Diagonal lines could be drawn from the upper-left to the lower-right corners of the graph to separate the two cases as was done in the kinematic method.

5. Omega Equation

The Laplacian of temperature advection used alone. The omega equation, Eq. (12) predicts that positive vertical motion will be proportional to positive values of $\left[-\vec{V}\cdot\vec{\nabla}\eta - \nabla^2(-\vec{V}\cdot\vec{\nabla}\bar{\theta})\right]$. The ability of the Laplacian term alone to explain rainfall areas compared to the advective and local rate-of-change terms of the adiabatic method is given in Table 19. When compared to the adiabatic method, the Laplacian term consistently explained rain areas more accurately. In the lowest level, a 29.3% improvement occurred, in the 850-700-mb layer a 15.0% improvement occurred, and in the 700-500-mb layer a 6.0% improvement was noted. Similar but slightly smaller decreases in accuracy occurred in the no-rain category. An average overall improvement of less than 1% took place in the three layers.

Table 19. A comparison of results of $-\nabla^2(-\vec{V}\cdot\vec{\nabla}\bar{\theta})$ with terms in the adiabatic method.

Layer and Method Used	Percent Explained		
	Rain Areas	No-Rain Areas	Overall
1000-850-mb layer			
$-\vec{V}\cdot\vec{\nabla}\bar{\theta}$	6.2	95.5	50.8
$-\frac{\partial\bar{\theta}}{\partial t} - \vec{V}\cdot\vec{\nabla}\bar{\theta}$	32.2	76.8	54.4
$-\nabla^2(-\vec{V}\cdot\vec{\nabla}\bar{\theta})$	61.5	50.8	56.1
850-700-mb layer			
$-\vec{V}\cdot\vec{\nabla}\bar{\theta}$	26.2	97.0	61.5
$-\frac{\partial\bar{\theta}}{\partial t} - \vec{V}\cdot\vec{\nabla}\bar{\theta}$	46.5	87.5	67.0
$-\nabla^2(-\vec{V}\cdot\vec{\nabla}\bar{\theta})$	61.5	72.5	66.9
700-500-mb layer			
$-\vec{V}\cdot\vec{\nabla}\bar{\theta}$	53.8	91.0	72.3
$-\frac{\partial\bar{\theta}}{\partial t} - \vec{V}\cdot\vec{\nabla}\bar{\theta}$	57.1	85.9	71.4
$-\nabla^2(-\vec{V}\cdot\vec{\nabla}\bar{\theta})$	63.1	81.7	72.3

At low levels, much less separation occurred between the CFD of rain and no-rain cases using the Laplacian compared with the advective term with or without the local rate-of-change term of the adiabatic method. The CFD for the 700-500-mb layer is shown in Fig. 24 where better separation occurred compared to terms of the adiabatic method (See Figs. 18-23). A median value of 5.0×10^{-16} deg sec^{-1} m^{-2} for rain cases and -15.0×10^{-16} deg sec^{-1} m^{-2} for no-rain cases is indicated.

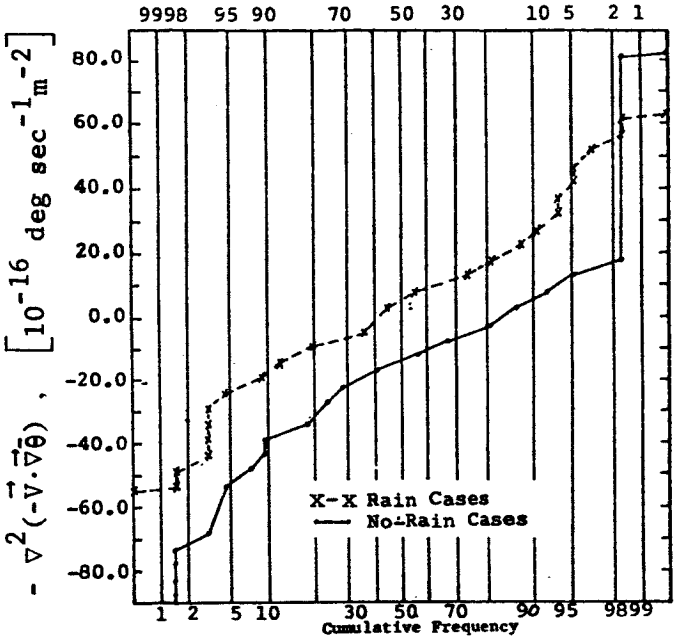

Fig. 24. Cumulative frequency distributions of $-\nabla^2(-\vec{V}\cdot\nabla\vec{\theta})$ for 700-500 mb.

Use of the Laplacian term. The advection of vorticity at 500 mb and the Laplacian of the advection of average potential temperature between 700-500 mb were used to evaluate the omega equation; Table 20 presents the results. The method gave correct explanations for rain and

Table 20. Contingency table of sign of $-\vec{V}\cdot\nabla\vec{\eta}$ at 500 mb and $-\nabla^2(-\vec{V}\cdot\nabla\vec{\theta})$ in the 700-500-mb layer as used in the omega equation.

Expected / Observed	Rain $-\vec{V}\cdot\nabla\vec{\eta} > 0$ $-\nabla^2(-\vec{V}\cdot\nabla\vec{\theta})>0$	Indeterminate Opposite Signs	No Rain $-\vec{V}\cdot\nabla\vec{\eta} < 0$ $-\nabla^2(-\vec{V}\cdot\nabla\vec{\theta})<0$
Rain	18	36	11
No Rain	4	36	25

Percent Explained: Correct 33.0%, Incorrect 11.5%, Indeterminate 55.5%

no-rain cases 33.0% of the time and incorrect explanations 11.5% of the time, but in 55.5% of the cases the signs of the terms were different thereby preventing the determination of the sign of vertical motion. (Note that the 700-500-mb layer consistently produced the best results in the adiabatic method and when the Laplacian alone was considered in the previous section.) In order to eliminate the indeterminate category, constant multipliers were introduced into the omega equation so that the two terms would have the same order of magnitude. The terms could then be added with each having about the same weight:

$$w = k_1\left[-\vec{V}\cdot\vec{\nabla}\eta\right] + k_2\left[-\nabla^2(-\vec{V}\cdot\vec{\nabla}\bar{\theta})\right] \quad . \tag{21}$$

The values chosen were $K_1 = 1$ and $K_2 = 10^6$. The results in Table 21 are much better than those obtained using vorticity advection alone, but worse than those obtained using the Laplacian alone. The no-rain cases were

Table 21. Contingency table of the sum of $k_1\left[-\vec{V}\cdot\vec{\nabla}\eta\right]$ at 500 mb and $k_2\left[-\nabla^2(-\vec{V}\cdot\vec{\nabla}\bar{\theta})\right]$ in the 700-500-mb layer.

Observed \ Expected	Rain $k_1\left[-\vec{V}\cdot\vec{\nabla}\eta\right] + k_2\left[-\nabla^2(-\vec{V}\cdot\vec{\nabla}\bar{\theta})\right] > 0$	No Rain $k_1\left[-\vec{V}\cdot\vec{\nabla}\eta\right] + k_2\left[-\nabla^2(-\vec{V}\cdot\vec{\nabla}\bar{\theta})\right] < 0$
Rain	35	30
No Rain	12	53

Percent Explained: Rain 53.8%, No Rain 81.7%, Overall 67.7%

explained with the same accuracy that was obtained using the Laplacian (81.7%), but the omega equation was about 10% less accurate in explaining the 65 rain cases. The use of temperature advection at 850-700 mb and vorticity advection at 500 mb produced less explanation than that obtained in the higher layer since temperature advection when used alone in the lower level was less accurate than when used at the upper level (Table 22). Table 23 shows that values obtained by adding terms in the omega equation for this layer also gave less explanation, especially for the no-rain cases. The equation yielded results which were intermediate to those obtained by evaluating each term separately. Both rain and no-rain cases were less accurate.

Table 22. Contingency table of sign of $-\vec{V}\cdot\vec{\nabla}\eta$ at 500 mb and $-\nabla^2(-\vec{V}\cdot\vec{\nabla}\theta)$ in the 850-700-mb layer as used in the omega equation.

Expected / Observed	Rain $-\vec{V}\cdot\vec{\nabla}\eta > 0$ $-\nabla^2(-\vec{V}\cdot\vec{\nabla}\theta)>0$	Indeterminate Opposite Signs	No Rain $-\vec{V}\cdot\vec{\nabla}\eta < 0$ $-\nabla^2(-\vec{V}\cdot\vec{\nabla}\theta)<0$
Rain	17	36	12
No Rain	7	38	20

Percent Explained: Correct 29.0%, Incorrect 15.0%, Indeterminate 56.0%

Table 23. Contingency table of the sum of $k_1\left[-\vec{V}\cdot\vec{\nabla}\eta\right]$ at 500 mb and $k_2\left[-\nabla^2(-\vec{V}\cdot\vec{\nabla}\theta)\right]$ in the 850-700-mb layer.

Expected / Observed	Rain $k_1\left[-\vec{V}\cdot\vec{\nabla}\eta\right] + k_2\left[-\nabla^2(-\vec{V}\cdot\vec{\nabla}\theta)\right]>0$	No Rain $k_1\left[-\vec{V}\cdot\vec{\nabla}\eta\right] + k_2\left[-\nabla^2(-\vec{V}\cdot\vec{\nabla}\theta)\right]<0$
Rain	34	31
No Rain	21	44

Percent Explained: Rain 52.3%, No Rain 67.7%, Overall 60.0%

Use of the temperature advection term. When temperature advection was considered instead of the Laplacian of temperature advection, similar results were obtained, if no addition was performed. Tables 24 and 25 indicate that advection, which is simple to determine, was nearly as accurate as the more complicated Laplacian term in explaining the 130 cases for the 700-500-mb layer and the 850-700-mb layer. The sign of vertical motion still could not be determined in many cases. Terms of this form of the equation were added as follows:

$$w = k_3\left[-\vec{V}\cdot\vec{\nabla}\eta\right] + k_4\left[-\vec{V}\cdot\vec{\nabla}\theta\right] \qquad (22)$$

Table 24. Contingency table of sign of $-\vec{V}\cdot\vec{\nabla}\eta$ at 500 mb and $-\vec{V}\cdot\vec{\nabla}\bar{\theta}$ in the 700-500-mb layer as used in the omega equation.

Expected / Observed	Rain $-\vec{V}\cdot\vec{\nabla}\eta > 0$ $-\vec{V}\cdot\vec{\nabla}\bar{\theta} > 0$	Indeterminate Opposite Signs	No Rain $-\vec{V}\cdot\vec{\nabla}\eta < 0$ $-\vec{V}\cdot\vec{\nabla}\bar{\theta} < 0$
Rain	14	37	14
No Rain	3	33	29

Percent Explained: Correct 33.0%, Incorrect 13.0%, Indeterminate 54.0%

Table 25. Contingency table of sign of $-\vec{V}\cdot\vec{\nabla}\eta$ at 500 mb and $-\vec{V}\cdot\vec{\nabla}\bar{\theta}$ in the 850-700-mb layer as used in the omega equation.

Expected / Observed	Rain $-\vec{V}\cdot\vec{\nabla}\eta > 0$ $-\vec{V}\cdot\vec{\nabla}\bar{\theta} > 0$	Indeterminate Opposite signs	No Rain $-\vec{V}\cdot\vec{\nabla}\eta < 0$ $-\vec{V}\cdot\vec{\nabla}\bar{\theta} < 0$
Rain	9	32	24
No Rain	1	34	30

Percent Explained: Correct 30.0%, Incorrect 19.0%, Indeterminate 51.0%

where $k_3 = 10^5$ and $k_4 = 1$. Table 26 shows a loss in overall explanation of 12.3% in the 700-500-mb layer when compared to results obtained using the Laplacian in the omega equation. A decrease in explanation of 9.3% occurred in the 850-700-mb layer when the advection term was used instead of the Laplacian term (Table 27). Rain cases showed the greatest loss in accuracy. Values of the Laplacian exhibited a large range and frequently were larger than those of advection even when multiplied by the constants. In each case, however, these terms had the same order of

Table 26. Contingency table of the sum of $k_3 [-\vec{V}\cdot\vec{\nabla}\eta]$ at 500 mb and $k_4 [-\vec{V}\cdot\vec{\nabla}\theta]$ in the 700-500-mb layer.

Observed \ Expected	Rain $k_3[-\vec{V}\cdot\vec{\nabla}\eta] + k_4[-\vec{V}\cdot\vec{\nabla}\theta] > 0$	No Rain $k_3[-\vec{V}\cdot\vec{\nabla}\eta] + k_4[-\vec{V}\cdot\vec{\nabla}\theta] < 0$
Rain	25	40
No Rain	18	47

Percent Explained: Rain 38.4%, No Rain 72.3%, Overall 55.4%

Table 27. Contingency table of the sum of $k_3 [-\vec{V}\cdot\vec{\nabla}\eta]$ at 500 mb and $k_4 [-\vec{V}\cdot\vec{\nabla}\theta]$ in the 850-700-mb layer.

Observed \ Expected	Rain $k_3[-\vec{V}\cdot\vec{\nabla}\eta] + k_4[-\vec{V}\cdot\vec{\nabla}\theta] > 0$	No Rain $k_3[-\vec{V}\cdot\vec{\nabla}\eta] + k_4[-\vec{V}\cdot\vec{\nabla}\theta] < 0$
Rain	16	49
No Rain	15	50

Percent Explained: Rain 24.6%, No Rain 77.0%, Overall 50.7%

magnitude as vorticity advection. Since the temperature terms were more accurate than the vorticity term, better results were obtained through use of the Laplacian than from temperature advection. If the less-accurate temperature-advection term were given greater weight, higher accuracies would result because the values obtained from the addition of terms would approach that obtained through use of the thermal term alone.

Maps of terms in the omega equation. In addition to checking the agreement between data points and results from the omega equation, maps were prepared that showed the rainfall areas with vorticity advection at 500 mb and either average potential temperature advection from 700-500 mb or the Laplacian of that quality. Values of w_s at several points were given in cm sec^{-1}. Examples are shown in Fig. 25 for rainfall

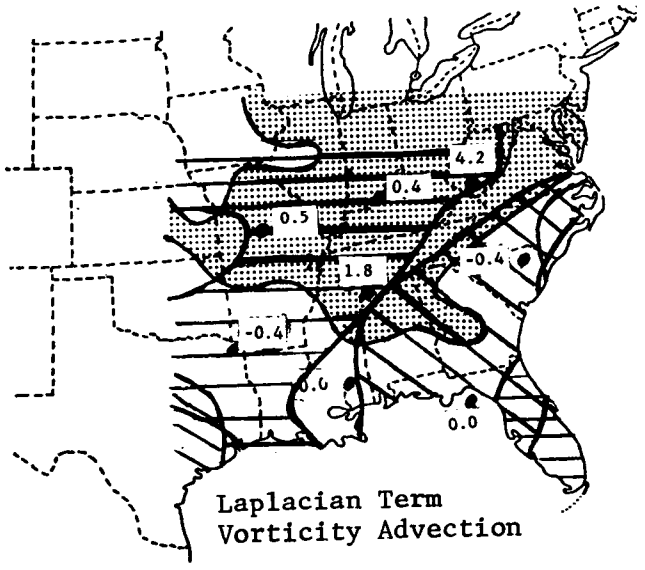

a. Period ending at 18 GMT, February 19.

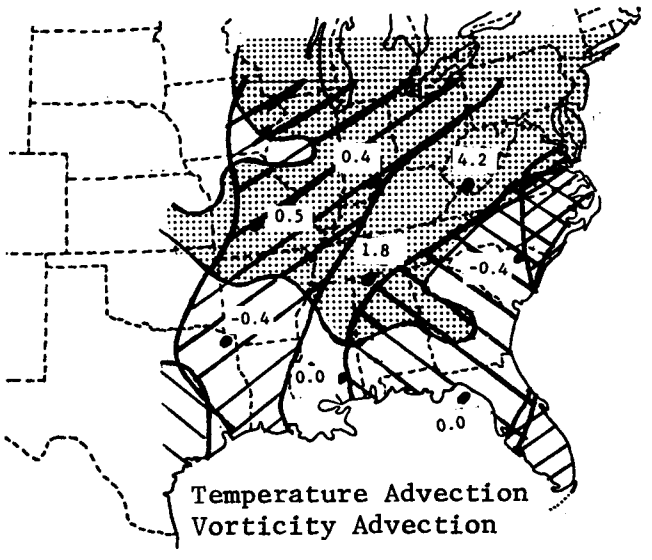

Rain Area

$(-\vec{V}\cdot\vec{\nabla}\eta)_{500} \geq 0$

$[-\nabla^2(-\vec{V}\cdot\vec{\nabla}\bar{\theta})]_{700\text{-}500} \geq 0$

$(-\vec{V}\cdot\vec{\nabla}\bar{\theta})_{700\text{-}500} \geq 0$

X.X w_s in cm sec^{-1}

Fig. 25. Maps of positive terms in the omega equation.

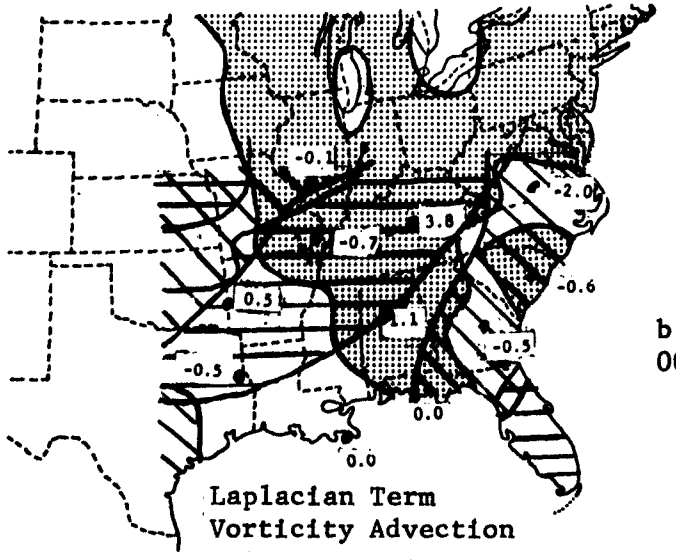

b. Period ending at 00 GMT, February 20.

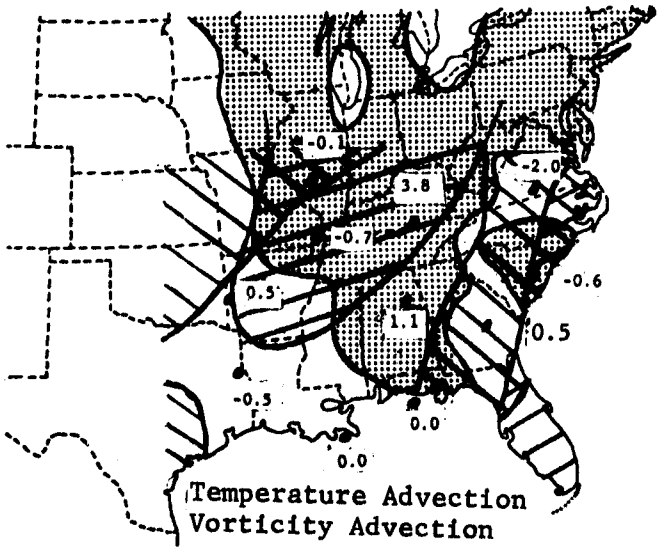

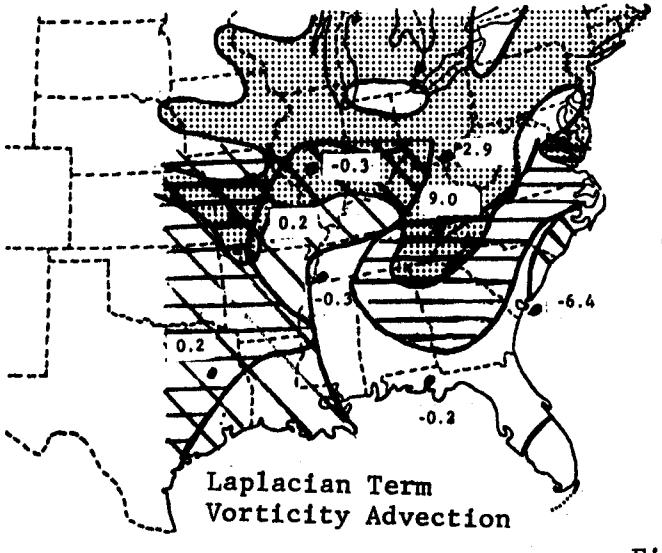

c. Period ending at 12 GMT, February 20.

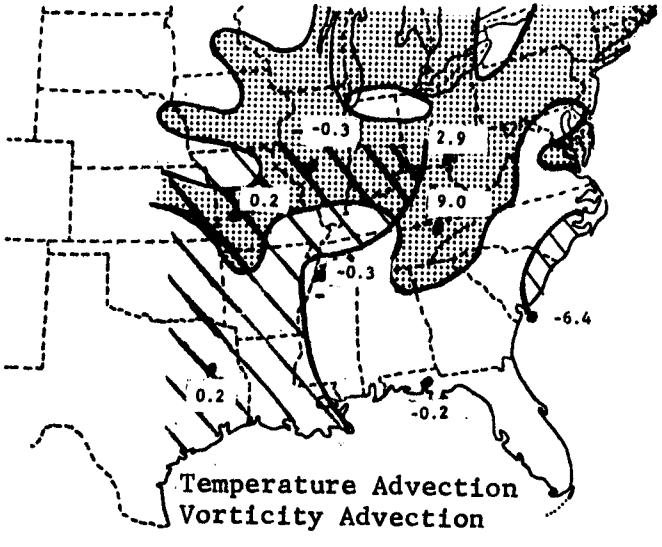

Fig. 25. (Continued)

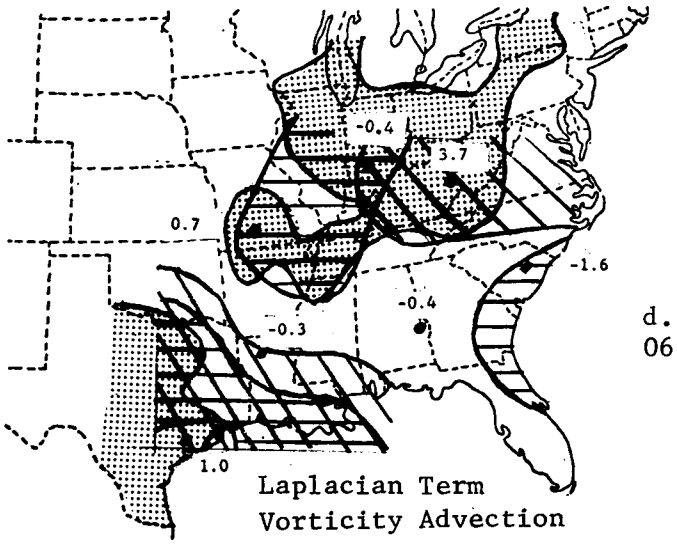

Laplacian Term
Vorticity Advection

d. Period ending at 06 GMT, February 21.

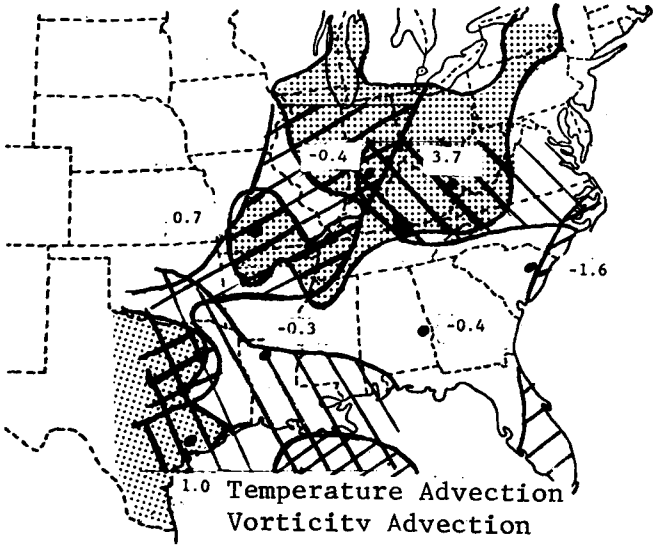

Temperature Advection
Vorticitv Advection

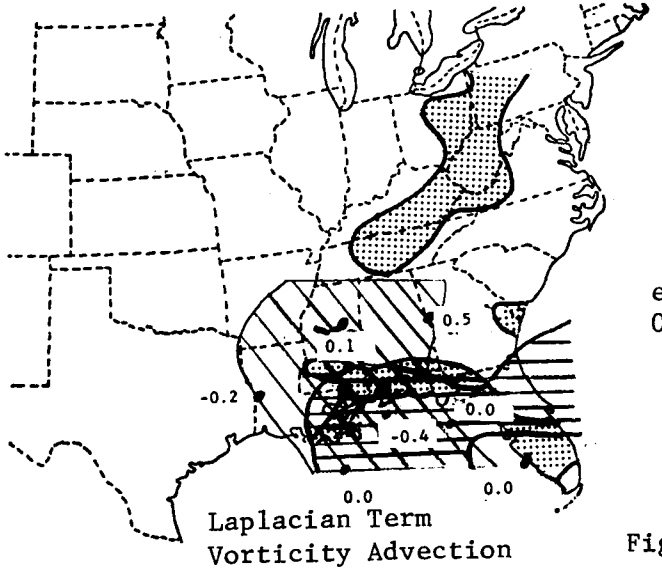

Laplacian Term
Vorticity Advection

e. Period ending at 06 GMT, February 22.

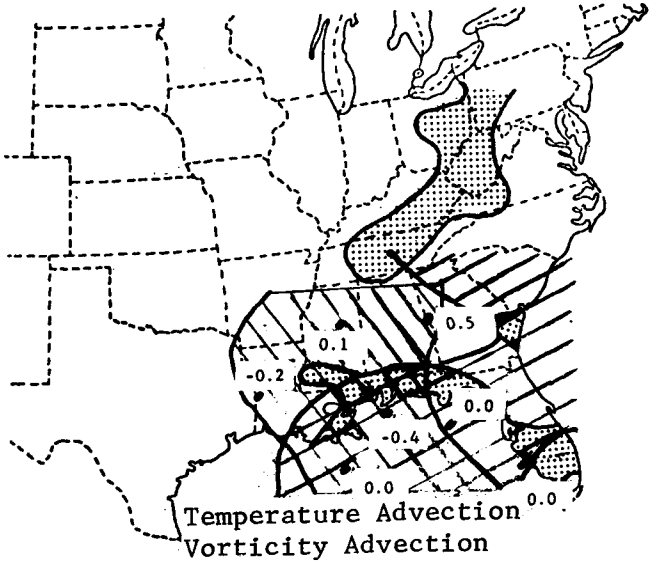

Temperature Advection
Vorticity Advection

Fig. 25. (Continued)

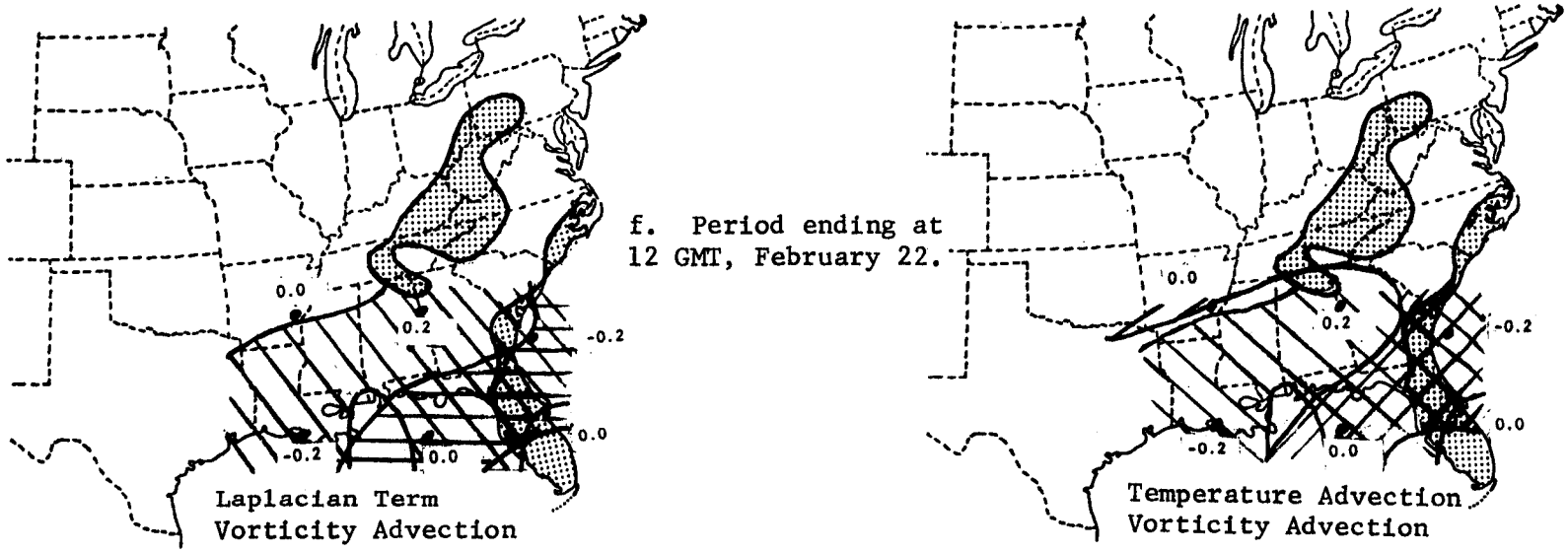

f. Period ending at 12 GMT, February 22.

Fig. 25. (Continued)

totals ending at 18 GMT, February 19, 00 GMT and 12 GMT, February 20, 06 GMT, February 21, and 06 GMT and 18 GMT, February 22. (The area for reliable data was reduced on the 22nd due to the failure of several rawinsonde stations to report.) The best results were associated with rainfall due to the Gulf cyclone, shown in the last three examples. Both positive temperature advection and a positive Laplacian term delineated areas of rainfall well when coupled with positive vorticity advection. Less agreement was found at 03 GMT, February 21, than the latter two examples because the cyclone was in the initial stages of development. Note that rain was expected in some regions where it did not occur and vice versa. Terrain-induced vertical motion was relatively small in this flat area along the coast.

Rainfall areas along the Appalachians and Ohio River Valley were not explained by the omega equation nearly as well as those occurring along the Gulf Coast. The orographic effect was found to be very important in the mountainous regions. The Laplacian of advection of average potential temperature rather than advection of that quantity was more accurate in explaining rain areas when coupled with vorticity advection. The advection of average potential temperature used with vorticity advection was more accurate in explaining no-rain areas. The overall accuracies were about the same. Few areas were found where either of the temperature terms overlapped the vorticity term in rainfall areas. There was no overlapping in rain areas between regions where the Laplacian term and the vorticity advection term were positive at 18 GMT, February 19. In addition, there was no overlapping of regions when temperature advection was used instead of the Laplacian. The opposite circumstances occurred at 12 GMT, February 20; the Laplacian term provided better agreement with rain areas than did the temperature advection term. The two forms of the omega equation (Eqs. 12-13) provided about equal agreement with the rain areas at 06 GMT, February 21. At all time periods, there were regions where overlapping is indicated but rainfall did not occur.

The values of terrain-induced vertical motion (w_s) explain much of the lack of agreement between observed rain areas in the Ohio River Valley and expected areas based on the omega equation. Each of the four unexplained data points in the rain area at 18 GMT, February 19, had positive values of w_s. The important effect of orographic lifting at 00 GMT, February 20, has been discussed previously (kinematic method, p.). At 12 GMT, February 20, upslope flow occurred at two of the three points in the rain area that were not explained by the omega equation when the Laplacian term was used. One point contained $w_s < 0$, however. At 06 GMT, February 21, one point in the rain area was explained by both forms of the omega equation although downslope flow was indicated. Two of the points were not explained by either form of the omega equation but can be explained on the basis of orographic lifting. Generally, rain areas coincided with positive regions of one of the terms, either the vorticity term or one of the temperature terms, but no-rain areas frequently did as well.

H. SUMMARY AND CONCLUSIONS

Five indicators of vertical motion were investigated to determine which gave the best explanation for rain and no-rain areas in the southeastern United States during the period February 19-22, 1964. The methods used were the terrain-induced vertical motion, the kinematic method including the terrain effect, the adiabatic method, the omega equation, and the vorticity equation combined with Dines' Compensation Principle. If particular terms in the equations were difficult to evaluate, the relative importance of each term to the particular method was investigated. Moisture availability and stability were considered, but less extensively. Values of terrain-induced vertical motion were computed manually, but other parameters needed in the methods were determined by computer through the use of a grid system which enveloped the area of interest. Areas where precipitation occurred within each 6-hr period were outlined, and points selected within rain and no-rain areas were used for verification purposes. The locations of these data points changed at each time period; a total of 65 points were selected in rain areas along with an equal number in no-rain areas. Subjective association between the methods for obtaining the sign of vertical motion and precipitation occurrence was made by overlaying the data points onto fields of the parameters computed at the middle of the particular 6-hr rainfall reporting period.

The following conclusions were drawn from the investigation:

1) Rainfall occurring along the Gulf States during the last two days of the period was due to vertical motion caused by a cyclone in the Gulf of Mexico; the omega equation, which does not include orographic lifting, explained the rainfall areas associated with this system quite accurately.

2) Rainfall occurring along the middle East Coast and in the Ohio River Valley was due to terrain-induced vertical motion and convergence occurring in the lower troposphere.

3) Orographic lifting, by itself, explained 63% of the 130 data points. Since the values of orographic lifting were determined on a smaller scale than other parameters which were interpolated and smoothed, this term was better related to the low-level phenomena producing rainfall than were terms in the kinematic, adiabatic, and vorticity methods. Based on this research, orographic lifting always should be considered in precipitation forecasting.

4) For this synoptic situation, the best explanation of the rain and no-rain areas was given by the kinematic method, including the orographic effect, at 850 mb; 80.8% of the data points was correctly explained. The method gave poorer correlations at 400 mb.

5) Use of the vorticity equation with Dines' Compensation Principle gave comparatively poor results at all levels. The inclusion of the local rate-of-change term did not greatly improve the results obtained by using advection alone.

6) The adiabatic method in the 700-500-mb layer produced the second best results. In the upper levels, overall results obtained by the addition of the local rate-of-change term were not significantly better

than those obtained using advection alone. Rainfall areas were explained more accurately, but no-rain areas were explained less accurately by the use of this term.

7) The omega equation at upper levels frequently could not be used to estimate the sign of vertical motion because the two terms involved differed in sign. When the terms of the equation were added through the use of constant multipliers, better results were obtained. Maps showing positive areas of the terms in the omega equation coincided well with precipitation areas along the Gulf Coast. Results were poor along the East Coast and the Appalachians.

8) The use of rather simple methods of computing vertical motion can give good explanations of rain and no-rain areas.

I. REFERENCES

I-1. Barnes, Stanley L., 1964: A technique for maximizing details in numerical weather analysis. J. Appl. Meteorol., 3, 396-409.

I-2. Booth, David M., 1970: A study of stability indexes and vertical motion in relation to convective clouds over Texas. Master's Thesis, Department of Meteorology, Texas A&M University, 70 pp. (unpublished).

I-3. Browne, Richard F., and Russel J. Younkin, 1970: Some relationships between 850-millibar lows and heavy snow occurrences over the Central and Eastern United States. Mon. Wea. Rev., 98, 388-401.

I-4. Collins, G. O., and P. M. Kuhn, 1954: A generalized study of precipitation forecasting. Part 3: Computation of precipitation resulting from vertical velocities deduced from vorticity changes. Mon. Wea. Rev., 82, 173-180.

I-5. Djuric, Dusan, 1969: Note on estimation of vertical motion by the omega equation. Mon. Wea. Rev., 97, 902-904.

I-6. Elliot, R. D., and R. W. Shaffer, 1962: The development of quantitative relationships between orographic precipitation and air mass parameters for use in forecasting and cloud seeding evaluation. J. Appl. Meteorol., 1, 218-228.

I-7. Haltiner, G. J., L. C. Clarke, and G. E. Lawniczak, Jr., 1963: Computation of large-scale vertical velocity. J. Appl. Meteorol., 2, 242-259.

I-8. Haltiner, G. J., and F. L. Martin, 1957: Dynamical and Physical Meteorology, New York, McGraw-Hill, 343-365.

I-9. Hansen, John, and Aylmer H. Thompson, 1965: Vertical motion calculations and satellite cloud observations over the western and central United States. J. Appl. Meteorol., 4, 18-30.

I-10. Harley, W. S., 1965: An operational method for quantitative precipitation forecasting. J. Appl. Meteorol., 4, 305-319.

I-11. Jarvis, E. C., and T. Agnew, 1970: A note on the computation of terrain and frictionally induced vertical velocities. J. Appl. Meteorol., 9, 942-946.

I-12. Jenrette, James P., 1960: An objective application of vorticity principles to precipitation forecasting. Bull. Amer. Meteorol. Soc., 41, 317-323.

I-13. Miller, A., and H. A. Panofsky, 1958: Large-scale vertical motion and weather in February, 1953. Bull. Amer. Meteorol. Soc., 39, 8-13.

I-14. Myers, Joel N., 1964: Preliminary radar climatology of central Pennsylvania. J. Appl. Meteorol., 3, 421-429.

I-15. Panofsky, H. A., 1946: Methods of computing vertical motion in the atmosphere. J. Meteorol., 3, 45-49.

I-16. _____, 1958: Introduction to Dynamic Meteorology, University Park, Pa., The Pennsylvania State University, 54-96.

I-17. Petterssen, Sverre, 1956: Weather Analysis and Forecasting, Vol. I, New York, McGraw-Hill, 292-304.

I-18. Sawyer, J. S., 1952: A study of rainfall in two synoptic situations. J. Roy. Meteorol. Soc., 78, 231-246.

I-19. Schwarz, Francis K., 1970: The unprecedented rains in Virginia associated with the remnants of hurricane Camille. Mon. Wea. Rev., 98, 851-859.

I-20. Thompson, J. C., and G. O. Collins, 1953: A generalized study of precipitation forecasting. Part I: Computation of precipitation from the fields of moisture and wind. Mon. Wea. Rev., 81, 91-100.

I-21. Thompson, P. D., 1961: Numerical Weather Analysis and Prediction, New York, MacMillan, 170 pp.

I-22. Vederman, Joseph, 1961: Forecasting precipitation with the aid of a high-speed electronic computer. Mon. Wea. Rev., 89, 243-250.

I-23. Williams, Philip Jr., 1963: Relationship of precipitation to vorticity and vertical motion at Salt Lake City, Utah. Mon. Wea. Rev., 91, 215-219.

I-24. _____, and Eugene L. Peck, 1962: Terrain influences on precipitation in the intermountain west as related to synoptic situations. J. Appl. Meteorol., 1, 343-347.

I-25. Younkin, Russel J., 1968: Circulation patterns associated with snowfall over the western United States. Mon. Wea. Rev., 96, 851-853.

J. LIST OF SYMBOLS

$\vec{V}$ = the horizontal wind vector

u = the wind speed component in the x (zonal) direction

v = the wind speed component in the y (meridional) direction

w = the wind speed component in the z (vertical) direction

t = time

ρ = the density of the air

∇ = the del operator

∇^2 = the Laplacian operator

w_L = the vertical motion at level L

w_s = the terrain induced vertical motion

p = pressure

g = the acceleration due to gravity

ζ = the relative vorticity

η = the absolute vorticity, $\eta = \zeta + f$

f = the coriolis parameter

$\omega = \frac{dp}{dt}$, α - w the vertical velocity

θ = the potential temperature

T = temperature

R = the gas constant

$k = R/c_p$

c_p = the specific heat at constant pressure

θ_E = the equivalent potential temperature

σ = the stability parameter, $\sigma = \frac{\partial \theta}{\partial p}$

e = the base of natural logarithms

L = the latent heat of condensation

c_s = the saturation mixing ratio

p_L = the pressure at level L

p_s = the pressure at the surface

K. LIST OF STATION IDENTIFIERS

AHN Athens, Georgia

BNA Nashville, Tennessee

BRJ Burrwood, Louisiana

CBI Columbia, Missouri

CHS Charleston, South Carolina

CRP Corpus Christi, Texas

DAY Dayton, Ohio

EYW Key West, Florida

FTW Fort Worth, Texas

GSO Greensboro, North Carolina

HSV Huntsville, Alabama

HTS Huntington, West Virginia

JAN Jackson, Mississippi

JAX Jacksonville, Florida

KSC Kennedy Space Center, Florida

LCH Lake Charles, Louisiana

LIT Little Rock, Arkansas

MIA Miami, Florida

MGM	Montgomery, Alabama
MTF	Mississippi Test Facility
OKC	Oklahoma City, Oklahoma
OMA	Omaha, Nebraska
PIA	Peoria, Illinois
PIT	Pittsburgh, Pennsylvania
SAT	San Antonio, Texas
SHV	Shreveport, Louisiana
TOP	Topeka, Kansas
TPA	Tampa, Florida
VPS	Valpariso, Florida
063	Grand Bahama Island

CHAPTER II. TIME CHANGES IN GRADIENT AND OBSERVED WINDS

by

Ronald Dale Carlson
Department of Meteorology
Texas A&M University, College Station, Texas

A. ABSTRACT

Local time changes of the observed and gradient wind speeds are examined at 500 mb for 3-, 6-, and 12-hour time intervals. The correlation coefficients between the changes in the two wind speeds over 3 and 6 hours are statistically not significantly different from zero at the 5% level. For the two 12-hour time intervals studied, the correlation coefficients between the local time changes in the two wind speeds were 0.38 and 0.51 which were statistically significant at the 5% level. A qualitative examination of the 3-, 6-, and 12-hour change of the components of the observed and gradient wind speeds also showed poor results over 3 and 6 hours with improvements over 12 hours. Although the gradient wind speed is generally an acceptable approximation to the actual wind speed, the results of this investigation show that the changes in the gradient wind speed are a poor approximation to changes in the actual wind speed over 3- and 6-hour time intervals with some improvement over 12-hour intervals.

An examination of the contributions to local changes in the gradient wind was made. Over 3 and 6 hours the changes in height gradient and the trajectory curvature are the largest contributors to changes in the gradient wind speed in approximately the same number of cases. Over 12 hours changes in the height gradient made the largest contribution to changes in the gradient wind speed in approximately 80% of the cases.

B. INTRODUCTION

The wind in the first few meters above the surface of Earth always has been of concern to man. The wind, its variability, and its effects in the lower layer of the atmosphere are more readily evident in everyday life than the wind in the upper atmosphere. However, with the advent of air travel, the space age, and numerical weather prediction, wind and its variability at all levels in the atmosphere have become important.

Wind variability in time and space is of great importance in numerical weather prediction. Part of the early failures in numerical weather prediction (Richardson, 1922) was attributed to wind variability

between grid points that resulted in erroneous computations of divergence. Today with more precise wind measurements this problem has been reduced but not eliminated.

There is considerable research under way at the present time to arrive at methods which will provide better wind measurements. Johnson (1970) discusses the Next Generation Upper Air System (NEXAIR) which is being developed through the Global Atmospheric Research Program (GARP). A new wind measurement system (NAVAID) is being developed as a part of NEXAIR in order to give meteorologists more accurate wind measurements. The design goal of the NAVAID system is 1-minute average wind data with a root-mean-square (rms) error of 0.5 sec^{-1} in the wind speed.

Wind variability in time and space also plays an important role in the design and operation of aerospace vehicles. Power-spectral techniques have been used (Houbolt, 1970) to analyze the variability of the vertical component of the wind. This variability spectrum is then used as an aid in the determination of design specifications. Similar techniques (Scoggins, 1970; Ryan et al., 1967) have been applied to the horizontal component of the wind for the design and operation of space vehicles. While on the launching pad a space vehicle is subjected to constant buffeting which is an example of the variability of horizontal wind in time. While in flight a space vehicle is subjected to wind variability in time and space. However, a speed is soon reached where, for all practical purposes, time variability in the wind can be ignored. If the limitation of wind variability experienced by an aerospace vehicle is exceeded, it is possible that structural damage could occur.

C. BACKGROUND AND STATEMENT OF THE PROBLEM

1. Previous Studies

One method of studying wind variability has been to look at the statistics of the wind. Durst (1948, 1952, 1954) has done extensive work on wind variability by correlating the wind at one time with that at the same place at a different time. He arrived at correlations and standard deviations between the winds at the two different times. As one would expect, as the time interval increased at each station, the standard deviation increased while the correlation decreased. These correlations and standard deviations tend to be constant with height (Lenhard et al., 1963) and to exhibit a seasonal variation which shows a maximum in fall and a minimum in spring (Ellsaesser, 1960).

Singer (1955) approached the variability problem by correlating different components of the wind with subsequent changes. Linear relationships were found between the initial observed wind speed and the magnitude of velocity change, initial wind speed and the change in wind speed, and the initial wind speed and the magnitude of direction change.

Other investigators have compared wind variability with various parameters related to the wind. Linear relationships were found between wind variability and surface wind, height above the terrain (Danard, 1965), and the changes in the gradient of pressure or height (Buell, 1957). The standard deviation of the wind from its average value at a given level has been shown (Brooks et al., 1950) to vary inversely as the density of the air at that level. Jenkinson (1956) established the empirical relation $\sigma = QS \cos EC \phi$, where σ is the standard vector deviation of the wind in knots, S is the standard deviation of the contour height in feet, ϕ is latitude, and Q is a constant dependent on the height of the pressure surface.

Some researchers have investigated the relationships between the wind at various levels in the atmosphere. Alexander et al. (1969) computed linear correlation coefficients between zonal and meridional wind components at different levels in the atmosphere. Tables were presented which showed these correlations for every kilometer up to 27 km for selected stations.

Another possible approach would be to use an approximation to the real wind and study its variability. It is accepted generally in middle latitudes that the geostrophic and gradient winds are, respectively, first- and second-order approximations to the real wind. Endlich (1961) states, "gradient winds provide an estimate of actual winds which is sufficiently accurate to make them useful in describing the dynamics of synoptic-scale processes."

2. Statement of the problem

Although many previous studies have been done to understand better the behavior of the wind in the atmosphere, the results of these studies leave much to be desired. Most of the previous studies have correlated the wind and its changes with some related parameters as opposed to obtaining an understanding of the factors which produce the wind and its changes. To understand fully the changes in the wind, one must attempt to understand the factors which produce the changes and the contributions of each factor.

The problem then is to try to obtain a better understanding of the changes in the wind field and the factors responsible for the changes. An examination of the gradient wind and its local changes will provide a basis for understanding some of the factors responsible for the observed changes. As stated earlier, the gradient wind generally is accepted as the best available approximation to the actual wind. Through an understanding of the gradient wind and the forces which contribute to it, the practicing meteorologist will obtain a better understanding of the local wind changes enabling him to produce a better forecast.

One must be aware, however, that there are certain phenomena in the atmosphere that may cause discrepancies between changes in the actual and gradient wind speeds. As mentioned by Mantis (1968), a problem exists with perturbations that have very small wave lengths. Although these

perturbations do affect meteorological parameters, they cannot be detected by the existing synoptic network. Since the average distance between the reporting stations for rawinsonde observations in the United States is approximately 300 km, any perturbation with a wave length equal to or less than approximately 600 km will not be detected.

Waves such as gravity and shear-gravity waves may also produce disagreements between changes in the actual and gradient wind speeds. Because of the speed of these waves, their effects are not resolvable in the wind measurements. However, the effects of these waves may be detectable in the height measurements. In turn, variations in the height gradient have a direct effect on the gradient wind speed.

Another factor which possibly could contribute to discrepancies between temporal changes in the actual and gradient wind speeds is the time lag between changes in the height field and the subsequent changes in the actual wind field. Changes in the height field will be noticed immediately as will changes in the gradient wind speeds. Haltiner (1971) mentioned that a 40-m change in height at a point requires 5 to 10 hours before a geostrophic balance is regained. This phenomenon would affect comparisons of the change in wind speed over all time intervals.

Although these phenomena which produce discrepancies between the changes in the actual and gradient wind speeds are present in the atmosphere, they are almost impossible to handle and will not be considered in this research.

3. Objectives

The objectives of this study are to:

a) examine the scalar relationships between the observed and gradient wind speeds,

b) compare local time changes of the observed wind speed with local time changes of the gradient wind speed over 3-, 6-, and 12-hour periods, and

c) evaluate the contributions of local changes in wind direction, height gradient, and trajectory curvature over 3-, 6-, and 12-hour time periods to the local changes of gradient wind speeds over the same time periods. All of the computations and comparisons in this study were done at the 500-mb level.

D. THEORETICAL CONSIDERATIONS

1. Gradient wind equation

The horizontal wind is a balance between the pressure gradient, coriolis, centrifugal, and frictional forces in the atmosphere. If and when these

forces become unbalanced, accelerations (tangential and/or centripetal) occur until a balance is obtained again. However, these accelerations vary and cannot be measured over a short period of time.

The derivation of the geostrophic approximation neglects accelerations, centrifugal force, and the influence of friction. The omission of these terms assumes that height contours are straight and parallel. However, it is obvious from an examination of any upper-level synoptic chart that the height contours are neither straight nor parallel over any great distance.

The gradient wind approximation also is a balance between selected forces that contribute to the actual wind. The forces considered in the gradient wind approximation are the pressure gradient, coriolis, and centrifugal. Centrifugal force, or centripetal acceleration, is the result of curved flow. Thus, the consideration of centrifugal force allows for curvature of the height contours on the upper-level synoptic charts.

Of the forces and accelerations contained in the complete horizontal equations of motion, those which do not appear in the gradient wind approximation are the frictional force and the tangential acceleration. It would be nice to conclude that any differences between changes in the gradient wind and changes in the actual wind are due to the frictional force and/or tangential acceleration. However, Mantis (1968) points out that in addition to friction and tangential acceleration, any difference between actual and gradient wind changes at a point in the atmosphere also could be due to observational errors, both human and instrumental, and/or changes due to wave lengths too small to be detected by the synoptic-scale network.

The vector equation for the gradient wind can be written as

$$\underset{\text{I}}{V_{gr}^2 K\vec{N}} + \underset{\text{II}}{f\vec{V}_{gr} \times \vec{k}} - \underset{\text{III}}{g\vec{\nabla}Z} = 0 , \qquad (1)$$

where $\vec{N}$ is a unit vector normal to the gradient wind vector and directed to the right of the flow, K is the curvature of the trajectory of the air parcel, $\vec{V}_{gr}$ is the gradient wind vector, V_{gr} is the magnitude of the gradient wind vector, f is the coriolis parameter, g is acceleration due to gravity, $\vec{k}$ the unit vector in the vertical, and ∇Z the gradient of height. Terms I, II, and III in Eq. (1) refer, respectively, to the centrifugal, coriolis, and pressure gradient forces.

Equation (1) can be written in scalar form as

$$V_{gr}^2 + fV_{gr} - g\left|\vec{\nabla}Z\right| = 0 , \qquad (2)$$

which can be solved for V_{gr} by use of the quadratic equation:

$$V_{gr} = \frac{-f \pm \sqrt{f^2 + 4Kg\left|\vec{\nabla}Z\right|}}{2K} \quad . \tag{3}$$

By definition, K is positive for cyclonic flow and negative for anticyclonic flow. Since V_{gr} cannot be less than zero, the plus sign must be used in front of the radical for cyclonic flow. It is accepted generally that the plus sign also is used in front of the radical for anticyclonic flow (Panofsky, 1964). For anticyclonic flow, it is possible for the sum under the radical to be negative; this produces an imaginary result for the gradient wind speed. For a real solution under anticyclonic flow the relation

$$f^2 \geq 4Kg\left|\vec{\nabla}Z\right| \tag{4}$$

must be preserved. Since the geostrophic wind speed, V_g, is given by

$$V_g = \frac{g}{f}\left|\vec{\nabla}Z\right| \quad , \tag{5}$$

the relation expressed in Eq. (4) may be written as

$$\frac{f}{4V_g} \geq K \quad . \tag{6}$$

Table 1 shows critical values of the radius of curvature, R = 1/K, for various latitudes and geostrophic wind speeds which must be met in order for Eq. (6) to be satisfied.

If the relation in Eqs. (4) and (6) cannot be satisfied, a gradient balance cannot be maintained, i.e., the wind speed and curvature become so large that the coriolis force cannot balance the centrifugal and pressure gradient forces. In this case, the air flow cannot continue parallel to the contours, and accelerations result.

2. Time rate-of-change of the gradient wind

The time rate-of-change of the gradient wind speed is calculated using equations for the components of the gradient wind. The x- and y-components of the gradient wind equation can be derived by taking the dot product of Eq. (1) by i and by j, respectively. The components of the

Table 1. Critical values for radius of curvature (Km) at various latitudes and geostrophic wind speeds.

Lat (deg) \ V_g (m sec^{-1})	10	20	30	40	50
30	550	1100	1650	2200	2750
45	390	780	1170	1560	1950
60	320	640	960	1180	1500

gradient wind in the x- and y-direction, respectively, then can be written as

$$V_{grx} = -\frac{g}{f}\frac{\partial Z}{\partial y} + \frac{KV_{gr}^2 N_y}{f} \quad , \tag{7}$$

and

$$V_{gry} = \frac{g}{f}\frac{\partial Z}{\partial x} - \frac{KV_{gr}^2 N_x}{f} \tag{8}$$

The local derivatives of Eqs. (7) and (8) now can be taken. However, since V_{gr}^2 contains V_{grx}^2 and V_{gry}^2, the differentiated forms of Eqs. (7) and (8) must be solved simultaneously. The result is

$$\frac{\partial V_{grx}}{\partial t} = \underbrace{\left[\frac{A'\partial N_x}{F'\partial t} + \frac{B'\partial N_y}{F'\partial t}\right]}_{\text{I}} + \underbrace{\frac{C'\partial K}{F'\partial t}}_{\text{II}} + \underbrace{\left[\frac{D'\partial}{F'\partial t}\left(\frac{\partial Z}{\partial x}\right) + \frac{E'\partial}{F'\partial t}\left(\frac{\partial Z}{\partial y}\right)\right]}_{\text{III}} \quad , \tag{9}$$

and

$$\frac{\partial V_{gry}}{\partial t} = \underbrace{\left[\frac{G'\partial N_x}{L'\partial t} + \frac{H'\partial N_y}{L'\partial t}\right]}_{\text{I}} + \underbrace{\frac{I'\partial K}{L'\partial t}}_{\text{II}} + \underbrace{\left[\frac{J'\partial}{L'\partial t}\left(\frac{\partial Z}{\partial x}\right) + \frac{M'\partial}{L'\partial t}\left(\frac{\partial Z}{\partial y}\right)\right]}_{\text{III}} \quad . \tag{10}$$

The explanation of the primed quantities in Eqs. (9) and (10) can be found in Appendix A along with the complete derivation.

Equations (9) and (10) are predictive equations for the x- and y-components of the gradient wind. Terms I, II, and III in Eqs. (9) and (10) represent the contributions to the changes in the gradient wind components due to changes in direction, curvature, and height gradient, respectively.

Equations (9) and (10) can be used to evaluate the local changes of the gradient wind components. The solution of these equations with actual rawinsonde data will be discussed in the next section.

E. ANALYTICAL APPROACH

1. The grid system

To facilitate numerical computations, a grid (Fig. 1) was used that covered the rawinsonde reporting network. The grid points were approximately 158 km apart, and the grid area consists of 13 x 16 points.

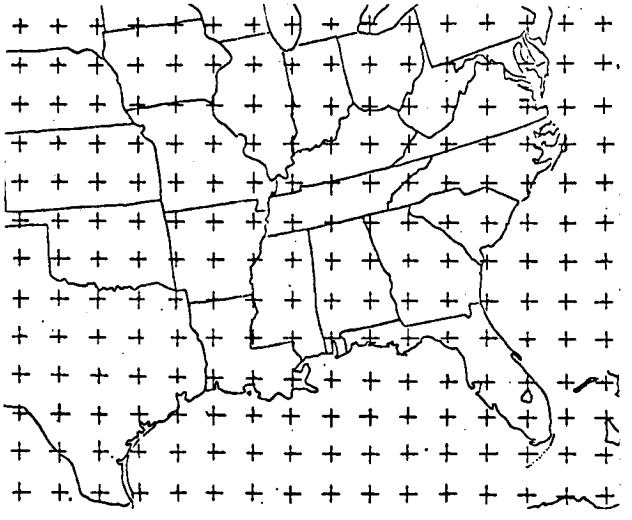

Fig. 1. Grid system used in finite-difference computations.

2. Data interpolation to the grid

Wind and height data were interpolated to the grid with the use of a technique developed by Barnes (1964). This technique is an interpolation method suitable for solution on a computer. Reported data at each station are interpolated to the grid points within a specified distance (scan radius) from the station. With the exception of Pittsburgh (PIT) and Greensboro (GSO), data from stations within a scan radius of 4.5 grid distances were used to assign values to a grid point. Since the grid

points in the northeast corner of the grid were so far away from any reporting stations, a scan radius of 5 grid distances was used that included PIT and GSO.

After a first guess was assigned to each grid point, a series of iterations was carried out to interpolate a new value for each grid point. Each grid point also was assigned a weighting factor proportional to the distance between the grid point and the reporting station. This weighting factor was used to assign values to grid points that were within the scan radius of two or more reporting stations.

For the first time period the first guess at each grid point was set at zero. Values calculated for the first time period were then used as a first guess for the second time period; values calculated for the second time period as a first guess for the third time period; etc. A total of five interations was used. The data were then smoothed using a 9-point smoothing function.

3. Evaluation of the gradient wind and its components

In order to solve the scalar gradient wind equation, Eq. (3), and the component gradient wind equations, Eqs. (7) and (8), the magnitude of the height gradient and the trajectory curvature must be computed at each grid point.

a) Height gradient.
The magnitude of the height gradient may be written as

$$\left| \vec{\nabla} Z \right| = \left[\left(\frac{\partial Z}{\partial x} \right)^2 + \left(\frac{\partial Z}{\partial y} \right)^2 \right]^{\frac{1}{2}} , \qquad (11)$$

where $\frac{\partial Z}{\partial x}$ and $\frac{\partial Z}{\partial y}$ were approximated with a centered finite-difference technique (Carnahan et al., 1964) over the grid system (Fig. 1, p. 66).

b) Trajectory curvature
Curvature is defined as $K = \frac{d\theta}{ds}$ where θ is the angle between the trajectory and the x axis, and s is a distance along the trajectory (see Fig. 2).

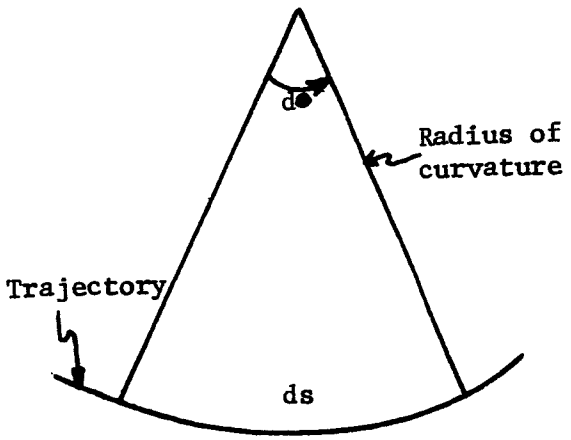

Fig. 2. Illustration of curvature

From Blaton's formula (Haltiner and Martin, 1957), K can be expressed as

$$K = \frac{1}{V}\left(\frac{\partial\theta}{\partial t} + V\frac{\partial\theta}{\partial s} + \omega\frac{\partial\theta}{\partial p}\right) \quad , \tag{12}$$

where V is wind speed, p is pressure, and ω is vertical velocity $(\frac{dp}{dt})$. Godson (1950) has shown that the last term (vertical advection) in Eq. (12) occasionally may contribute up to 30% of trajectory curvature. However, the vertical advection term generally is much smaller than the other terms in Eq. (12). By neglecting vertical motion, Eq. (12) may now be written

$$K = \frac{1}{V}\left(\frac{\partial\theta}{\partial t} + \frac{\partial\theta}{\partial s}\right) \quad . \tag{13}$$

Endlich (1961) solved Eq. (13) in terms of the height field in the form

$$K = \frac{(Z_y^2 Z_{xx} - 2Z_x Z_y Z_{xy} + Z_x^2 Z_{yy})}{(Z_x^2 + Z_y^2)^{3/2}} + \frac{f(Z_x Z_{yt} - Z_y Z_{xt})}{g(Z_x^2 + Z_y^2)^{3/2}} \quad . \tag{14}$$

The complete derivation of Eq. (14) is given in Appendix B.

Equation (14) was solved by numerical methods using centered differences for all space derivatives and 3-hour backward differences for all time derivatives. Time derivatives were computed over a 3-hour period to insure that time changes as small as 3 hours would be incorporated into the computations.

4. Evaluations of time changes

The time changes of the actual and gradient wind speeds and their components were calculated at each grid point over 3-, 6-, and 12-hour intervals, starting at 0300 GMT on each day. Thus, the 3-hour time change was from 0300 to 0600 GMT, the 6-hour from 0300 to 0900 GMT, and the 12-hour from 0300 to 1500 GMT.

Terms I, II, and III in Eqs. (9) and (10) were evaluated at each grid point over the same 3-, 6-, and 12-hour time intervals mentioned above. The time derivatives in these terms were approximated using 3-, 6-, and 12-hour backward differences.

5. Output

The following values were output at each grid point:

1) Actual and gradient wind speed at all time periods;
2) The 3-, 6-, and 12-hour changes in the actual and gradient wind speeds;

3) Observed 3-, 6-, and 12-hour changes of the x- and y-components of the actual wind;

4) Observed 3-, 6-, and 12-hour changes of the x- and y-components of the gradient wind;

5) Computed 3-, 6-, and 12-hour changes of the x- and y-components of the gradient wind;

6) Computed 3-, 6-, and 12-hour changes of Terms I, II, and III in Eqs. (13) and (14); and

7) All the possible summations of Terms I, II, and III in Eqs. (9) and (10).

F. DATA USED IN THE PRESENT RESEARCH

Data used in this study were supplied on magnetic tape by the Aerospace Environment Division, Aero-Astrodynamics Laboratory, National Aeronautics and Space Administration (NASA), Huntsville, Alabama. The data consist of observations from 30 rawinsonde stations in the southeastern United States (Fig. 3), and are unique in both their frequency and accuracy. The frequency of observations was unique in that the observations were taken every 3 hours from 0000 GMT, 19 February 1964, to 0000 GMT, 22 February 1964.

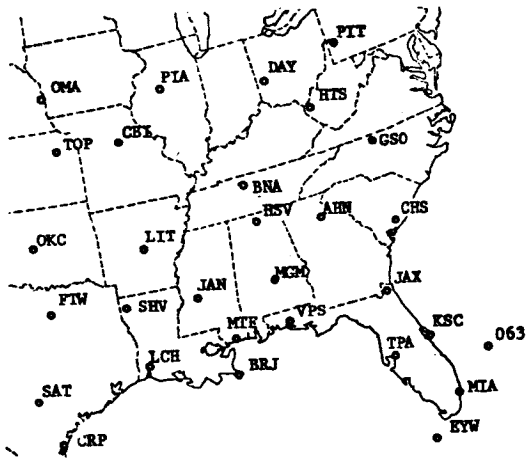

Fig. 3. Data Network. (See Appendix C for station listing.)

Extra care was taken in data processing to insure that the data were as accurate and representative as possible. Information on errors in the data were obtained from Mr. William W. Vaughan.[1] Data from all stations also were double checked by trained meteorologists for any inconsistencies or errors as a result of mechanical failures. When there was any question, the raw data were checked for verification and/or correction.

---

1. Personal communication.

Other than a more concerted effort to eliminate some of the human and mechanical errors inherent in any measuring system, the height data were obtained in the usual manner. For a systematic temperature error of 1°C from the surface to 500 mb, the height error at the 500-mb level would be 20 geopotential meters. Although the height data were obtained in the standard manner, an attempt was made to arrive at more accurate wind measurements.

Normally rawinsonde wind measurements are obtained from the horizontal distance traveled by the balloon in a 2- to 4-minute time period. This value is then assigned to the midpoint of the vertical layer which the balloon passed through during the time period. However, the measurements obtained by NASA for this study were computed over a 0.2- to 0.4-minute time period. This means that the winds also are averaged over a smaller layer since the balloon travels a shorter distance vertically in 0.2 to 0.4 minutes than it does in 2 to 4 minutes.

Errors in wind measurements at the 500-mb level for various elevation angles and mean wind speeds are shown in Table 2. At an elevation angle of 10° the error in wind speed shown in Table 1 is approximately 43% less than the error obtained under normal rawinsonde procedure as reported by Reiter (1963).

Table 2. Wind measurement errors at 500 mb.[2]

ELEVATION ANGLE (°)	20	14	10
MEAN WIND SPEED (m sec^{-1})	14	20	28
RMS ERRORS:			
Wind Speed (m sec^{-1})	1.1	2.0	3.6
Wind Direction (°)	1.3	1.8	2.6

The sum or difference of rms errors from two independent sets of data is equal to the square root of the sum of the squares of the rms errors of each data set (Brooks and Carruthers, 1953). If the average wind-speed error (Table 1) is assumed to be 3.4 m sec^{-1} for each data set, the rms error in the time change of the wind speed will be approximately 4.8 m sec^{-1}.

2. William W. Vaughan, NASA Marshall Space Flight Center, Huntsville, Alabama. Personal communication.

G. SYNOPTIC SITUATION

1. 19 February 1964, 0300 to 1500 GMT

The main feature present on 19 February 1964 (Fig. 4) is a frontal system which extends from eastern Virginia eastward over the Atlantic Ocean then to the southern tip of Florida. The frontal system is evident at several levels and has a slow easterly movement throughout the time period. At the later times the system shows a weakening at the 1000-mb level although it is quite evident on the upper-level charts.

In the upper levels a long wave trough is oriented north-south over the area throughout the entire period. A number of short waves moved through the area during the time period. At 0300 GMT (Fig. 4a) all upper levels indicate a closed low-pressure center with a double center at the 500-mb level. The low centers are still present at the 700- and 500-mb levels at 1500 GMT (Fig. 4e) with deepening indicated.

The temperature field indicates general advection of cold air over the entire area at all levels. The -16C isotherm at 700 mb and -34C isotherm at 500 mb can be followed from the western part of the area (Fig. 4a) to the central part (Fig. 4e). A cold pocket of air is evident in the upper levels at 1500 GMT (Fig. 4e).

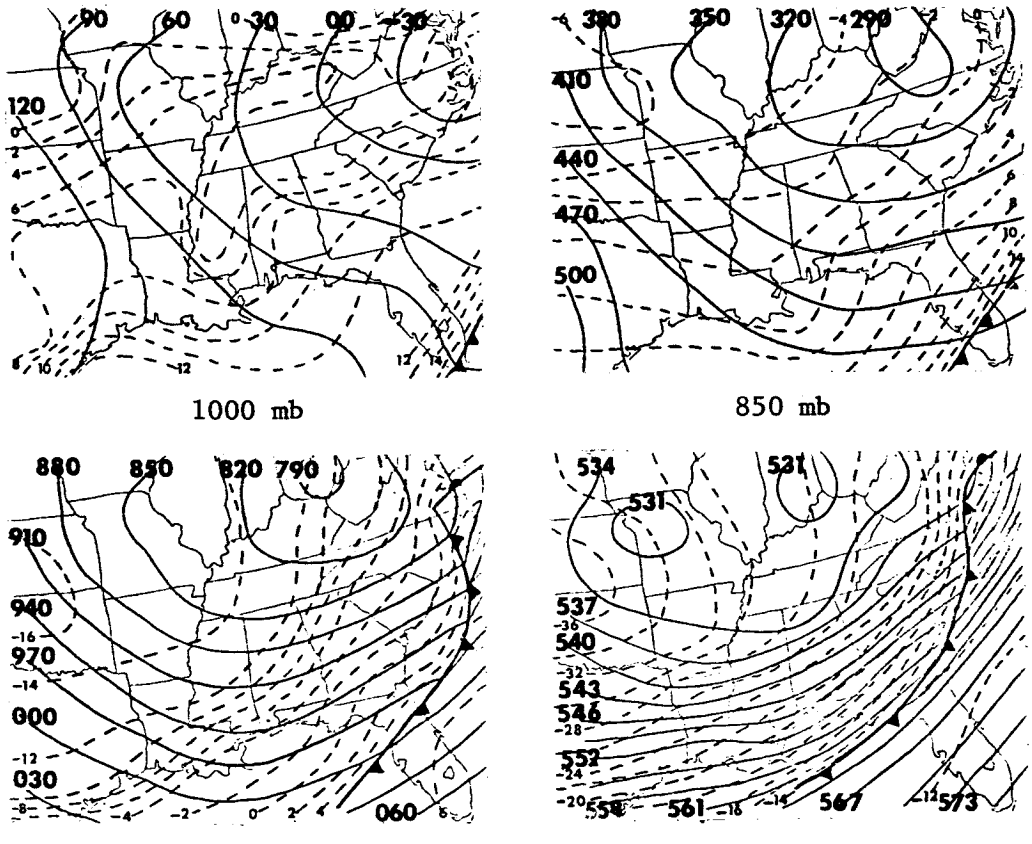

a) 0300 GMT, 19 February 1964

Fig. 4. Synoptic maps for 19 February 1964. (Dashed lines are temperature in degrees Celsius.)

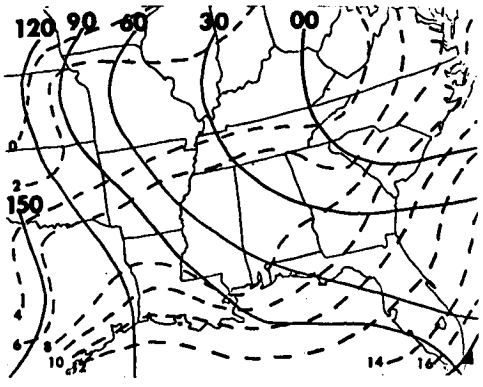

1000 mb

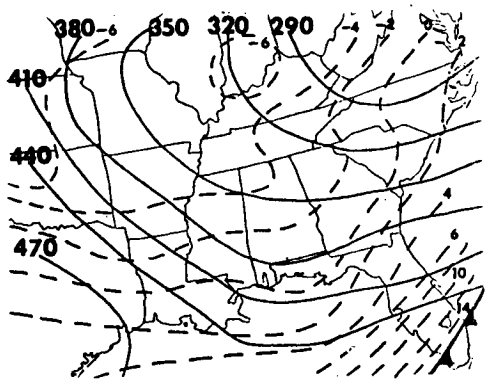

850 mb

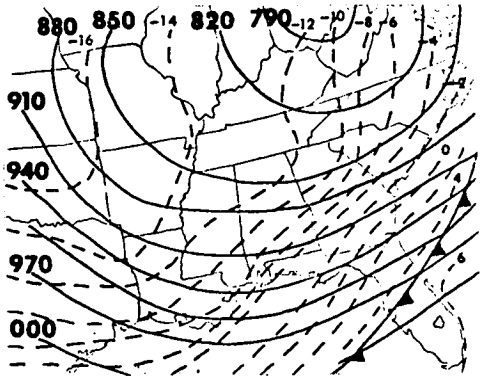

700 mb

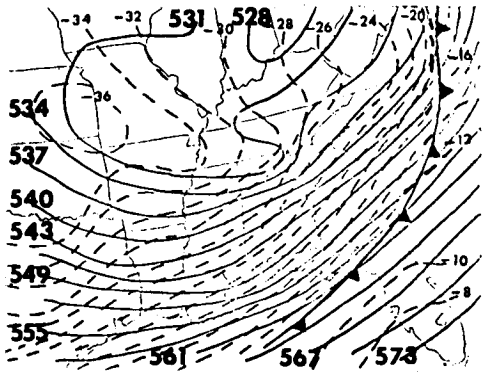

500 mb

b) 0600 GMT, 19 February 1964

Fig. 4. (Continued)

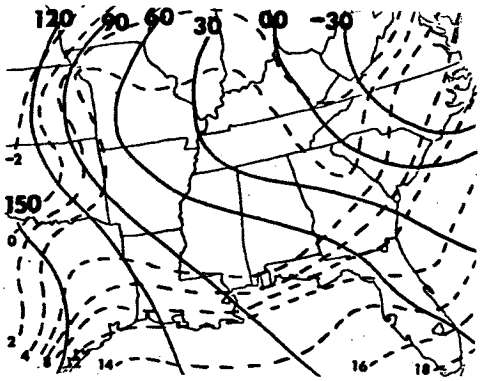

1000 mb

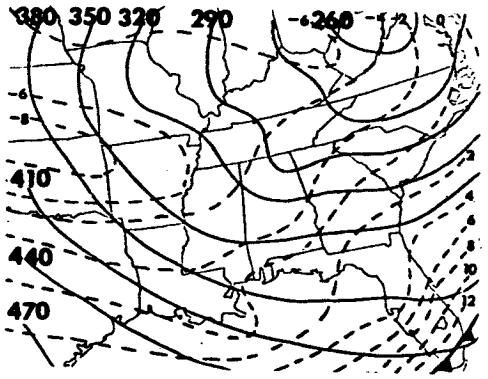

850 mb

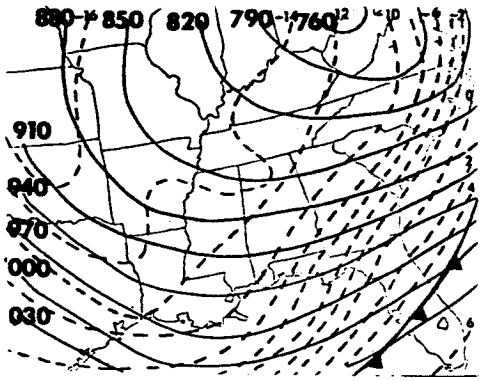

700 mb

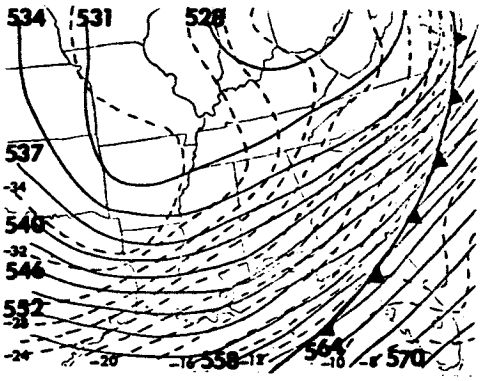

500 mb

c) 0900 GMT, 19 February 1964

Fig. 4. (Continued)

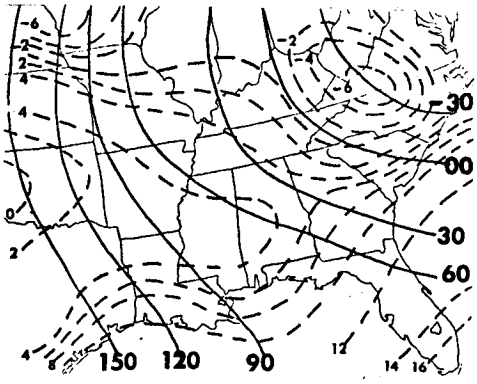

1000 mb

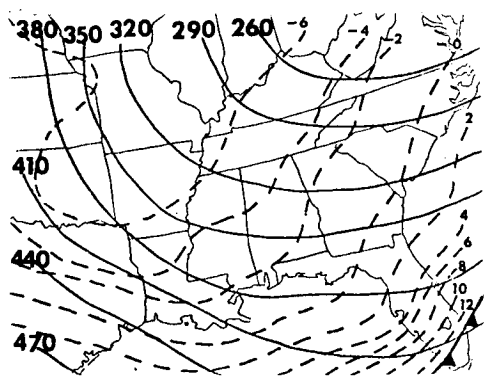

850 mb

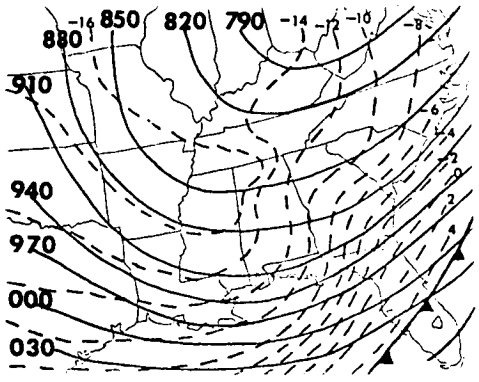

700 mb

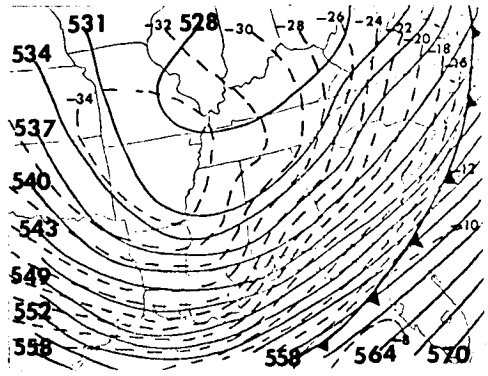

500 mb

d) 1200 GMT, 19 February 1964

Fig. 4. (Continued)

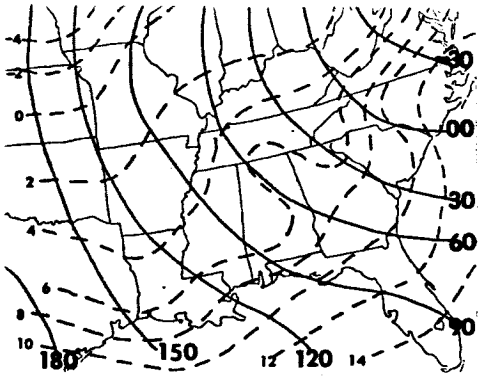

1000 mb

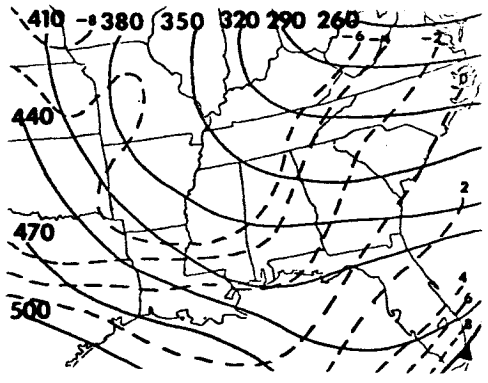

850 mb

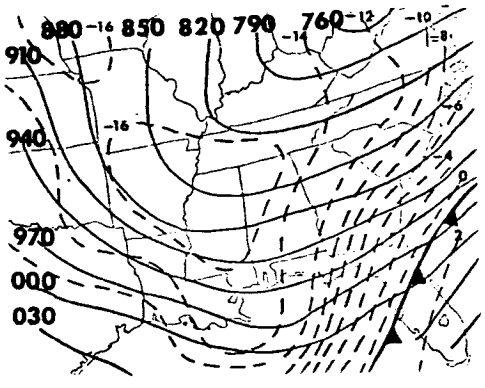

700 mb

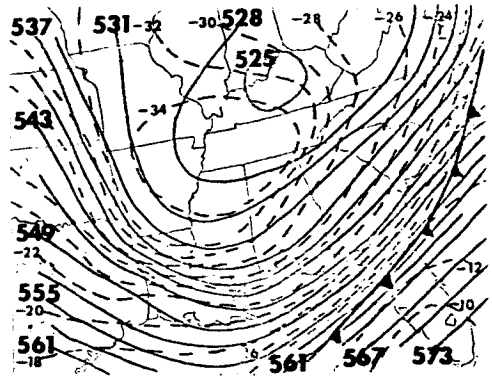

500 mb

e) 1500 GMT, 19 February 1964

Fig. 4. (Continued)

2. 21 February 1964, 0300 to 1500 GMT

There are no frontal systems present during this time period (see Fig. 5). The upper-level charts indicate the presence of a very broad long-wave trough over the area with evidence, particularly in the temperature field, of short waves moving through the area during the entire period.

The lower levels, 1000 and 850 mb, indicate weak cold-air advection in the east with warm-air advection over the western portion of the map. At the 700- and 500-mb levels, weak cold-air advection generally is present over the entire area.

There appears to be a number of thermal waves which move through the temperature field during this time period. One of these waves is evident at the 1000-mb level at 0900 GMT (Fig. 5c) but has dissipated by 1200 GMT (Fig. 5d).

The synoptic situations on the two days discussed differ significantly. Whereas the conditions on 21 February 1964 are quite stagnant, there is an active frontal system moving through the eastern part of the area on 19 February 1964. The wind speeds generally are larger at all levels on 19 February than on 21 February, particularly over the southeastern United States. Temperature gradients and advection also are larger and stronger on the 19th than the 21st. There also appears to be generally more curvature in the height contours on the 19th. This would indicate the flow to be more quasi-geostrophic on the 21st than on the 19th.

H. RESULTS OF ANALYSES

1. Correlation between observed and gradient wind speeds

Comparisons between the observed and gradient wind speeds at 500 mb for five times on 19 and 21 February 1964 are shown in Figs. 6 and 7, respectively. The isotachs of the two wind speeds generally are in acceptable agreement over the entire map at the end of each time period. At all times, the observed wind speeds have a maximum in the southeastern United States with speeds of 60 m sec^{-1} on 19 February and 40 m sec^{-1} on 21 February. This same portion of the map also has a maximum in the gradient wind-speed field at all times with the speeds approximately equal to those of the observed wind.

A linear correlation coefficient, r, was computed between the observed and gradient wind speeds at each time period on the two days. The results of these correlations are shown in Table 3.

All of the correlation coefficients in Table 3 are statistically significant at the 5% level (Brooks and Carruthers, 1953). Although the correlation coefficients on 21 February are lower than those on 19 February, the Fisher Z' Transformation Test showed that the correlations for the two days were not significantly different and could have come from the same population (Brooks and Carruthers, 1953). Because of the

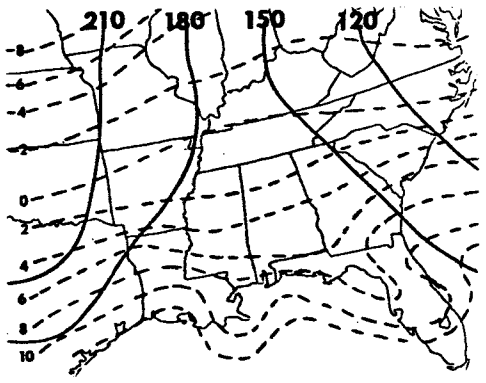

1000 mb

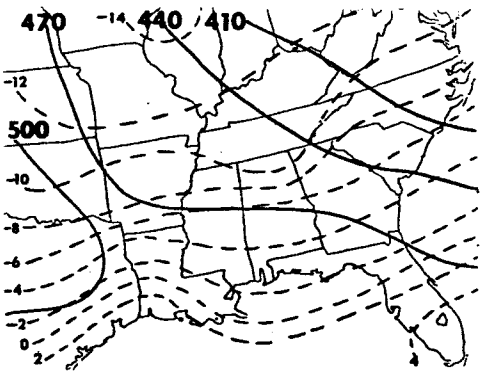

850 mb

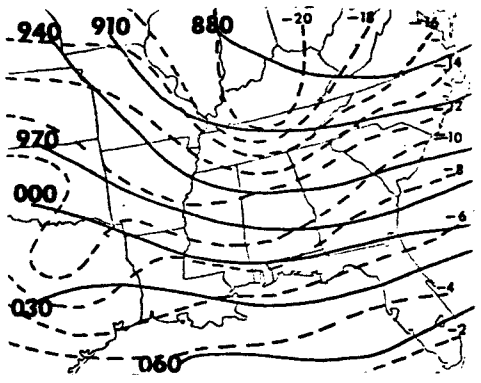

700 mb

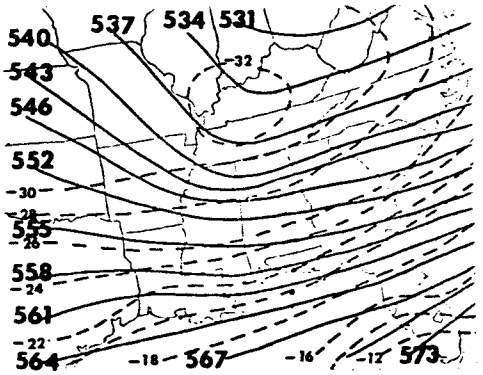

500 mb

a) 0300 GMT, 21 February 1964

Fig. 5. Synoptic maps for 21 February 1964. (Dashed lines are temperature in degrees Celsius.)

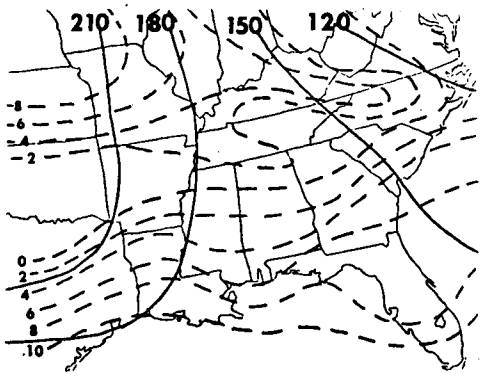

1000 mb

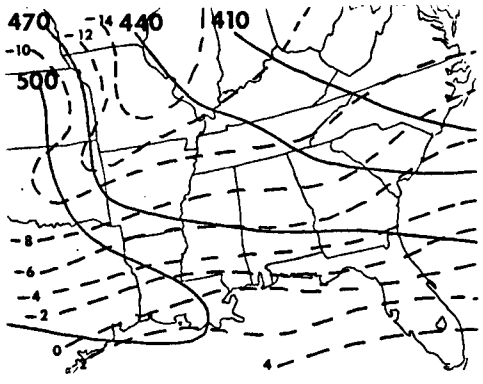

850 mb

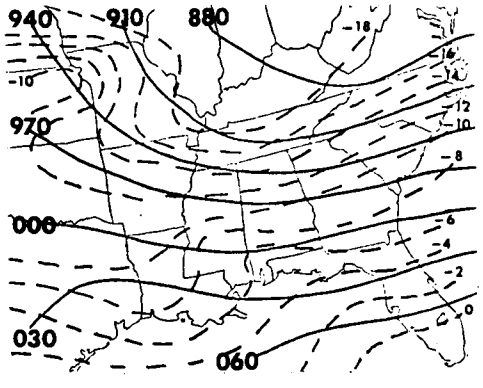

700 mb

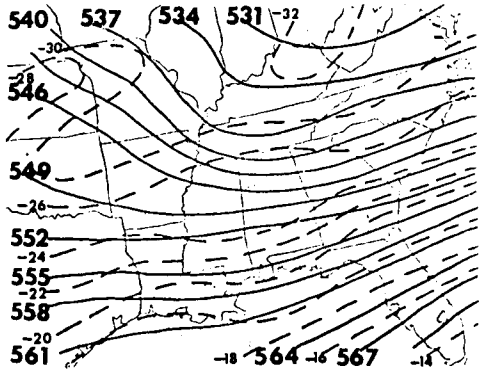

500 mb

b) 0600 GMT, 21 February 1964

Fig. 5. (Continued)

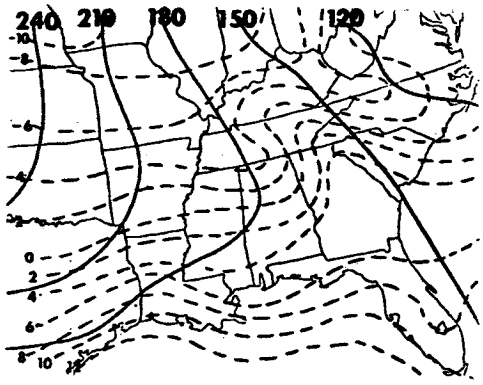

1000 mb

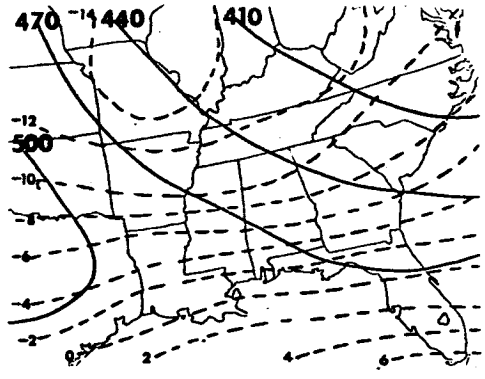

850 mb

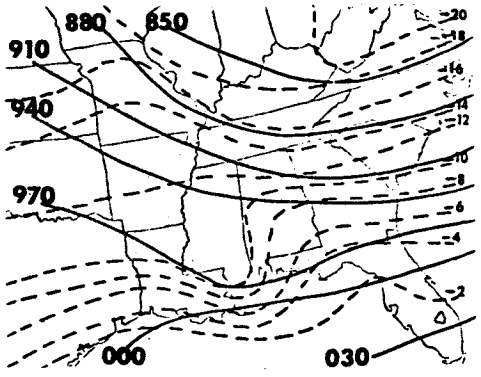

700 mb

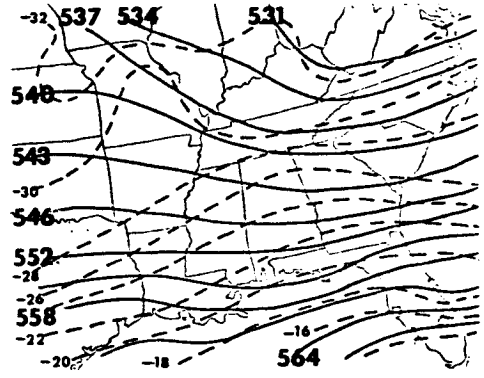

500 mb

c) 0900 GMT, 21 February 1964

Fig. 5. (Continued)

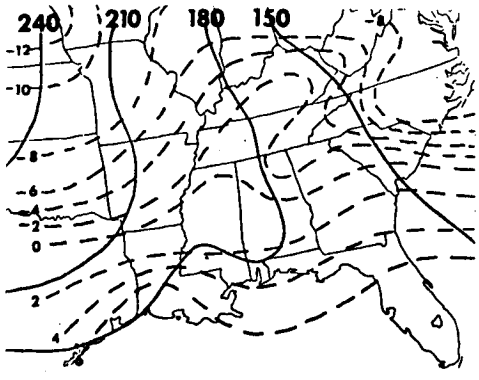

1000 mb

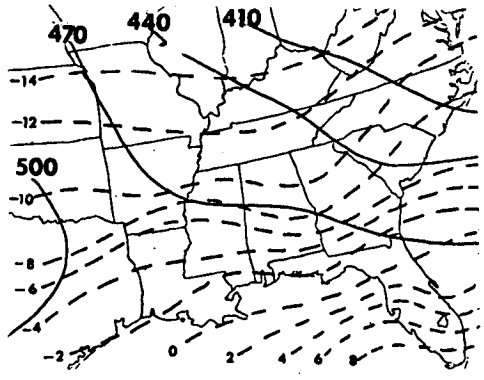

850 mb

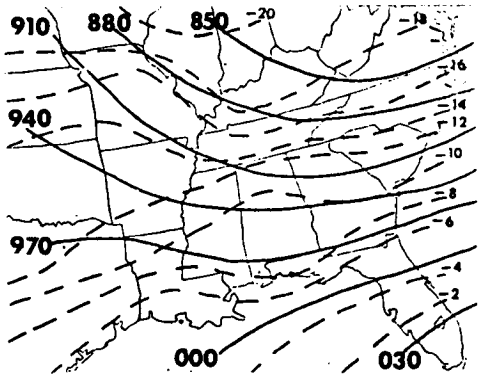

700 mb

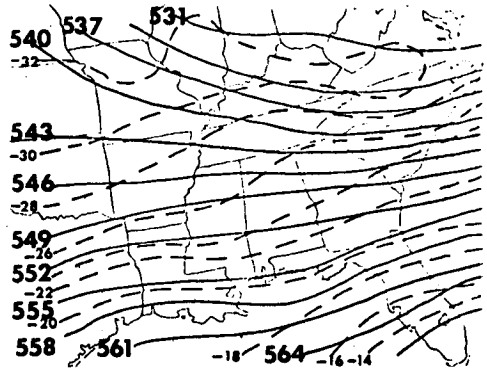

500 mb

d) 1200 GMT, 21 February 1964

Fig. 5. (Continued)

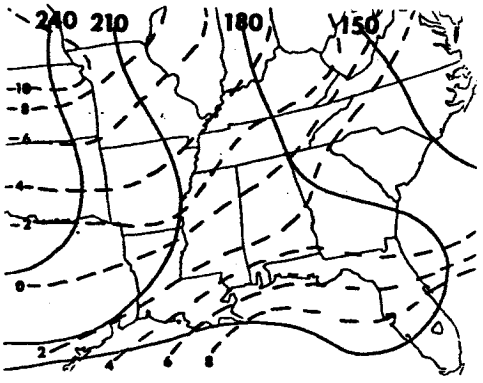

1000 mb

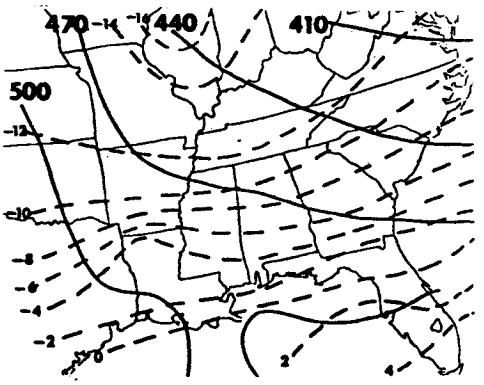

850 mb

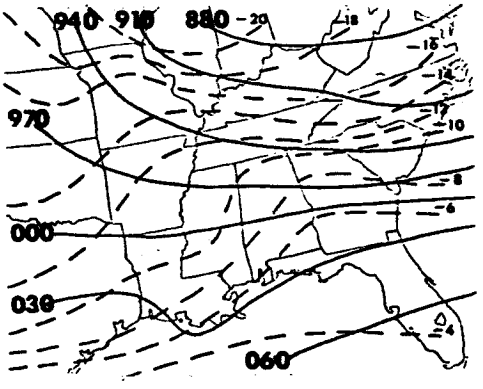

700 mb

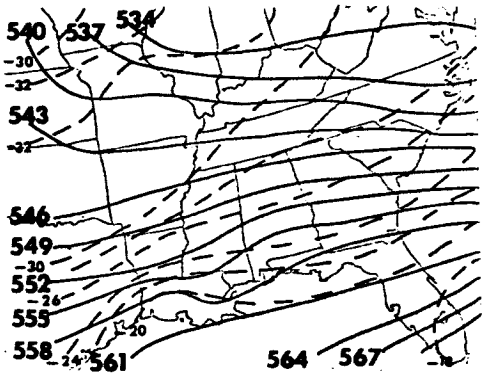

500 mb

e) 1500 GMT, 21 February 1964

Fig. 5. (Continued)

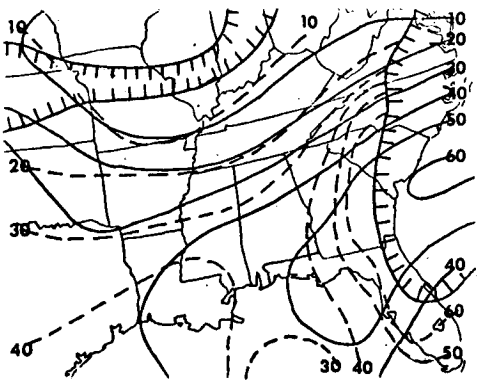

a) 0300 GMT

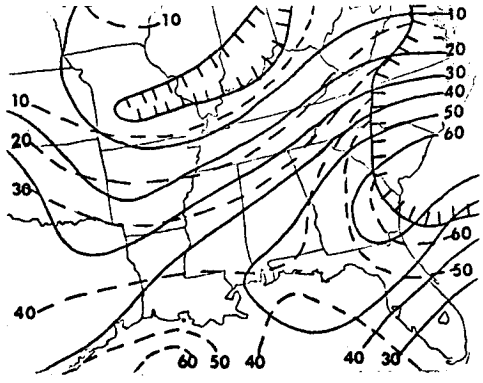

b) 0600 GMT

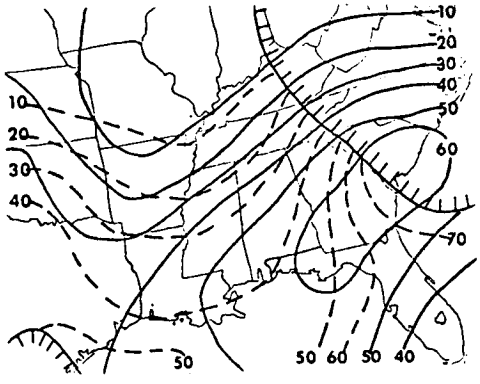

c) 0900 GMT

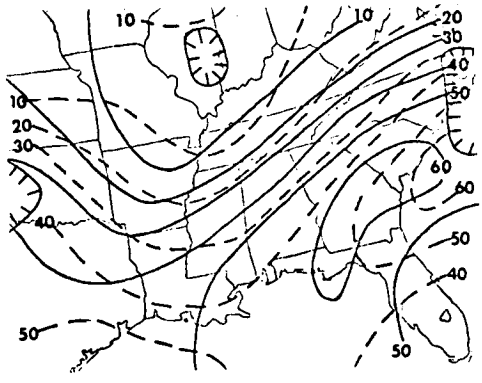

d) 1200 GMT

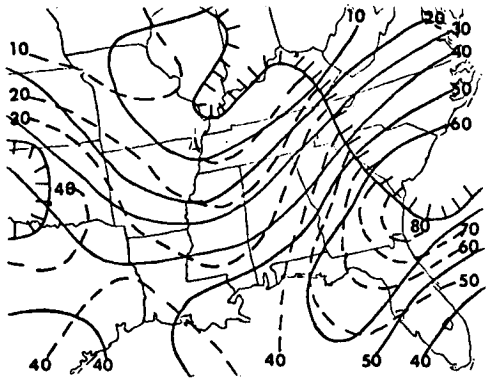

e) 1500 GMT

Fig. 6. Observed and gradient wind speeds (m/sec) at the 500-mb level on 19 February 1964. (Ticked lines outline areas of non-gradient balance.)

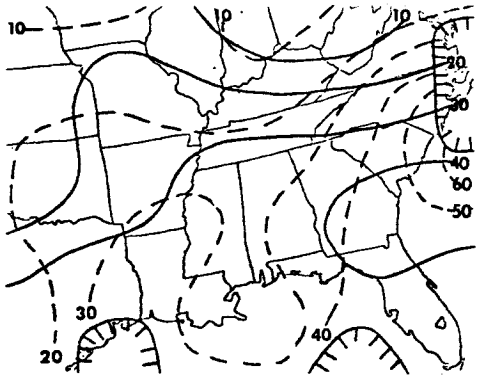

a) 0300 GMT

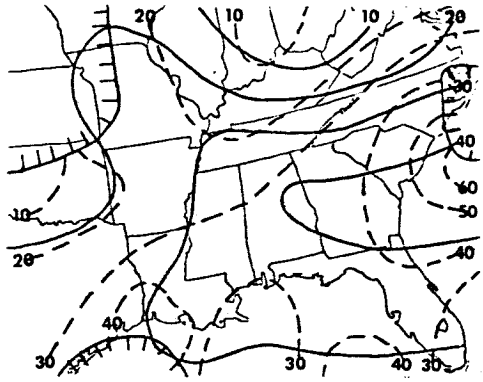

b) 0600 GMT

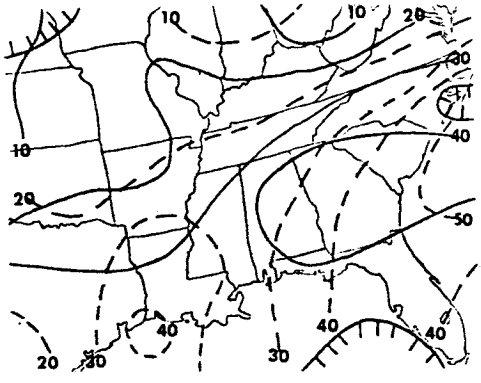

c) 0900 GMT

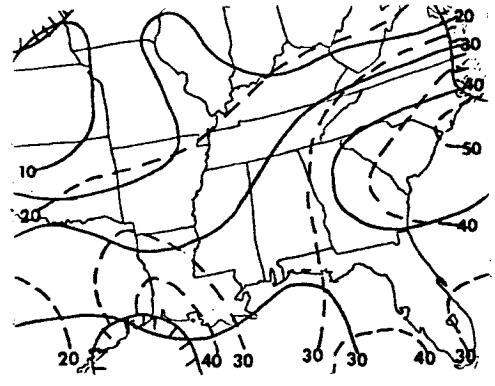

d) 1200 GMT

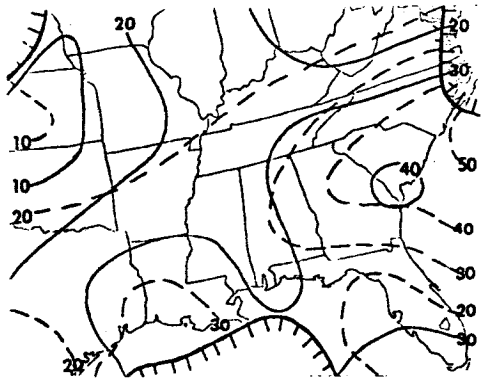

e) 1500 GMT

Fig. 7. Observed and gradient wind speeds (m/sec) at the 500-mb level on 21 February 1964. (Ticked lines outline areas of non-gradient balance.)

correlation between gradient and measured wind speeds, it may be expected that changes in the gradient wind speed will provide an acceptable approximation to changes in the observed wind speed.

Table 3. Linear correlation coefficients between observed and gradient wind speeds.

TIME (GMT)	03	06	09	12	15	AVG
r (19 FEB)	0.84	0.90	0.82	0.85	0.83	0.85
r (21 FEB)	0.76	0.74	0.77	0.82	0.76	0.77

As stated earlier, there are certain combinations of height gradient and trajectory curvature that will produce a complex solution for the gradient wind speed. The areas where a complex solution exists for the gradient wind speed will be referred to as areas of non-gradient balance; these are outlined by ticked lines in the figures.

On 19 February (Fig. 6, p. 82) there are basically two areas of non-gradient balance at each time at 500 mb. The first area of non-gradient balance is located essentially in the midwestern United States. At 0300 GMT (Fig. 6a, p. 82), the area extends from the Kansas-Nebraska border through Missouri into Indiana. This area is smaller at 0600 GMT (Fig. 6b, p. 82) and non-existent by 0900 GMT (Fig. 6c, p. 82). At 1200 GMT (Fig. 6d, p. 82) a small region of non-gradient balance exists over Illinois. These areas of non-gradient balance generally are in the regions of lowest height at the 500-mb level (Fig. 4, p. 71).

Bjerknes (1951) formulated the theory that a cutoff low will develop downstream of an area where a gradient balance cannot be maintained. The areas of non-gradient balance in the midwest at 0300 GMT (Fig. 6a, p. 82) and the small area over Illinois at 1200 GMT (Fig. 6d, p. 82) both show evidence in support of Bjerknes' theory. The 500-mb analyses at 0600 and 1500 GMT on 19 February (Figs. 4b and 4c, pp. 72 and 73) have cutoff lows developing downstream from the areas of non-gradient balance noted 3 hours earlier.

The second main area of non-gradient balance present on 19 February (Fig. 6, p. 82) is a large area over the east and northeastern part of the map. The synoptic conditions (Fig. 4, p. 71) show that this area of non-gradient balance surrounds the frontal system present over the eastern United States. There also are a few small areas of non-gradient balance on the edges of the map. However, since these areas are small and on the outer edge of the data network, they will not be discussed further.

On 21 February (Fig. 7, p. 83) the majority of the non-gradient areas are on the edge of the map where the data are sparse. There is one area of non-gradient balance over the northwest portion of the map at 0600 GMT

(Fig. 7b, p. 83). In this general area, the 500-mb contours appear to become increasingly zonal from 0300 to 0600 GMT (Figs. 5a and 5b, pp. 77 and 78) as the pressure trough over Indiana fills.

2. Changes in observed and gradient winds

The changes in the observed and gradient wind speeds over 3-, 6-, and 12-hour time periods were examined at the 500-mb level for 19 and 21 February 1964. The time periods were from 0300 to 0600 GMT, 0300 to 0900 GMT, and 0300 to 1500 GMT on both days.

As discussed earlier, the rms error in the changes of the observed wind speed over any time period was 4.8 m sec^{-1}. For this study, the rms error in the time changes of the gradient wind speed is assumed also to be 4.8 m sec^{-1}. Therefore, the only changes in gradient and observed wind speeds which will be discussed in this study will be those changes equal to or greater than 5 m sec^{-1}.

An attempt was made to analyze changes in the observed and gradient wind speeds over a time period with respect to changes in the synoptic conditions over the same period. However, because of data resolution, changes in the wind speed of less than 10 m sec^{-1} over a large area may not be detected on the synoptic charts in the form of changes in the height gradient. Similarly, changes in the wind speed over a small geographical area may be due to a phenomenon too small to be detected by the synoptic network. The changes in the gradient wind speed over a given time period also were analyzed in their component form with the aid of Terms I, II, and III in Eqs. (9) and (10).

Changes in the gradient wind speed could be computed only when there was a gradient wind defined at both ends of the time period. Thus, in the figures which follow, areas of non-gradient balance at either end of a time period prevented calculation for that time period.

a) Changes over a period of 3 hours

1) Observed and gradient wind speeds

The 3-hour changes in the observed and gradient scalar wind speeds on 19 and 21 February 1964 are shown in Figs. 8 and 9, respectively. Linear correlation coefficients were computed between the changes in the observed and gradient wind speeds on the two days. The correlation coefficient between the changes was 0.14 for 19 February, and 0.16 for 21 February. These correlation coefficients are quite low and statistically are not significantly different from zero at the 5% level (Brooks and Carruthers, 1953).

The small correlation coefficients may be attributed to the fact that the majority of changes in the observed and gradient wind speeds over the map on both 19 and 21 February are less than the time-change rms error of

4.8 m sec^{-1}. However, there are areas present on both days in which the observed and gradient wind speed changes are greater than the rms error.

The principal area of changes in both the observed and gradient wind speeds between 0300 and 0600 GMT on 19 February (Fig. 8) is centered over Georgia where the observed wind speed increased by 5 m sec^{-1} $(3\ hr)^{-1}$, and the gradient wind speed decreased by as much as 2 m sec^{-1} $(3\ hr)^{-1}$. A secondary area of changes in the gradient wind speed exists in the Gulf of Mexico where the gradient wind speed increased by 5 m sec^{-1} $(3\ hr)^{-1}$.

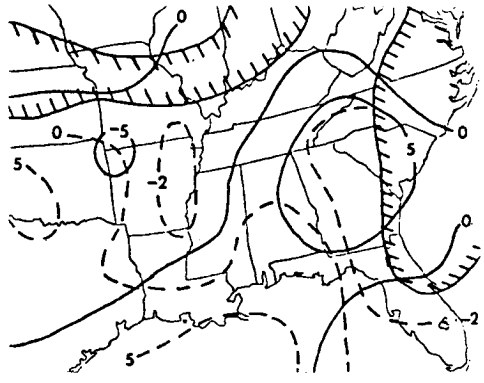

Fig. 8. Changes in observed and gradient wind speeds at 500 mb from 0300 to 0600 GMT, 19 February 1964. (Solid and dashed lines indicate, respectively, changes in observed and gradient wind speeds in m sec^{-1} $(3\ hr)^{-1}$. Ticked lines outline areas of non-gradient balance.)

An investigation of the synoptic conditions in the area of observed and gradient wind speed changes over Georgia shows that this area was behind the frontal system at both 0300 and 0600 GMT (Figs. 4a and 4b, pp. 71 and 72). There are no changes in the synoptic conditions such as height gradient or temperature advection evident over the time period. However, the changes in the height gradient required to produce a 5 m sec^{-1} $(3\ hr)^{-1}$ change in the observed wind speed over an area this large are small and may not be resolved accurately on these maps.

Between 0300 and 0600 GMT on 21 February (Fig. 9, p. 87), the significant changes in the observed wind speed are in an area centered over east Texas and extending into Oklahoma where the wind speed decreased by 5 m sec^{-1} $(3\ hr)^{-1}$. Significant changes in the gradient wind speed also occurred in this area. In the northern portion of this area the gradient wind speed decreased by as much as 10 m sec^{-1} $(3\ hr)^{-1}$, while it increased as much as 5 m sec^{-1} $(3\ hr)^{-1}$ in the southern portion. The only prominent feature on the synoptic charts (Figs. 5a and 5b, pp. 77 and 78) that changes with time is a thermal wave moving through the region; it is most pronounced at 700 mb. As before, the changes in the height gradient required for a 5 m sec^{-1} $(3\ hr)^{-1}$ change in the observed wind speed is within the noise level of the data. The areas of significant changes in the gradient wind speed will be discussed in the next section with respect to the changes in the x- and y-components of the gradient wind speed.

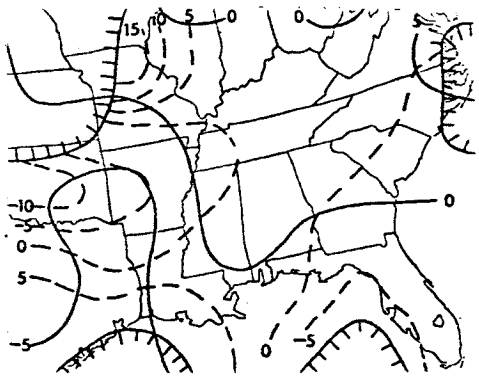

Fig. 9. Changes in observed and gradient wind speeds at 500 mb from 0300 to 0600 GMT, 21 February 1964. (Solid and dashed lines indicate, respectively, changes in observed and gradient wind speeds in m sec^{-1} $(3\ hr)^{-1}$. Ticked lines outline areas of non-gradient balance.)

2) Contributions to changes in gradient wind

The changes in the x- and y-components of the gradient wind speed are shown in Figs. 10 through 13. Each figure contains four parts; a), b), c), and d). Part a) is a comparison between the changes in the components of the observed and gradient wind speeds. For part a) of each figure, the changes in the components of the gradient wind speed are the changes observed during the time period. Parts b) and c) of each figure show, respectively, the contribution of Terms II and III in Eqs. (9) and (10) to changes in the gradient wind speed. Throughout this study the contribution from Term I was negligible. Part d) of each figure shows the sum of Terms II and III and, for all practical purposes, represents the changes in the components of the gradient wind speed, as calculated from Eqs. (9) and (10).

Equations (9) and (10) were solved by the use of finite difference methods. Due to the long incremental time steps, 3 to 12 hours, the changes in the components of the gradient wind speed obtained numerically from Eqs. (9) and (10) may differ slightly from the changes observed due to the numerical techniques employed. However, the patterns obtained by the two methods should agree.

There are two principal areas of significant changes in the x-component of the gradient wind speed on 19 February (Fig. 10a). An area centered over western South Carolina shows decreases of 10 m sec^{-1} $(3\ hr)^{-1}$, while an area centered over the Gulf of Mexico has increases of 5 m sec^{-1} $(3\ hr)^{-1}$. The changes in the x-component of the observed wind speed over the South Carolina area are of a different sign than the changes in the x-component of the gradient wind speed. Over the Gulf of Mexico, the changes in the x-components of the two wind speeds agree in sign.

The area over South Carolina of 10 m sec^{-1} $(3\ hr)^{-1}$ decreases in the x-component of the gradient wind speed received a larger contribution from a change in curvature (Fig. 10, p. 88) than from a change in height gradient (Fig. 10c, p. 88). Synoptically, this area is located close behind the frontal system at 500 mb and has cold-air advection at all levels (Figs. 4a

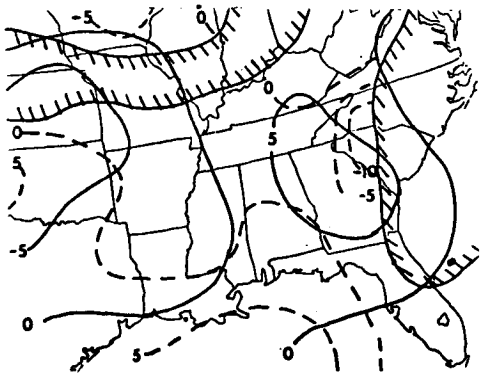

a) Dashed lines indicate changes in x-component of gradient wind speed (m sec^{-1} (3 $hr)^{-1}$).

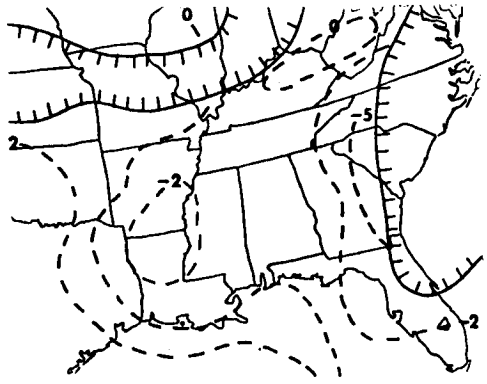

b) Dashed lines indicate changes in x-component of gradient wind speed due to changes in curvature (m sec^{-1} (3 $hr)^{-1}$).

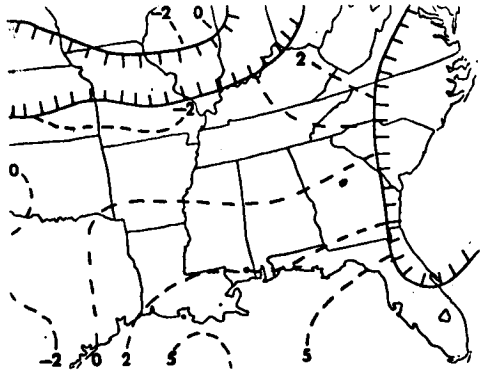

c) Dashed lines indicate changes in x-component of gradient wind speed due to changes in height gradient (m sec^{-1} (3 $hr)^{-1}$).

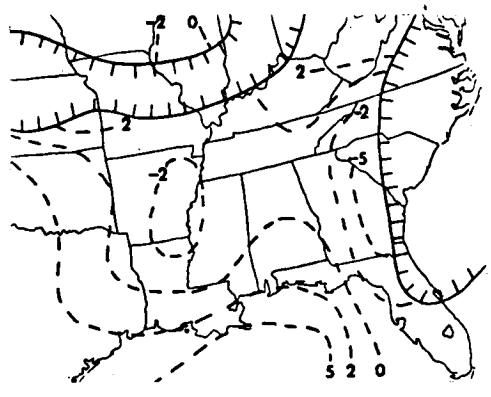

d) Dashed lines indicate sum of b) and c) (m sec^{-1} (3 $hr)^{-1}$).

Fig. 10. Analysis of changes in x-component of gradient wind speed from 0300 to 0600 GMT, 19 February 1964. (Solid lines indicate changes in the x-component of the observed wind speed (m sec^{-1} (3 $hr)^{-1}$). Ticked lines outline areas of non-gradient balance.)

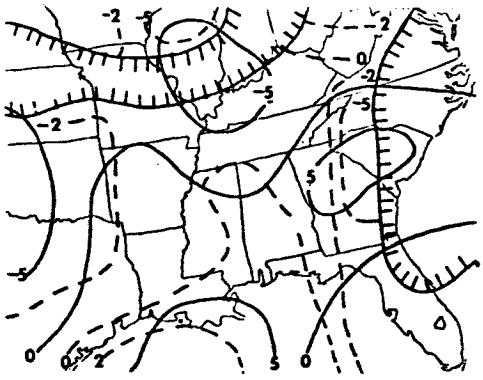

a) Dashed lines indicate changes in y-component of gradient wind speed (m sec^{-1} (3 $hr)^{-1}$).

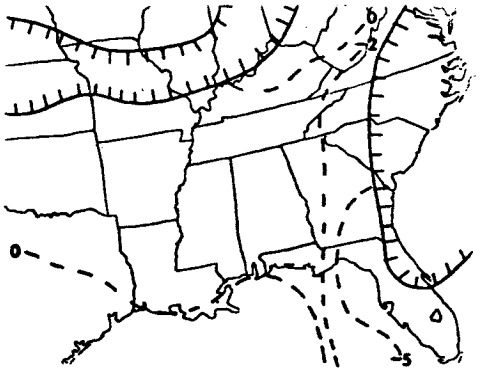

b) Dashed lines indicate changes in y-component of gradient wind speed due to changes in curvature (m sec^{-1} (3 $hr)^{-1}$).

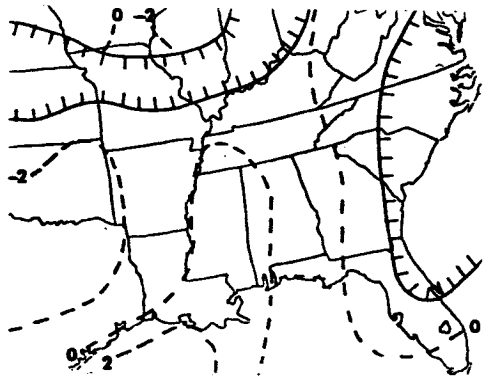

c) Dashed lines indicate changes in y-component of gradient wind speed due to changes in height gradient (m sec^{-1} (3 $hr)^{-1}$).

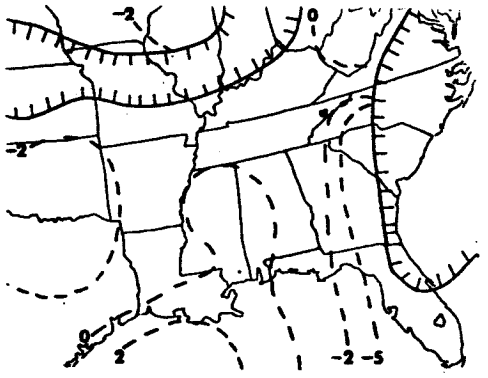

d) Dashed lines indicate sum of b) and c) (m sec^{-1} (3 $hr)^{-1}$).

Fig. 11. Analysis of changes in y-component of gradient wind speed from 0300 to 0600 GMT, 19 February 1964. (Solid lines indicate changes in the y-component of the observed wind speed (m sec^{-1} (3 $hr)^{-1}$). Ticked lines outline areas of non-gradient balance.)

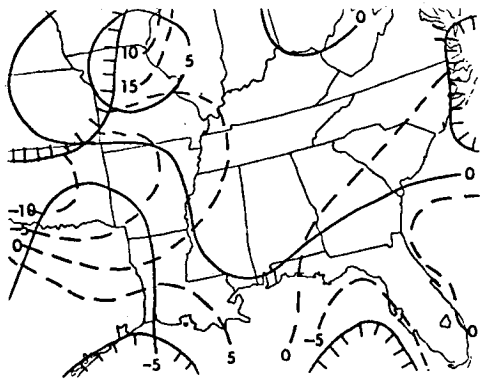

a) Dashed lines indicate changes in x-component of gradient wind speed (m sec^{-1} (3 $hr)^{-1}$).

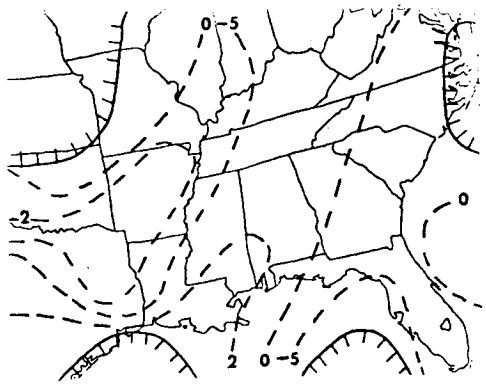

b) Dashed lines indicate changes in x-component of gradient wind speed due to changes in curvature (m sec^{-1} (3 $hr)^{-1}$).

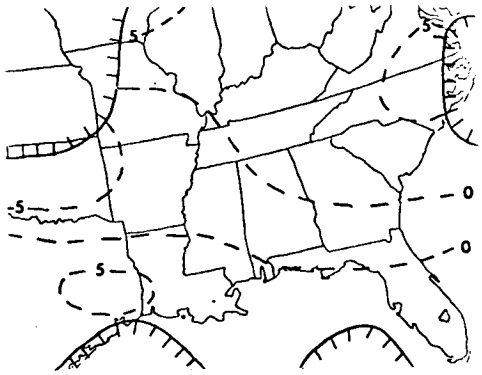

c) Dashed lines indicate changes in x-component of gradient wind speed due to changes in height gradient (m sec^{-1} (3 $hr)^{-1}$).

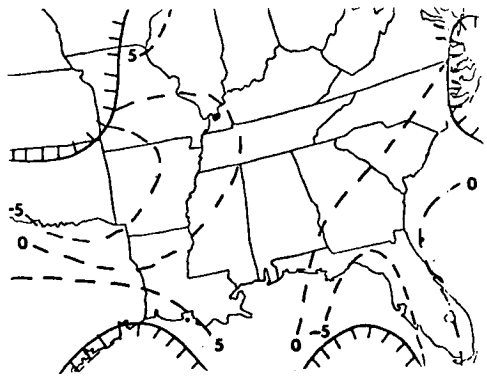

d) Dashed lines indicate sum of b) and c) (m sec^{-1} (3 $hr)^{-1}$).

Fig. 12. Analysis of changes in x-component of gradient wind speed from 0300 to 0600 GMT, 21 February 1964. (Solid lines indicate changes in the x-component of the observed wind speed (m sec^{-1} (3 $hr)^{-1}$). Ticked lines outline areas of non-gradient balance.)

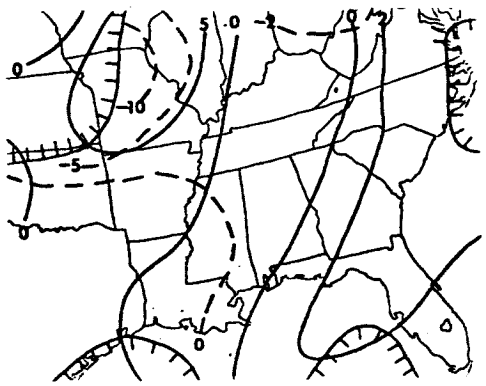

a) Dashed lines indicate changes in y-component of gradient wind speed ($m\ sec^{-1}\ (3\ hr)^{-1}$).

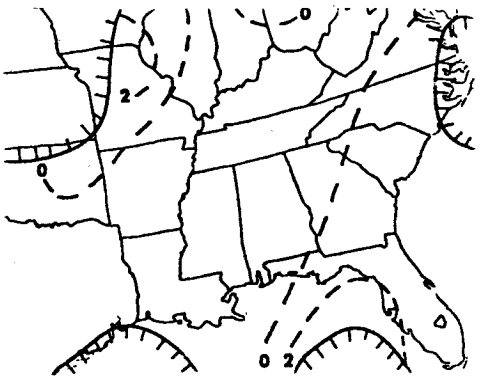

b) Dashed lines indicate changes in y-component of gradient wind speed due to changes in curvature ($m\ sec^{-1}\ (3\ hr)^{-1}$).

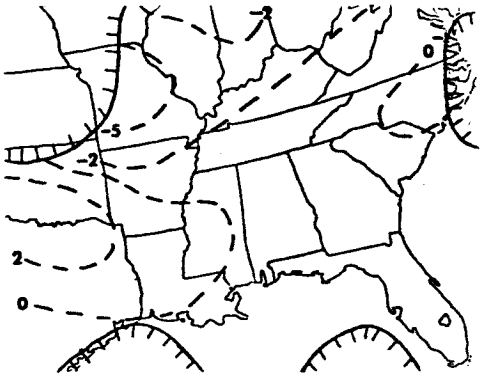

c) Dashed lines indicate changes in y-component of gradient wind speed due to changes in height gradient ($m\ sec^{-1}\ (3\ hr)^{-1}$).

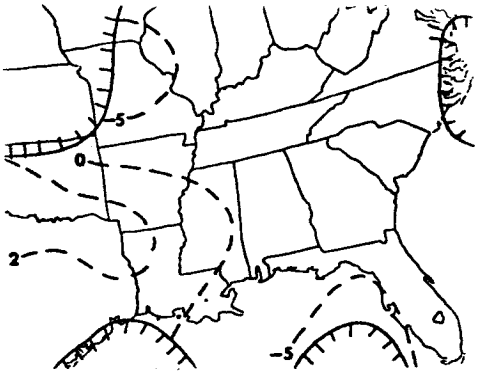

d) Dashed lines indicate sum of b) and c) ($m\ sec^{-1}\ (3\ hr)^{-1}$).

Fig. 13. Analysis of changes in y-component of gradient wind speed from 0300 to 0600 GMT, 21 February 1964. (Solid lines indicate changes in the y-component of the observed wind speed ($m\ sec^{-1}\ (3\ hr)^{-1}$). Ticked lines outline areas of non-gradient balance.)

and 4b, pp. 71 and 72). The area of 5 m sec^{-1} $(3\ hr)^{-1}$ increases in the x-component of the gradient wind speed over the Gulf of Mexico appears to receive the largest contributions from a change in the height gradient term. The synoptic conditions in this area are much the same as in the South Carolina area. At 500 mb, the frontal system extends into the eastern portion of the area. There also is cold-air advection evident in the area at all levels.

The principal change in the y-component of the gradient wind speed on 19 February (Fig. 11a, p. 89) was a decrease of 5 m sec^{-1} $(3\ hr)^{-1}$ in an area centered over western South Carolina. The changes in the x-component of the observed wind speed in this area showed an increase of 5 m sec^{-1} $(3\ hr)^{-1}$.

The changes in the y-component of the gradient wind speed over South Carolina are due more to a change in curvature (Fig. 11b, p. 89) than to a change in height gradient (Fig. 11c, p. 89). This area is located closely behind the frontal system at 500 mb and has cold-air advection present at all levels for both time periods (Figs. 4a and 4b, pp. 71 and 72).

On 21 February (Fig. 12a, p. 90) there are two principal areas where the x-component of the gradient wind speed changes by 5 m sec^{-1} $(3\ hr)^{-1}$ or more. These areas are centered over Oklahoma where a 10 m sec^{-1} $(3\ hr)^{-1}$ decrease occurred, and over the southwest corner of the map where increases of 5 m sec^{-1} $(3\ hr)^{-1}$ were observed. Over both Oklahoma and the entire southwest corner of the map, the x-component of the observed wind speed decreased.

The contributions to the changes in the x-component of the gradient wind speed over Oklahoma from a change in curvature (Fig. 12b, p. 90) are quite small. However, the contributions from the changes in height gradient (Fig. 12c, p. 90) are approximately -5 m sec^{-1} $(3\ hr)^{-1}$. Over the southwest corner of the map, the majority of the area receives the largest contributions to the changes in the x-component of the gradient wind speed from the height gradient term. There are no prominent changes in the synoptic conditions in these areas from 0300 to 0600 GMT.

In addition to the two principal areas mentioned above, there are two smaller areas of significant changes in the x-component of the gradient wind speed on 21 February (Fig. 12a, p. 90). An area centered over southeastern Iowa shows an increase of 10 m sec^{-1} $(3\ hr)^{-1}$, while an area over the Gulf of Mexico immediately west of Florida has a decrease of 5 m sec^{-1} $(3\ hr)^{-1}$. The changes in the x-component of the observed wind speed in these areas show, respectively, an increase of 5 m sec^{-1} $(3\ hr)^{-1}$ and a slight decrease.

The changes in the x-component of the gradient wind speed over Iowa received the largest contribution from a change in height gradient (Fig. 12c, p. 90), while almost all of the change in the area over the Gulf of Mexico was due to a change in curvature (Fig. 12b, p. 90). Both of these areas are fairly small and close to the edge of the map. This makes it difficult to determine any changes in the synoptic patterns in these areas.

There is only one area of significant change in the y-component of the gradient wind speed on 21 February (Fig. 13a, p. 91). This is an area of 10 m sec^{-1} (3 hr)$^{-1}$ decrease centered over northeastern Missouri. This same area shows an increase of 5 m sec^{-1} (3 hr)$^{-1}$ in the y-component of the observed wind speed.

The contributions of the curvature and height gradient to the changes in the y-component of the gradient wind speed are shown in Figs. 13a and 13b (p. 91). These figures indicate that the largest contributions come from the height gradient term in this area. Synoptically, this area has a wave in the temperature field present at the 850-, 700-, and 500-mb levels at 0600 GMT (Fig. 5b, p. 78).

In summary, eight areas of significant changes in the x- and y-components of the gradient wind speed were observed over a 3-hour period on 19 and 21 February. Four of the areas disagreed and four agreed in sign with the changes in the x- and y-components of the observed wind speed. The areas where the changes in the components of the two wind speeds differed in sign were associated more often with some predominant synoptic changes such as a front or thermal wave than the areas where the changes agreed in sign.

Of the eight areas observed where there were significant changes in the components of the gradient wind speed, five of the areas received the largest contribution from the height gradient (Term III in Eqs. (9) and (10)), and three of the areas received the largest contributions from curvature (Term II). The contribution from direction changes (Term I) was negligible in all cases. Of the four areas where the changes in the components disagreed in sign, the changes in the component of the gradient wind speed were due to curvature in two areas and height gradient in the other two.

b) Changes over a period of 6 hours

1) Observed and gradient wind speeds

The 6-hour changes in the observed and gradient wind speeds between 0300 and 0900 GMT on 19 and 21 February are shown in Figs. 14 and 15, respectively. The correlation coefficients between the changes in the two wind speeds were 0.10 for both days. As with the correlations between the 3-hour changes, the correlation coefficients for the 6-hour changes are not statistically different from zero at the 5% level (Brooks and Carruthers, 1953). However, as before, there are areas where the changes in the observed and gradient wind speeds over 6 hours exceeded the rms error.

On 19 February, an area of 15 m sec^{-1} (6 hr)$^{-1}$ increase in the observed wind speed is centered over Georgia with changes of 5 m sec^{-1} (6 hr)$^{-1}$ or larger extending over a large portion of the southeastern United States (Fig. 14, p. 94). The eastern part of this area also has increases in the gradient wind speed larger than 5 m sec^{-1} (6 hr)-1. Synoptically, this area is located behind the frontal system at both 0300 and 0900 GMT (Figs. 4a and 4c, pp. 71 and 73). At 500 mb, there is no change evident in the height gradient from 0300 to 0900 GMT to account for increases as large as 15 m sec^{-1} (6 hr)$^{-1}$

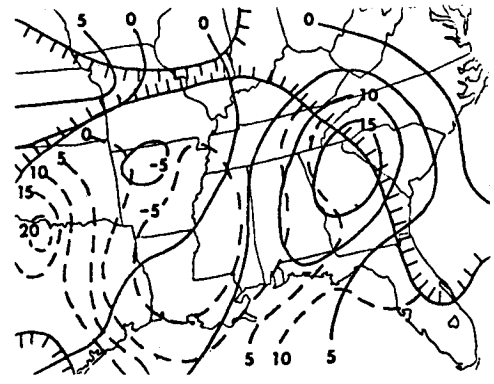

Fig. 14. Changes in observed and gradient wind speeds at 500 mb from 0300 to 0900 GMT, 19 February 1964. (Solid and dashed lines indicate, respectively, changes in observed and gradient wind speeds in m sec^{-1} $(6\ hr)^{-1}$. Ticked lines outline areas of non-gradient balance.)

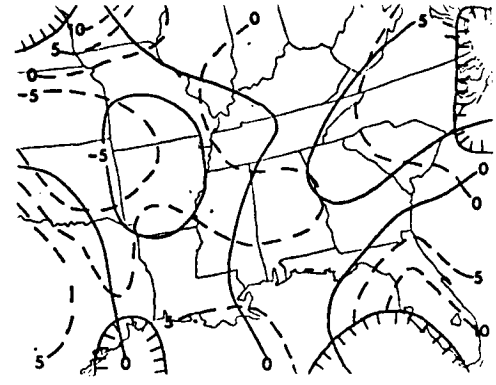

Fig. 15. Changes in observed and gradient wind speeds at 500 mb from 0300 to 0900 GMT, 21 February 1964. (Solid and dashed lines indicate, respectively, changes in observed and gradient wind speeds in m sec^{-1} $(6\ hr)^{-1}$. Ticked lines outline areas of non-gradient balance.)

in the observed wind speeds. However, the area of 15 m sec^{-1} (6 hr)$^{-1}$ change contains only one reporting station, Athens, Georgia (Fig. 3, p. 69). The large change in the observed wind speed in this area possibly could be due to an observational error or a meso-scale phenomenon affecting only the wind measurements at Athens. The change in the gradient of height over the area where the 10 m sec^{-1} (6 hr)$^{-1}$ increase occurred is large enough, approximately 45 m in 450 km, to support an increase of the order of 10 m sec^{-1} (6 hr)$^{-1}$.

The gradient wind speed changes significantly over the southwestern part of the map during this time period (Fig. 14, p. 94) with an area of 5 m sec^{-1} (6 hr)$^{-1}$ decrease centered over northeast Louisiana. An area of increase in the gradient wind speed is centered over northern Texas with a maximum increase of 20 m sec^{-1} (6 hr)$^{-1}$ indicated. This area appears to have a low-pressure trough which deepened from 0300 to 0900 GMT (Figs. 4a and 4c, pp. 71 and 73). The analysis of this area of changes in the gradient wind speed will be discussed in the next section.

The observed wind speed had two areas of significant change on 21 February (Fig. 15, p. 94) between 0300 and 0900 GMT. An area of 5 m sec^{-1} (6 hr)$^{-1}$ increase is centered over North Carolina, and an area of 5 m sec^{-1} (6 hr)$^{-1}$ decrease is centered over Missouri. The synoptic charts showed no appreciable changes in the height gradient over the North Carolina area (Figs. 5a and 5c, pp. 77 and 79). On the other hand, there is a decrease in the height gradient associated with the area of decrease in the observed wind speed centered over Missouri. There is also a thermal wave present at 1000 mb (Fig. 5c, p. 79) over North Carolina.

There is a large number of areas present on 21 February between 0300 and 0900 GMT where a significant change has occurred in the gradient wind speed (Fig. 15, p. 94). The principal area is one of 5 m sec^{-1} (6 hr)$^{-1}$ decrease centered over the Kansas-Oklahoma border. The height gradient in this area also decreased over the time period (Figs. 5a and 5c, pp. 77 and 79). The other areas of significant changes in the gradient wind speed are relatively small and located on the edge of the data reporting network. They will not be discussed further.

2) Contributions to changes in the gradient wind

The 6-hour changes of the x- and y-components of the observed and gradient wind speeds for 19 and 21 February are shown in Figs. 16 through 19. The contributions of Terms II and III in Eqs. (9) and (10) to changes in the components of the gradient wind speed also are shown in these figures. Again, the contribution of Term I in Eqs. (9) and (10) was negligible and is not presented.

There are four areas where the changes in the x-component of the gradient wind speed exceeded 5 m sec^{-1} (6 hr)$^{-1}$ on 19 February (Fig. 16a, p. 96). The largest of these areas is one of 5 m sec^{-1} (6 hr)$^{-1}$ decrease centered over southeastern Arkansas. Approximately one half of this area shows an increase in the x-component of the observed wind speed while the other half shows a decrease. The second and third areas of significant change are

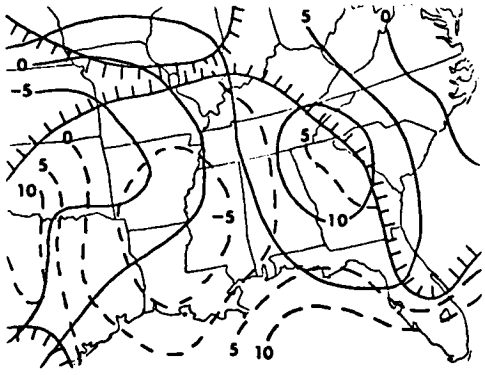

a) Dashed lines indicate changes in x-component of gradient wind speed (m sec^{-1} (6 hr)$^{-1}$).

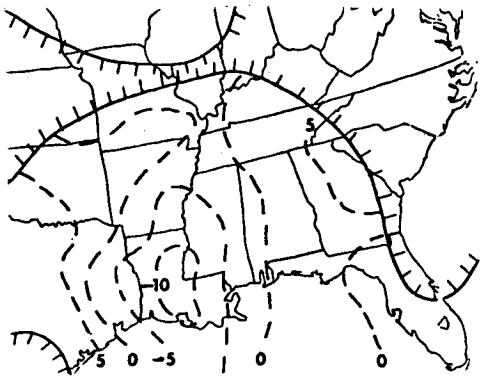

b) Dashed lines indicate changes in x-component of gradient wind speed due to changes in curvature (m sec^{-1} (6 hr)$^{-1}$).

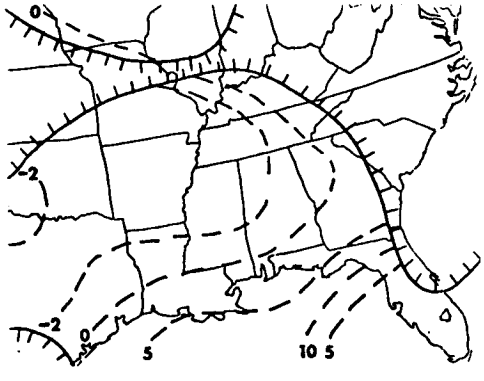

c) Dashed lines indicate changes in x-component of gradient wind speed due to changes in height gradient (m sec^{-1} (6 hr)$^{-1}$).

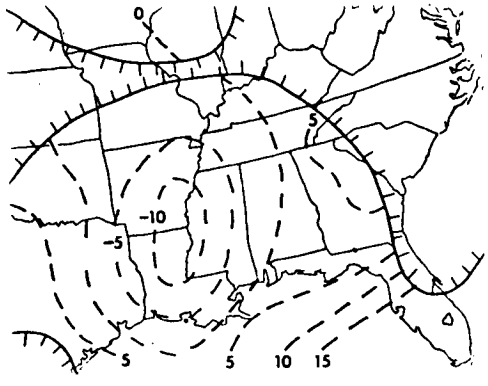

d) Dashed lines indicate sum of b) and c) (m sec^{-1} (6 hr)$^{-1}$).

Fig. 16. Analysis of changes in x-component of gradient wind speed from 0300 to 0900 GMT, 19 February 1964. (Solid lines indicate changes in the x-component of the observed wind speed (m sec^{-1} (6 hr)$^{-1}$). Ticked lines outline areas of non-gradient balance.)

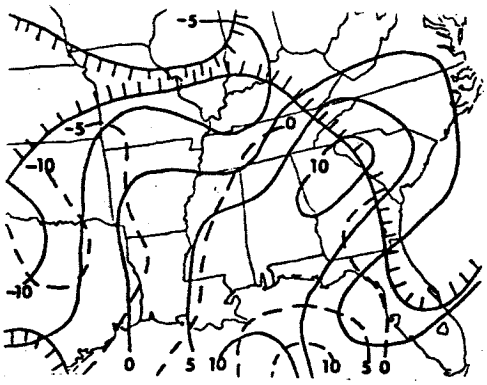

a) Dashed lines indicate changes in y-component of gradient wind speed (m sec^{-1} (6 $hr)^{-1}$).

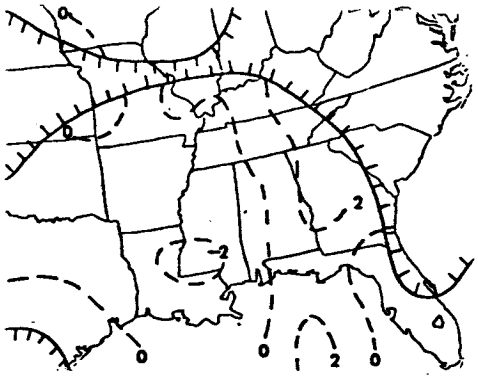

b) Dashed lines indicate changes in y-component of gradient wind speed due to changes in curvature (m sec^{-1} (6 $hr)^{-1}$).

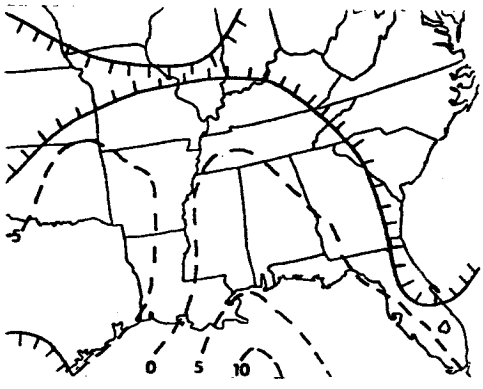

c) Dashed lines indicate changes in y-component of gradient wind speed due to changes in height gradient (m sec^{-1} (6 $hr)^{-1}$).

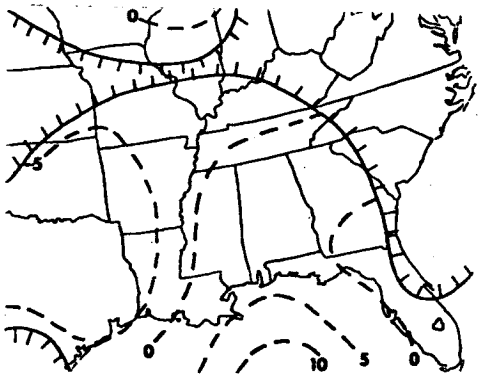

d) Dashed lines indicate sum of b) and c) (m sec^{-1} (6 $hr)^{-1}$).

Fig. 17. Analysis of changes in y-component of gradient wind speed from 0300 to 0900 GMT, 19 February 1964. (Solid lines indicate changes in the y-component of the observed wind speed (m sec^{-1} (6 $hr)^{-1}$). Ticked lines outline areas of non-gradient balance.)

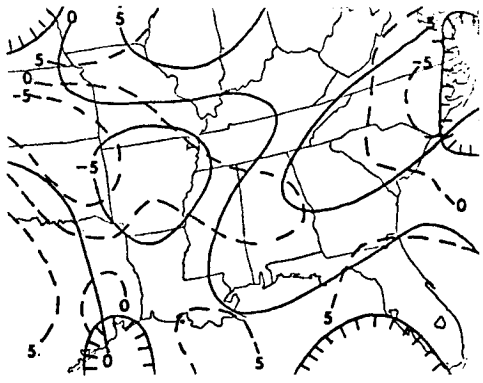

a) Dashed lines indicate changes in x-component of gradient wind speed (m sec^{-1} (6 $hr)^{-1}$).

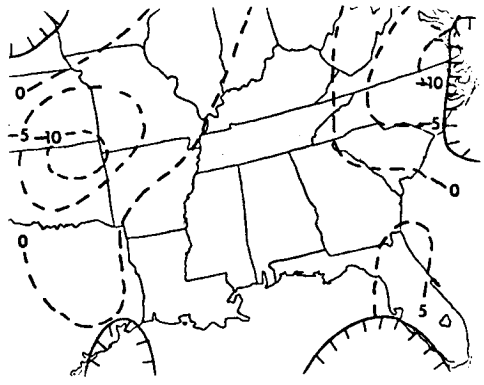

b) Dashed lines indicate changes in x-component of gradient wind speed due to changes in curvature (m sec^{-1} (6 $hr)^{-1}$).

c) Dashed lines indicate changes in x-component of gradient wind speed due to changes in height gradient (m sec^{-1} (6 $hr)^{-1}$).

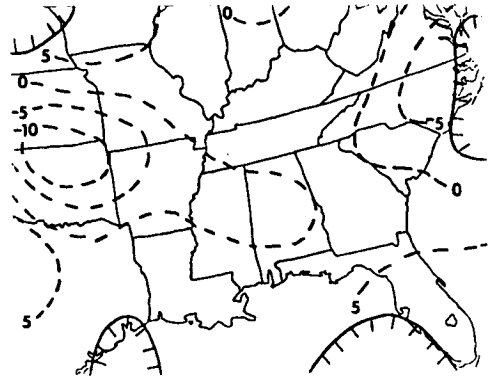

d) Dashed lines indicate sum of b) and c) (m sec^{-1} (6 $hr)^{-1}$).

Fig. 18. Analysis of changes in x-component of gradient wind speed from 0300 to 0900 GMT, 21 February 1964. (Solid lines indicate changes in the x-component of the observed wind speed (m sec^{-1} (6 $hr)^{-1}$). Ticked lines outline areas of non-gradient balance.)

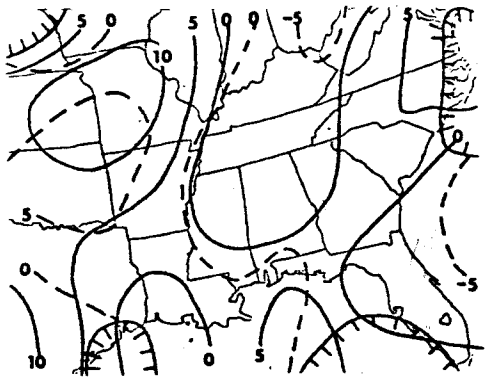

a) Dashed lines indicate changes in y-component of gradient wind speed (m sec^{-1} (6 $hr)^{-1}$).

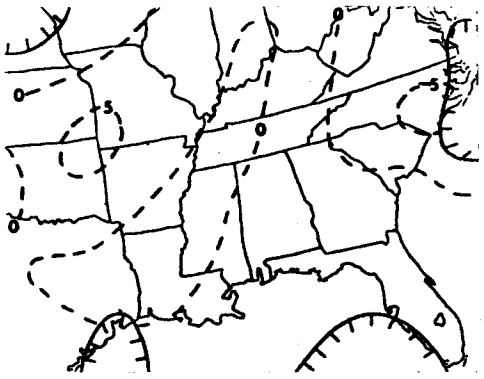

b) Dashed lines indicate changes in y-component of gradient wind speed due to changes in curvature (m sec^{-1} (6 $hr)^{-1}$).

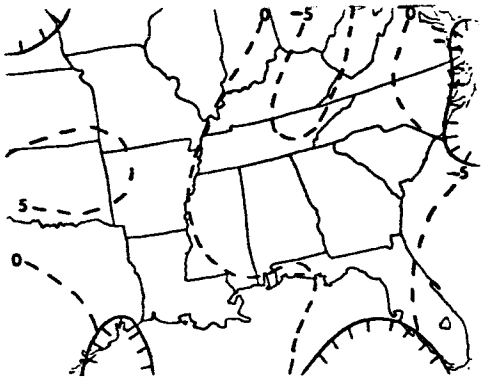

c) Dashed lines indicate changes in y-component of gradient wind speed due to changes in height gradient (m sec^{-1} (6 $hr)^{-1}$).

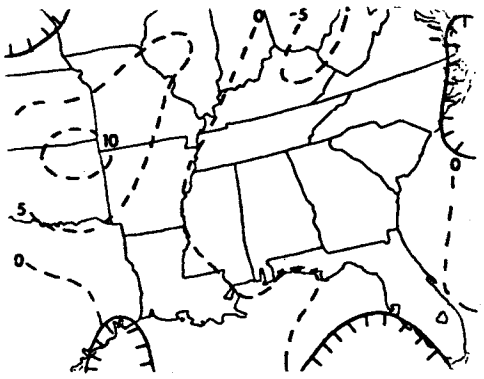

d) Dashed lines indicate sum of b) and c) (m sec^{-1} (6 $hr)^{-1}$).

Fig. 19. Analysis of changes in y-component of gradient wind speed from 0300 to 0900 GMT, 21 February 1964. (Solid lines indicate changes in the y-component of the observed wind speed (m sec^{-1} (6 $hr)^{-1}$). Ticked lines outline areas of non-gradient balance.)

located over north-central Texas and over the Gulf of Mexico immediately west of Florida, respectively. Both of these areas have increases as large as 10 m sec^{-1} $(6\ hr)^{-1}$ in the x-component of the gradient wind speed. However, the area over north-central Texas shows a decrease of 5 m sec^{-1} $(6\ hr)^{-1}$ in the x-component of the observed wind speed. The fourth area of significant change in the x-component of the gradient wind speed is a small area of 5 m sec^{-1} $(6\ hr)^{-1}$ increase centered over northeast Georgia. An increase in the x-component of the observed wind speed also is present in this area.

The analysis of the contributions from curvature and height gradients (Figs. 16b and 16c, p. 96) to the changes in the x-component of the gradient wind speed shows that three of the areas received the largest contribution from the curvature term. These were the areas centered over north-central Texas, southwest Arkansas, and northeast Georgia. In the area over the Gulf of Mexico, the largest contribution to the changes in the x-component of the gradient wind speed came from the height gradient term.

The only predominant synoptic features associated with any of these areas of change in the x-component of the gradient wind speed is the frontal system ahead of the areas in Georgia and the Gulf of Mexico (Figs. 4a and 4c, pp. 71 and 73). There is a pocket of warm air present at the 1000-mb level centered over Arkansas at both 0300 and 0600 GMT.

There are two areas that contain changes of 5 m sec^{-1} $(6\ hr)^{-1}$ or larger in the y-component of the gradient wind speed on 19 February (Fig. 17a, p. 97). The first area encompasses eastern Texas and Oklahoma and shows a decrease larger than 10 m sec^{-1} $(6\ hr)^{-1}$. This area also shows a decrease as large as 10 m sec^{-1} $(6\ hr)^{-1}$ in the y-component of the observed wind speed. The second area is located in the Gulf of Mexico and shows an increase of 10 m sec^{-1} $(6\ hr)^{-1}$ in both the y-component of the gradient and observed wind speeds.

An examination of Figs. 17b and 17c (p. 97) shows that the largest contribution to the change of the y-component of the gradient wind speed in both the area over Texas and the area over the Gulf of Mexico comes from the height-gradient term. There are no dominant synoptic features present at either 0300 or 0900 GMT over the Texas area (Figs. 4a and 4c, pp. 71 and 73). However, the area over the Gulf of Mexico is situated close to the front at 500 mb at both 0300 and 0900 GMT.

On 21 February (Fig. 18a, p. 98) there are six small areas where the change in the x-component of the gradient wind speed exceeded 5 m sec^{-1} $(6\ hr)^{-1}$ between 0300 and 0900 GMT. Areas of increase in the x-component of the gradient wind speed are centered over southern Iowa, central Texas, the Gulf of Mexico, and Florida. In the Iowa and Texas areas, the x-components of the observed wind speed also increase, while decreases are indicated in the Florida and Gulf of Mexico areas. The areas of decrease in the x-component of the gradient wind speed are over Kansas and Oklahoma and over eastern North Carolina. A decrease in the x-component of the observed wind speed is present over the Kansas-Oklahoma area, while an increase is present over North Carolina.

An examination of Figs. 18b and 18c, p. 98, reveals that, of the areas mentioned above, the curvature term provides the largest contribution to the changes in the x-component of the gradient wind speed over Kansas-Oklahoma, eastern North Carolina, and Florida. Over central Texas and Iowa, the largest contribution comes from the height-gradient term. The change in the x-component of the gradient wind speed over the Gulf of Mexico receives approximately the same contribution from both the curvature and height-gradient terms. Synoptically, there are thermal waves present at 1000 mb at both 0300 and 0900 GMT (Figs. 5a and 5c, pp. 77 and 79) over the areas where the changes in the x-components of the two wind speeds differed in sign. There are no predominant synoptic features present in the other areas of significant change in the x-component of the gradient wind speed.

There are two principal areas of significant change in the y-component of the gradient wind speed on 21 February (Fig. 19a, p. 99) over the 6-hour time period. An area of 5 m sec^{-1} $(6\ hr)^{-1}$ increase is centered over northeastern Oklahoma and an area of 5 m sec^{-1} $(6\ hr)^{-1}$ decrease is centered over the Atlantic Ocean east of Georgia. In both of these areas the change in the y-component of the observed wind speed agrees in sign with the change of the y-component of the gradient wind speed.

In the area of increase in the y-component of the gradient wind speed over Oklahoma, the curvature and height gradient terms contribute approximately the same to the increase. Over the Atlantic area the largest contribution comes from the height-gradient term (Figs. 19b and 19c, p. 99).

In summary, 14 areas of significant change in the x- and y-components of the gradient wind speed were observed over a 6-hour period on 19 and 21 February. Five of the areas disagreed and nine agreed in sign with the changes in the x- and y-components of the observed wind speed. Although many of the areas were small and not associated with predominant synoptic features, a few of the larger areas in which the changes in the components of the two wind speeds disagreed in sign contained waves in the thermal field.

Of the 14 areas, six received the largest contribution from the height gradient (Term III in Eqs. (9) and (10)), six received the largest contribution from curvature (Term II), and two received equal contributions from curvature and height gradient (Terms II and III). The contributions from a change in direction (Term I) were negligible in all of the areas. Of the five areas in which the changes in the components of the observed and gradient wind speeds disagreed in sign, the changes in the component of the gradient wind speed were due to curvature in four areas, and height gradient in the fifth.

c) Changes over a period of 12 hours

1) Observed and gradient wind speeds

The 12-hour changes in the observed and gradient wind speeds on 19 and 21 February are shown in Figs. 20 and 21, respectively. The correlation coefficients computed between the changes in the observed and gradient

wind speeds were 0.51 for 19 February and 0.37 for 21 February. These correlation coefficients were the highest obtained and are statistically significant at the 5% level (Brooks and Carruthers, 1953). These higher correlation coefficients may be attributed to the fact that there are more changes larger than the time-change rms error of 4.8 m sec-1 over 12 hours than over 3 or 6 hours.

On 19 February (Fig. 20) a large majority of the changes in the observed and gradient wind speeds are larger than 5 m sec^{-1} $(12\ hr)^{-1}$. The principal area of changes in both wind speeds is centered over northern Mississippi and has a maximum decrease of 10 m sec^{-1} $(12\ hr)^{-1}$. The change in pressure gradient over this area from 0300 to 1500 GMT (Figs. 4a and 4e, pp. 71 and 75) is approximately 40 m in 450 km, which is large enough to account for the wind speed changes observed.

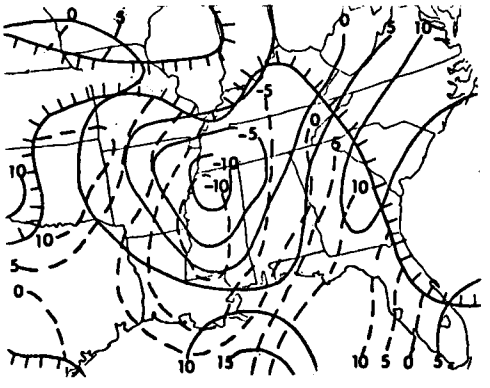

Fig. 20. Changes in observed and gradient wind speeds at 500 mb from 0300 to 1500 GMT, 19 February 1964. (Solid and dashed lines indicate, respectively, changes in observed and gradient wind speeds in m sec^{-1} $(12\ hr)^{-1}$. Ticked lines outline areas of non-gradient balance.)

On 21 February, there are two relatively large areas that contain significant changes in the observed wind speed. Northeast of a line from eastern Iowa to the North-South Carolina border, the observed wind speed increased over this time period (Fig. 21, p.103). The increase over Indiana is in excess of 15 m sec^{-1} $(12\ hr)^{-1}$. It is difficult to determine the synoptic changes which take place on the edges of the map. However, from Figs. 5a and 5d, pp. 77 and 80, it appears that there is a slight increase in the pressure gradient over this general area at 500 mb.

The second area of significant change in the observed wind speed on 21 February (Fig. 21, p.103) is an area of 5 m sec^{-1} $(12\ hr)^{-1}$ decrease stretching from Kansas to northern Florida. Although the change in the pressure gradient required to produce a 5 m sec^{-1} $(12\ hr)^{-1}$ change over this area would be quite small, one can see a slight decrease in the pressure gradient over this general area from 0300 to 1500 GMT (Figs. 5a and 5e, pp. 77 and 81). In other words, both of the large areas of change in the observed wind speed on 21 February correspond with similar changes in the pressure gradient.

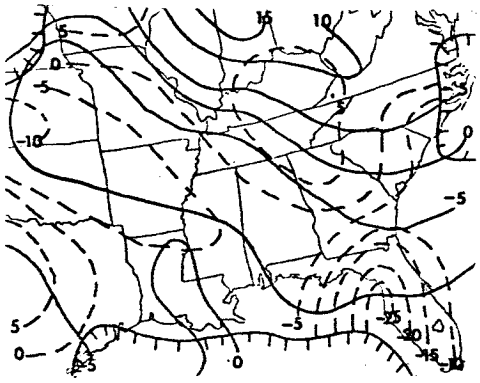

Fig. 21. Changes in observed and gradient wind speeds at 500 mb from 0300 to 1500 GMT, 21 February 1964. (Solid and dashed lines indicate, respectively, changes in observed and gradient wind speeds in m sec^{-1} $(12\ hr)^{-1}$. Ticked lines outline areas of non-gradient balance.)

There is an area of large decrease in the gradient wind speed centered over the west coast of Florida (Fig. 21). Although there is a decrease in the pressure gradient over this general region at 500 mb (Figs. 5a and 5e, pp. 77 and 81), it is not large enough to produce a 25 m sec^{-1} $(12\ hr)^{-1}$ change. It is possible that the small center of maximum change is the result of an error in the height field. The gradient wind speed was computed from the height field and, therefore, large changes in the gradient wind speed could be caused by an error in the height that would not correspond with changes in the observed wind speed.

2) Contributions to changes in the gradient wind

The 12-hour changes of the x- and y-components of the observed and gradient wind speeds for 19 and 21 February are shown in Figs. 22 through 25. The contributions of Terms II and III in Eqs. (9) and (10) to changes in the gradient wind speed also are shown in these figures. As for the previous time periods, the contributions of Term I in Eqs. (9) and (10) were negligible.

The principal area of significant change in the x-component of the gradient wind speed on 19 February is an area of 10 m sec^{-1} $(12\ hr)^{-1}$ decrease over eastern Mississippi (Fig. 22a). Throughout the northern two-thirds of this area the x-component of the observed wind speed also shows a decrease as large as 5 m sec^{-1} $(12\ hr)^{-1}$. The southern one-third of the area contains a slight increase in the x-component of the observed wind speed.

Throughout the area of decrease in the x-component of the gradient wind speed centered over Mississippi, the largest contribution comes from the curvature term (Fig. 22b) rather than from the height-gradient term (Fig. 22c, pp.104). It is quite evident from the synoptic charts that the contour curvature has increased cyclonically, and the height gradient decreased from 0300 to 1500 GMT (Figs. 4a and 4e, pp. 71 and 75).

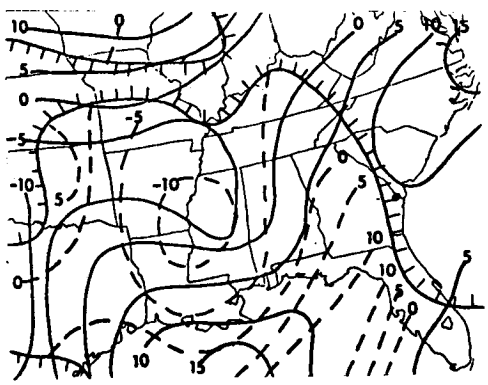

a) Dashed lines indicate changes in x-component of gradient wind speed (m sec^{-1} (12 $hr)^{-1}$).

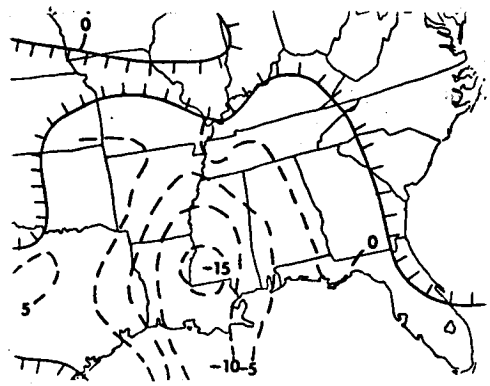

b) Dashed lines indicate changes in x-component of gradient wind speed due to changes in curvature (m sec^{-1} (12 $hr)^{-1}$).

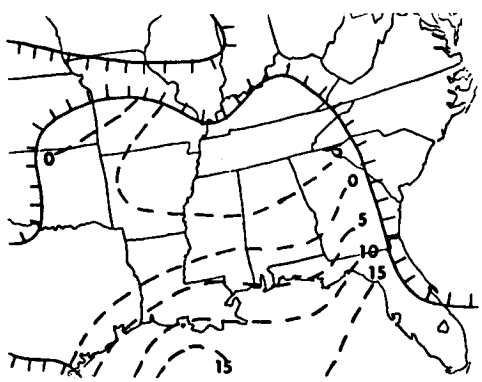

c) Dashed lines indicate changes in x-component of gradient wind speed due to changes in height gradient (m sec^{-1} (12 $hr)^{-1}$).

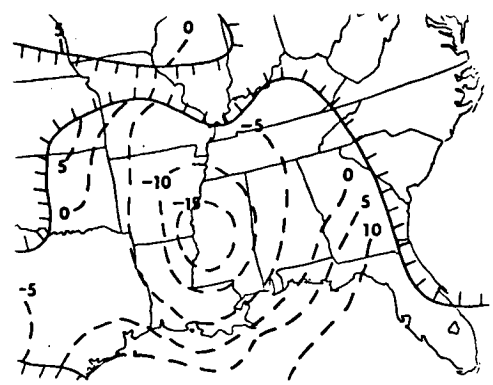

d) Dashed lines indicate sum of b) and c) (m sec^{-1} (12 $hr)^{-1}$).

Fig. 22. Analysis of changes in x-component of gradient wind speed from 0300 to 1500 GMT, 19 February 1964. (Solid lines indicate changes in the x-component of the observed wind speed (m sec^{-1} (12 $hr)^{-1}$). Ticked lines outline areas of non-gradient balance.)

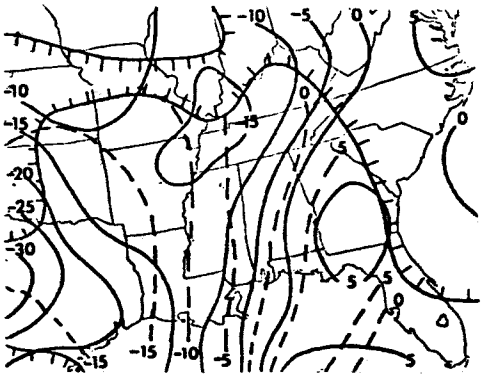

a) Dashed lines indicate changes in y-component of gradient wind speed (m sec^{-1} (12 hr)$^{-1}$).

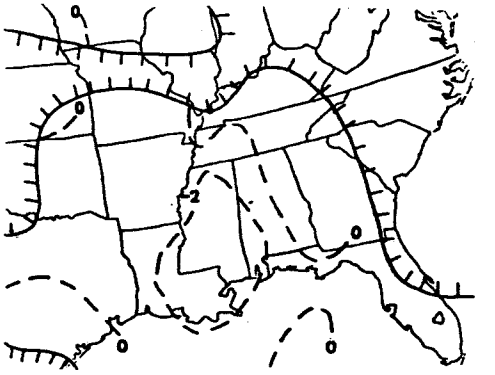

b) Dashed lines indicate changes in y-component of gradient wind speed due to changes in curvature (m sec^{-1} (12 hr)$^{-1}$).

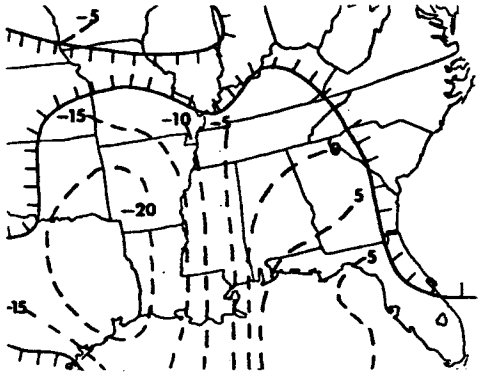

c) Dashed lines indicate changes in y-component of gradient wind speed due to changes in height gradient (m sec^{-1} (12 hr)$^{-1}$).

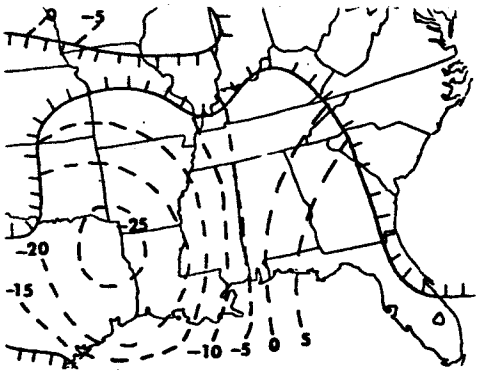

d) Dashed lines indicate sum of b) and c) (m sec^{-1} (12 hr)-1).

Fig. 23. Analysis of changes in y-component of gradient wind speed from 0300 to 1500 GMT, 19 February 1964. (Solid lines indicate changes in the y-component of the observed wind speed (m sec-1 (12 hr)$^{-1}$). Ticked lines outline areas of non-gradient balance.)

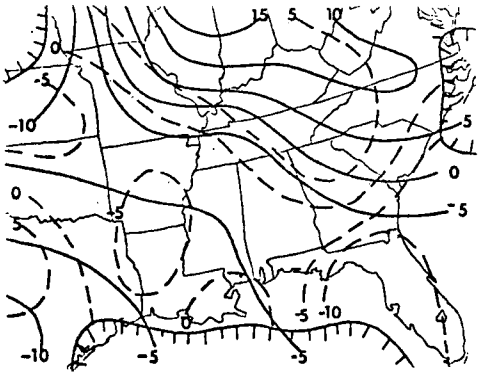

a) Dashed lines indicate changes in x-component of gradient wind speed (m sec^{-1} $(12\ hr)^{-1}$).

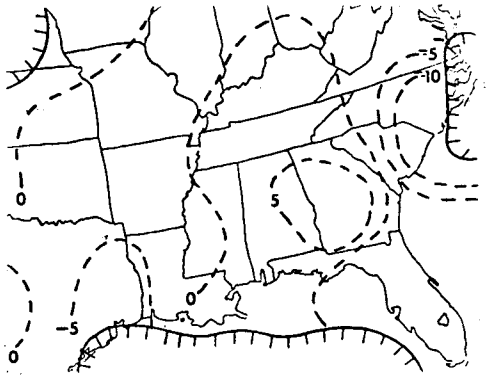

b) Dashed lines indicate changes in x-component of gradient wind speed due to changes in curvature (m sec^{-1} $(12\ hr)^{-1}$).

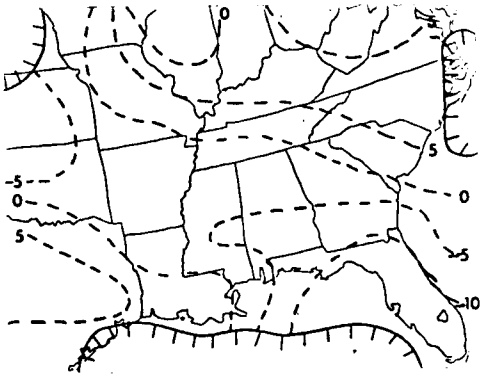

c) Dashed lines indicate changes in x-component of gradient wind speed due to changes in height gradient (m sec^{-1} $(12\ hr)^{-1}$).

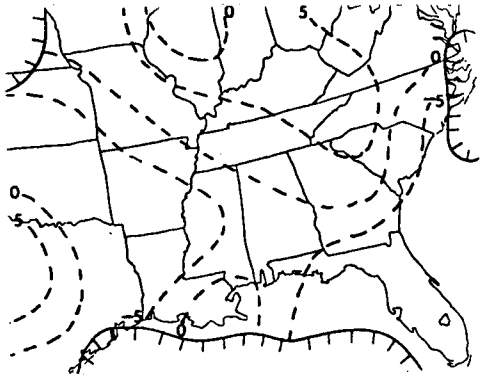

d) Dashed lines indicate sum of b) and c) (m sec^{-1} $(12\ hr)^{-1}$).

Fig. 24. Analysis of changes in x-component of gradient wind speed from 0300 to 1500 GMT, 21 February 1964. (Solid lines indicate changes in the x-component of the observed wind speed (m sec^{-1} $(12\ hr)^{-1}$). Ticked lines outline areas of non-gradient balance.)

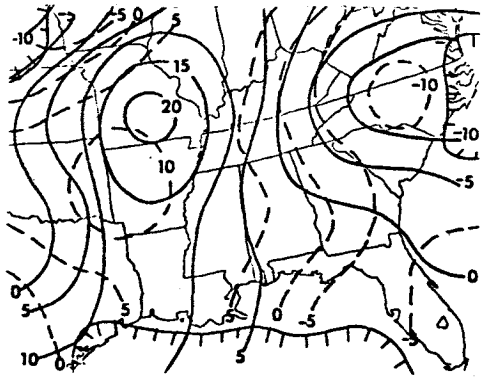

a) Dashed lines indicate changes in y-component of gradient wind speed (m sec^{-1} (12 hr)$^{-1}$).

b) Dashed lines indicate changes in y-component of gradient wind speed due to changes in curvature (m sec^{-1} (12 hr)$^{-1}$).

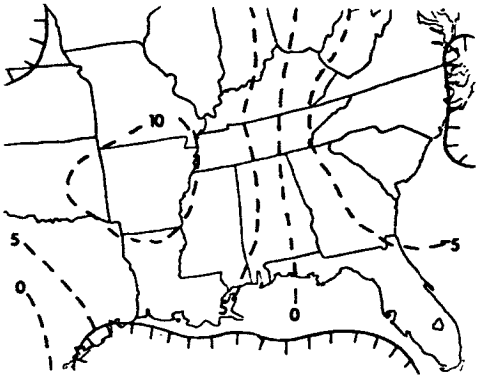

c) Dashed lines indicate changes in y-component of gradient wind speed due to changes in height gradient (m sec^{-1} (12 hr)$^{-1}$).

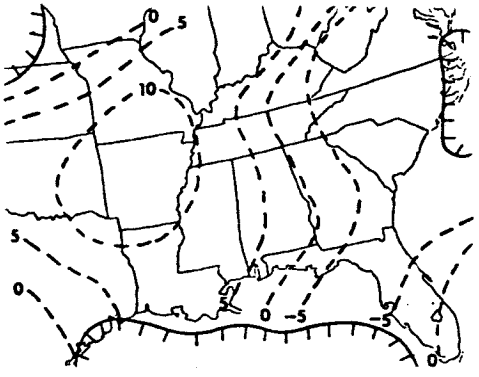

d) Dashed lines indicate sum of b) and c) (m sec^{-1} (12 hr)$^{-1}$).

Fig. 25. Analysis of changes in y-component of gradient wind speed from 0300 to 1500 GMT, 21 February 1964. (Solid lines indicate changes in the y-component of the observed wind speed (m sec^{-1} (12 hr)$^{-1}$). Ticked lines outline areas of non-gradient balance.)

The principal area of significant change in the y-component of the gradient wind speed is an area of decrease located generally to the west of the Mississippi River (Fig. 23a, p.105). The maximum decrease in this area is in excess of 15 m sec^{-1} $(12\ hr)^{-1}$. The y-component of the observed wind speed in this area also decreased.

The contributions to the change in the y-component of the gradient wind speed west of the Mississippi River definitely come from the height-gradient term (Fig. 23c, p.105) rather than the curvature term (Fig. 23b, p.105). The synoptic conditions in this area (Figs. 4a and 4e, pp. 71 and 75) show a decrease in the height gradient and an increase in the cyclonic curvature of the height contours from 0300 to 1500 GMT.

On 21 February (Fig. 24a, p.106) there are five areas in which the change in the x-component of the gradient wind speed is larger than 5 m sec^{-1} $(12\ hr)^{-1}$. Areas of increase are centered over Kentucky, 5 m sec^{-1} $(12\ hr)^{-1}$, and central Texas, 5 m sec^{-1} $(12\ hr)^{-1}$. The area over Kentucky also shows an increase in the x-component of the observed wind speed, while the area over Texas shows a decrease. The areas which show significant decrease in the x-component of the gradient wind speed are centered over Kansas, 5 m sec^{-1} $(12\ hr)^{-1}$, north Louisiana, 5 m sec^{-1} $(12\ hr)^{-1}$, and Florida, 10 m sec^{-1} $(12\ hr)^{-1}$. All three of these areas also show decreases in the x-component of the observed wind speed.

The analyses of the change in the x-component of the gradient wind speed are shown in Figs. 24b through 24d, p.106. The areas of change centered over Kansas, central Texas, Kentucky, and Florida received the largest contribution from the height-gradient term. The area of change over Kentucky received approximately the same contribution from both the curvature and height-gradient terms.

The largest synoptic changes between 0300 and 1500 GMT (Figs. 5a and 5e, pp. 77 and 81) took place in the area where the x-component of the gradient wind speed had its greatest increase. The flow at 500 mb became more zonal which in itself caused an increase in the x-component. A wave in the temperature field also is evident moving through the area from 0300 to 1500 GMT at the 700-mb level.

There are two areas of significant change in the y-component of the gradient wind speed on 21 February (Fig. 25a, p.107). An area of 10 m sec^{-1} $(12\ hr)^{-1}$ increase is centered over Missouri and an area of 10 m sec^{-1} $(12\ hr)^{-1}$ decrease is centered over North Carolina. Both of these areas have similar changes in the y-component of the observed wind speed.

An examination of Figs. 25b through 25c, p.107, shows that the areas of change in the y-component of the gradient wind speed over Missouri and North Carolina both received the largest contribution from the height-gradient term. An examination of the 500-mb synoptic conditions in these areas for 0300 and 1500 GMT (Figs. 5a and 5e, pp. 77 and 81) shows that the height gradient in the x-direction over Missouri and North Carolina decreases slightly.

All together, on 19 and 21 February, for the 12-hour time period, there were nine areas of significant change in the x- and y-components of

the gradient wind speed. In only one of the nine areas did the changes in the x-components of the gradient and observed wind speeds disagree in sign. In almost all of the areas, the changes in the components of the gradient and observed wind speeds were explainable by changes in the synoptic conditions, such as the height gradient.

Of the nine areas observed where there were significant changes in the components of the gradient wind speed, seven of the areas received the largest contribution from the height-gradient term, one from the curvature term, and one area received an equal contribution from both the curvature and height-gradient terms. In the one area where the components of the two wind speeds disagreed in sign, the changes in the component of the gradient wind speed received the largest contribution from the height-gradient term.

3. Comparison of changes over time intervals from 3 to 12 hours

The correlations between the 3- and 6-hour changes of the observed and gradient wind speeds were generally poor, while the comparisons of the 12-hour changes were more satisfactory. Although the comparisons of the 3- and 6-hour changes were poor in a quantitative sense, there were isolated areas where the patterns of the changes were in general agreement. The linear correlation coefficients between the changes at the different time periods are shown in Fig. 26. The correlation coefficients for the 9-hour changes also were computed. With the number of data points considered, only the correlation coefficients over the 12-hour intervals and the 9-hour interval on 21 February were statistically significant at the 5% level (Brooks and Carruthers, 1953).

A possible explanation for the poor correlations over the 3- and 6-hour intervals with improvements over the 9- and 12-hour intervals could lie in the rms errors of the changes in the observed and gradient wind speeds. As mentioned previously, the rms error associated with time changes in the observed wind speed is approximately 4.8 m sec^{-1}. The rms error in the time changes of the gradient wind speed also was assumed to be 4.8 m sec^{-1}. Over the 3- and 6-hour intervals there were few changes in the observed and gradient wind speeds larger than 4.8 m sec^{-1}. However, as the time interval increased to 9 and 12 hours, the number of observed and gradient wind speeds larger than 4.8 m sec^{-1} increased.

In the qualitative comparison between the changes in the components of the observed and gradient wind speeds, the results also were poor over the 3- and 6-hour intervals and better over the 12-hour intervals. There were 22 areas over 3 and 6 hours with significant changes in the x- or y-components of the gradient wind speed. In 13 of the 22 areas the changes in the x- or y-components of the observed wind speed agreed in sign with the changes in the x- or y-components of the gradient wind speed. In nine of the 22 areas the changes disagreed in sign. Over the 12-hour interval there were nine areas in which the x- or y-components of the gradient wind speed changed by more than 5 m sec^{-1} $(12\ hr)^{-1}$. In eight of these areas, the changes in the x- or y-components of the observed wind speed agreed in sign with the changes in the components of the gradient wind speed.

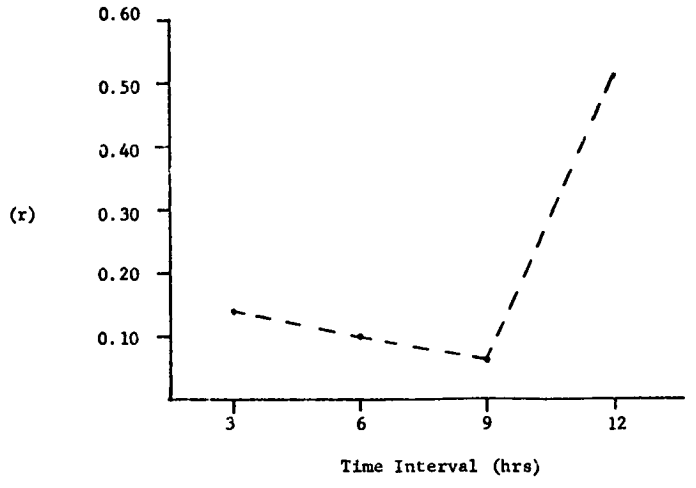

a) 19 February 1964

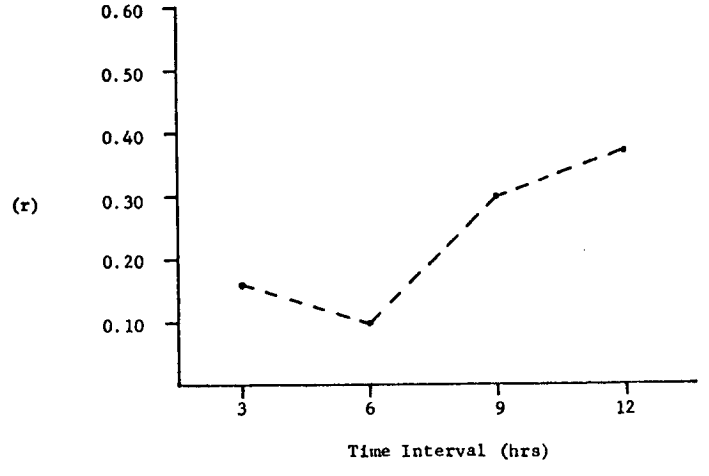

b) 21 February 1964

Fig. 26. Correlation coefficient (r) between changes in the observed and gradient wind speeds over various time intervals.

The frequency that each term in Eqs. (9) and (10) made the largest contribution to changes in the gradient wind speed is shown in Table 4. Over the 3- and 6-hour time intervals, Terms II and III are the largest

Table 4. Terms in Eqs. (9) and (10) giving the largest contribution to changes in the gradient wind speed.

Interval	No. Areas	Term I	Term II	Term III	II & III equal
3-hr	8	*	4	4	0
6-hr	14	*	7	5	2
12-hr	9	*	1	7	1

*The contributions from Term I were negligible over all time periods.

contributors approximately the same number of times. However, over the 12-hour interval, Term III is the largest contributor approximately 80% of the time. This would imply that the changes in trajectory curvature are not as important to the gradient wind speed changes over longer time periods as are changes in the height gradient, which could be due to the difficulties in computing trajectory curvature. The highest correlation coefficients between the changes in the observed and gradient wind speeds were over 12 hours where the height-gradient term was the largest contributor to changes in the gradient wind speed.

Over the 3- and 6-hour time intervals, Terms II and III were the largest contributors to the changes in the components of the gradient wind speed approximately the same amount of time. However, of the ten areas over 3 and 6 hours where the changes in the components of the gradient and observed wind speeds differed in sign, changes in curvature (Term II) provided the largest contribution to the changes in the component of the gradient wind speed in seven of the ten. In other words, over intervals of 3- and 6-hours the curvature term was responsible for the disagreement in signs of the changes in the components of the gradient and observed wind speeds 70% of the time.

It appears that the poor correlations, both quantitative and qualitative, between the changes in the observed and gradient wind speeds are due to the curvature term (Term III). The poorer correlations were found over 3 and 6 hours and the curvature term was the largest contributor to the changes in the gradient wind speed in approximately half of the areas. Better correlations were found over 12 hours and the curvature term was the largest contributor in only one area. However, this possibly would be expected because of the difficulty in accurately computing trajectory curvature.

I. SUMMARY AND CONCLUSIONS

1. Summary

According to Endlich (1961), the "gradient winds provide an estimate of actual winds which is sufficiently accurate to make them useful in describing the dynamics of synoptic-scale processes." The forces which control changes in the horizontal wind speed are pressure gradient, coriolis, centrifugal, and frictional. The frictional force is the only one not considered in the derivation of the gradient wind approximation. It would seem, then, that the local changes in the observed wind speed at a level in the atmosphere could be approximated with a fair degree of accuracy by the local changes in the gradient wind speed. The purpose of this study was to examine the relationship between local changes in the gradient and observed wind speeds over varying time intervals at the 500-mb level.

Rawinsonde data which were unique in both accuracy and frequency were provided by NASA. Three-hour reports were taken from 30 stations located in the southeastern United States during the period 19 to 22 February 1964. These data are available at 25-mb intervals from 1025 to 75 mb. A special procedure was used in obtaining wind measurements in order to insure increased accuracy. At 500 mb, the average rms error in the wind speed was 3.6 m sec^{-1}. Extra care also was taken in the processing of the height data. The 500-mb wind and height reports were extracted from these data and interpolated to a grid. The grid points were spaced evenly over the region with a distance of approximately 158 km between grid points. Computer programs were written to compute the height gradient, trajectory curvature, and gradient wind speed at each grid point. An identifying symbol was used to denote areas where a gradient balance was not achieved.

Local time changes were computed for the gradient and observed wind speeds over time intervals of 3-, 6-, and 12-hours on both 19 and 21 February 1964. The 3-hour changes on each day were computed from 0300 to 0600 GMT, the 6-hour changes from 0300 to 0900 GMT, and the 12-hour changes from 0300 to 1500 GMT. Correlation coefficients were computed between the changes in the two wind speeds over each time interval. For the 3- and 6-hour time intervals these correlation coefficients were not significantly different from zero. The correlation coefficients over the two 12-hour intervals were significantly different from zero but not exceptionally large, 0.38 and 0.51.

A set of forecast equations was derived for the local time rate-of-change of the x- and y-components of the gradient wind speed. These equations were analyzed over 3-, 6-, and 12-hour time intervals to determine the influence of changes in wind direction, height gradient, and trajectory curvature on the local changes in the gradient wind speed. Over the 3- and 6-hour intervals, the height gradient and the trajectory curvature provided the largest contribution to the changes in the gradient wind speed approximately an equal number of times. Over the 12-hour intervals the

change in height gradient was the largest contributor to changes in the gradient wind speed 80% of the time. The contributions of the changes in wind direction to the changes in the components of the gradient wind speed were negligible over all time intervals.

In addition, correlation coefficients were calculated between the observed and gradient wind speeds for ten different time periods. These correlations ranged from 0.74 to 0.90 and verified Endlich's statement that the gradient wind is a good estimate of the actual wind, at least as far as wind speed is concerned.

2. Conclusions

From the data examined in this study it can be concluded that:

1) Over short time intervals, 3 and 6 hours, the correlation coefficients between the local changes in the observed and gradient wind speeds were not statistically different from zero. This may be attributed partly to the fact that few of the observed and gradient wind-speed changes over these time intervals were larger than the rms errors in the changes, and partly to the difficulty of accurately computing the curvature in the gradient wind equation.

2) Over the longer time intervals, 9- and 12-hours, the correlation coefficients between the local changes in the observed and gradient wind speeds were significant at the 5% level.

3) Over the 3- and 6-hour time intervals, the changes in the x- and y-components of the gradient wind speed received the largest contribution an equal number of times from changes in the height gradient and trajectory curvature. The changes in the components of the gradient wind speed due to a change in the wind direction were negligible over the 3- and 6-hour intervals.

4) Over the 12-hour interval, the changes in the x- and y-components of the gradient wind speed received the largest contribution from changes in the gradient of height 80% of the time. Changes in the components of the gradient wind speed due to changes in the wind direction were negligible over the 12-hour intervals.

5) The correlation coefficients between the observed and gradient wind speeds were quite good ranging from 0.74 to 0.90. The gradient wind speed is a good approximation to the observed wind speed.

J. REFERENCES

II-1. Alexander, M. B., S. C. Brown, D. W. Camp, G. E. Daniels, G. H. Fichtl, K. Hill, J. Kaufman, O. E. Smith, and W. W. Vaughan, 1969: Terrestrial environment (climatic) criteria guidelines for use in space vehicle development, G. E. Daniels, Ed., Rpt. No. 53872, NASA, George C. Marshall Space Flight Center, Marshall Space Flight Center, Alabama, 5.150-5.151.

II-2. Barnes, S. L., 1964: A technique for maximizing details in numerical weather map analysis. J. Appl. Meteorol., 3, 396-409.

II-3. Bjerknes, J., 1951: Compendium of Meteorology, Boston, American Meteorological Society, 577-598.

II-4. Brooks, C. E. P., C. S. Durst, N. Carruthers, D. Dewar, and J. S. Sawyer, 1950: Upper winds over the world. Geophy. Mem. #85, Meteorol. Office, London, 105 pp.

II-5. Brooks, C. E. P., and N. Carruthers, 1953: Handbook of Statistical Methods in Meteorology, London, Her Majesty's Stationery Office, 412 pp.

II-6. Buell, C. E., 1957: An approximate relation between the variability of pressure or height in the atmosphere. Bull. Am. Meteorol. Soc., 38, No. 2, 47-51.

II-7. Carnahan, B., H. A. Luther, and J. O. Wilkes, 1964: Applied Numerical Methods, Vol. II, New York, Wiley and Sons, Inc., 511-512.

II-8. Danard, M. B., 1965: On the dependence of wind variability on surface wind speed, Richardson number and height above terrain. J. Appl. Meteorol., 4, 394-399.

II-9. Durst, C. S., 1948: The fine structure of wind in the free air. Quart. J. Roy. Meteorol. Soc., 74, 349-360.

II-10. _____, 1952: The variation of wind in short periods of time between 30,000 and 35,000 feet, January 1950 to January 1952. Meteorol. Res. Pap. 745, Meteorol. Office, London, 2 pp., plus app.

II-11. _____, 1954: Variation of wind with time and distance. Geophy. Mem. #93, Meteorol. Office, London, 32 pp.

II-12. Ellsaesser, H. W., 1960: Wind variability. AWS Tech. Rep. 105-2, Headquarters, Air Weather Service, Scott AFB, Illinois, 91 pp.

II-13. Endlich, R. M., 1961: Computation and uses of gradient winds. Mon. Wea. Rev., 89, No. 6, 187-191.

II-14. George, J. J., 1960: Weather Forecasting for Aeronautics, New York, Academic Press, 673 pp.

II-15. Godson, W. L., 1950: A study of the deviations of wind speeds and directions from geostrophic values. Quart. J. Roy. Meteorol. Soc., 76, No. 327, 3-15.

II-16. Haltiner, G. J., 1971: Numerical Weather Prediction, New York, Wiley and Sons, Inc., 317 pp.

II-17. Haltiner, G. J., and F. L. Martin, 1957: Dynamical and Physical Meteorology, New York, McGraw-Hill, 470 pp.

II-18. Houbolt, J. C., 1970: Design manual for vertical gusts based on power spectral techniques. Air Force Flight Dynamics Laboratory Tech. Rpt. 70-106, Wright-Patterson AFB, Ohio, 137 pp.

II-19. Jenkinson, A. F., 1956: The relation between standard deviation of contour height and standard vector deviation of wind. Quart. J. Roy. Meteorol. Soc., 82, 198-208.

II-20. Johnson, R. E., 1970: NEXAIR. Bull. Am. Meteorol. Soc., 51, No. 9, 857-859.

II-21. Lenhard, R. W. Jr., A. Court, and H. A. Salmela, 1963: Variability shown by hourly soundings. J. Appl. Meteorol., 2, 99-104.

II-22. Mantis, H. T., 1968: Magnitude of terms in the equation for large-scale atmospheric motions. J. Geophy. Res., 73, No. 16, 5045-5060.

II-23. Panofsky, H., 1964: Introduction to Dynamic Meteorology, University Park, Pennsylvania, College of Mineral Industries, The Pennsylvania State University, p. 77.

II-24. Petterssen, S., 1956: Weather Analysis and Forecasting, New York, McGraw-Hill, 428 pp.

II-25. Reiter, R. R., 1963: Jet Stream Meteorology, Chicago, University of Chicago Press, p. 29.

II-26. Richardson, L. F., 1922: Weather Prediction by Numerical Process, Cambridge, University Press, 236 pp.

II-27. Ryan, R. S., J. R. Scoggins, and A. W. King, 1967: Use of wind shears in the design of aerospace vehicles. J. Spacecraft and Rockets, 4, No. 11, 1526-1532.

II-28. Scoggins, J. R., 1970: Wind Effects on Launch Vehicles, E. D. Geissler, Ed., Slough, England, Technivision Services, Chp. 2.

II-29. Singer, B. M., 1955: Wind variability as a function of time. TN-55-221, Air Force Cambridge Research Center, L. G. Hanscom Field, Bedford, Massachusetts, 19 pp.

K. APPENDIX A

LOCAL TIME RATE-OF-CHANGE OF THE GRADIENT WIND COMPONENTS

As shown earlier in the text, the x- and y-components of the gradient wind may be written as

$$V_{grx} = -\frac{g}{f}\frac{\partial Z}{\partial y} + \frac{KV_{gr}^2 N_y}{f} \quad , \qquad (1)$$

and

$$V_{gry} = \frac{g}{f}\frac{\partial Z}{\partial x} - \frac{KV_{gr}^2 N_x}{f} \quad . \tag{2}$$

The partial derivatives with respect to time of Eqs. (1) and (2) can be taken, to produce

$$\frac{\partial V_{grx}}{\partial t} = \frac{g}{f}\frac{\partial}{\partial t}\left(\frac{\partial Z}{\partial y}\right) + \frac{KV_{gr}^2}{f}\frac{\partial N_y}{\partial t} + \frac{KN_y}{f}\frac{\partial V_{gr}^2}{\partial t} + \frac{N_y V_{gr}^2}{f}\frac{\partial K}{\partial t} \quad , \tag{3}$$

and

$$\frac{\partial V_{gry}}{\partial t} = \frac{g}{f}\frac{\partial}{\partial t}\left(\frac{\partial Z}{\partial x}\right) - \frac{KV_{gr}^2}{f}\frac{\partial N_x}{\partial t} - \frac{KN_x}{f}\frac{\partial V_{gr}^2}{\partial t} - \frac{N_x V_{gr}^2}{f}\frac{\partial K}{\partial t} \quad . \tag{4}$$

But, since $V_{gr}^2 = V_{grx}^2 + V_{gry}^2$, differentiation with respect to time gives

$$\frac{\partial V_{gr}^2}{\partial t} = 2\,V_{grx}\frac{\partial V_{grx}}{\partial t} + 2\,V_{gry}\frac{\partial V_{gry}}{\partial t} \quad , \tag{5}$$

which when substituted into Eqs. (3) and (4) yields,

$$\frac{\partial V_{grx}}{\partial t} = -\frac{g}{f}\frac{\partial}{\partial t}\left(\frac{\partial Z}{\partial y}\right) + \frac{KV_{gr}^2}{f}\frac{\partial N_y}{\partial t} + \frac{KN_y}{f}\left(2V_{grx}\frac{\partial V_{grx}}{\partial t} + 2V_{gry}\frac{\partial V_{gry}}{\partial t}\right) + \frac{N_y V_{gr}^2}{f}\frac{\partial K}{\partial t} \quad . \tag{6}$$

and

$$\frac{\partial V_{gry}}{\partial t} = \frac{g}{f}\frac{\partial}{\partial t}\left(\frac{\partial Z}{\partial x}\right) - \frac{KV_{gr}^2}{f}\frac{\partial N_x}{\partial t} - \frac{KN_x}{f}\left(2V_{grx}\frac{\partial V_{grx}}{\partial t} + 2V_{gry}\frac{\partial V_{gry}}{\partial t}\right) - \frac{N_x V_{gr}^2}{f}\frac{\partial K}{\partial t} \quad . \tag{7}$$

Since Eqs. (6) and (7) both contain V_{grx} and V_{gry}, they must be solved simultaneously. When this is done, the results are

$$\frac{\partial V_{grx}}{\partial t} = \frac{2V_{gry}K^2 N_y V_{gr}^2}{f(f+2V_{gry}KN_x)}\left(\frac{\partial N_x}{\partial t}\right) - \frac{KV_{gr}^2}{f}\left(\frac{\partial N_y}{\partial t}\right) -$$

A' B'

$$\frac{2V_{gry}KN_yN_xV_{gr}^2}{f(f+2V_{gry}KN_x)}\left(\frac{\partial K}{\partial t}\right) + \frac{2V_{gry}KN_yg}{f(f+2V_{gry}KN_x)}\frac{\partial}{\partial t}\left(\frac{\partial Z}{\partial x}\right) -$$

C' D'

$$\frac{g}{f}\frac{\partial}{\partial t}\left(\frac{\partial Z}{\partial y}\right) * \left(1 - \frac{2V_{grx}KN_y}{f} + \frac{4V_{grx}V_{gry}K^2N_xN_y}{f(f+2V_{gry}KN_x)}\right)^{-1},$$

E' F' (8)

and

$$\frac{\partial V_{gry}}{\partial t} = \frac{2V_{grx}K^2N_xV_{gr}^2}{f(f-2V_{grx}KN_y)}\left(\frac{\partial N_y}{\partial t}\right) + \frac{KV_{gr}^2}{f}\left(\frac{\partial N_x}{\partial t}\right) -$$

G' H'

$$\frac{2V_{grx}KN_yN_xV_{gr}^2}{f(f-2V_{grx}KN_y)}\left(\frac{\partial K}{\partial t}\right) + \frac{2V_{grx}KN_xg}{f(f-2V_{grx}KN_y)}\frac{\partial}{\partial t}\left(\frac{\partial Z}{\partial y}\right) +$$

I' J'

$$\frac{g}{f}\frac{\partial}{\partial t}\left(\frac{\partial Z}{\partial x}\right) * \left(1 + \frac{2V_{gry}KN_x}{f} + \frac{4V_{grx}V_{gry}K^2N_xN_y}{f(f-2V_{grx}KN_y)}\right)^{-1}.$$

(9)

L. APPENDIX B

SOLUTION OF TRAJECTORY CURVATURE AS A FUNCTION OF HEIGHT

From Blaton's Equation and by neglecting vertical motion, we can express trajectory curvature as

$$K = \frac{1}{V}\frac{\partial \theta}{\partial t} + \frac{\partial \theta}{\partial s}, \quad (1)$$

where V is the wind speed, θ the angle between the trajectory and the x-axis, t is time, and s is a distance along the trajectory. The curvature, K, will be expressed as a function of height by finding expressions for the terms on the R.H.S. of Eq. (1) in terms of height.

From the chain rule, $\frac{\partial\theta}{\partial s}$ may be expressed as

$$\frac{\partial\theta}{\partial s} = \frac{\partial\theta}{\partial x}\frac{\partial x}{\partial s} + \frac{\partial\theta}{\partial y}\frac{\partial y}{\partial s} \quad . \tag{2}$$

Each term on the R.H.S. of (2) can be expressed as a function of height.

Figure B-1 shows the geometry associated with a short segment of a trajectory, ds. One can relabel the sides of the right triangle in Fig. 1 with respect to the geostrophic wind approximation,

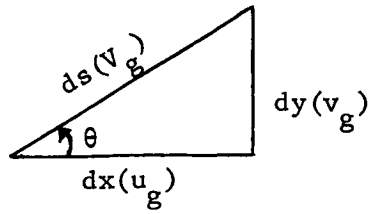

Fig. B-1. Geometry of a trajectory.

$$V_g = \frac{g}{f}\left|\vec{\nabla}Z\right| = (u_g^2 + v_g^2)^{\frac{1}{2}} \quad , \tag{3}$$

$$u_g = -\frac{g}{f} Z_y \quad , \tag{4}$$

and

$$v_g = \frac{g}{f} Z_x \quad . \tag{5}$$

where V_g is the geostrophic wind speed, and u_g and v_g are the x- and y-components of the geostrophic wind speed. The partial differentiation of height with respect to x and y will be denoted by Z_x and Z_y, respectively.

From Fig. 1,

$$\frac{\partial x}{\partial s} = \cos\theta = \frac{u_g}{V_g} = \frac{Z_y}{(Z_x^2 + Z_y^2)^{\frac{1}{2}}} \quad , \tag{6}$$

and

$$\frac{\partial y}{\partial s} = \sin\theta = \frac{v_g}{V_g} = \frac{Z_x}{(Z_x^2 + Z_y^2)^{\frac{1}{2}}} \quad . \tag{7}$$

Also from Fig. 1 it can be seen that

$$\tan\theta = \frac{v_g}{u_g} = -\frac{Z_y}{Z_x} \quad , \tag{8}$$

and, solving for θ,

$$\theta = \tan^{-1}\left(-\frac{Z_y}{Z_x}\right) \quad . \tag{9}$$

Equation (8) can be differentiated partially with respect to x and y to give

$$\theta_x = \frac{Z_x Z_{yx} - Z_y Z_{xx}}{Z_x^2 + Z_y^2} \quad , \tag{10}$$

and

$$\theta_y = \frac{Z_x Z_{yy} - Z_y Z_{xy}}{Z_x^2 + Z_y^2} \quad . \tag{11}$$

Equations (6), (7), (10), and (11) can be substituted into the R.H.S. of Eq. (2) to give

$$\frac{\partial\theta}{\partial s} = \frac{Z_y^2 Z_{xx} - 2Z_x Z_y Z_{xy} + Z_x^2 Z_{yy}}{(Z_x^2 + Z_y^2)^{3/2}} \quad . \tag{12}$$

Equation (8) also can be differentiated partially with respect to time to give

$$\theta_t = \frac{Z_x Z_{yt} - Z_y Z_{xt}}{(Z_x^2 + Z_y^2)} \quad . \tag{13}$$

By making the geostrophic assumption, $V = V_g$,

$$\frac{1}{V} = \frac{f}{g(Z_x^2 + Z_y^2)^{\frac{1}{2}}} \quad . \tag{14}$$

Equations (12), (13), and (14) are now substituted into Eq. (1) to give

$$K = \frac{Z_y^2 Z_{xx} - 2Z_x Z_y Z_{xy} + Z_x^2 Z_{xy}}{(Z_x^2 + Z_y^2)^{3/2}} + \frac{f(Z_x Z_{yt} - Z_y Z_{xt})}{g(Z_x^2 + Z_y^2)^{3/2}} \qquad (15)$$

which expresses curvature as a function of height only.

M. APPENDIX C

LIST OF STATION IDENTIFIERS

AHN Athens, Georgia

BNA Nashville, Tennessee

BRJ Burrwood, Louisiana

CBI Columbia, Missouri

CHS Charleston, South Carolina

CRP Corpus Christi, Texas

DAY Dayton, Ohio

EYW Key West, Florida

FTW Fort Worth, Texas

GSO Greensboro, North Carolina

HSV Huntsville, Alabama

HTS Huntington, West Virginia

JAN Jackson, Mississippi

JAX Jacksonville, Florida

KSC Kennedy Space Center, Florida

LCH Lake Charles, Louisiana

LIT Little Rock, Arkansas

MIA Miami, Florida

MGM Montgomery, Alabama

MTF Mississippi Test Facility

OKC Oklahoma City, Oklahoma

OMA Omaha, Nebraska

PIA Peoria, Illinois

PIT Pittsburgh, Pennsylvania

SAT San Antonio, Texas

SHV Shreveport, Louisiana

TOP Topeka, Kansas

TPA Tampa, Florida

VPS Valpariso, Florida

063 Grand Bahama Island

This page left blank intentionally.

CHAPTER III. AN ANALYSIS OF INTERNAL ZONES OF DISCONTINUITY

by

Dan Gordon Bellue
Department of Meteorology
Texas A&M University, College Station, Texas

A. ABSTRACT

Internal zones of discontinuity were investigated which resulted when an open wave in the Gulf of Mexico developed into an east coast cyclone on February 19, 1964. Cross sections of equivalent potential temperature (θ_e) were employed in the location of these zones, which were delineated on the basis of strong θ_e gradients. Processes which caused variations in these zones with time were investigated by use of the frontogenetic function. The x- and z-component equations of this function were evaluated term-by-term and compared with the observed conditions in the cross sections of θ_e. The results indicated that regions of intense frontogenesis were associated with strong gradients of θ_e within the zones of discontinuity, and regions of intense frontolysis were associated with weak gradients of θ_e. Also, changes in the slope of the discontinuities were associated with frontolytic/frontogenetic regions. The relationship between these changes in slope and changes in the precipitation patterns was examined, and a close association was found. Finally, the usefulness of the frontogenetic function in the study of the zones of discontinuity was pointed out, and the need was emphasized for more frequent and more accurate rawinsonde data.

B. INTRODUCTION

1. Statement of the Problem

Ultimately, any study of synoptic meteorology seeks to aid in producing a better forecast. The interaction between meso- and synoptic-scale features is of particular interest to the station forecaster. Internal zones of discontinuity exist on both scales.

Soundings taken with conventional rawinsonde equipment often show several temperature inversions and isothermal layers in the lower atmosphere. In many instances these layers are not associated with frontal systems. Miller (1948) discusses certain transition layers within the atmosphere that are fundamentally equivalent to frontal zones but usually are not regarded as such in meteorology. If the upper boundaries of these zones of discontinuity slope, they may act as surfaces which could create vertical motion. This vertical motion could lead then to changes in vertical wind shear, baroclinity, and to processes which produce precipitation. Therefore,

internal zones of discontinuity are a major factor in the formation of significant weather on the synoptic scale. When one considers factors such as the concentration of vertical wind shear in the production of clear air turbulence, they become extremely important on the meso-scale. Watson (1971) in a meso-scale study of an intense subsidence inversion states that significant spatial variations in the intensity of the inversion are related closely to certain features in the wind field.

In a synoptic sense, these zones are often treated as zero-order discontinuities in which case they are called fronts. In many cases they are filtered out of synoptic data as being erroneous, but the station forecaster may degrade his forecast when such erroneous-looking data are ignored. The problem, then, is to identify these zones and investigate the factors/processes which lead to changes in their character.

2. Background

Air masses of varied origin exhibit different thermodynamic properties. According to the Norwegian school, fronts represent discontinuities in these thermodynamic properties on the synoptic scale at the boundaries between air masses. Haltiner and Martin (1957) define a front as being "...a surface of discontinuity of density or virtual temperature." They point out that actual discontinuities do not exist in the atmosphere, and that instead of discontinuities there exist zones of transition between air masses. Also, they state that since these zones are relatively narrow compared to the scale of the atmospheric processes involved and the horizontal map scale on which they are depicted, they are treated as discontinuities.

Zones of discontinuity also occur on the meso-scale. Danielsen (1959) found that in original radiosonde records, which were reprocessed to preserve the observational details, there were indicated many zones of large hydrostatic stability often separated by zones of neutral stability. He pointed out that the upper and lower boundaries of these zones were characterized by rapid variations in stability which could be considered discontinuous. Danielsen stated also that these discontinuities often are ignored due to smoothing and operator procedures.

One may question the subjectivity with which discontinuities are treated. Historically, the parameters used to define them have been density, temperature, water-vapor content, and wind. Margules (1906) derived an equation which used these parameters to determine the slope of the upper boundary of a discontinuity. The equation is known as the frontal slope formula. If the temperature difference ($T_2 - T_1$) is not too large and the wind difference is appreciable, this equation reduces to:

$$\text{Tan } \theta = \frac{fT_m}{g} \frac{v_1 - v_2}{T_2 - T_1} \quad , \tag{1}$$

where f is the coriolis parameter, T_m is the mean temperature of the layer, g is the acceleration due to gravity, v is the component of the wind parallel

to the front, T is temperature, and the subscripts 1 and 2 refer to the lower (colder) air mass and the upper (warmer) air mass, respectively.

Recently, other parameters have been sought to characterize these zones. Godson (1951) discussed fronts as being "hyperbaroclinic" zones in which the cyclonic curvature is greater than that of the surrounding region. He stated that these zones are more stable than their surroundings. Sawyer (1955) used aerological data and demonstrated that fronts were found in regions of high baroclinity.

Byers (1959) examined the components of the equation of Margules and illustrated the importance of wind shear to the existence of fronts. He noted that fronts are possible only where there is a cyclonic wind shift or cyclonic wind shear, and not possible in anti-cyclonic shear zones. It should be noted that only the component of wind parallel to the front enters into the frontal slope determination.

Newton and Palmén (1971) pointed out that Bergeron defined a front as being "the region where horizontal cyclonic wind shear is greatest." Renard and Clarke (1965), Kirk (1965), and Kirk (1966) suggested a parameter which they feel is appropriate. This parameter, which incorporates partial derivatives, employs the Laplacian operator on any parameter which is normally used to define a front.

Newton (1954) stated that frontal zones possess four characteristics, viz., (1) a strong horizontal temperature gradient, (2) pronounced vertical stability, (3) strong vertical shear, and (4) higher vorticity values than those of the surroundings. Newton used the equation of Miller (1948) to evaluate the above characteristics. Miller's equation defines the frontogenetic function, $\vec{F}_3$, such that (in three dimensions),

$$\vec{F}_3(t) = \frac{d}{dt}(\vec{\nabla}S) \quad , \tag{2}$$

where S is a property of an air mass. The theory behind Miller's equation is not restricted to fronts and may be applied to any internal zone of discontinuity.

Bosart (1969) with 3-hr rawinsonde data used the equation of Miller in his study of mid-tropospheric frontogenesis and potential vorticity. He applied this equation to a mid-tropospheric baroclinic zone which was intensifying and delineated regions of frontogenesis and frontolysis. Also, he used isentropic trajectories of the velocity field to describe the frontogenesis in space and time.

A much simpler technique is that of Sanders (1955) who also employed the equation of Miller. His work described the frontal structure of an intense front at low levels which occurred in the central United States. He found that certain aspects in both the temperature and wind fields could be explained by the consideration of the pattern of frontogenetical and frontolytical effects which followed the motion of the air. Also, he stated that these effects are extremely intense in the vicinity of marked frontal zones.

Sanders' data consisted of upper-air soundings taken at 6-hr intervals for significant levels. Although these were taken more frequently than usual, meso-scale features can develop and dissipate within this time period. Data taken at closer intervals and for more levels can provide clues as to the processes involved in the development and dissipation of these zones of discontinuity that otherwise might be missed.

3. Objectives

Although many meso-scale features do not appear on synoptic charts, they may produce significant weather. Problems arise for the station forecaster because he must infer from synoptic-scale maps the occurrence of significant weather resulting from meso-scale systems. Internal zones of discontinuity which occur on both scales may produce or enhance significant weather. Therefore, the objectives of this study are to investigate areas where internal zones of discontinuity form and/or change in intensity with time, and to examine the extent to which they are associated with significant weather.

C. DATA AND SYNOPTIC CONDITIONS

1. Source and Extent of Data

The data used in this study were obtained by NASA under Project AVE (Atmospheric Variability Experiment), in which 30 stations in the southeastern United States undertook a concentrated observational effort during a 4-day period in 1964. This data network is shown in Figure 1.

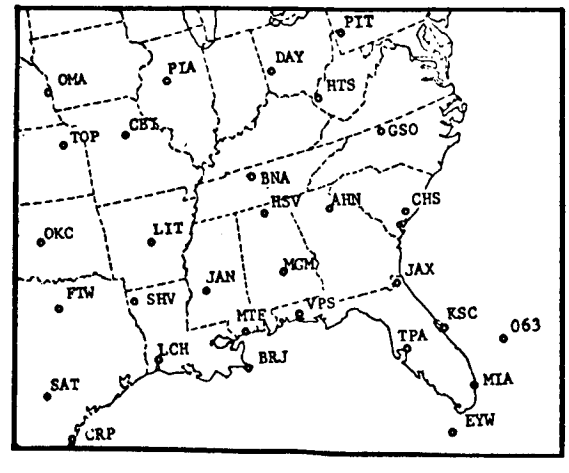

Fig. 1. AVE Data network. (Station identifiers are given in the Appendix.)

Observations were made with conventional rawinsonde equipment, but additional procedures were employed to obtain the maximum resolution possible with the equipment.

The data consisted of standard rawinsonde parameters which included temperature, pressure, humidity, and wind. Soundings were taken at 3-hr intervals to a height of 50 mb when possible. Observations began at 00 GMT, February 19, 1964, and ended at 00 GMT, February 22, 1964. The Marshall Space Flight Center and The Mississippi Test Facility took additional observations before and after this period, and at one and one-half hour intervals during the period. Extra care was taken in processing the data to insure that they were as accurate and as representative as possible. The data were checked carefully for inconsistencies which could have arisen from human and/or mechanical error and corrected if errors were found. Values of each parameter were interpolated for every 25-mb level and recorded on magnetic tape. The data tapes were provided to Texas A&M University by personnel of the Aerospace Environment Division of the NASA Marshall Space Flight Center.

Estimates of the accuracy of the data were provided by Mr. William W. Vaughan* of the Marshall Space Flight Center. These accuracies are:

1) Temperature: RMS errors of 1.4°C to the 400-mb level, and 2.8°C above the 400-mb level are accepted.
2) Pressure: RMS error is 1.3 mb for pressures greater than 400 mb, 1.1 mb for pressures between 400 and 100 mb, and 0.7 mb for pressures between 100 and 10 mb.
3) Humidity: The moisture element of the standard rawinsonde package is the least accurate of any of the sensors; an rms error of 10 percent is accepted. This error would affect values of the dewpoint temperature as well.
4) Pressure Altitude (height): Errors in this parameter are dependent on the errors in all of the parameters listed above. Therefore, the above rms errors were used to determine the errors in the pressure altitude values. These values varied from 3 gpm at 900 mb to 20 gpm at 500 mb to 87 gpm at 50 mb.
5) Wind: Special procedures were used to determine wind velocity due to the better-than-normal vertical resolution. The wind speeds had an approximate rms error of 1.5 m sec^{-1} at 700 mb, 2.5 m sec^{-1} at 500 mb, and 4.0 m sec^{-1} at 300 mb. The wind direction had rms errors of 2° at 700 mb, 3° at 500 mb, and 5° at 300 mb, based on speeds of 10 m sec^{-1}.

The extra care used to read the recording charts and the precision used in the evaluation of the AVE data resulted in a substantial improvement over the thermodynamic data than is available routinely. The procedures used to process the wind data reduced errors considerably compared with usual techniques.

2. Synoptic Conditions

The main synoptic feature for the 4-day observational period was an east coast cyclone. There were no other synoptic features which had frontal systems associated with them. The times chosen for study were 00 GMT, 03 GMT, and

---

*Personal communication.

06 GMT on February 19, 1964. This date was chosen for study because the frontal systems appeared better defined on this date than the following three days.

A storm developed in the western Gulf of Mexico 18 hours prior to the first observation time. Figure 2 is the surface analysis for 06 GMT, February 18 prepared by the National Weather Service (NWS). The open wave intensified and developed into an east coast cyclone, and the frontal system associated with it occluded rapidly. Figure 3 shows this system 24 hours later as it moved out of the data region.

The predominate low-level feature at 00 GMT, February 19 was this east coast cyclone and its frontal system. The 1000-mb chart (Figure 4a) showed that the cyclone was centered approximately 100 nm northeast of Greensboro, North Carolina. It continued to track northeasterly and at 06 GMT was centered in the vicinity of Chesapeake Bay. The 1000-mb thermal pattern showed a weak gradient directly behind the front and a larger gradient in the lee of the Appalachian Mountains.

Cyclone and frontal movement at the 850-mb level were similar to that at the surface (Figure 4b). The thermal gradient behind the front was uniform, but it showed a pronounced trough in the region of Kentucky, Tennessee, Mississippi, and Alabama. Minor waves distorted this pattern.

The 700-mb chart (Figure 4c) was a transition between the closed cyclone in the low levels and a long-wave trough in the upper levels. The thermal gradient was pronounced behind the front at this level.

A long-wave trough dominated the upper-level charts. Figure 4d shows this trough to be well established at 500 mb. Strong southwesterly flow was indicated over the eastern portion of the region. The frontal system was located in the lee of the Appalachian Mountains as an open wave.

The flow pattern at the 300-mb level (Figure 4e) was similar to that at the 500-mb level, but the frontal system was not discernable in the thermal pattern. Strong southwesterly winds were indicated over the eastern region.

Little change occurred in the synoptic pattern over the remainder of the period considered, but the precipitation patterns varied greatly. Cold-air advection continued at all levels while subsequent charts showed an eastward movement of the entire system.

D. THEORY OF THE FORMATION OF AND CHANGES IN INTERNAL ZONES OF DISCONTINUITY

In the study of the interaction between synoptic and meso-scale features a term such as "front" becomes ambiguous. To be as general as possible all zones of concentrated transition were studied. These zones have been termed "internal zones of discontinuity" in order to include meso-scale features with those of a synoptic scale.

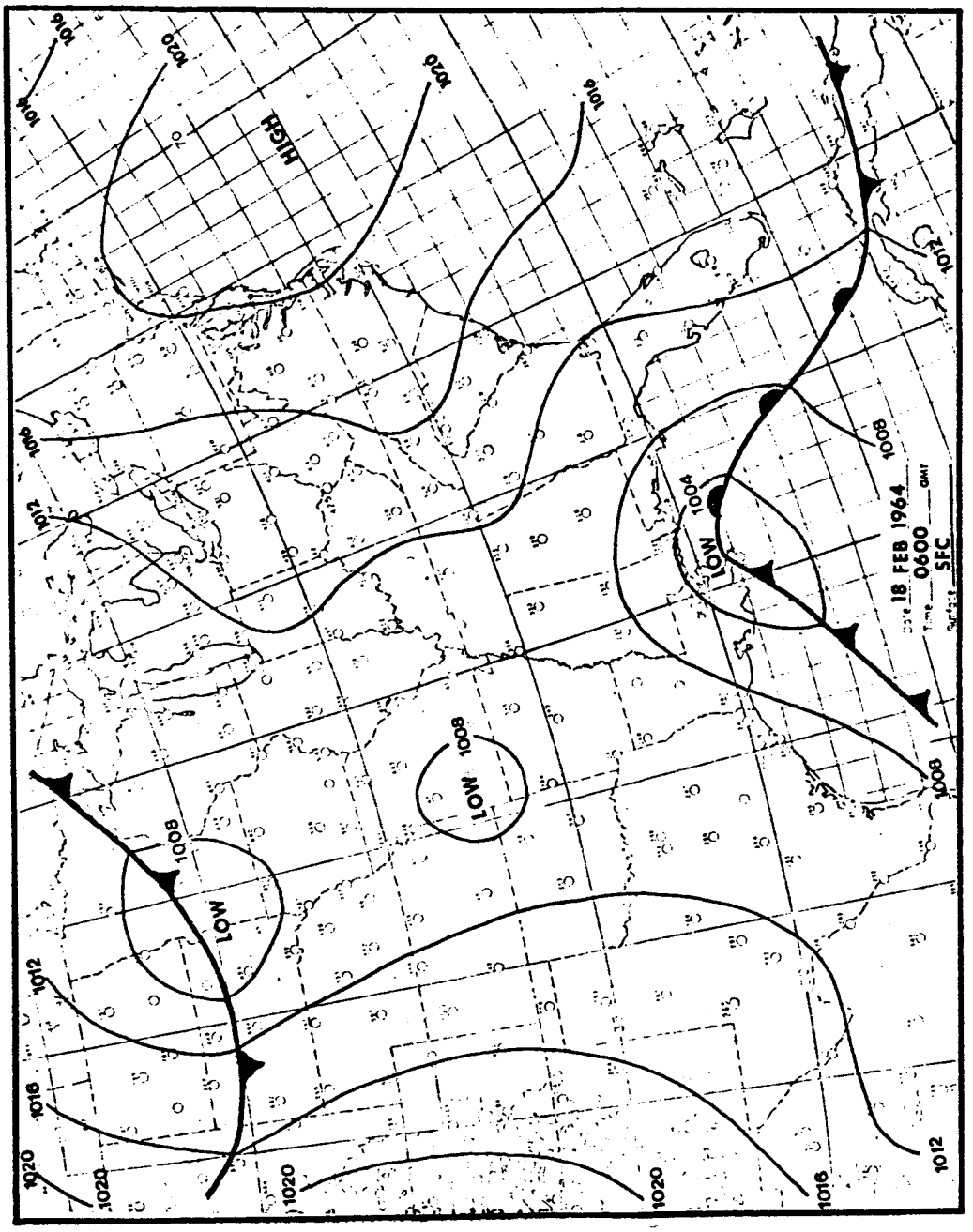

Fig. 2. National Weather Service surface analysis for 0600 GMT, February 18, 1964.

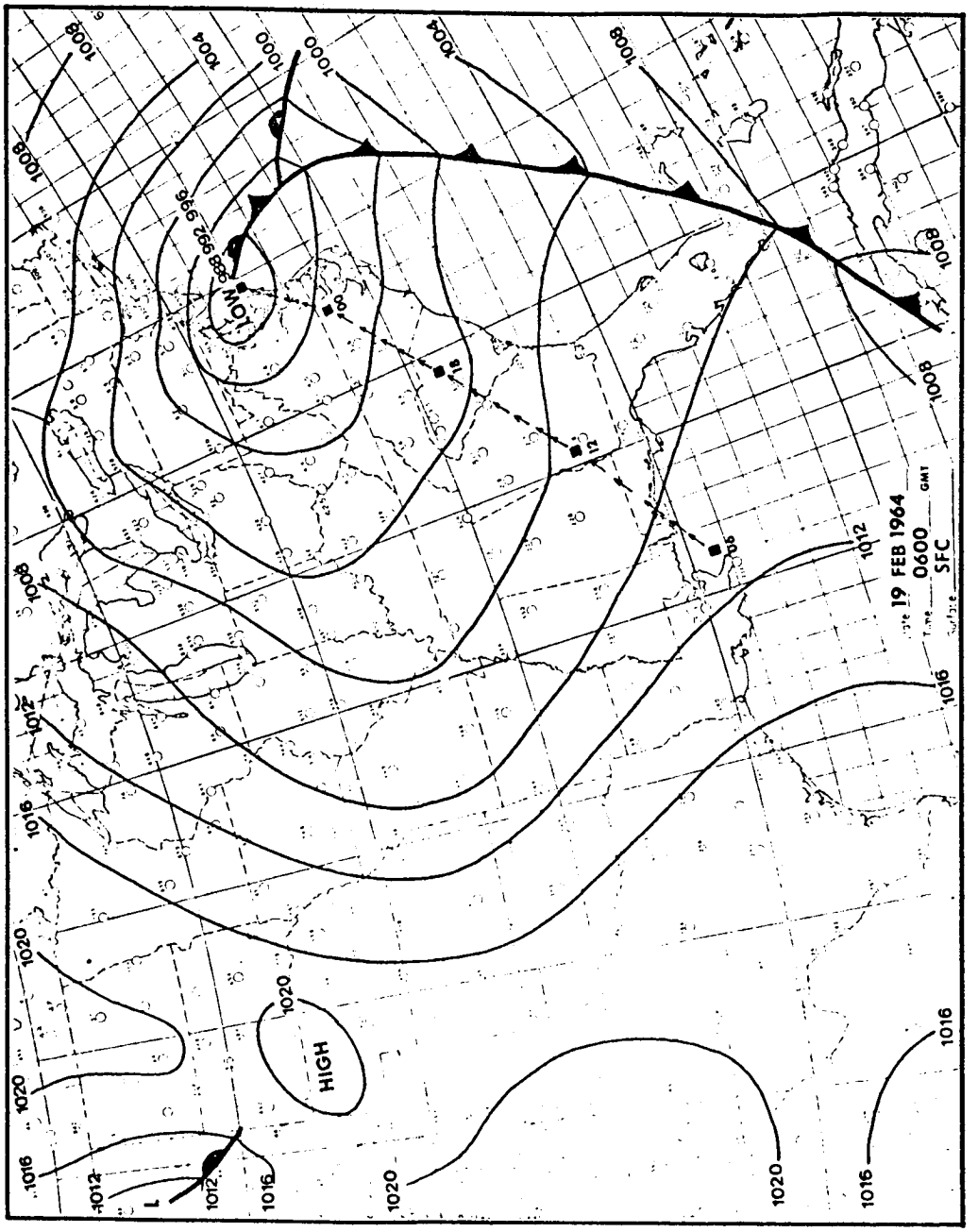

Fig. 3. National Weather Service surface analysis for 0600 GMT, February 19, 1964.

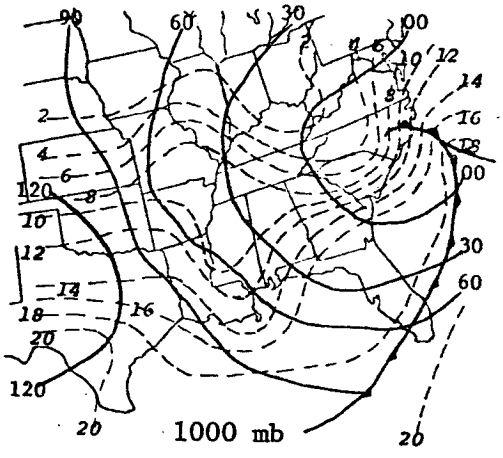

a

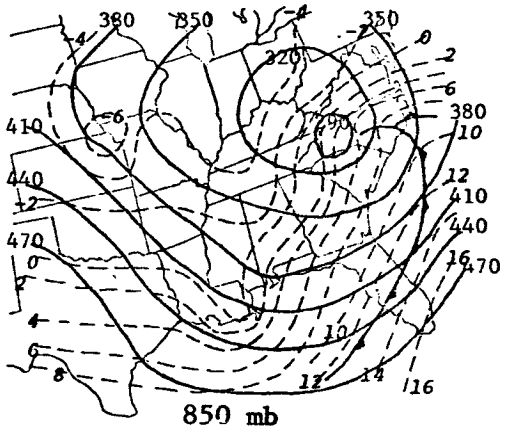

b

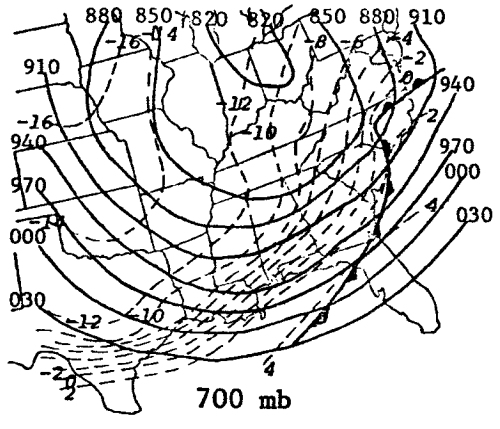

c

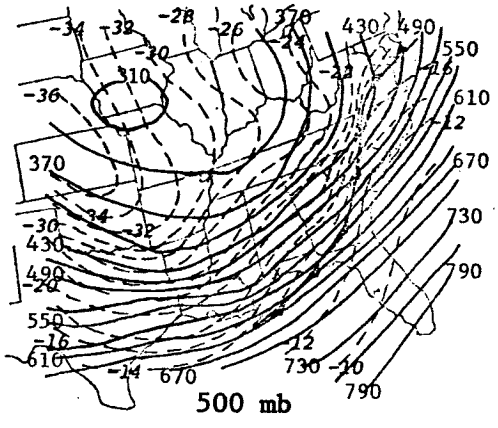

d

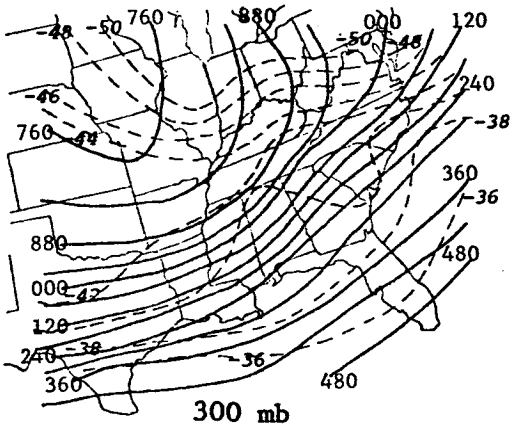

e

Fig. 4. Synoptic maps for 00 GMT, February 19, 1964.

If one considers a broad definition of a front as being a zone of discontinuity, then reference to the terms frontogenesis and frontolysis will indicate the concentration of certain characteristic properties. How are these zones of discontinuity formed? Any discontinuity implies that a rapid change in a characteristic property of an air mass over a short distance has occurred. This change implies the existence of a gradient of this property. Petterssen (1956) defines frontogenesis as the process that concentrates the gradient of a property S, such as potential temperature, and defines frontolysis as the opposite of frontogenesis. Thus, the theory of the formation and dissipation of these zones of discontinuity merely deals with the amount of concentration that occurs for any given parameter over a finite distance or period of time.

The change in the concentration of a property is given by the frontogenetic function, which was written previously as Equation 2. This equation may be written in the form (Newton and Palmén, 1971):

$$\vec{F}_3(t) = \vec{\nabla} \frac{dS}{dt} - \left(\frac{\partial S}{\partial x} \vec{\nabla} u + \frac{\partial S}{\partial y} \vec{\nabla} v + \frac{\partial S}{\partial z} w\right) \tag{3}$$

or in component form as follows:

$$F_x(t) = \frac{d}{dt}\left(\frac{\partial S}{\partial x}\right) = \frac{\partial}{\partial x}\left(\frac{dS}{dt}\right) - \left(\frac{\partial S}{\partial x}\frac{\partial u}{\partial x} + \frac{\partial S}{\partial y}\frac{\partial v}{\partial x} + \frac{\partial S}{\partial z}\frac{\partial w}{\partial x}\right), \tag{4}$$

$$\qquad\qquad\qquad\qquad\qquad\quad A \qquad\quad B \qquad\quad C \qquad\quad D$$

$$F_y(t) = \frac{d}{dt}\left(\frac{\partial S}{\partial y}\right) = \frac{\partial}{\partial y}\left(\frac{dS}{dt}\right) - \left(\frac{\partial S}{\partial x}\frac{\partial u}{\partial y} + \frac{\partial S}{\partial y}\frac{\partial v}{\partial y} + \frac{\partial S}{\partial z}\frac{\partial w}{\partial y}\right), \tag{5}$$

$$\qquad\qquad\qquad\qquad\qquad\quad E \qquad\quad F \qquad\quad G \qquad\quad H$$

and

$$F_z(t) = \frac{d}{dt}\left(\frac{\partial S}{\partial z}\right) = \frac{\partial}{\partial z}\left(\frac{dS}{dt}\right) - \left(\frac{\partial S}{\partial x}\frac{\partial u}{\partial z} + \frac{\partial S}{\partial y}\frac{\partial v}{\partial z} + \frac{\partial S}{\partial z}\frac{\partial w}{\partial z}\right). \tag{6}$$

$$\qquad\qquad\qquad\qquad\qquad\quad I \qquad\quad J \qquad\quad K \qquad\quad L$$

The terms in the above equations may be interpreted in terms of physical processes. These processes occur simultaneously and in varying proportions. Therefore, any description of a single process is theoretical and highly unlikely to occur alone in nature.

The interpretation of the above terms is as follows (Newton and Palmén, 1971). Terms B, G, and L represent the concentration of the gradient by vertical and lateral confluence fields. Figure 5 shows a deformation field which could represent processes which occur on any two of the three axes. Terms C, F, and J represent the increase in intensity of the gradient due to differential advection by the winds. Figure 6 illustrates this process

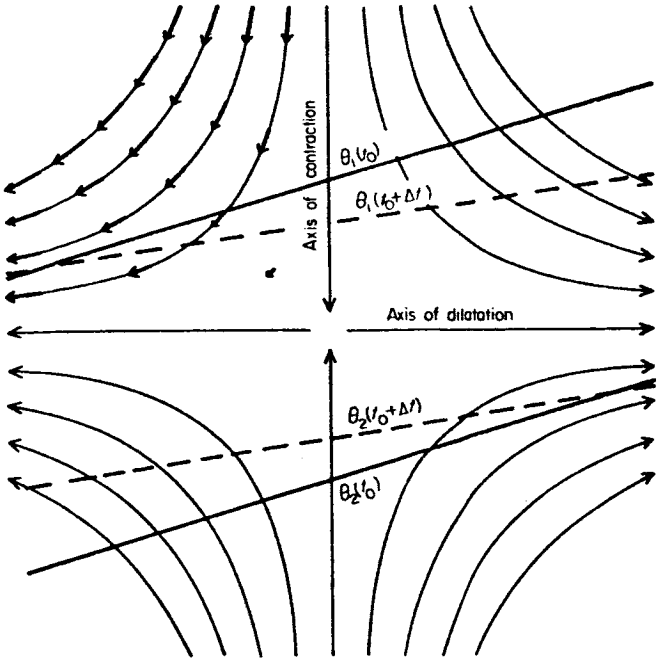

Fig. 5. Streamlines of a pure deformation field. (Successive positions of two potential-temperature isopleths are denoted with dashed lines (Newton and Palmén, 1971)).

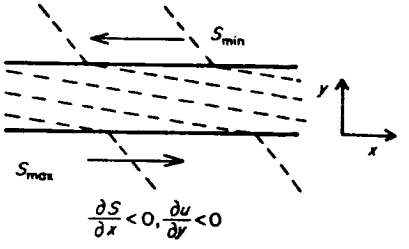

Fig. 6. Increase of a gradient of property S across a zone through the advection by the winds parallel to the zone (Newton and Palmén, 1971).

as it occurrs in the x-y plane. Terms D, H, and K represent the change in the distribution of S in a vertical section. They contribute to the simultaneous vertical and horizontal concentration. Figure 7 gives only the representation in the y-z plane, but the term could apply to the other two planes as well. Terms A, E, and I represent the non-conservative influences which are superimposed on the flow. An example of these influences is diabatic heating or cooling.

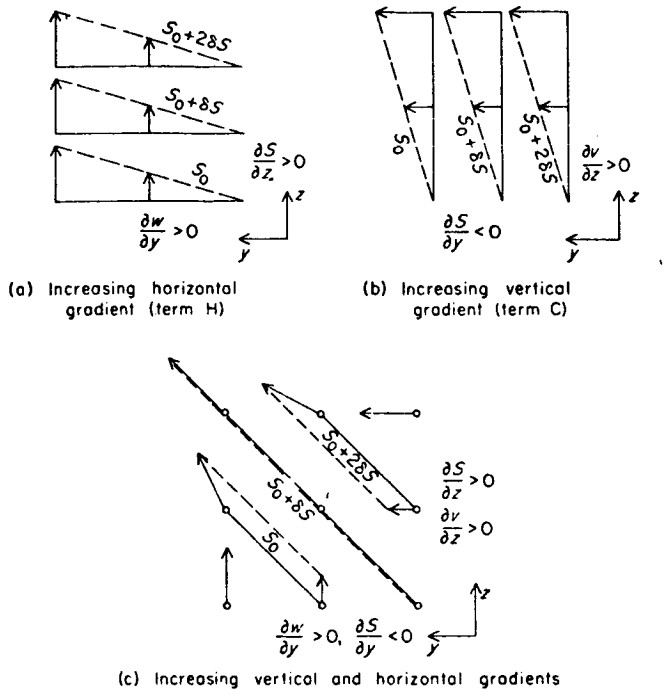

Fig. 7. Simultaneous vertical and horizontal concentration (Newton and Palmén, 1971).

The magnitude of a term in the component equations will show the importance of that term in the concentration of a given property. Once the importance of a term is established, one can infer something about the physical and thermodynamical processes occurring in a region which contribute to the formation of, or changes in, the characteristic of the internal zones of discontinuity.

One evident characteristic of a zone of discontinuity is the slope of its boundary. Processes shown in the frontogenetic function can cause changes in this characteristic. Upon examination of Equation 1, it can be seen that there are certain factors which cause the slope of a zone of discontinuity to be large. These factors are: 1) a large velocity difference, 2) a small temperature difference, 3) higher latitudes which increase f, and 4) a high mean-virtual temperature. The effect of the change of the mean-virtual temperature on the magnitude of the slope is small in comparison to the effects of the other factors, and if a study is undertaken at low latitudes, factor 3) is small also. Changes in any of the above factors could cause the magnitude of the slope to vary, but only the changes in the wind and temperature fields can be related directly to the processes shown in the frontogenetic function.

Frontogenetic processes also may lead to a change in the slope of a zone of discontinuity. For example, if strong frontogenesis occurs along a portion of the frontal cross section, and frontolysis along another portion of the same cross section, a change in slope would result.

E. ANALYTICAL RESULTS

1. Delineation of Zones of Discontinuity

Cross-sectional and constant-pressure analyses were used to study the conditions attending the passage of the east coast cyclone through the data region. Cross sections were selected as nearly normal through the frontal zone as possible. The paths of the cross sections selected for study are shown in Figure 8. Two cross sections were considered in order to investigate the influence of the Appalachian Mountains on the frontogenetic process.

On the synoptic scale, the thermal pattern has been a useful indicator for the location of zones of discontinuity. Potential temperature has been employed frequently in cross-sectional analyses, but because it is not conservative for pseudo-adiabatic processes, it proved to be inadequate for this study. Equivalent potential temperature, θ_e, was selected for use because it is a conservative property for both dry- and pseudo-adiabatic processes. This selection proved fortuitous since precipitation occurred randomly over the data region.

Equivalent potential temperature was calculated with the use of the standard Skew-T, Log-P Diagram. It was calculated for every 25-mb level from the surface to the 250-mb level for three time periods, and for each station shown on the cross sections in Figure 8. These cross sections of θ_e then were analyzed at intervals of 1° Kelvin.

The more prominent zones of discontinuity are shown in Figures 9 and 10 as the regions bounded by the prominent dashed lines. The boundaries were determined on the basis of large gradients of θ_e, i.e., close packing of θ_e indicated the presence of a zone of discontinuity. Boundaries of the zones of discontinuity were drawn in such a way that they crossed as few isentropic surfaces as possible, yet enclosed the regions of large gradients of θ_e. Although this method was subjective, it provided a reasonable method for delineation of the zones of discontinuity.

Three zones of discontinuity were delineated in the northern cross section (Figure 9) at 00 GMT. The major zone extended the length of the cross section; its upper boundary varied from 600 mb over JAX to 300 mb over DAY. The characteristics of this zone varied during the period of study. The slope of the upper boundary decreased from 00 GMT to 03 GMT and increased in part from 03 to 06 GMT. During this time period the zone broadened as well. At 00 GMT over JAX it was 180 mb deep, while at 06 GMT it increased to 310 mb in depth. Also, the gradient within the zone varied. At 00 GMT it was uniform except near the lower boundary of the zone where it became distorted. At 03 GMT the gradient was more uniform than at 00 GMT, while at 06 GMT it became distorted again in places. The two remaining zones of discontinuity on the 00 GMT chart showed little change in slope throughout the period, but changes were noted in the gradients of these zones. Both zones weakened gradually from 00 GMT to 06 GMT.

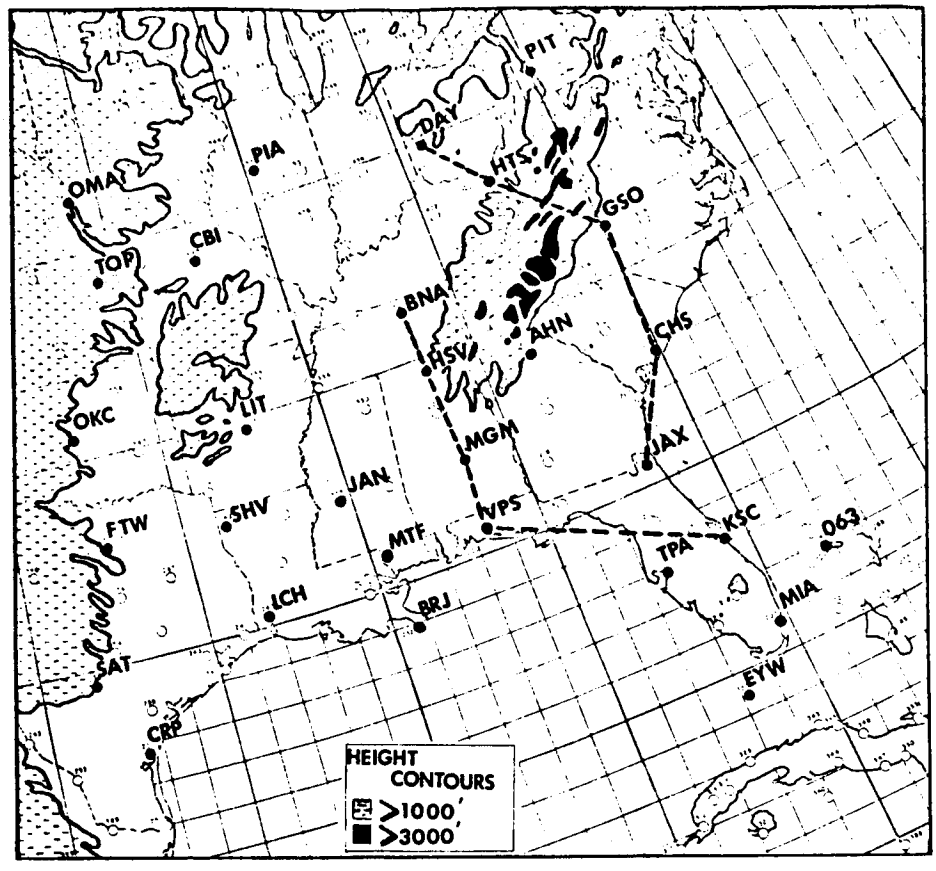

Fig. 8. Paths of cross sections used in the study. (The north cross section extends from DAY to JAX; the south cross section from BNA to KSC).

Another interesting feature of these northern cross sections was the appearance of a θ_e maximum centered over GSO at 700 mb on the 00 GMT chart. This maximum could have occurred by the addition of moisture to the layer and/or by subsidence. In this study its significance is not how it occurred, but how it changed with time. The center weakened as time progressed. It was well defined at 03 GMT but somewhat weaker at 00 GMT. By 06 GMT the center had dissipated and all that remained was a distorted thermal pattern.

The southern cross sections of θ_e also show the major zone of discontinuity (Figure 10). At 00 GMT it extended from the surface at KSC to 300 mb over BNA. There was some variation in the slope of the upper boundary of this discontinuity, but it was not as great as that shown by the northern cross sections. The lack of data for MGM and VPS at 03 GMT caused the analysis to be unreliable, but comparisons could be made between the northern and southern cross sections at 00 and 06 GMT.

2. Evaluation of Conditions Contributing to Changes in the Intensity of Internal Zones of Discontinuity

The evaluation of conditions which contributed to changes in the intensity of the internal zones of discontinuity was done with the use of

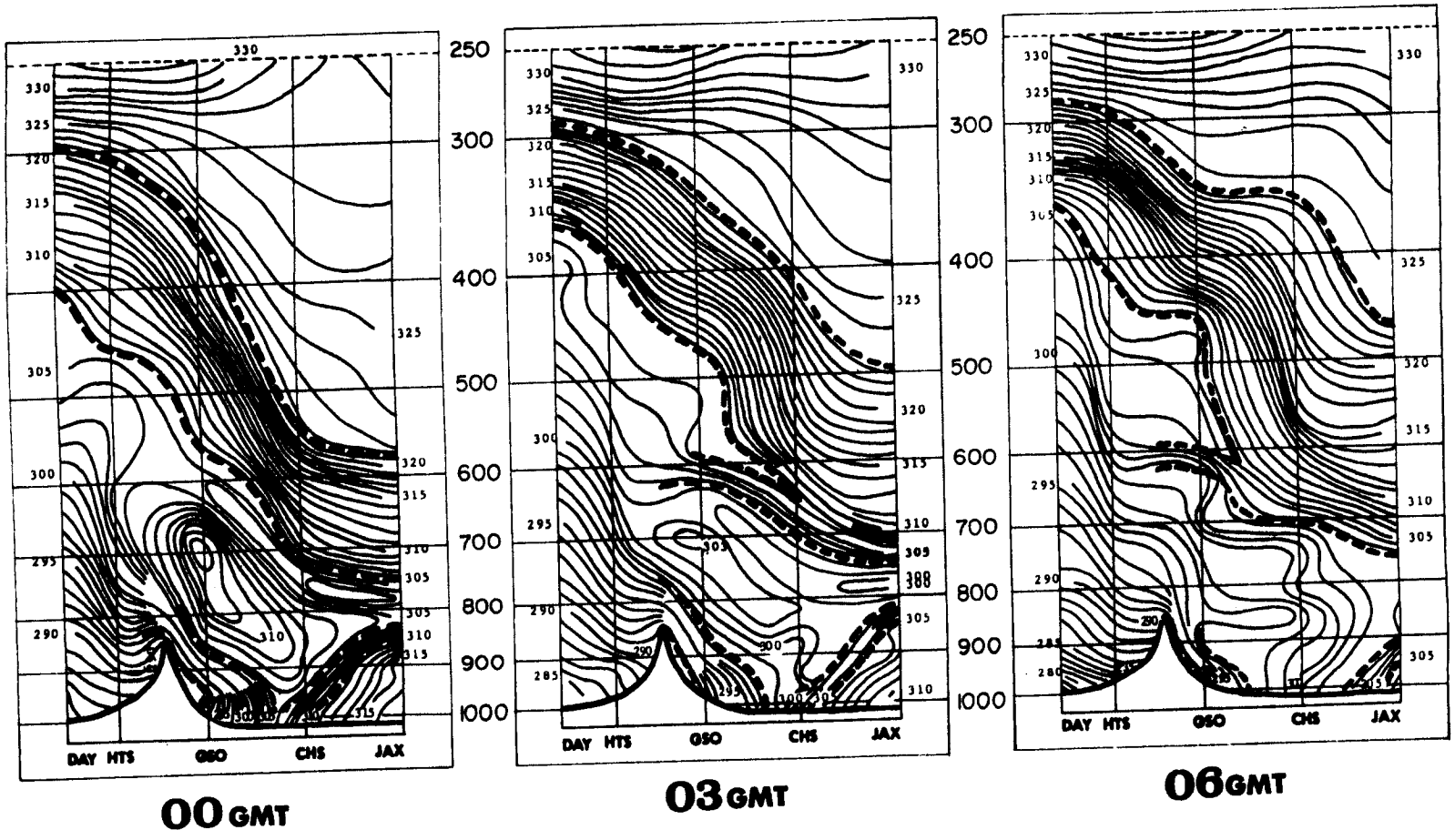

Fig. 9. Northern cross sections of equivalent potential temperature, θ_e (°K), for February 19, 1964.

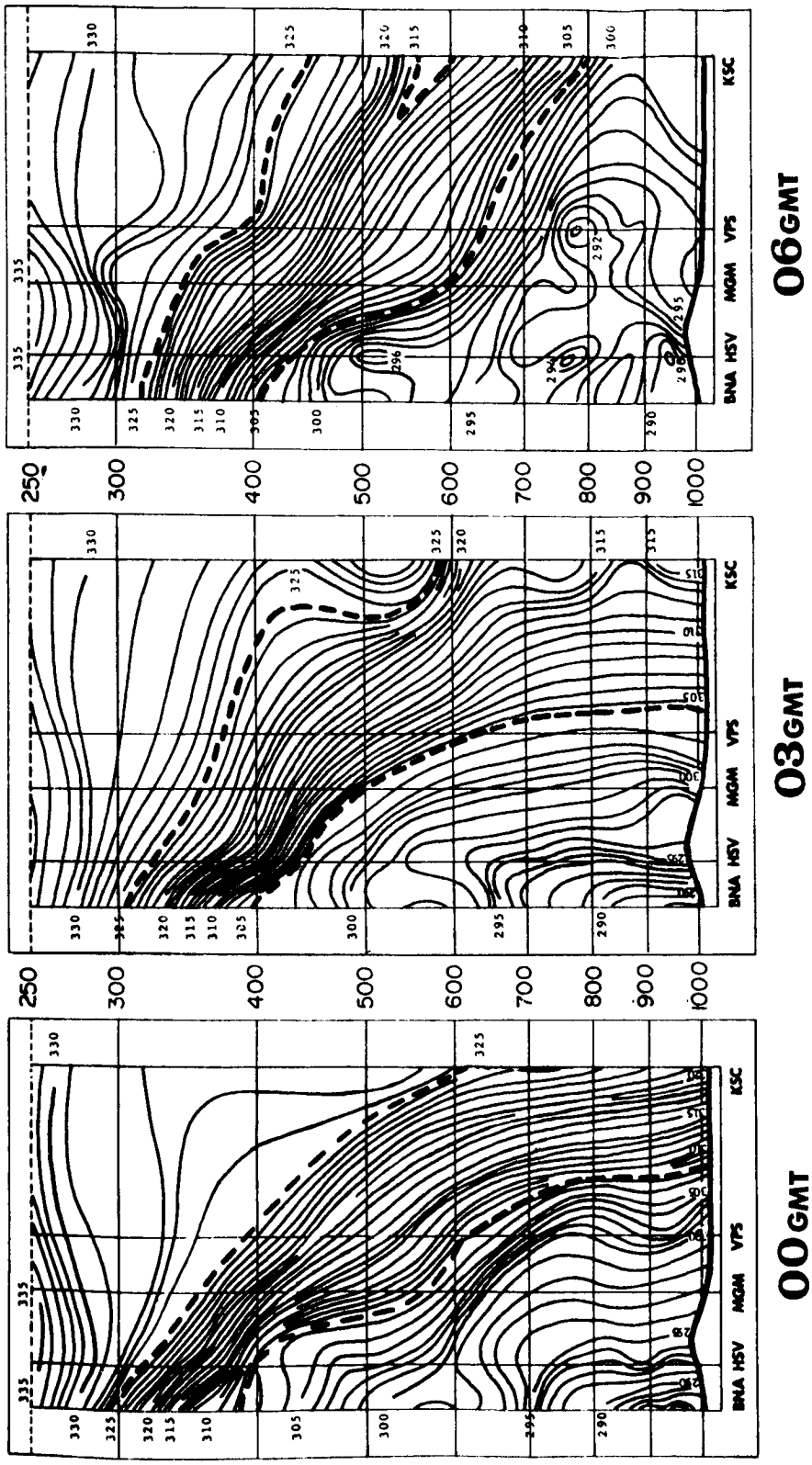

Fig. 10. Southern cross sections of equivalent potential temperature, θ_e (°K), for February 19, 1964.

the frontogenetic function. For the variable θ_e, Equation 2 may be rewritten as:

$$\vec{F}_3(t) = \vec{\nabla} \frac{d\theta_e}{dt} - \left(\frac{\partial\theta_e}{\partial x} \vec{\nabla}u + \frac{\partial\theta_e}{\partial y} \vec{\nabla}v + \frac{\partial\theta_e}{\partial z} \vec{\nabla}w\right) . \tag{7}$$

If the y-axis is chosen parallel to the zone of discontinuity, the component equations are:

$$F_x(t) = \underset{A}{\frac{\partial}{\partial x}\left(\frac{d\theta_e}{dt}\right)} - \left(\underset{B}{\frac{\partial\theta_e}{\partial x}\frac{\partial u}{\partial x}} + \underset{C}{\frac{\partial\theta_e}{\partial y}\frac{\partial v}{\partial x}} + \underset{D}{\frac{\partial\theta_e}{\partial z}\frac{\partial w}{\partial x}}\right) \tag{8}$$

and

$$F_z(t) = \underset{E}{\frac{\partial}{\partial z}\left(\frac{d\theta_e}{dt}\right)} - \left(\underset{F}{\frac{\partial\theta_e}{\partial x}\frac{\partial u}{\partial z}} + \underset{G}{\frac{\partial\theta_e}{\partial y}\frac{\partial v}{\partial z}} + \underset{H}{\frac{\partial\theta_e}{\partial z}\frac{\partial w}{\partial z}}\right) . \tag{9}$$

Terms A and E, which represent the non-conservative influences, were neglected since θ_e could be treated as a conservative parameter. Terms D and H include gradients of vertical velocity which can not be evaluated easily and usually are considered to be smaller than the other terms. Therefore, no attempt was made to incorporate the values of these terms in the final calculations. With these simplifications, Equations 8 and 9 become

$$F_x(t) = \left(\underset{I}{\frac{\partial\theta_e}{\partial x}\frac{\partial u}{\partial x}} + \underset{II}{\frac{\partial\theta_e}{\partial y}\frac{\partial v}{\partial x}}\right) \tag{10}$$

and

$$F_z(t) = \left(\underset{III}{\frac{\partial\theta_e}{\partial x}\frac{\partial u}{\partial z}} + \underset{IV}{\frac{\partial\theta_e}{\partial y}\frac{\partial v}{\partial z}}\right) . \tag{11}$$

Terms I, II, III, and IV were evaluated individually, and then Terms I and II, and III and IV were summed to determine the value of $F_x(t)$ and $F_z(t)$, respectively.

The terms were evaluated as follows. Fields of θ_e and wind components were obtained from the original data. A grid mesh was constructed to evaluate the partial derivatives by finite differences. The grid mesh had five points spaced 2.5° latitude apart in the horizontal plane and 15 points spaced 50 mb apart in the vertical plane. Derivatives were evaluated over 2 grid units and applied at the center of the interval.

3. Relationship Between Analytical Results and Observed Conditions

The evaluation of each term in Equations 10 and 11 for the north and south cross sections is represented in later figures. A comparison of each figure to the respective θ_e cross section should indicate the processes which occurred in and near the zones of discontinuity. Gradients of θ_e generally would be expected to be strong in regions of frontogenesis and weak in regions of frontolysis. The zones of discontinuity have been superimposed on these figures for reference.

The evaluation of Term I for the northern cross section is represented by Figure 11. These cross sections were dominated by regions of frontolysis. At 00 GMT frontolytic regions were centered over GSO at 500 mb and 850 mb. These centers weakened with time but covered a large depth of the cross section at 06 GMT. With such broad regions of frontolysis occurring, one would expect to see a weakening of gradients on the θ_e cross sections. The major zone of discontinuity did broaden from 00 GMT to 06 GMT, but its gradient remained strong. It is seen in Figure 9 that where frontogenesis did occur in Figure 11, a stronger gradient of θ_e was observed.

The slope of the upper boundary of the major zone of discontinuity gradually decreased between 00 and 06 GMT. Frontolysis occurred throughout the region associated with this boundary. Also, the perturbation of the slope between GSO and JAX at 06 GMT was coincident with a frontolytic center. The minor zone of discontinuity in the lee of the Appalachian Mountains was associated with a frontolytic region throughout the time period and, hence, weakened between 00 and 06 GMT. Although the other minor zone was associated with this same frontolytic region, it was associated with a weak frontogenetic region as well. This zone weakened with time also, but not as rapidly as the other minor zone of discontinuity.

The southern cross sections of Term I are represented in Figure 12. These cross sections show frontolytic regions which intensify, and frontogenetic regions which weaken with time. A frontolytic region covered most of the cross section from BNA to VPS. The thermal pattern was distorted in this region in Figure 10, and the zone of discontinuity became broader there as well. A perturbation was noted on the upper boundary of the zone of discontinuity between VPS and KSC at 03 GMT. The frontogenetic center below this region had weakened, and frontolysis had occurred between 00 and 03 GMT in the vicinity of this perturbation.

The frontogenetic regions of Figure 12 weakened from 00 to 06 GMT, and the isentropic gradient within the zone of discontinuity weakened as well.

The evaluation of Term II for the northern cross section if represented in Figure 13. Two regions of frontolysis are observed in the northern cross section of this term at 00 GMT. One region is centered over HTS near 350 mb, and the other is centered over CHS at 700 mb. The latter center weakened rapidly from 00 to 06 GMT. The center over HTS weakened also, but less rapidly. Regions of frontogenesis which were separated at 00 GMT merged by 06 GMT, and their centers intensified as well.

The regions of frontolysis (Figure 13) coincided well with regions within the zones of discontinuity where the gradient had weakened. The region in

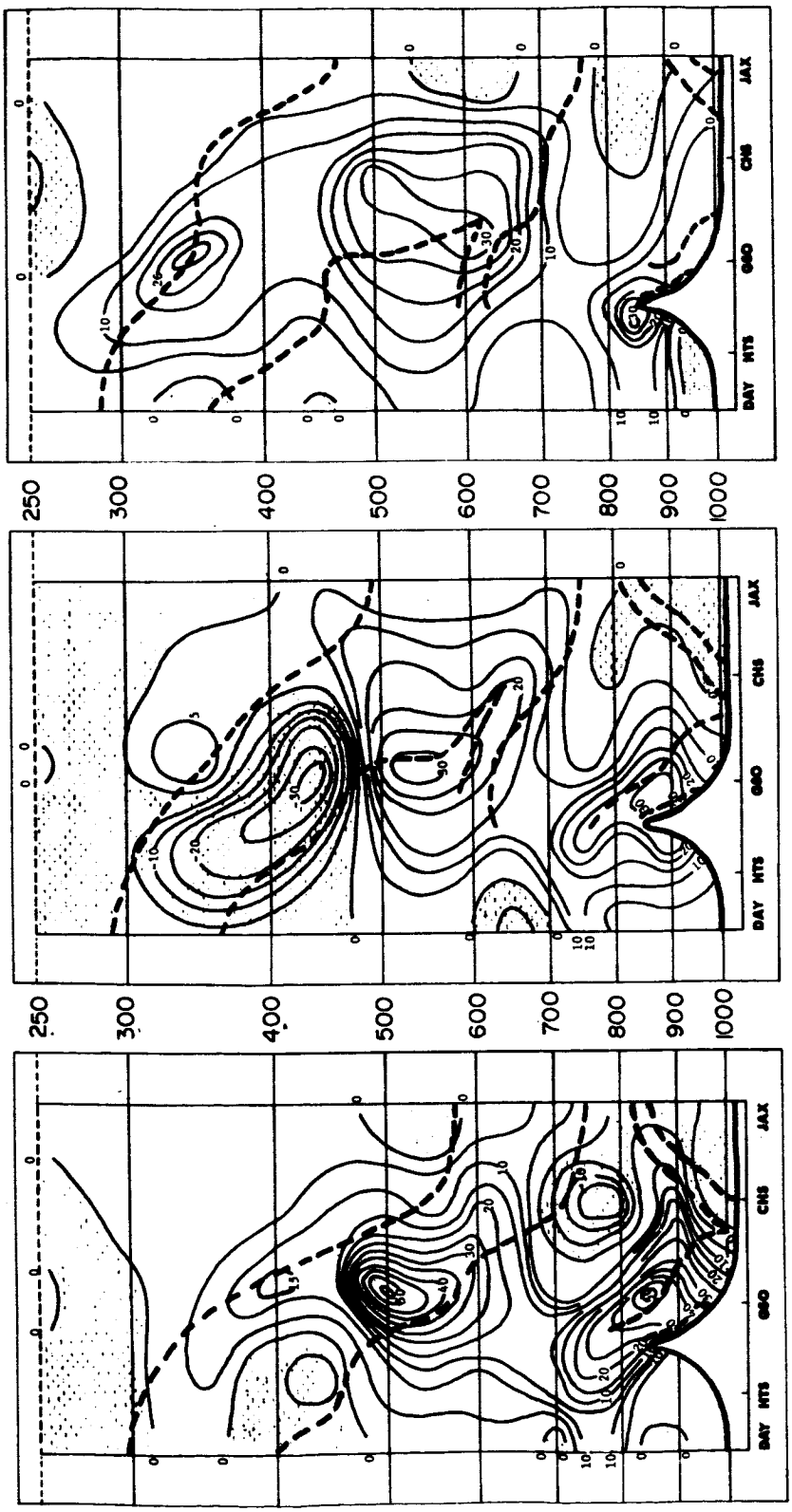

Fig. 11. Northern cross sections of Term I for February 19, 1964. (Frontogenetic regions are stipled, and zones of discontinuity are enclosed by dashed lines. Term I is $(\frac{\partial \theta_e}{\partial x} \frac{\partial u}{\partial x})$. Units are 10^{-11} deg m^{-1} sec^{-1}.)

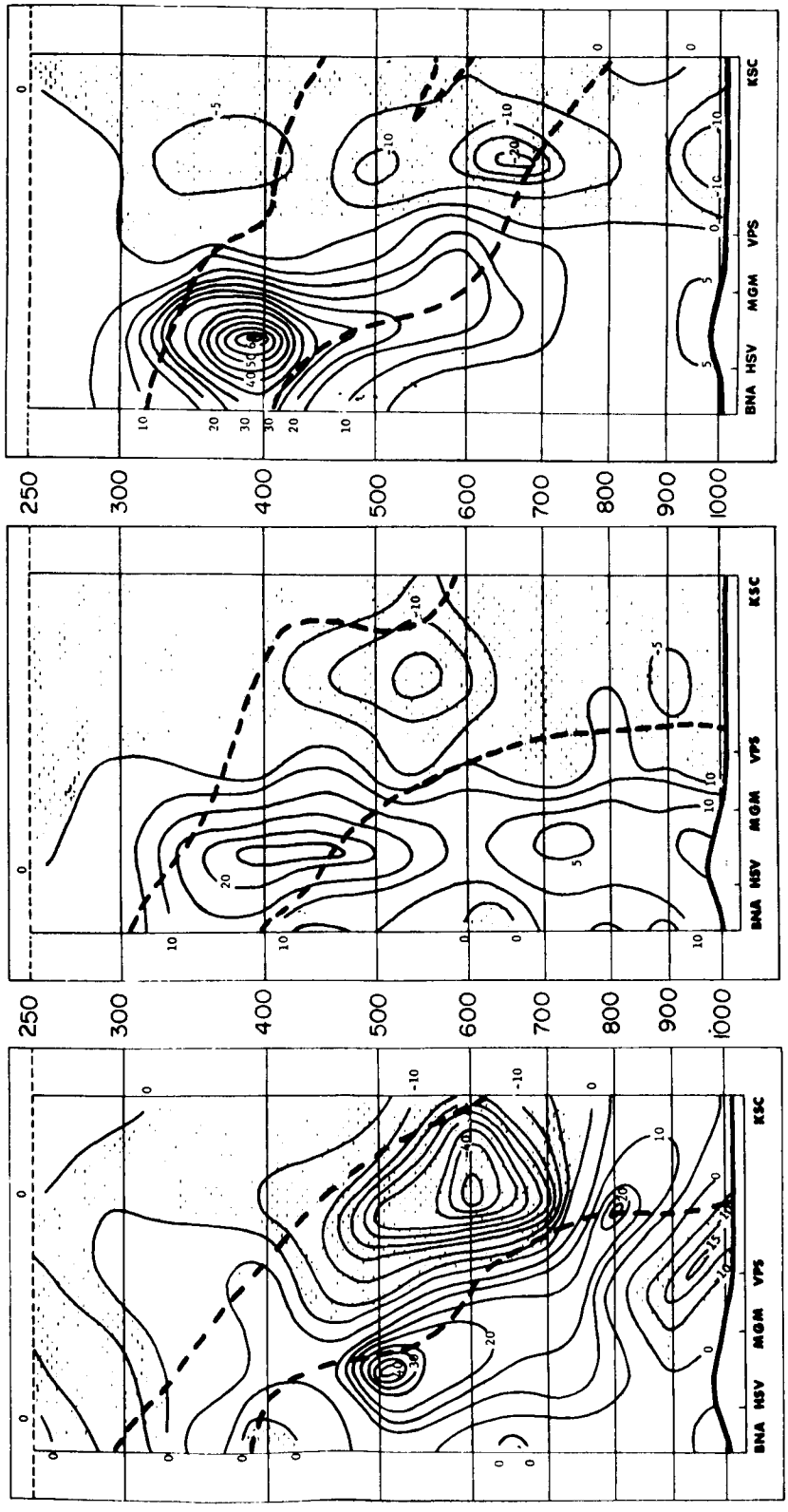

Fig. 12. Southern cross sections of Term I for February 19, 1964. (Frontogenetic regions are stipled, and zones of discontinuity are enclosed by dashed lines. Term I is $\partial\theta/\partial x\ (e\ \partial u/\partial x)$. Units are 10^{-11} deg m^{-1} sec^{-1}.)

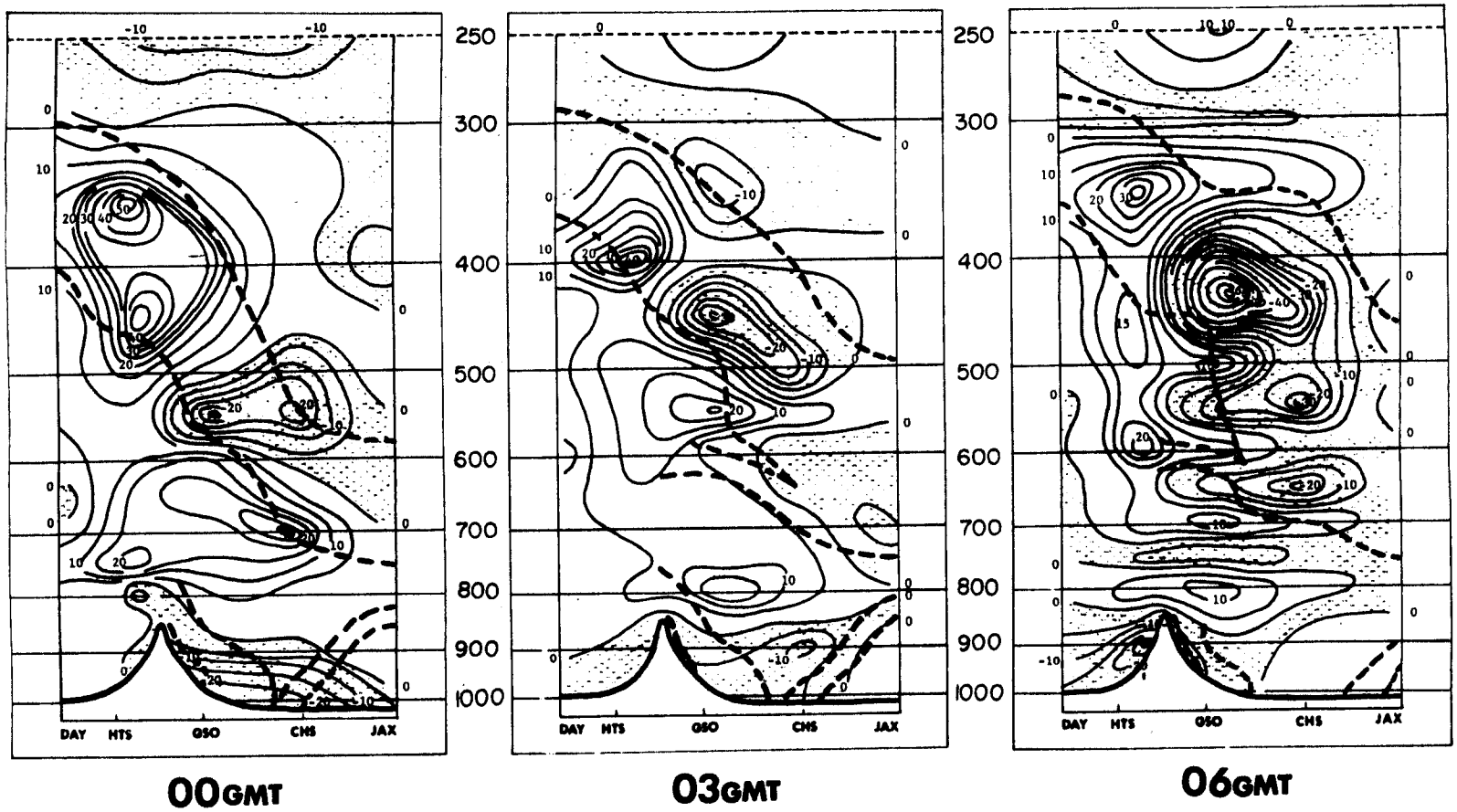

Fig. 13. Northern cross sections of Term II for February 19, 1964. (Frontogenetic regions are stipled, and zones of discontinuity are enclosed by dashed lines. Term II is $(\frac{\partial \theta_e}{\partial y} \frac{\partial v}{\partial x})$. Units are 10^{-11} deg m^{-1} sec^{-1}.)

Figure 9 over HTS below 400 mb and that over GSO near the 850-mb level are examples of this. Also, the thermal patterns of Figure 9 were irregular, and the distortions on the boundary of the major zone of discontinuity occurred in proximity to the centers of frontolysis (Figure 13).

The major region of frontogenesis in Figure 13 on the 00 GMT chart was located between GSO and CHS at 550 mb. This center intensified and had moved to a higher level by 06 GMT. In Figure 9 it can be seen that within this region of the zone of discontinuity there was a strong gradient which continued to strengthen with time. A secondary region of frontogenesis in Figure 13 was located below 850 mb in the lee of the Appalachian Mountains. This region weakened rapidly but was still present at 06 GMT. Thus, the two minor zones of discontinuity in Figure 9, which coincided with this region, had weakened.

The southern cross section for Term II (Figure 14) were dominated by regions of frontogenesis. The centers intensified with time, particularly those over HSV between 450 mb and 300 mb. They coincided also with a strong gradient within the zone of discontinuity in Figure 10. Little effect on the slope of the discontinuity was observed.

The evaluation of Term III is represented by Figures 15 and 16. Large regions of frontogenesis are evident on all cross sections of Figure 15. The major frontogenetic center on the 00 GMT chart was located over GSO at 500 mb. This center intensified between 00 and 03 GMT, but weakened between 03 and 06 GMT. Changes in slope of the major zone appeared to be related to this frontogenetic center. One other frontogenetic region was located in the lee of the Appalachian Mountains below 850 mb. This region weakened between 00 and 03 GMT and was replaced by a frontolytic zone between 03 and 06 GMT. The zones of discontinuity within this region had weakened by 06 GMT. Intensification of the gradient with time within the major zone of discontinuity was anticipated since the major frontogenetic region in Figure 15 was still present at 06 GMT.

The southern cross sections for Term III (Figure 16) show a large frontogenetic region on the 00 GMT chart centered over VPS at 480 mb. This center decreased in intensity between 00 and 03 GMT and weakened rapidly between 03 and 06 GMT. A center of frontolysis located at 830 mb between VPS and KSC on the 00 GMT chart weakened into a broad zone by 06 GMT, which corresponded to a weakening in the θ_e gradient of this region in Figure 10. The perturbation on the upper boundary of the zone of discontinuity at 03 GMT was not associated with a frontolytic center. The frontogenetic center at 550 mb between VPS and KSC at 03 GMT could be associated with this perturbation, however.

Term IV represents a combination of the vertical and horizontal effects on the θ_e gradient. The evaluation of this term is represented in Figure 17 for the northern cross sections. They show frontogenetic regions which intensified with time. A frontogenetic center located at 550 mb over CHS on the 00 GMT chart intensified from 00 to 06 GMT. Its location coincided with a strong gradient of the isentropic surfaces within the zone of discontinuity. Another frontogenetic region at 00 GMT was located over GSO below 850 mb. This region dissipated by 03 GMT and it became frontolytic by 06 GMT. This indicated that the isentropic gradient in this region would weaken greatly within this period. In Figure 9 it can be seen that the low-level zones of discontinuity weakened significantly from 00 to 06 GMT.

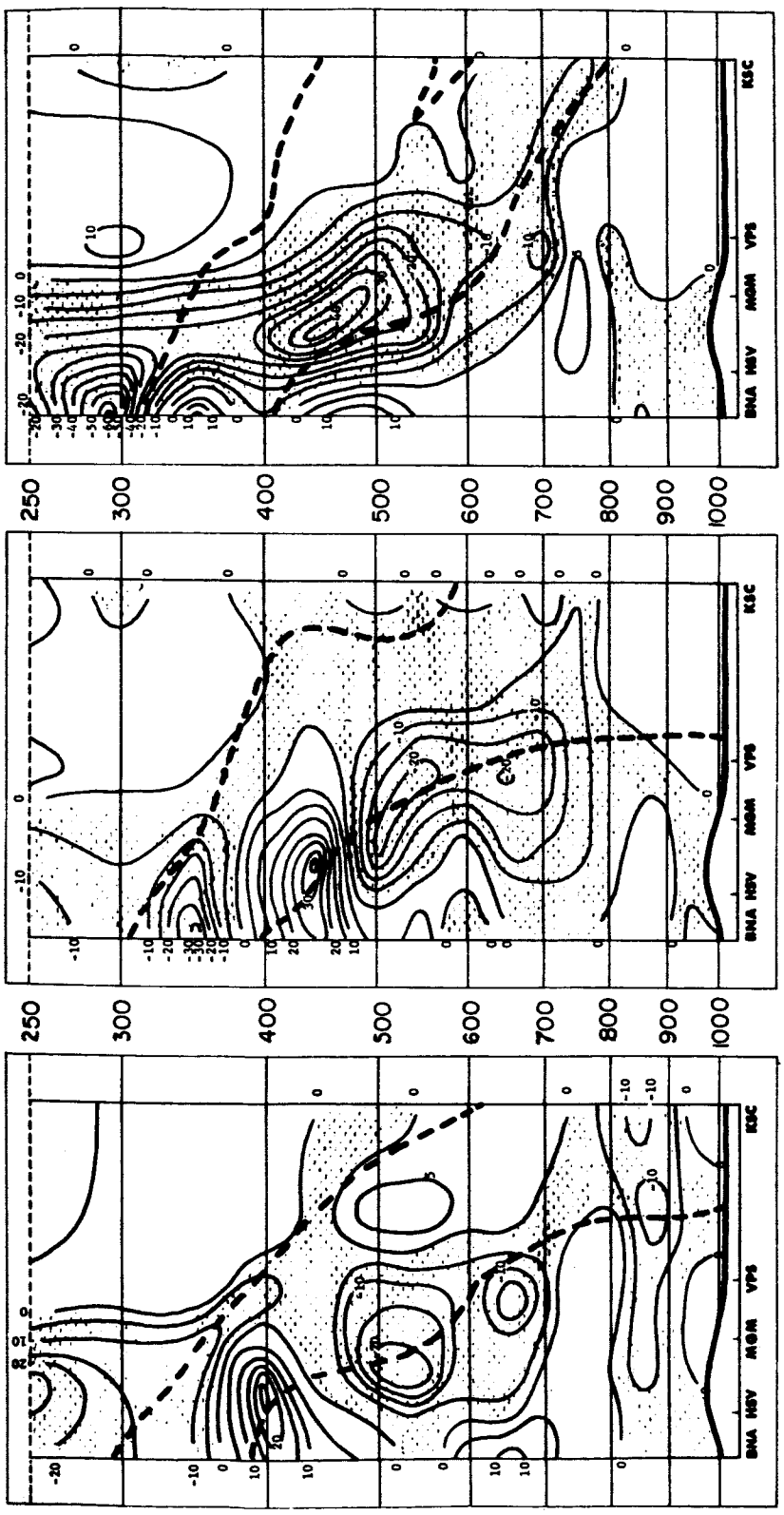

Fig. 14. Southern cross sections of Term II for February 19, 1964. (Frontogenetic regions are stipled, and zones of discontinuity are enclosed by dashed lines. Term II is $(\frac{\partial \theta_e}{\partial y} \frac{\partial v}{\partial x})$. Units are 10^{-11} deg m^{-1} sec^{-1}.)

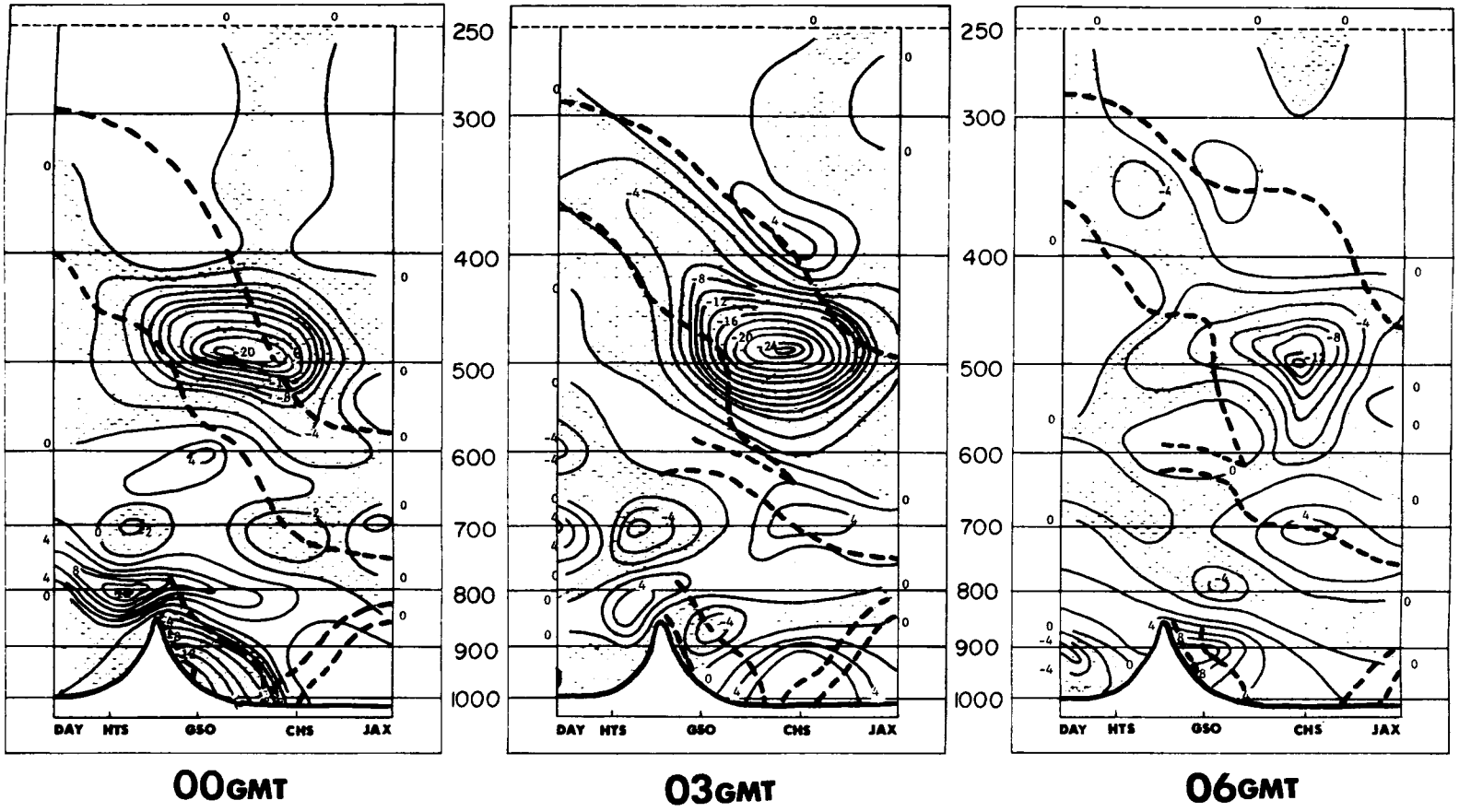

Fig. 15. Northern cross sections of Term III for February 19, 1964. (Frontogenetic regions are stipled, and zones of discontinuity are enclosed by dashed lines. Term III is $(\frac{\partial \theta_e}{\partial x} \frac{\partial u}{\partial z})$. Units are 10^{-8} deg m^{-1} sec^{-1}.)

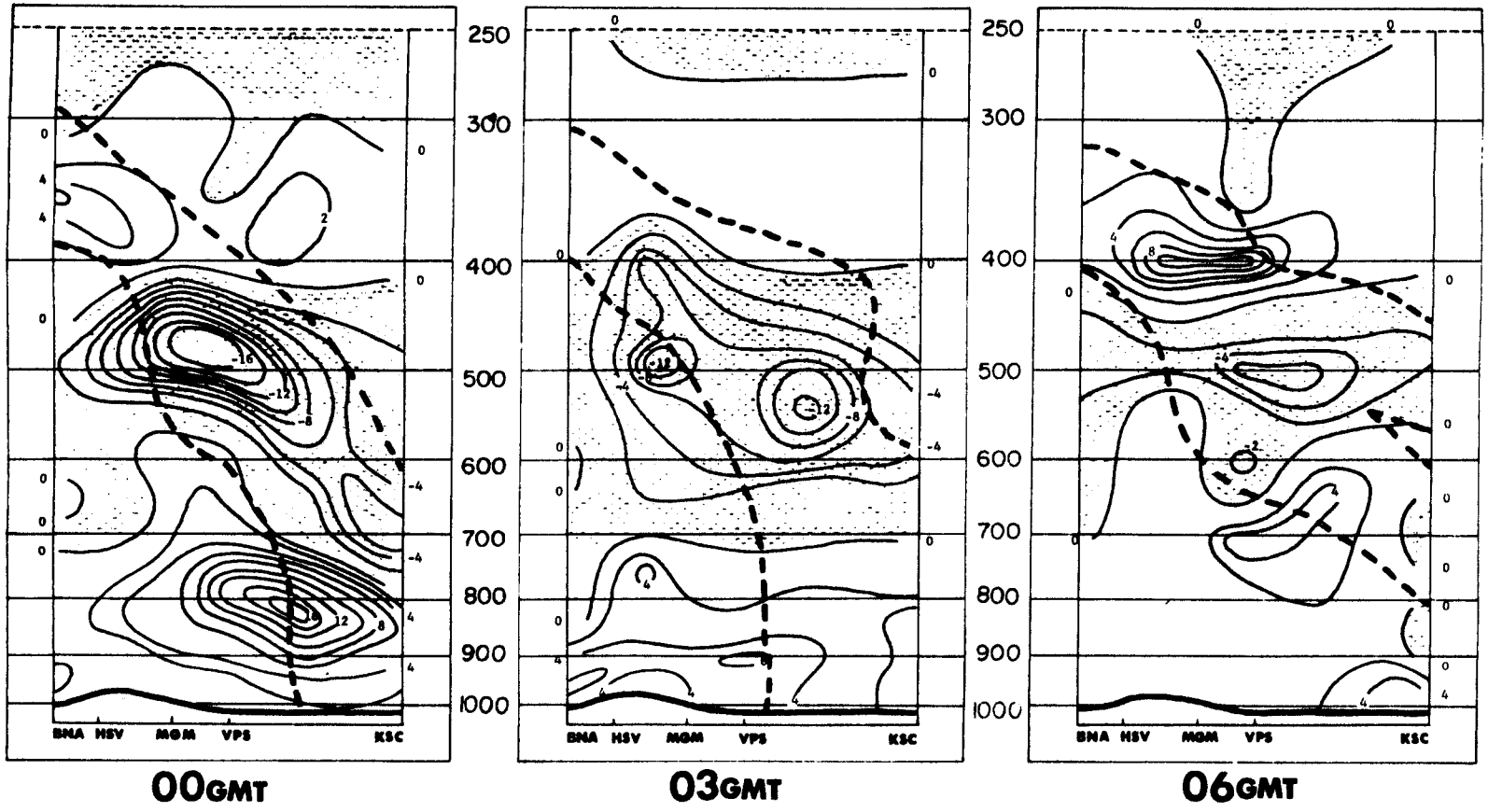

Fig. 16. Southern cross sections of Term III for February 19, 1964. (Frontogenetic regions are stipled, and zones of discontinuity are enclosed by dashed lines. Term III is $(\frac{\partial \theta_e}{\partial x} \frac{\partial u}{\partial z})$. Units are 10^{-8} deg m^{-1} sec^{-1}.)

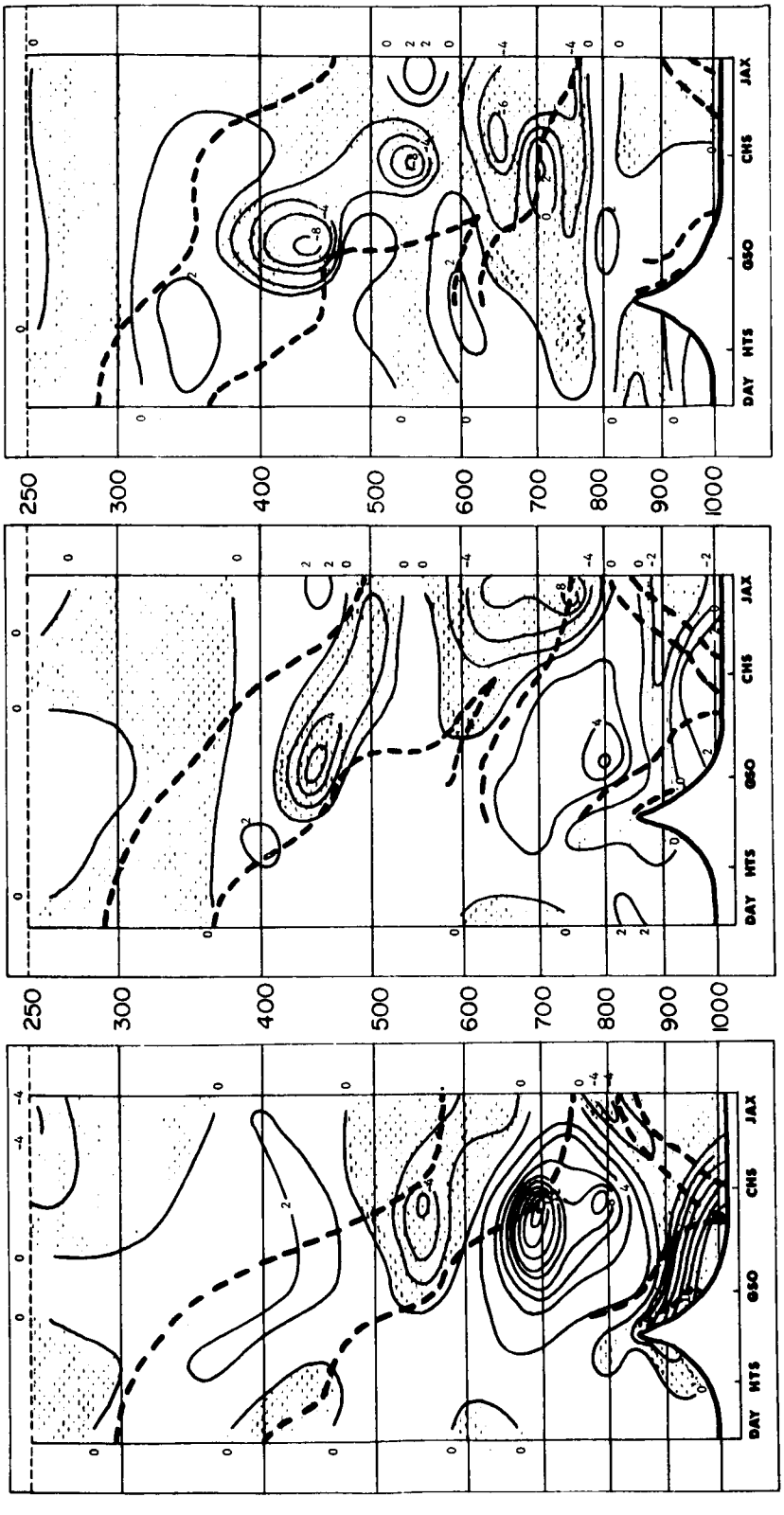

Fig. 17. Northern cross sections of Term IV for February 19, 1964. (Frontogenetic regions are stipled, and zones of discontinuity are enclosed by dashed lines. Term IV is $(\frac{\partial \theta_e}{\partial y} \frac{\partial v}{\partial z})$. Units are 10^{-8} deg m^{-1} sec^{-1}.)

The frontolytic regions in the cross sections of Figure 17 were restricted by the frontogenetic regions. A frontolytic center on the 00 GMT chart was located at 700 mb over CHS. This center weakened and dissipated by 06 GMT. The gradient in this region on the 00 GMT chart (Figure 9) was weak. It continued to be distorted at both 03 and 06 GMT.

The southern cross sections of Term IV (Figure 18) were dominated by a frontogenetic region. The center of this region showed little intensification during the period of study. The zone of discontinuity in Figure 10 conformed well with this region, and the strong gradient within the zone was coincident with the frontogenetic center. The perturbation on the upper boundary of the zone of the discontinuity at 03 GMT coincided also with a frontolytic zone.

The sum of Terms I and II represents the evaluation of Equation 10. The northern cross sections (Figure 19) are dominated by regions of frontolysis. The frontolytic centers weakened with time, but remained well defined at 06 GMT. With frontolysis having occurred over most of the cross section, one would expect that the zones of discontinuity would have weakened significantly. Figure 9 reveals that the major zone broadened, changed slope, and weakened. Also, the distorted patterns in the low levels of Figure 9 corresponded to the frontolytic centers in Figure 19. Bands of a strong isentropic gradient were coincident with regions where strong frontogenesis was indicated in Figure 19.

Southern cross sections of the sum of Terms I and II are shown in Figure 20. Frontogenetic regions at 00 GMT had weakened by 06 GMT, but the centers remained well defined. The zone of discontinuity corresponded well with these regions of frontogenesis. A frontolytic center on the 00 GMT cross section intensified from 00 to 03 GMT, but it weakened from 03 to 06 GMT. Little evidence of this center was seen on the θ_e cross sections, but considerable distortion in the isentropic pattern occurred at levels below this center.

The evaluation of the sum of Terms III and IV is shown in Figures 21 and 22. The northern cross sections (Figure 21) show one major region of frontogenesis centered at 500 mb between GSO and CHS at 00 GMT. The center intensified between 00 and 03 GMT, but weakened considerably between 03 and 06 GMT. A strong gradient within the major zone of discontinuity coincided with this center at 00 GMT. The θ_e gradient in this region strengthened by 03 GMT, but weakened again by 06 GMT. A minor frontolytic band on the 00 GMT cross section occurred over GSO below 850 mb. This band weakened by 03 GMT and became frontolytic by 06 GMT. The low-level zones of discontinuity on the 00 GMT cross section of Figure 9 corresponded to this frontolytic band. The zones weakened with time, but still were present on the 06 GMT chart. The frontolytic centers on the 00 GMT cross section (Figure 21) weakened with time but they still could be associated with the perturbations on the upper boundary of the zone of discontinuity at 06 GMT. The distorted θ_e patterns at low levels in Figure 9 resulted in part from these frontolytic centers.

The southern cross sections (Figure 22) are dominated by a broad frontogenetic region. The center of this region was located over VPS at 500 mb. Little change was seen in this frontogenetic region but the center weakened slightly by 06 GMT. Regions within the zone of discontinuity which were coincident with this center maintained a strong gradient throughout the period.

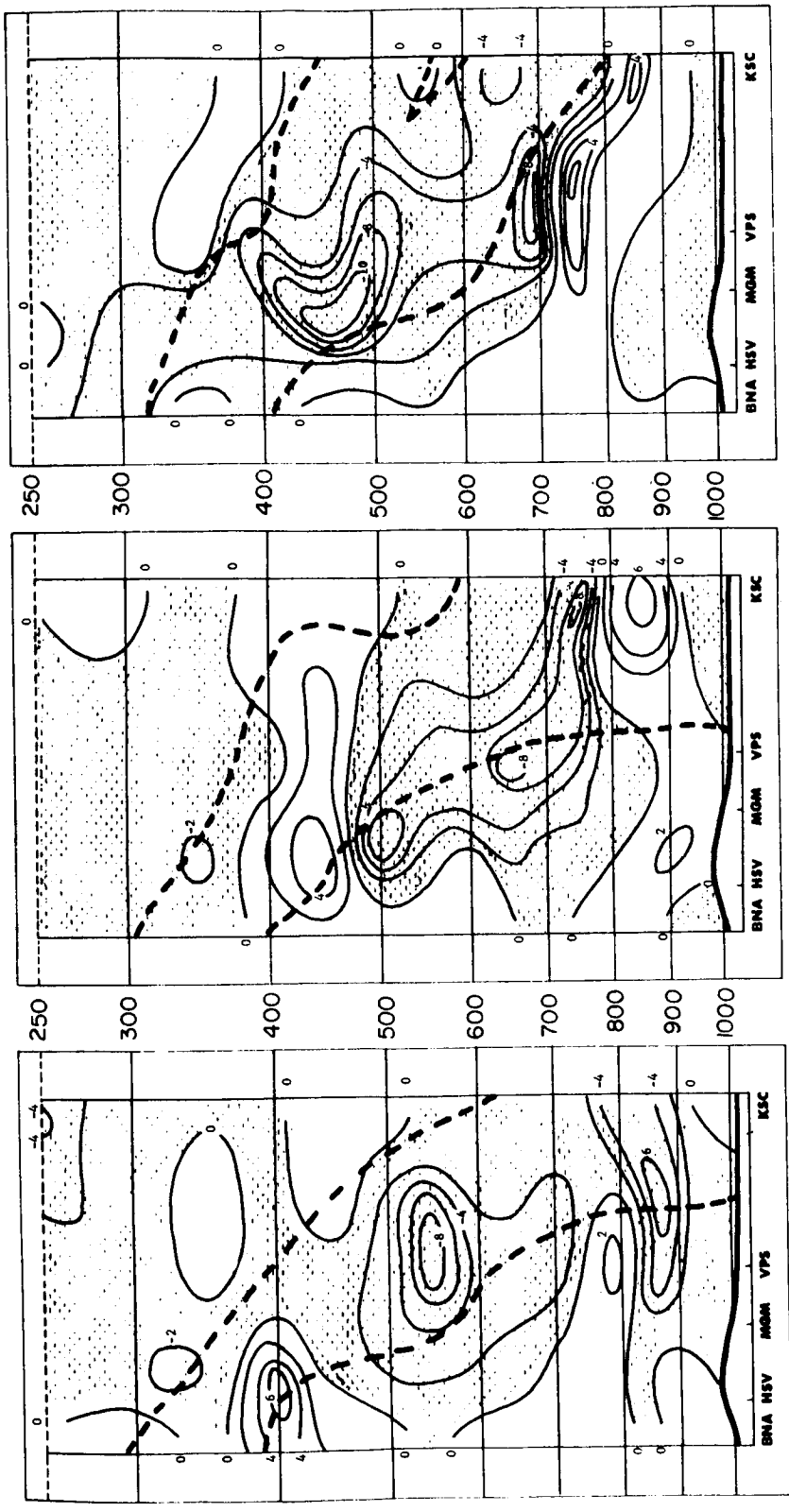

Fig. 18. Southern cross sections of Term IV for February 19, 1964. (Frontogenetic regions are stipled, and zones of discontinuity are enclosed by dashed lines. Term IV is $\frac{\partial \theta}{\partial y}\left(\frac{e}{\partial z}\frac{\partial v}{\partial z}\right)$. Units are 10^{-8} deg m^{-1} sec^{-1}.)

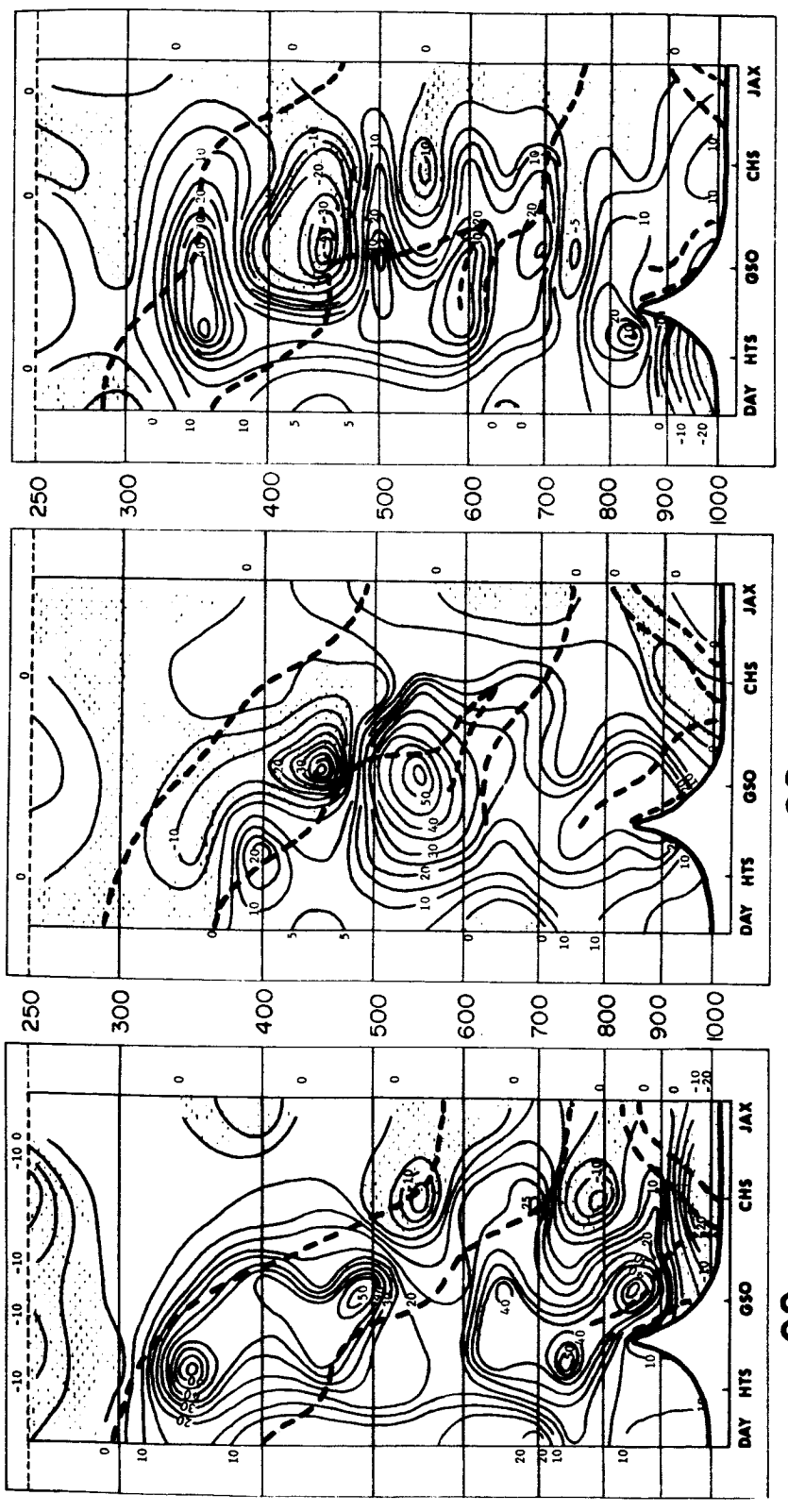

Fig. 19. Northern cross sections of the sum of Terms I and II for February 19, 1964. (Frontogenetic regions are stipled, and zones of discontinuity are enclosed by dashed lines.)

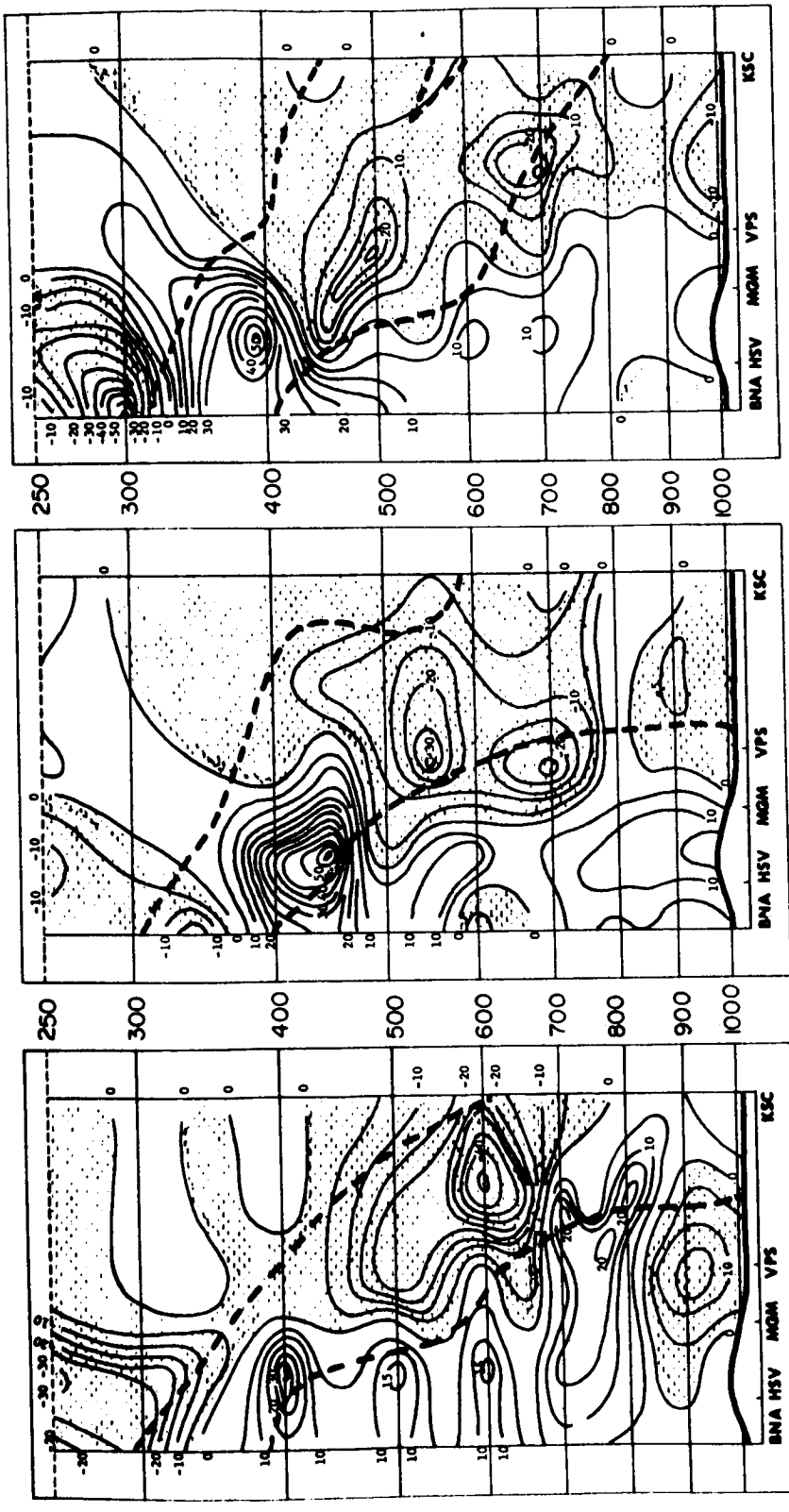

Fig. 20. Southern cross sections of the sum of Terms I and II for February 19, 1964. (Frontogenetic regions are stipled, and zones of discontinuity are enclosed by dashed lines.)

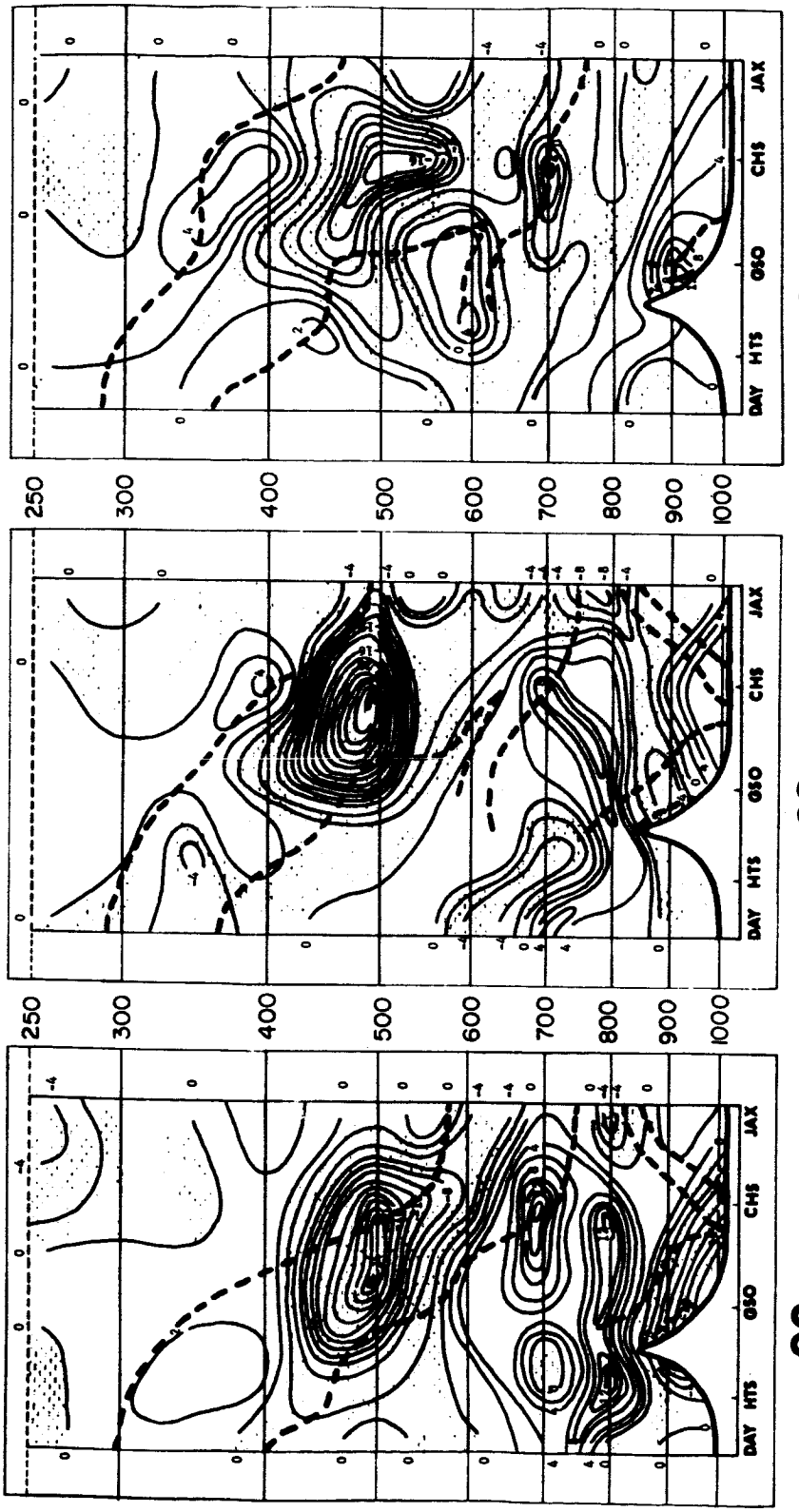

Fig. 21. Northern cross sections of the sum of Terms III and IV for February 19, 1964. (Frontogenetic regions are stipled, and zones of discontinuity are enclosed by dashed lines.)

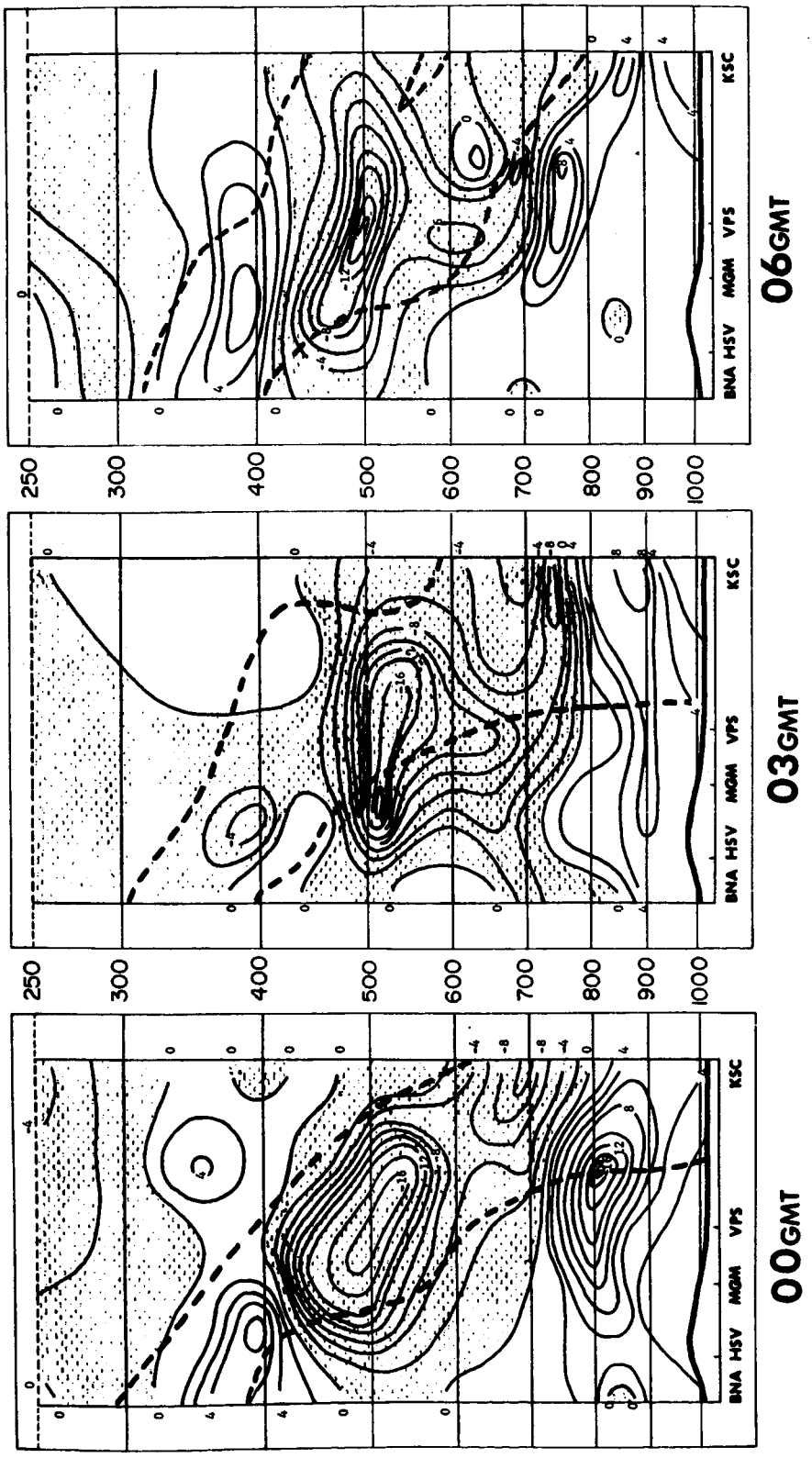

Fig. 22. Southern cross sections of the sum of Terms III and IV for February 19, 1964. (Frontogenetic regions are stipled, and zones of discontinuity are enclosed by dashed lines.)

A frontolytic center, located at 800 mb between VPS and KSC on the 00 GMT chart (Figure 22), weakened rapidly into a broad band by 06 GMT, and the gradient within the zone of discontinuity at this level indicated much distortion. The frontolytic center at 380 mb on the 06 GMT cross section coincided with the perturbation on the upper boundary of the zone of discontinuity.

In summary, in most cases it was seen that in intense frontogenetic regions the zones of discontinuity became better defined. In regions where extreme frontolysis occurred the zones of discontinuity became less defined and, in some cases, dissipated.

Various hypotheses may be advanced as to the reasons for the variations of these zones. One such hypothesis is the existence of mountain waves in the region under study. This hypothesis can be supported by the comparison of the north and south cross sections. The northern θ_e cross sections show more distortion than do the southern θ_e cross sections.

4. Key Terms of the Horizontal and Vertical Equations

Equation 10 referred to the horizontal, while Equation 11 dealt with the vertical components of the frontogenetic function. Newton and Palmén (1971) stated that vertical gradients of various meteorological properties in frontal regions are ordinarily two orders of magnitude greater than the horizontal gradients. They stated further that because of this the magnitude of $\vec{F}_3(t)$ is dominated by these vertical gradients. In some cases, more emphasis may be placed on the horizontal (constant pressure surfaces) rather than the vertical gradients in the location of zones of discontinuity, but both variations should be considered.

In some cases, it was observed that a frontogenetic region was associated with a region of weak gradient in the θ_e cross section. In such cases, it should be realized that only the component equations of the frontogenetic function were evaluated, and the processes which occurred in a region may not be represented solely by one term or one equation. Certain terms, however, may be better indicators of the processes than other terms.

The relationship was examined between the frontogenetic regions of the terms of Equations 10 and 11 and the zones of discontinuity. It was found that the frontogenetic regions of Terms II and III were associated best with the zones of discontinuity. The regions and their centers coincided more frequently to the zones of discontinuity than did those of the other terms. The frontogenetic regions of the combined terms of Equation 11 were better associated with the zones than were those of Equation 10.

F. RELATIONSHIP BETWEEN ZONES OF DISCONTINUITY AND PRECIPITATION

Surfaces of zones of discontinuity can create upslope vertical motion in the flow as these zones move. This vertical motion in turn may produce clouds and precipitation. An investigation into the relationship between the zones

of discontinuity and the precipitation patterns which occurred during the period of study was undertaken to verify these expectations.

Maps of 6-hr precipitation totals and cloud types were plotted and associated with characteristics of the zones of discontinuity. Figures 23 and 24 show the analysis of the precipitation patterns for the 6-hr periods prior to 00 and 06 GMT. Precipitation totals for the 6-hr period prior to 03 GMT were not available. The cross section paths were drawn on these figures for reference.

The precipitation amounts for the 6-hr period prior to 00 GMT along the northern path were greater than those along the southern path. The precipitation that occurred between DAY and GSO was greater than or equal to 0.1 inch. No precipitation had occurred between CHS and JAX 6 hrs prior to the 00 GMT chart. Cloud types along the northern path were stratoform and did not indicate vertical development.

At 00 GMT the major zone of discontinuity had its greatest slope between HTS and CHS. This coincided with the region of heaviest precipitation. Also, the slope of this zone lessened significantly from CHS to JAX where no precipitation occurred. The slope of the minor zone of discontinuity in the lee of the Appalachian Mountains was steep and coincided with an area of heavy precipitation. The other minor zone of discontinuity between CHS and JAX at 00 GMT could not be associated with a precipitation area. Perhaps subsidence occurred on the surface of this discontinuity which precluded the production of any precipitation or cloud activity in the area.

Precipitation amounts were small along the path of the southern cross section for the 6-hr period prior to 00 GMT. The only portions of the cross section traversing a precipitation area were near BNA and along the path between VPS and KSC in the Florida panhandle. The precipitation amount at KSC was greater than or equal to 0.1 inch. Cloud types along the path of this cross section were stratocumulus, altocumulus, and cirrus. Some towering cumulus were reported between MGM and VPS.

The slope of the zone of discontinuity at 00 GMT in the southern cross section was constant from BNA to VPS. No precipitation occurred along this path. The slope changed abruptly between VPS and KSC and became steep. The steep slope could be associated with the heavier precipitation that occurred around KSC over the previous 6 hrs.

At 06 GMT, the precipitation pattern still showed precipitation to have occurred between DAY and GSO on the northern cross section. The amount of this precipitation was less than that of the previous 6-hr time period. No precipitation occurred between GSO and JAX during this 6-hr period. The slope of the zone of discontinuity at 06 GMT varied along the path of the cross section. It was pronounced between DAY and GSO, and although it was not as steep as it had been 6 hrs earlier, it coincided with a precipitation area. The slope lessened between GSO and CHS, and no precipitation occurred during the past 6 hrs along this portion of the cross section. It increased again, though between CHS and JAX. No precipitation occurred in this area either, but an examination of the 00 GMT and the 03 GMT charts showed that the slope in this portion of the cross section was small. Thus, it is likely that little or no vertical motion occurred on this surface during the previous 6 hrs.

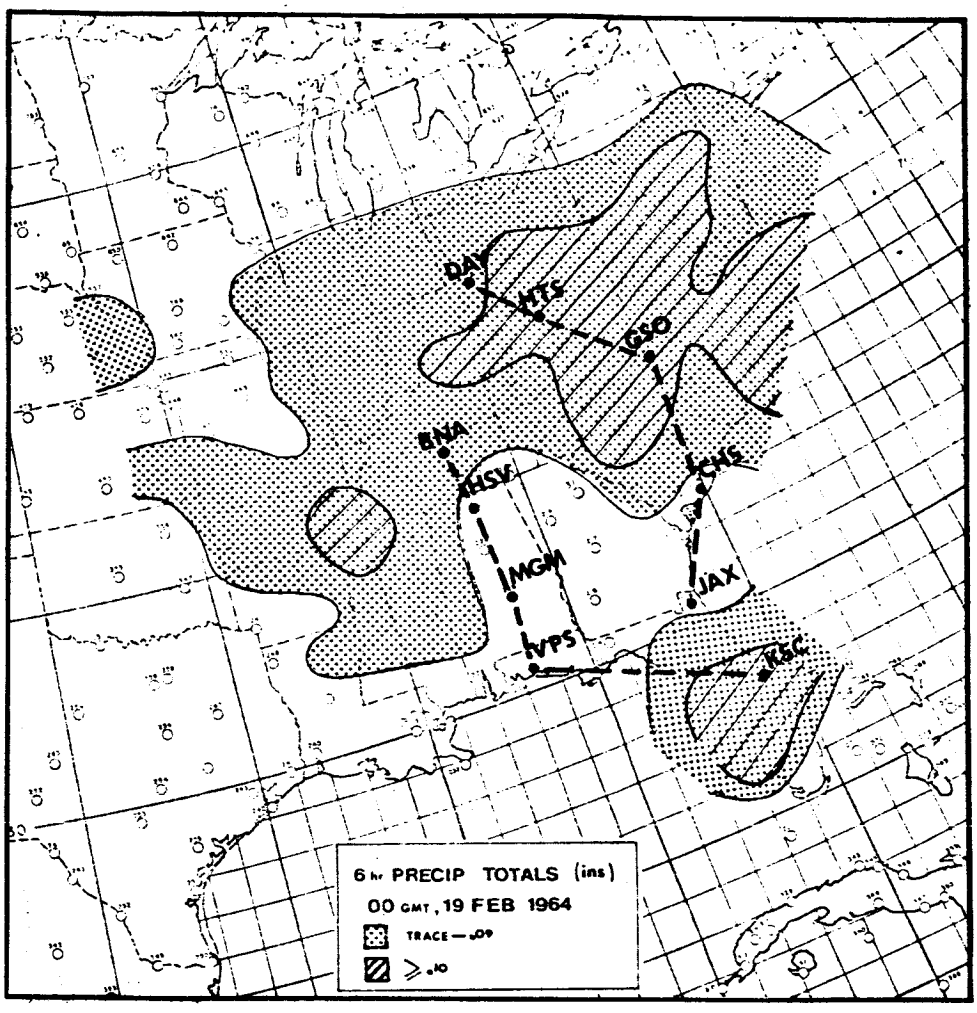

Fig. 23. Precipitation totals for the 6-hr period prior to 00 GMT, February 19, 1964.

The minor zone of discontinuity in the lee of the Appalachian Mountains was weaker at 06 GMT than at 00 GMT. Its slope had lessened, but it could be associated with the precipitation area around GSO. The remaining zone of discontinuity was ill-defined and its gradient was weak. No precipitation occurred in this region of the cross section.

The path of the southern cross section at 06 GMT traversed a precipitation area for the previous 6 hrs. This area extended from BNA to a point between MGM and VPS, and it coincided well with the increased slope of the zone of discontinuity on the 06 GMT chart. The slope decreased between VPS and KSC, where no precipitation occurred.

Changes in the slopes of the zones of discontinuity appeared between 00 and 06 GMT. The precipitation patterns also changed significantly during this period, and these pattern changes appeared to be related to the changes in the slope of the discontinuities.

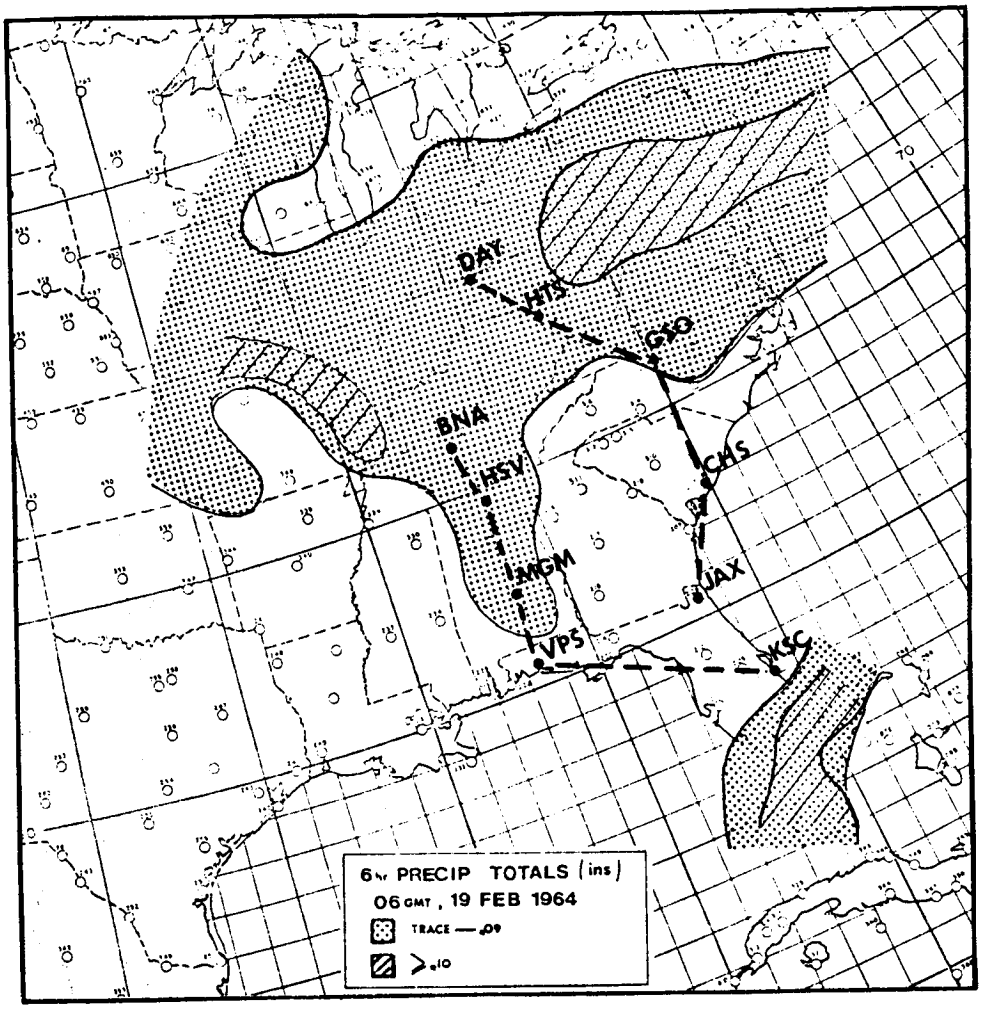

Fig. 24. Precipitation totals for the 6-hr period prior to 06 GMT, February 19, 1964.

G. SUMMARY AND CONCLUSIONS

1. Summary

Zones of discontinuity in the temperature field on February 19, 1964, associated with an east coast cyclone, were investigated. The zones were delineated in cross sections on the basis of strong θ_e gradients. The characteristics of these zones changed from one time period to the next.

The frontogenetic function was used to investigate changes in zones of discontinuity with time. This function was expanded into its three-dimensional component equations, and for simplification, only the terms of the x- and z-component equations were evaluated. Terms involving vertical velocity were ignored, however. The results were compared with the observed conditions in the θ_e cross sections. In most cases it was found that regions of intense

frontogenesis were associated with regions of strong θ_e gradients, and regions of intense frontolysis were associated with weak θ_e gradients within the zones of discontinuity. Also, changes in the slope of the upper boundary of the zones of discontinuity could be associated with intense frontolytic/frontogenetic regions.

Precipitation amounts over the entire southeastern United States were analyzed for the 6-hr period preceeding the first and last observation times. These patterns then were compared with changes in the slope of the zones of discontinuity to determine if a relationship existed. A close association was found between changes in slope and changes in the precipitation patterns for these time periods. An increase in slope appeared to enhance precipitation.

2. Conclusions

The frontogenetic function was found to be useful in the explanation of how zones of discontinuity form and change with time. It aided in the illustration of how the slope of a discontinuity also may change. It was instructive in helping one to understand the processes involved in the formation and dissipation of internal zones of discontinuity which produce significant weather. Also, the data used were measured at 3-hr intervals. Even though the frequency of this data was four times greater than that of conventional data, large variations within the zones of discontinuity occurred in the 3-hr interval between observations. Since many variations may occur within a 12-hr period, the forecasting of such variations in the zones of discontinuity is extremely difficult. Yet, this is what is demanded of the station forecaster if he is to provide accurate forecasts. Three-hour rawinsonde data is essential if variations in these zones of discontinuity are to be forecast with reasonable accuracy.

H. REFERENCES

III-1. Bosart, L. F., 1969: Mid-tropospheric frontogenesis and potential vorticity behavior, Ph.D. Thesis, Massachusetts Institute of Technology.

III-2. Byers, H. R., 1959: General Meteorology, McGraw-Hill, New York, pp. 295-302.

III-3. Danielsen, E. F., 1959: The laminar structure of the atmosphere and its relation to the concept of a tropopause, Arch. Meteorol., Geophys. Bioklimatol., A3, 293-332.

III-4. Godson, W. L., 1951: Synoptic properties of frontal surfaces, Quart. J. Roy. Meteorol. Soc., 77, 633-653.

III-5. Haltiner, G. J., and Martin, F. L., 1957: Dynamical and Physical Meteorology, McGraw-Hill, New York, pp. 287-296.

III-6. Kirk, T. H., 1965: A parameter for the objective location of frontal zones, Meteorol. Mag. (London), 94, 351-353.

III-7. _____ 1966: Some aspects of the theory of fronts and frontal analysis, Quart. J. Roy. Meteorol. Soc., 92, 374-381.

III-8. Margules, M., 1906: Über temperaturschichtung in stationär bewegter und in ruhender luft, Hann-Band. Meteorol. Z., pp. 243-254.

III-9. Miller, J. E., 1948: On the concept of frontogenêsis, J. Meteorol., 5, 169-171.

III-10. Newton, C. W., 1954: Frontogenesis and frontolysis as a three dimensional process, J. Meteorol., 11, 449-461.

III-11. Newton, C. W., and Palmén, E., 1971: Atmospheric Circulation Systems, Academic Press, New York, 603 pp.

III-12. Petterssen, S., 1956: Wea. Analysis and Forecasting, 2nd ed., McGraw-Hill, New York, pp. 189-212.

III-13. Renard, R., and Clarke, L., 1965: Experiments in numerical objective frontal analysis, Mon. Wea. Rev., 93, 547-556.

III-14. Sanders, F., 1955: An investigation of the structure and dynamics of an intense surface frontal zone, J. Meteorol., 12, 542-552.

III-15. Sawyer, J. S., 1955: The free atmosphere in the vicinity of fronts, G. B. Met. Office Geop. Mem. 96, 24 pp.

III-16. Watson, G. F., 1971: A diagnostic study of the kinematical and physical processes maintaining a strong low-level subsidence inversion over land, Report No. 71-3, Florida State University, Tallahassee.

I. APPENDIX

LIST OF STATION IDENTIFIERS

AHN	Athens, Georgia
BNA	Nashville, Tennessee
BRJ	Burrwood, Louisiana
CBI	Columbia, Missouri
CHS	Charleston, South Carolina
CRP	Corpus Christi, Texas
DAY	Dayton, Ohio
EYW	Key West, Florida

FTW	Fort Worth, Texas
GSO	Greensboro, North Carolina
HSV	Huntsville, Alabama
HTS	Huntington, West Virginia
JAN	Jackson, Mississippi
JAX	Jacksonville, Florida
KSC	Kennedy Space Center, Florida
LCH	Lake Charles, Louisiana
LIT	Little Rock, Arkansas
MIA	Miami, Florida
MGM	Montgomery, Alabama
MTF	Mississippi Test Facility
OKC	Oklahoma City, Oklahoma
OMA	Omaha, Nebraska
PIA	Peoria, Illinois
PIT	Pittsburgh, Pennsylvania
SHV	Shreveport, Louisiana
TOP	Topeka, Kansas
TPA	Tampa, Florida
VPS	Valpariso, Florida
063	Grand Bahama Island

This page left blank intentionally.

CHAPTER IV. AN APPROACH TO THE DETERMINATION OF THE VARIABILITY OF WIND THROUGH THE USE OF QUASI-CONSERVATIVE THICKNESS FIELDS

by

James R. Scoggins and Ronald W. Phelps
Department of Meteorology
Texas A&M University, College Station, Texas

A. ABSTRACT

Atmospheric Variability Experiment (AVE) data are analyzed for 19-20 February 1964 to relate changes in measured wind on selected constant-pressure surfaces to changes in the thermal wind for a layer below the constant-pressure surface. Layers of various thicknesses are considered with the base at 950 mb, and others with bases at higher levels. The tops of the layers ranged from 700 to 300 mb. With the assumption of constant wind direction with height, it was found that areas with changes in the measured wind at the top of a layer and changes in the thermal wind within the layer $\geq$ 5 m/sec coincided closely for thick layers and time intervals exceeding about 6 hrs. The linear correlation coefficient between changes in the measured and thermal winds $\geq$ 5 m/sec (positive or negative) was positive and significantly different from zero at the 5% level. Changes over periods of 3, 6, 9, and 12 hrs were considered in the analysis.

B. INTRODUCTION

With the advent of modern aerospace technology, a growing demand has arisen for accurate and up-to-date forecasts of local wind changes over short time periods. Mesoscale phenomena such as short-term wind variations are quite difficult to predict. The most promising effort to date in the prediction of small-scale systems appears to be the application of the "article of faith" (Scoggins, et al., 1972). This refers to the hypothesis that mesoscale systems are associated with synoptic-scale systems. With this assumption, a forecaster may utilize synoptic maps to infer the small-scale perturbations which might be associated with the synoptic events. Refinement of the technique, hopefully, will result in accurate, short range forecasts of wind variations, so important in air stagnation alerts, space vehicle launchings, and especially, severe local weather phenomena.

A better understanding of the causal relationships between measured wind changes and various meteorological parameters which influence such variations, necessitates an investigation into possible theoretical considerations which may or may not prove to be substantiated by actual observations. Relations between meteorological variables are given by the fundamental equations relating two or more of the parameters. From the equations of

motion, wind speed is related to pressure gradient, while the thermal wind equation gives the relationship between vertical wind shear and horizontal temperature gradient. These equations can be used to describe relationships between measured wind, thermal wind, and thickness.

It was found by Carlson (1972) that changes in the actual wind are correlated with changes in the gradient wind over time periods of 9 and 12 hours. The correlation decreased in significance, however, when applied to 3- and 6-hr time intervals. An extension of the type of study performed by Carlson would be to study the thermal wind changes in relation to actual wind changes. Relationships between changes in these parameters over various time intervals are investigated in this study.

C. THEORETICAL BACKGROUND

Above the friction level it is often assumed that the wind is geostrophic. With this assumption, the thermal wind, $\vec{V}_T$, is defined by

$$\vec{V}_T = \vec{V}_{z_2} - \vec{V}_{z_1} \tag{1}$$

where $\vec{V}_{z_2}$ and $\vec{V}_{z_1}$ represent the geostrophic wind at heights z_2 and z_1, respectively, and $z_2 > z_1$. The thermal wind is given also by the equation (Panofsky, 1957)

$$f\vec{V}_T \times \vec{k} = 980\, \vec{\nabla} (\Delta h) \tag{2}$$

where f is the coriolis parameter, $\vec{k}$ is a unit vector in the z direction, and Δh is the thickness between two constant pressure surfaces. The equation for thickness is (Panofsky, 1958)

$$\Delta h = \frac{R\bar{T}_v}{980} \ln \frac{P_1}{P_2} \tag{3}$$

where R is the specific gas constant, and $\bar{T}_v$ is the average virtual temperature of the layer between the pressure surfaces P_1 and P_2, where $P_1 > P_2$.

Solving Eq. 1 for $\vec{V}_{z_2}$, making use of Eqs. 2 and 3, and differentiating with respect to time, leads to

$$\frac{\partial \vec{V}_{z_2}}{\partial t} = \vec{k} \times \frac{980}{f} \vec{\nabla} \frac{\partial (\Delta h)}{\partial t} + \frac{\partial \vec{V}_{z_1}}{\partial t} \quad . \tag{4}$$

This equation relates local changes in the geostrophic wind at height z_2 to local changes in the gradient of thickness between heights z_2 and z_1, and local changes in the geostrophic wind at height z_1. If the wind is geostrophic at heights z_1 and z_2, and if local changes in V_{z_1} and the gradient of thickness could be determined, local changes in V_{z_2} would be known. This appears reasonable since changes in V_{z_2} often result from the movement of systems which can be determined with reasonable accuracy, and since $\bar{T}_v(\Delta h \propto \bar{T}_v)$ is a conservative quantity whose local change can be determined by advection or the movement of synoptic systems.

With the assumption of constant wind direction with height, Eq. 4 may be written in scalar form as follows:

$$\frac{\partial V_{z_2}}{\partial t} = \left| \vec{k} \times \frac{980}{f} \vec{\nabla} \frac{\partial(\Delta h)}{\partial t} \right| + \frac{\partial V_{z_1}}{\partial t} \quad . \tag{5}$$

This equation is used in this study to relate the magnitude of local changes in V_{z_2} to corresponding changes in V_{z_1} and the thermal wind. It should be noted that the first term on the right-hand side of Eqs. 4 and 5 represents local changes in the thermal wind.

D. DATA USED IN THIS STUDY

Data used in this report were provided by the Aerospace Environment Division, Aero-Astrodynamics Laboratory, National Aeronautics and Space Administration, Marshall Space Flight Center, Alabama. Rawinsonde soundings from thirty stations in the southeastern United States (Fig. 1), were taken at 3-hr intervals, with the Huntsville, Alabama, and Mississippi Test Facility stations providing reports at an interval of one- and one-half hours. Observations studied were from 00Z, 19 February 1964 to 21Z, 20 February 1964, at 3-, 6-, 9-, and 12-hr intervals.

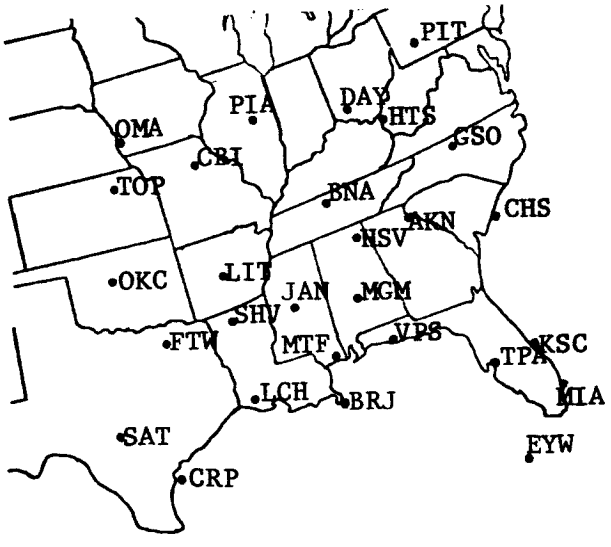

Fig. 1. Location of rawinsonde stations.

Care was taken in the analysis of the data to reduce measurement errors. Winds were computed from horizontal displacements over an 0.2- to 0.4-min interval, instead of the normal 2- to 4-min interval. An error analysis by NASA indicated RMS errors of 3.4 m sec^{-1} in the measured wind speeds, which corresponds to an RMS error of 4.8 m sec^{-1} in the differences between wind speeds. This latter value was used as the threshold value of changes in wind speed studied in this investigation. A more complete explanation of the observational errors inherent in the data was reported by Carlson (1972).

E. ANALYSIS OF DATA

In the analysis which follows, changes in measured wind speeds (direction was not considered) at 700, 500, 400, and 300 mb are related to changes in the thermal wind between 950 mb and each of these pressure surfaces. Based on errors in the measured wind, only those changes ≥ 5 m/sec were considered. Changes were computed over time periods of 3, 6, 9, and 12 hr beginning at 00Z, 19 February and continuing through 06Z, 20 February 1964. The changes were plotted on sectional maps to permit a visual comparison between changes in measured and thermal winds.

The rationale for this approach to the study of changes in measured wind (variability) is that the thermal wind is determined from temperature averaged through a layer (thickness) which can be treated as quasi-conservative over relatively short time periods, whereas wind is determined by several forces which vary in space and time. If changes in the (geostrophic) wind on any constant-pressure surface are negligibly small or can be determined, changes in the measured wind on any other constant-pressure surface can be determined, at least in principle, from changes in the thermal wind for the layer.

1. Changes in the 700-mb Measured Wind and the 950-700-mb Thermal Wind

Changes ≥ 5 m/sec in the measured wind at the 700-mb level and changes in the 950-700-mb thermal wind for time periods of 3, 6, 9, and 12 hrs on 19 February, 1964, are compared graphically in Fig. 2. As shown by Eq. 5, a change in wind speed at the upper boundary of the layer may be caused by a change in the thermal wind, a change in the wind at the lower boundary, or a combination of the two. No attempt has been made here to distinguish between changes in the wind at the lower boundary and the thermal wind in terms of leading to a change at the upper boundary. In Fig. 2, and in all subsequent figures of this type, areas are shown where the wind speed change was ≥ 5 m/sec, both negative and positive. These areas were determined from scalar analysis charts of the change fields and areas denoted where the change was ≥ 5 m/sec. In many instances, the change areas are near the boundaries of the data field, and some of the changes were based on only one station. In both of these cases, the reliability of the data is probably low.

In Fig. 2, some of the change areas for the measured wind at 700 mb and the thermal wind between 950 and 700 coincide, while in other cases they overlap partially or not at all. It is encouraging, however, that the change areas generally fall in the same geographic region. There does not appear to be a noticeable difference between the correspondence of areas for any of the time periods. No attempt will be made here to relate these changes to synoptic patterns; however, synoptic charts are given in Appendix A for reference.

2. Changes in the 500-mb Measured Wind and the 950-500-mb Thermal Wind

Changes in the measured wind at 500 mb and the thermal wind between 950-500 mb are shown in Fig. 3. The correspondence between areas in this

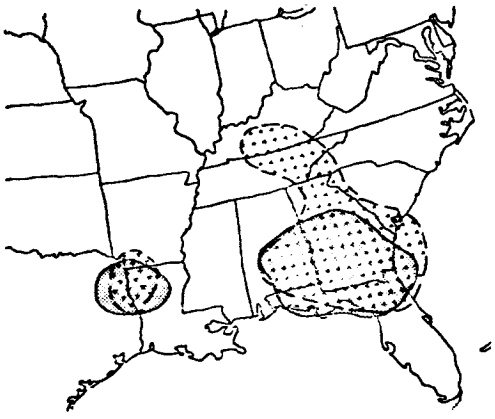

a) Negative changes for the 3-hr period 18-21Z.

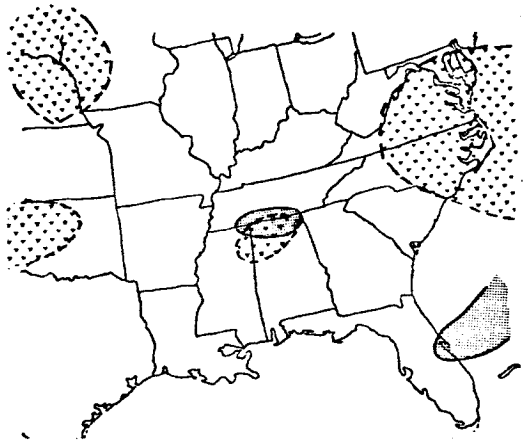

b) Positive changes for the 3-hr period 18-21Z.

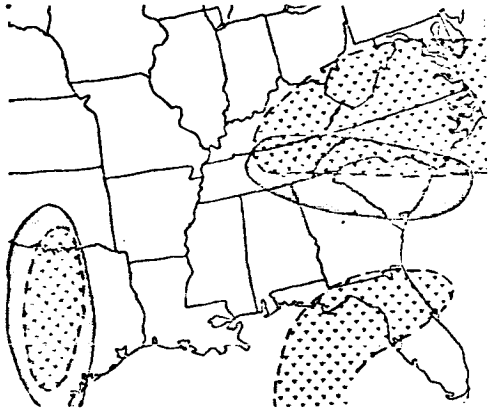

c) Negative changes for the 6-hr period 09-15Z.

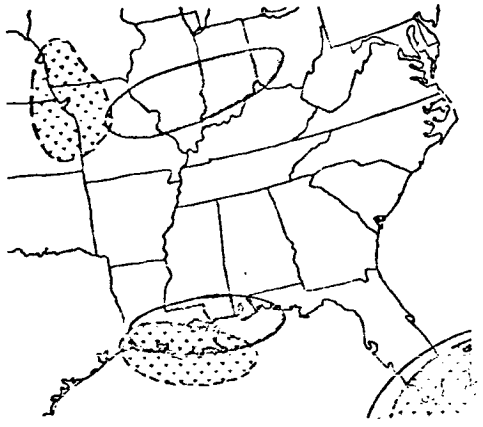

d) Positive changes for the 6-hr period 09-15Z.

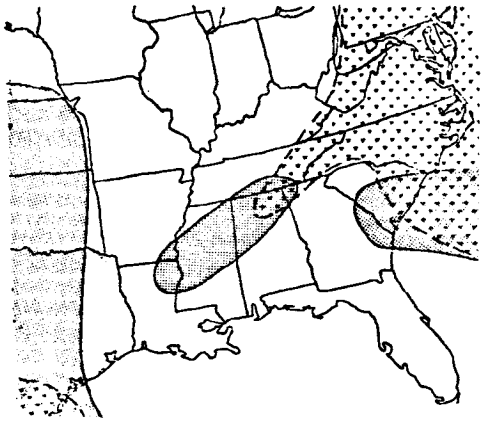

e) Negative changes for the 9-hr period 09-18Z.

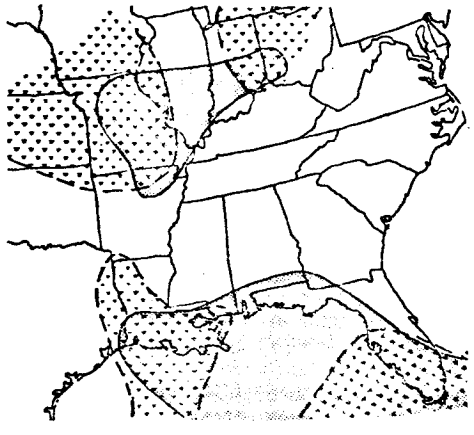

f) Positive changes for the 9-hr period 09-18Z.

Fig. 2. (Continued on following page)

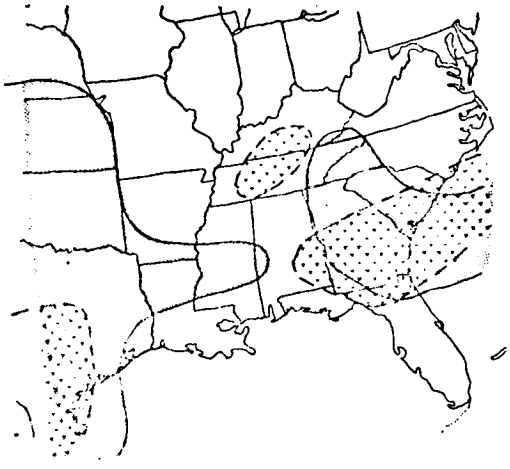

g) Negative changes for the 12-hr period 09-21Z.

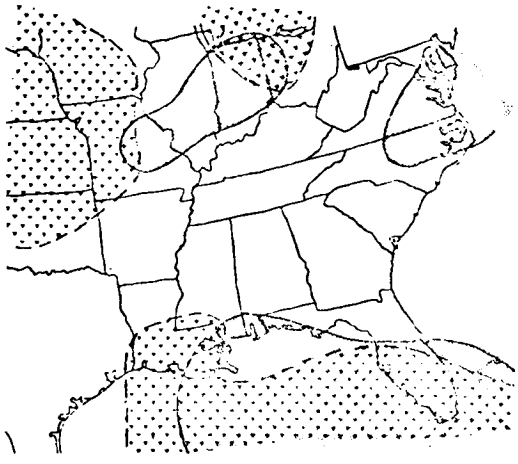

h) Positive changes for the 12-hr period 09-21Z.

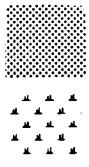

Fig. 2. Changes in the measured wind speed at 700 mb and those in the 950-700 mb thermal wind $\geq$ 5 m/sec over various time intervals on February 19, 1964.

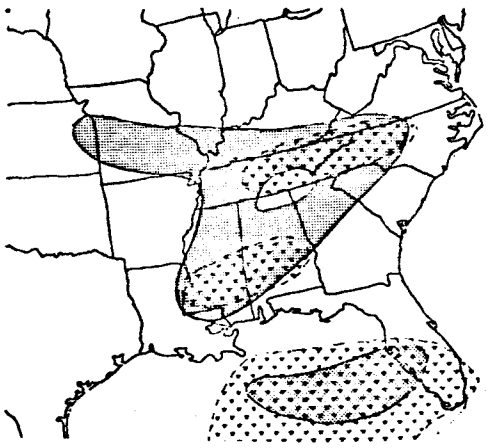

a) Positive changes for the 3-hr period 06-09Z.

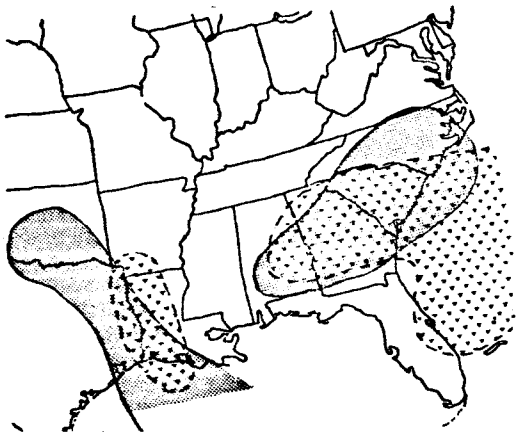

b) Positive changes for the 3-hr period 18-21Z.

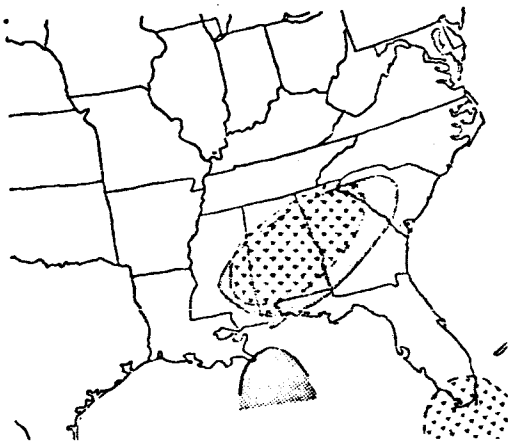

c) Negative changes for the 6-hr period 03-09Z.

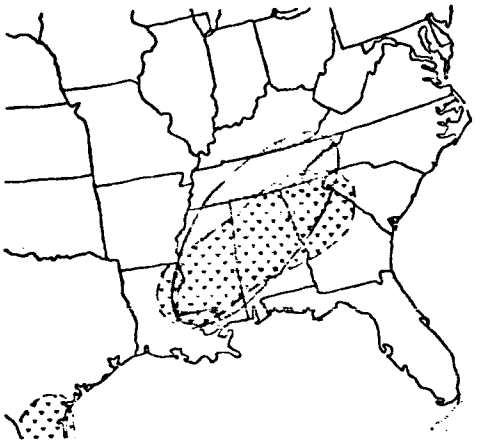

d) Negative changes for the 6-hr period 09-15Z.

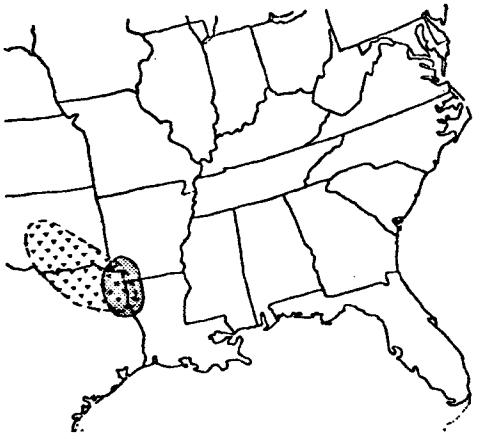

e) Positive changes for the 9-hr period 09-18Z.

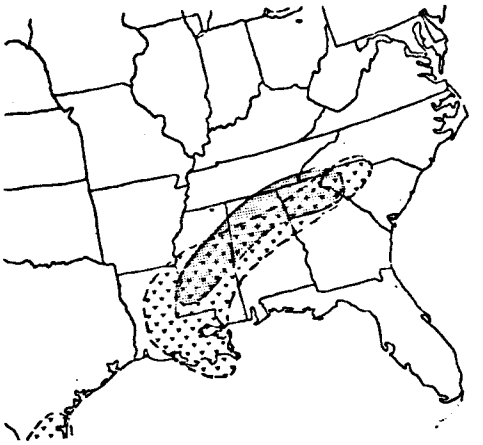

f) Negative changes for the 9-hr period 09-18Z.

Fig. 3. (Continued on following page)

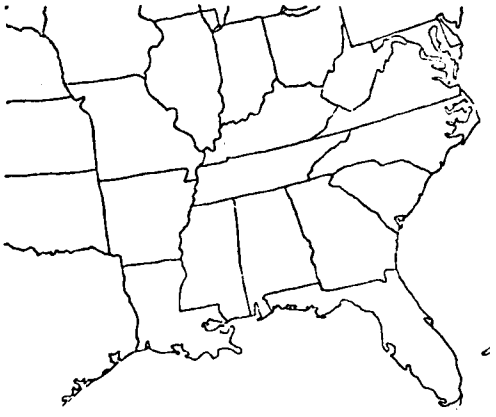

g) Positive changes for the 12-hr period 00-12Z.

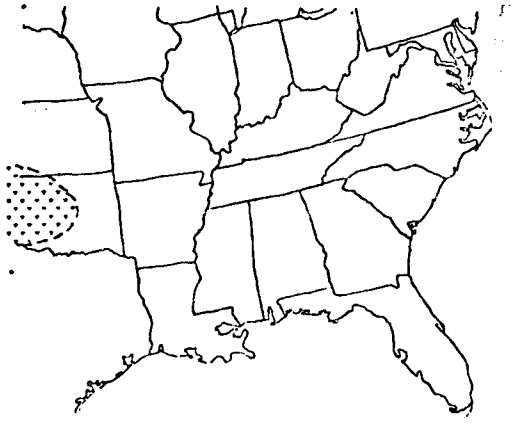

h) Positive changes for the 12-hr period 12Z, 19 February to 00Z, 20 February, 1964.

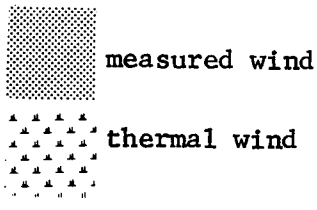

Fig. 3. Changes in the measured wind speed at 500 mb and those in the 950-500-mb thermal wind $\geq$ 5 m/sec over various time intervals on February 19, 1964.

figure is much better than that in Fig. 2. This better correspondence is probably due to the fact that the thermal wind has a larger magnitude for this deeper layer than for the shallow layer considered in Fig. 2, thus decreasing the influence of changes in the wind at 950 mb on changes at 500 mb. Also, the thickness (average temperature) field for a deep layer may be treated as quasi-conservative. For all time periods, except near the boundaries of the data field, the change areas coincided quite closely. It is encouraging to note that in Figs. 3c and 3d the areas of correspondence show continuity in time. This was observed in a number of cases, and is probably related to the conservative properties of the thickness field and the lack of a major influence upon the wind near the ground. From Fig. 3, it would appear reasonable to base changes in the measured wind at 500 mb on changes in the thermal wind which can be determined with reasonable certainty since the thermal wind may be treated as quasi-conservative.

3. Changes in the 400-mb Measured Wind and the 950-400-mb Thermal Wind

Changes $\geq$ 5 m/sec in the measured wind at 400 mb, and the thermal wind between 950-400 mb, are shown in Fig. 4 for 3-, 6-, 9-, and 12-hr periods. The correspondence of areas for all time periods is quite good for both negative and positive changes. The change areas are considerably larger than those considered in Figs. 2 and 3 and, therefore, encompass a greater number of stations. As in Fig. 3, it may be inferred from Eq. 5 that changes in the wind at 950 mb are small compared to changes in the thermal wind and, hence, the changes in the thermal wind correspond closely to those in the measured wind at the upper level. There does not appear to be a significant degradation of the results for a time period of 12 hrs as compared to the shorter time periods. Again, this is probably due to the fact that the thickness field (average temperature) for the layer is quasi-conservative.

4. Changes in the 300-mb Measured Wind and the 900-300-mb Thermal Wind

Changes $\geq$ 5 m/sec in the measured wind speed at 300 mb and changes in the thermal wind between 950-300 mb for various time intervals are shown in Fig. 5. The correspondence of areas in this figure is similar to those in Figs. 3 and 4. The correspondence of areas is quite good in most instances, except near the data boundaries.

5. Changes in Measured Wind Speed at Selected Levels Corresponding to Changes in the Thermal Wind Through Various Layers

A comparison of Fig. 2 with Figs. 3-5 shows that a better correspondence between changes in the measured and thermal winds over time intervals from 3-12 hrs is better for the thicker layers (Figs. 3-5) than for the shallow layer (Fig. 2). Large changes in measured and thermal winds may occur in the layers near the ground because of the influence of surface roughness and diabatic heating. In Figs. 2-5, the 950-mb surface was chosen as the bottom of each layer through which changes in the thermal wind were computed. In Figs. 6-9, conditions are shown for various layers and for time intervals ranging from 3-12 hours. The purpose of this part of the analysis is to determine if changes in the thermal wind within intermediate layers are associated with changes in the measured wind at the top of these layers.

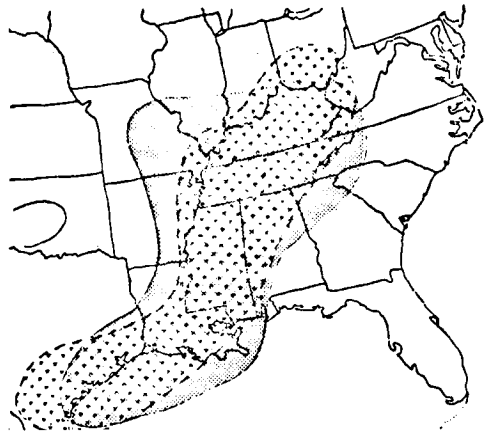

a) Negative changes for the 3-hr period 12-15Z.

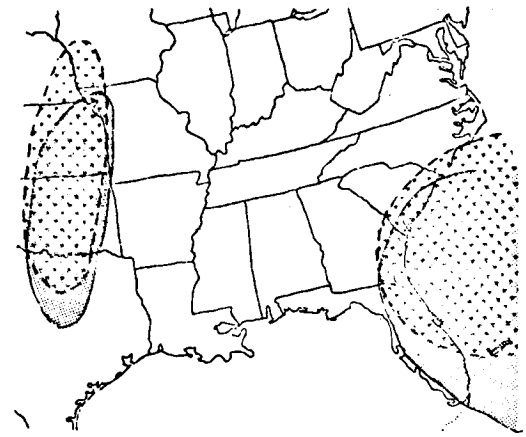

b) Positive changes for the 6-hr period 09-15Z.

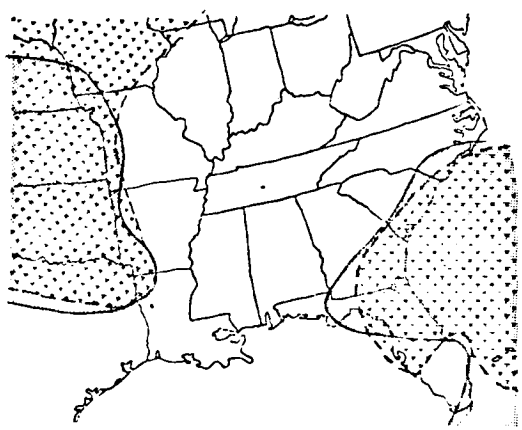

c) Positive changes for the 9-hr period 09-18Z.

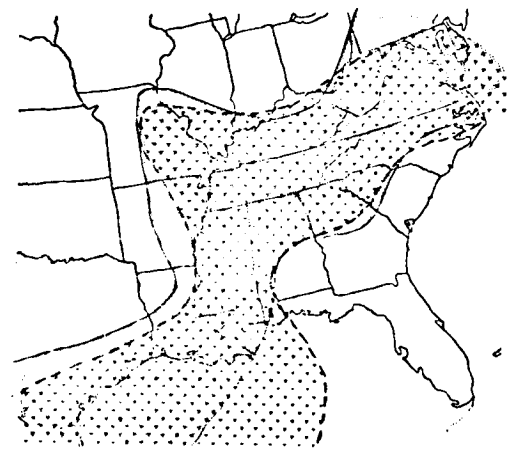

d) Negative changes for the 9-hr period 09-18Z.

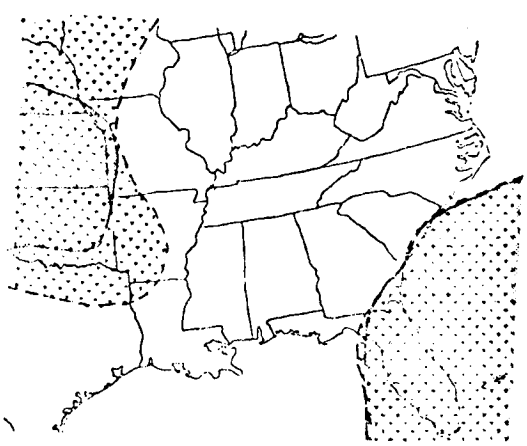

e) Positive changes for the 12-hr period 09-21Z.

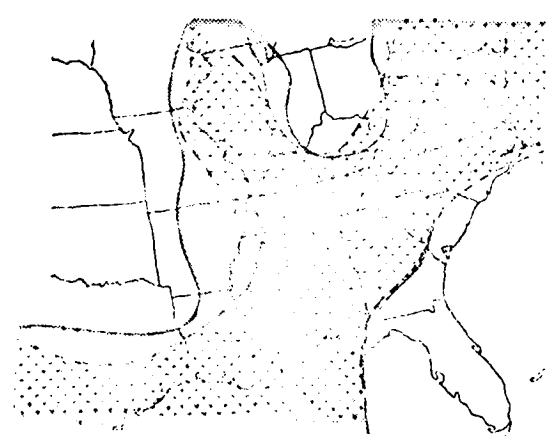

f) Negative changes for the 12-hr period 09-21Z.

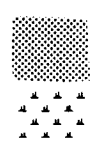

Fig. 4. Changes in the measured wind speed and those in the 950-400-mb thermal wind $\geq$ 5 m/sec over various time intervals on February 19, 1964.

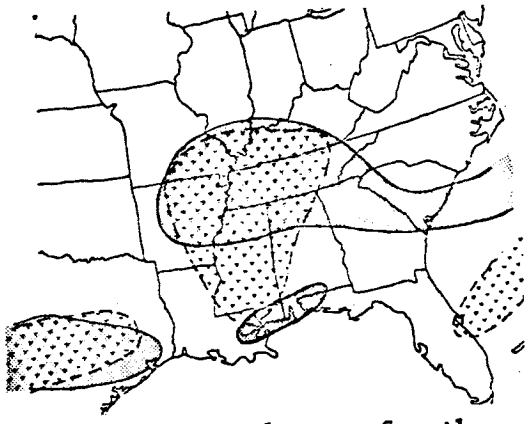

a) Negative changes for the 3-hr period 09-12Z.

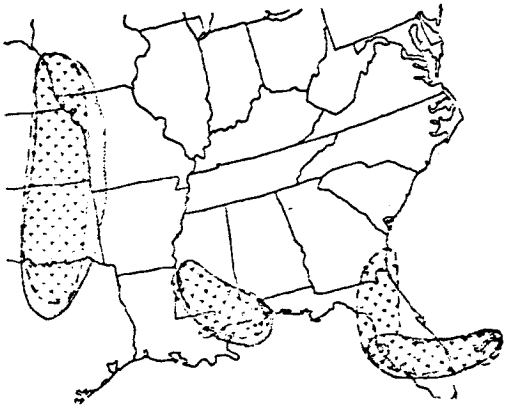

b) Positive changes for the 6-hr period 09-15Z.

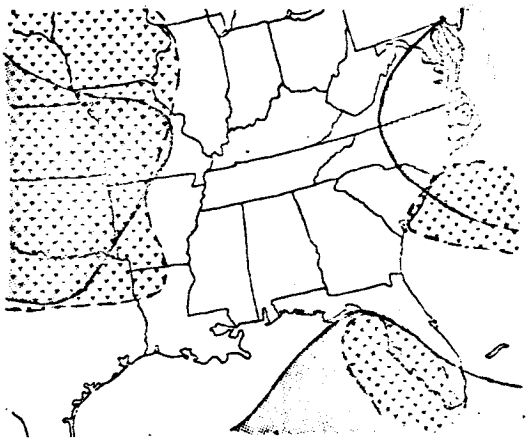

c) Positive changes for the 9-hr period 09-18Z.

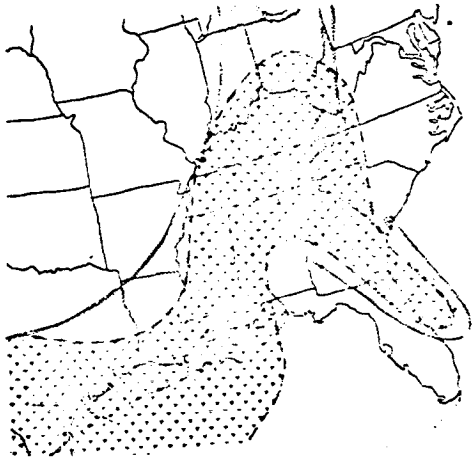

d) Negative changes for the 9-hr period 09-18Z.

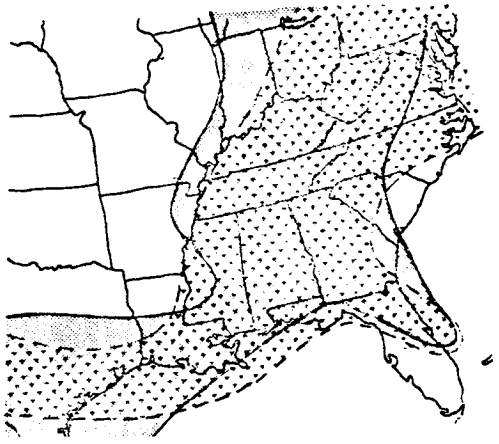

e) Negative changes for the 12-hr period 09-21Z.

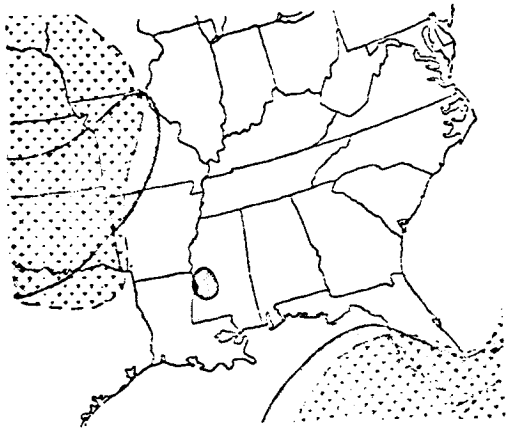

f) Positive changes for the 12-hr period 09-21Z.

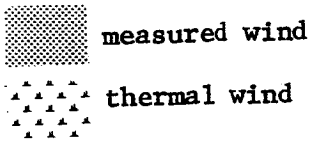

Fig. 5. Changes in the measured wind speed and those in the 950-300 mb thermal wind ≥ 5 m/sec over various time intervals on February 19, 1964.

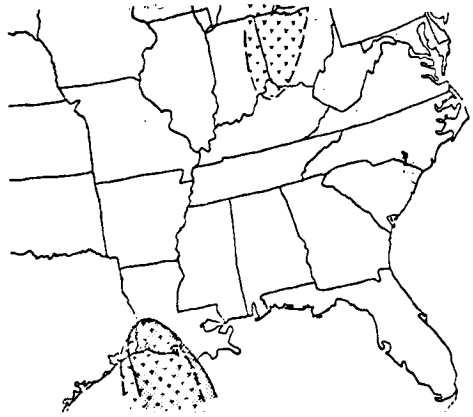

a) Positive changes in the measured wind at 700 mb and the thermal wind for the 950-700 mb layer.

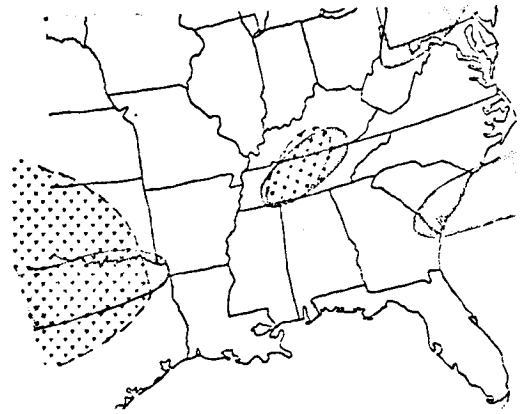

b) Negative changes in the measured wind at 700 mb and the thermal wind for the 950-700 mb layer.

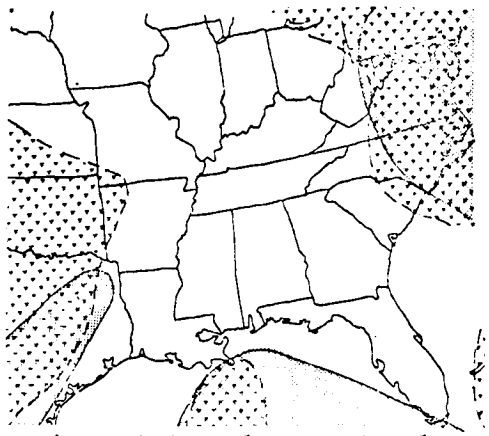

c) Positive changes in the measured wind at 500 mb and the thermal wind for the 700-500 mb layer.

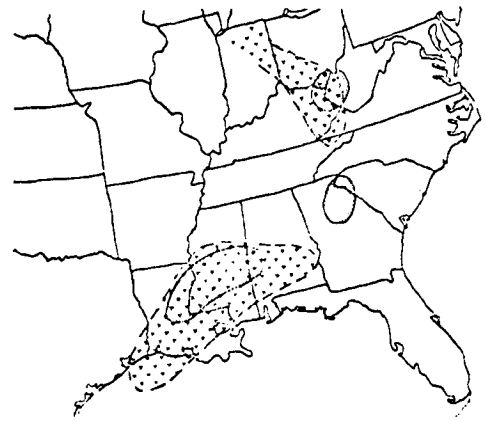

d) Negative changes in the measured wind at 500 mb and the thermal wind for the 700-500 mb layer.

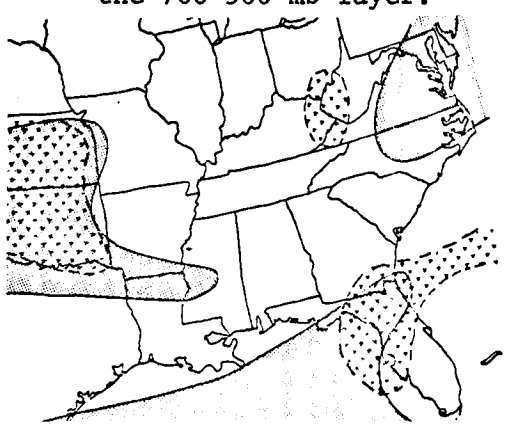

e) Positive changes in the measured wind at 300 mb and the thermal wind for the 500-300 mb layer.

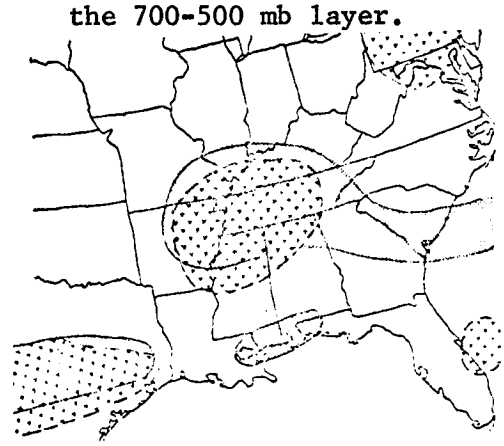

f) Negative changes in the measured wind at 300 mb and the thermal wind for the 500-300 mb layer.

measured wind

thermal wind

Fig. 6. Changes in the measured wind speed at selected constant-pressure surfaces and those in the thermal wind $\geq$ 5 m/sec for various layers for the 3-hr period 09-12Z on February 19, 1964.

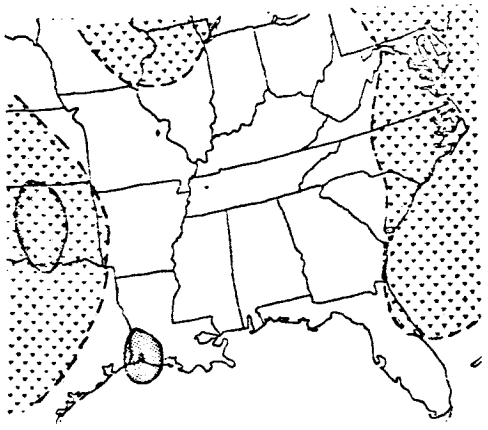

a) Positive changes in the measured wind at 500 mb and the thermal wind for the 700-500 mb layer.

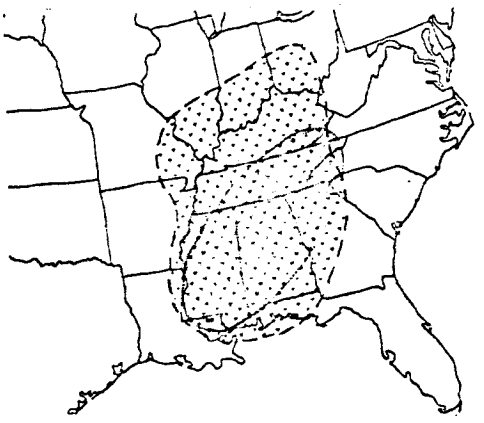

b) Negative changes in the measured wind at 500 mb and the thermal wind for the 700-500 mb layer.

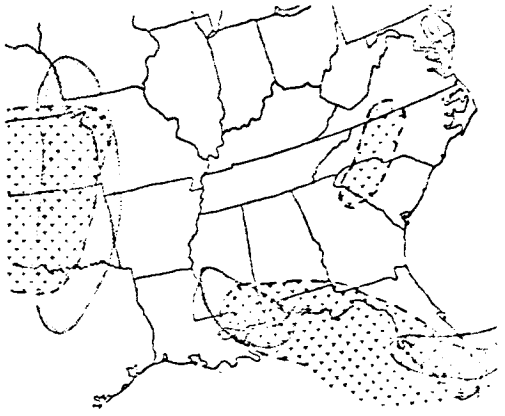

c) Positive changes in the measured wind at 300 mb and the thermal wind for the 500-300 mb layer.

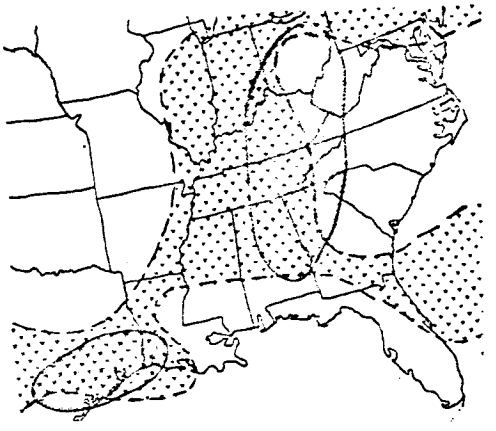

d) Negative changes in the measured wind at 300 mb and the thermal wind for the 500-300 mb layer.

measured wind

thermal wind

Fig. 7. Changes in the measured wind speed at selected constant-pressure surfaces and those in the thermal wind $\geq$ 5 m/sec for various layers for the 6-hr period 09-15Z on February 19, 1964.

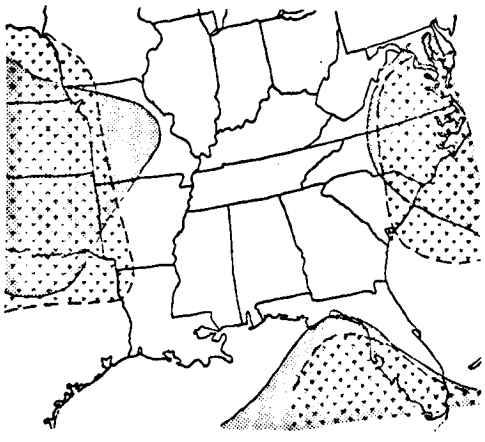

a) Positive changes in the measured wind at 300 mb and the thermal wind for the 700-300 mb layer.

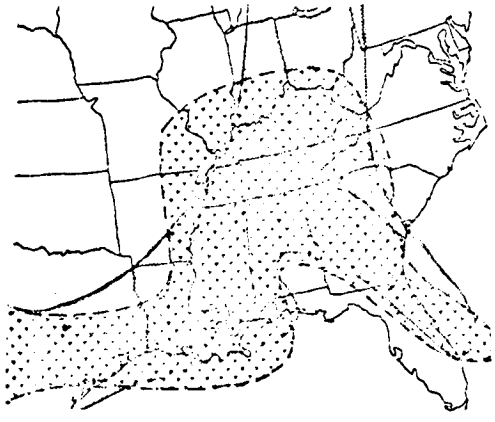

b) Negative changes in the measured wind at 300 mb and the thermal wind for the 700-300 mb layer.

measured wind

thermal wind

Fig. 8. Changes in the measured wind speed at selected constant-pressure surfaces and those in the thermal wind ≥ 5 m/sec for various layers for the 9-hr period 09-18Z on February 19, 1964.

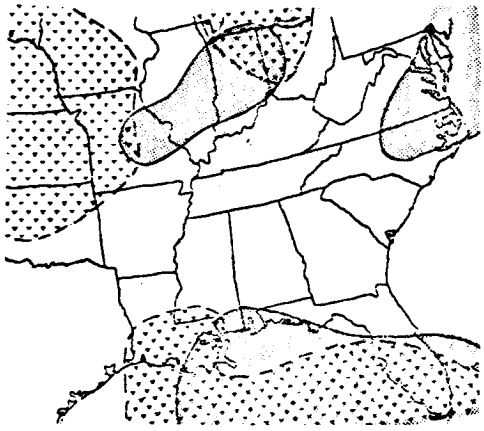

a) Positive changes in the measured wind at 700 mb and the thermal wind for the 950-700 mb layer.

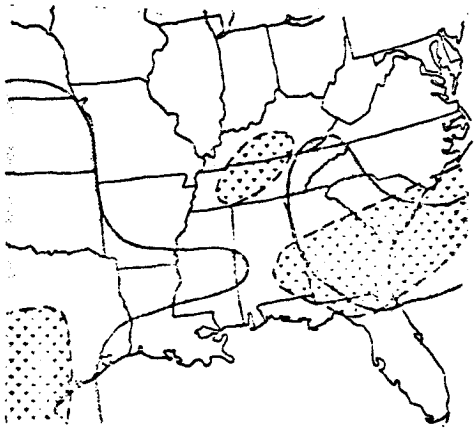

b) Negative changes in the measured wind at 700 mb and the thermal wind for the 950-700 mb layer.

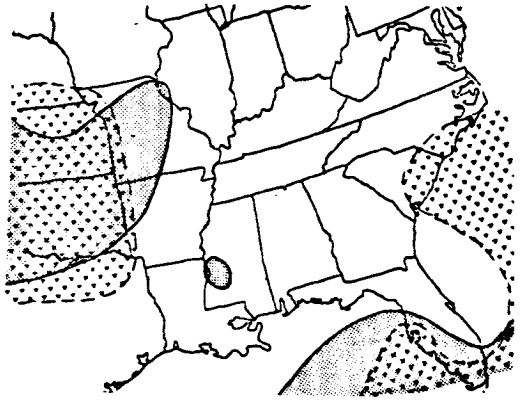

c) Positive changes in the measured wind at 300 mb and the thermal wind for the 700-300 mb layer.

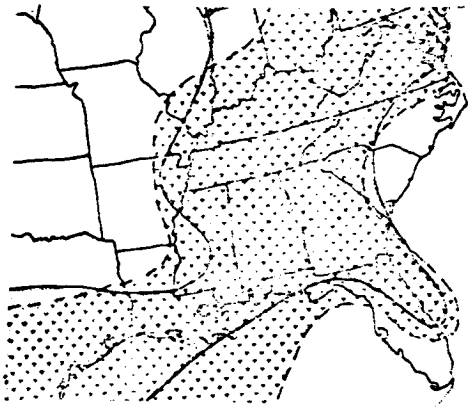

d) Negative changes in the measured wind at 300 mb and the thermal wind for the 700-300 mb layer.

measured wind

thermal wind

Fig. 9. Changes in the measured wind speed at selected constant-pressure surfaces and those in the thermal wind ≥ 5 m/sec for various layers for the 12-hr period 09-21Z on February 19, 1964.

The correspondence between areas of change in the measured and thermal winds shown in Fig. 6 for a period of 3 hrs do not indicate a close correspondence for any of the layers. These layers were chosen to be relatively thin as opposed to the deeper layers in Figs. 3-5. The results in Fig. 6 indicate that large changes may occur within thin layers. Hence, the changes in the wind at the bottom of the layer and/or changes in the thermal wind within the layer may be too great to permit any conclusions to be drawn regarding wind fluctuations at the top of the layer. Similar conditions are shown in Fig. 7 where the time interval is 6 hrs. In Fig. 8, the thickness of the layer is considerably greater than that for the layers in Fig. 7, and the correspondence between changes in the measured wind at 300 mb and the thermal wind in the 700-300-mb layer is quite good. A comparison of Fig. 8 with Figs. 6 and 7 shows the importance of layer thickness in the determination of changes in measured wind at the top of the layer.

Changes over a period of 12 hrs are shown in Fig. 9. Again, the correspondence of areas representing changes in the measured wind at the top of the relatively thin layer between 950 and 700 mb and the thermal wind change measured through this layer is quite poor, but for the deeper layer between 700-300 mb the change areas correspond closely.

To summarize the results of this section, changes of the thermal wind through a relatively thin layer do not correspond to changes in the measured wind at the top of the layer, but changes in the thermal wind through a deep layer correspond closely with changes in the measured wind at the top of the layer. In the analysis, only those areas were compared where changes in the measured wind and those in the thermal wind were equal to or exceeded 5 m/sec.

6. Correlation Between Changes in the Measured Wind Speed and Changes in the Thermal Wind

The linear correlation coefficient between 3-hr changes in the measured wind at 500 mb and changes in the thermal wind through the layer 950-500 mb was computed only for those areas where either change was $\geq$ 5 m/sec. The coefficient was found to be 0.84, which is significant at approximately the 1% level. In addition, correlation coefficients were computed for 3-, 6-, 9-, and 12-hr changes for the period 00Z, February to 06Z, 20 February 1964. The correlation coefficients corresponding to these time changes were 0.73, 0.65, 0.64, and 0.61, respectively. All of these coefficients were found to be significant at the 5% level.

While the linear correlation coefficients were not computed between changes in the measured wind and changes in the thermal wind for all layers considered, it is clear from Figs. 3-9 that the correlation is better for deep layers than for shallow layers. The correlation results for the 950-500-mb layer show that it is possible to determine changes in the wind at 500 mb from changes in the thermal wind for the layer below 500 mb, and that similar results hold for other relatively thick layers.

F. SUMMARY

Atmospheric Variability Experiment (AVE) data for 19-20 February 1964 measured at 3-hr intervals were used in the analysis of changes in measured and thermal winds over 3-, 6-, 9-, and 12-hr intervals. The objective of the study was to relate changes in measured wind on selected constant-pressure surfaces to changes in the thermal wind within a layer below the constant-pressure surface.

A number of layers were considered in the analysis with the base at 950 mb and tops ranging from 700 to 300 mb. Also, layers were considered with bases at higher altitudes (700 and 500 mb).

Based upon an error analysis of the data provided by NASA personnel, only those changes $\geq$ 5 m/sec were considered. Changes smaller than this magnitude could result from random error. To make the analysis more meaningful, patterns of changes $\geq$ 5 m/sec (positive and negative), based usually on several stations, were prepared. Computations were performed on a digital computer and a scalar analysis performed to establish the change areas.

The results showed that areas of measured changes in wind $\geq$ 5 m/sec at the top of a relatively thick layer coincided very closely with corresponding changes in the thermal wind within the layer for periods of 3, 6, 9, and 12 hrs, but for thin layers and time intervals of 3 and 6 hrs the relationship was poor. The correlation coefficient between 3-hr changes in the 950-500-mb thermal wind and the measured wind at 500 mb when either was $\geq$ 5 m/sec was found to be 0.84 which is significant at the 1% level. Similar correlation coefficients computed for periods up to 12 hr were significant at the 5% level.

To summarize the results of this study, the variability of wind (changes over periods of 12 hr and less) at the top of a relatively thick layer is related to and may be determined from the variability of the thermal wind within the layer. The results need to be verified with additional data, and if found to be of general validity, it may be possible to forecast small-scale changes in measured wind from the quasi-conservative thickness fields.

G. REFERENCES

IV-1. Carlson, Ronald Dale, 1972: Time Changes in Gradient and Observed Winds. Master's Thesis, Department of Meteorology, Texas A&M University, 63 pp. (also appears elsewhere in this document.)

IV-2. Panofsky, Hans, 1957: Introduction to Dynamic Meteorology, The Pennsylvania State University, University Park, Pennsylvania, 243 pp.

IV-3. Scoggins, James R., et al., 1972: An Investigation of Relationships Between Meso- and Synoptic-Scale Phenomena. NASA Contractor Report CR-2030, 179 pp.

H. APPENDIX A

SELECTED SYNOPTIC CHARTS FOR FEBRUARY 19-20, 1964

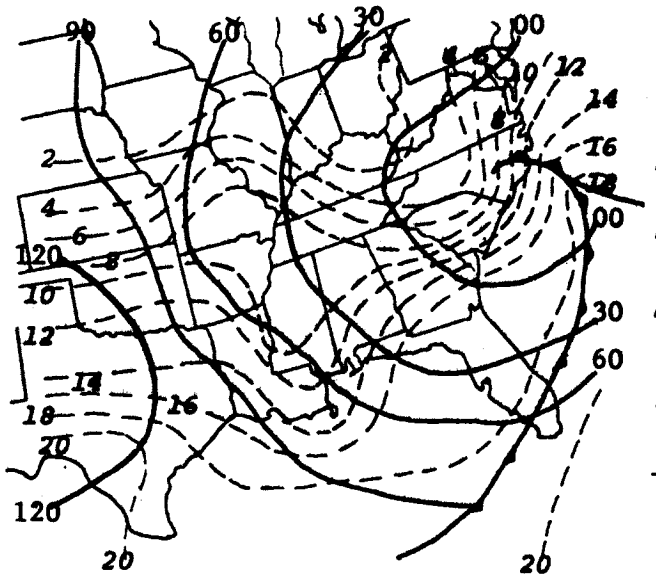

a) 1000 mb

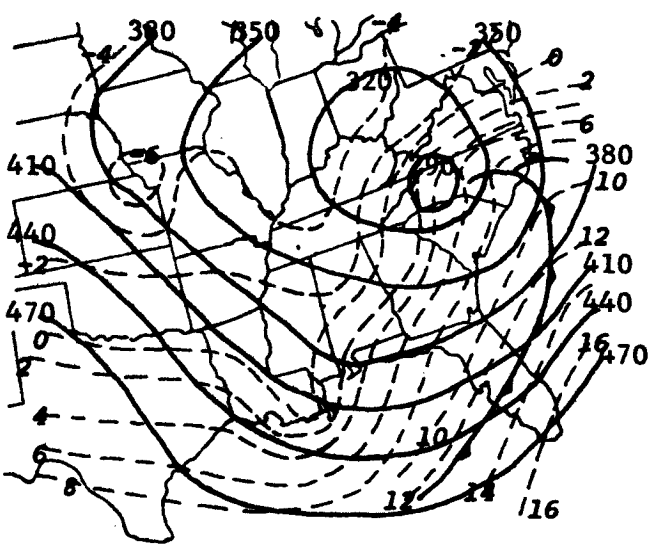

b) 850 mb

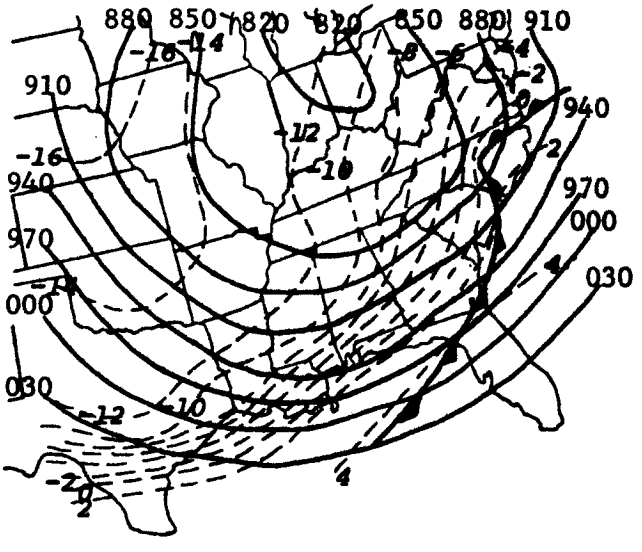

c) 700 mb

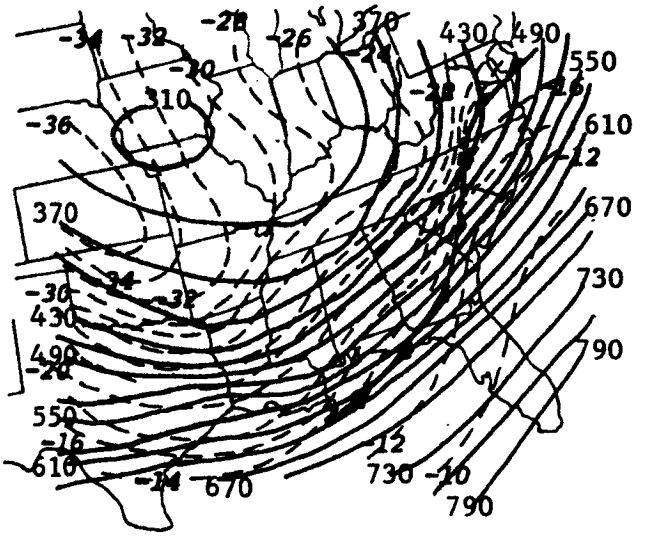

d) 500 mb

Fig. A-1. (Continued on following page)

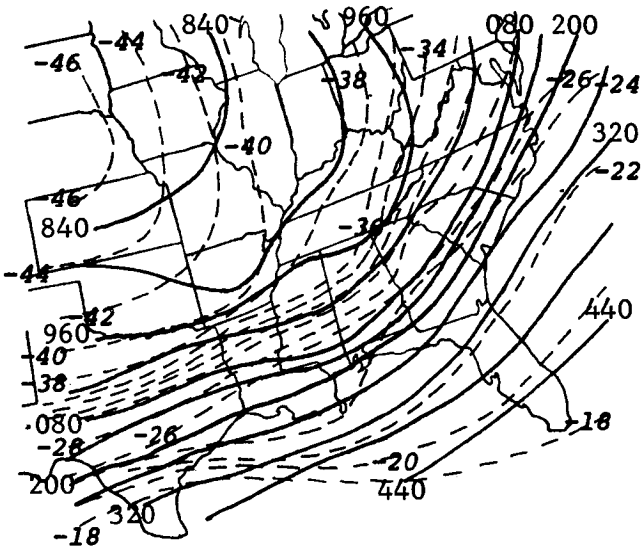

e) 400 mb

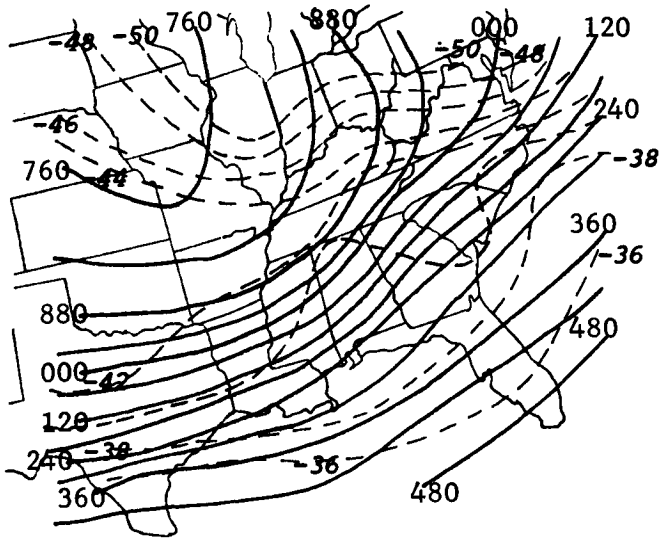

f) 300 mb

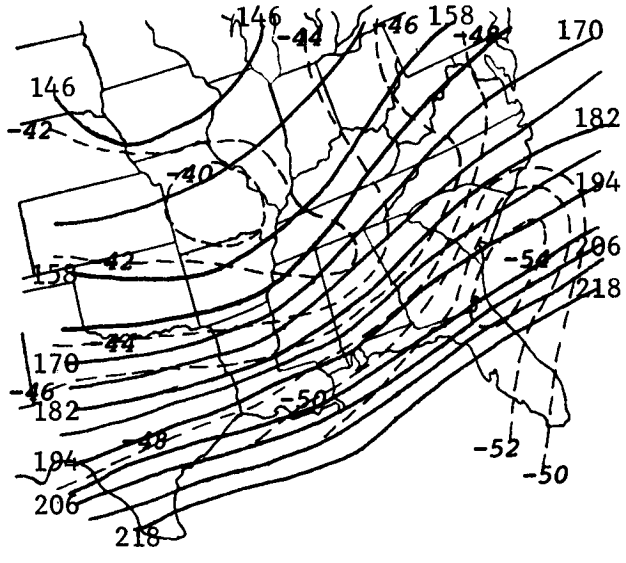

g) 200 mb

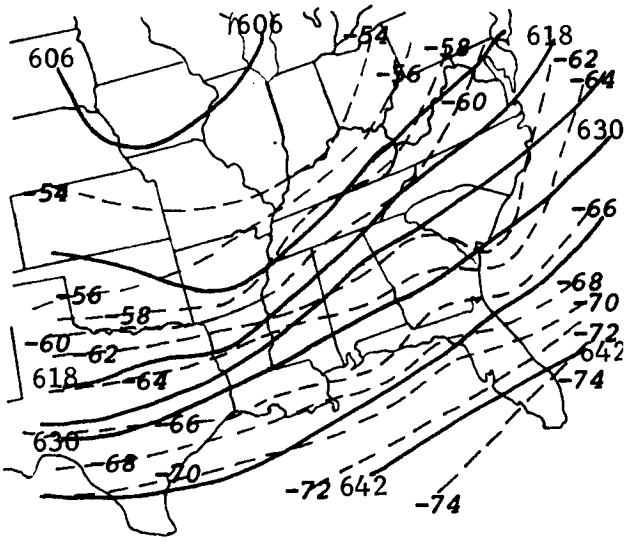

h) 100 mb

Fig. A-1. Synoptic charts for 00Z, February 19, 1964.

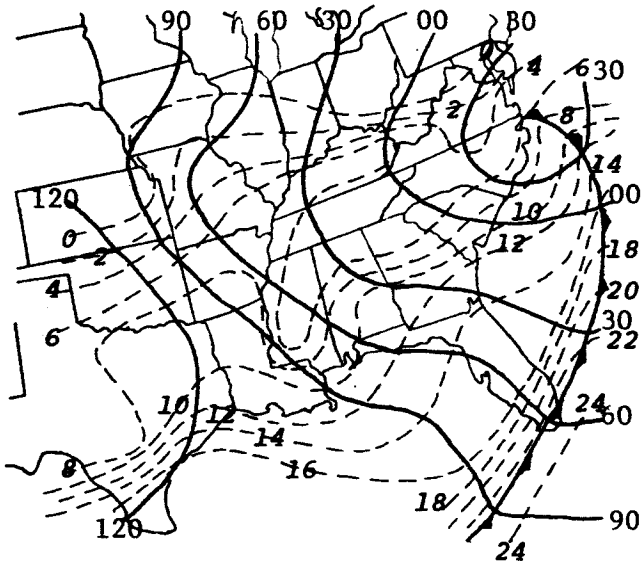

a) 1000 mb

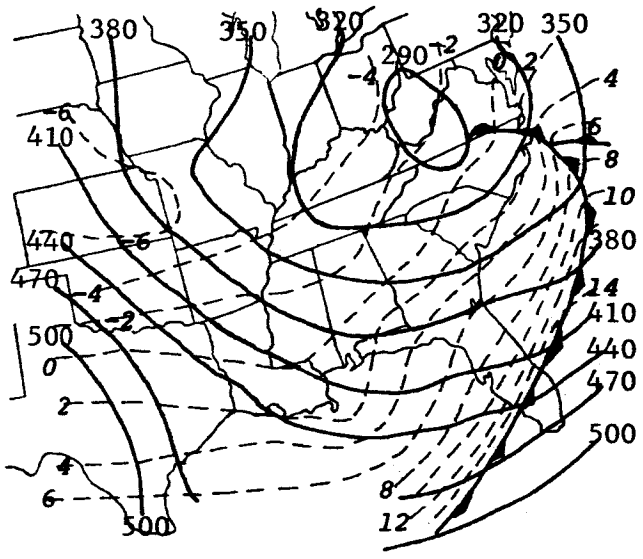

b) 850 mb

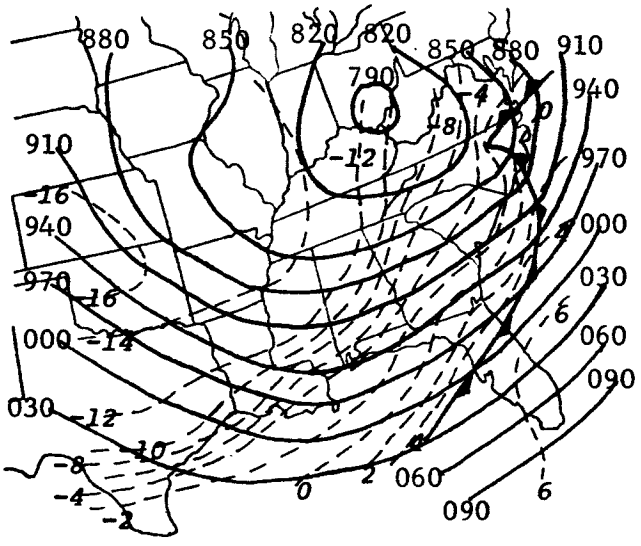

c) 700 mb

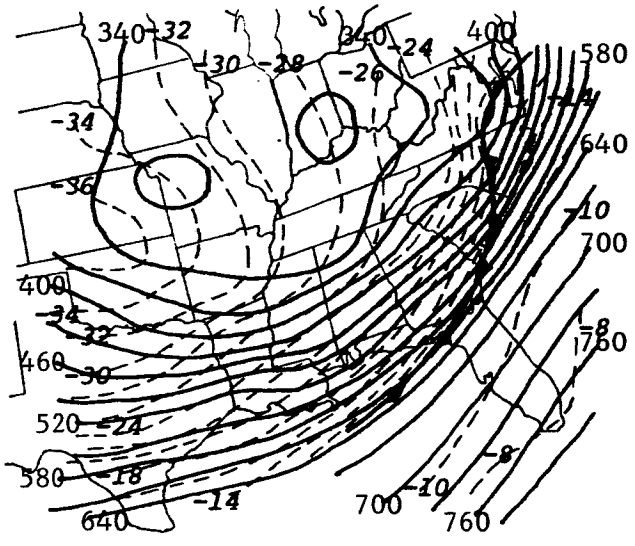

d) 500 mb

Fig. A-2. (Continued on following page)

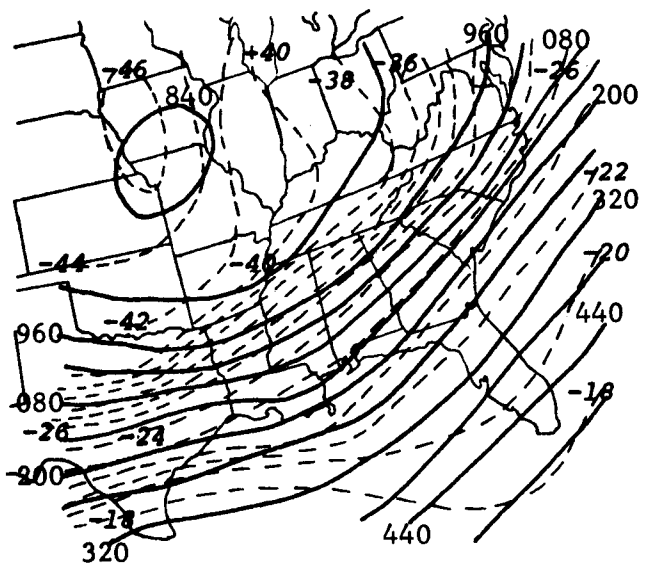

e) 400 mb

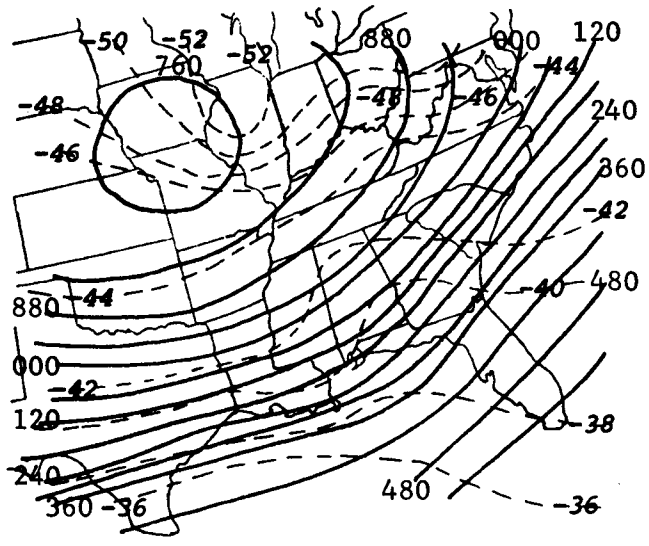

f) 300 mb

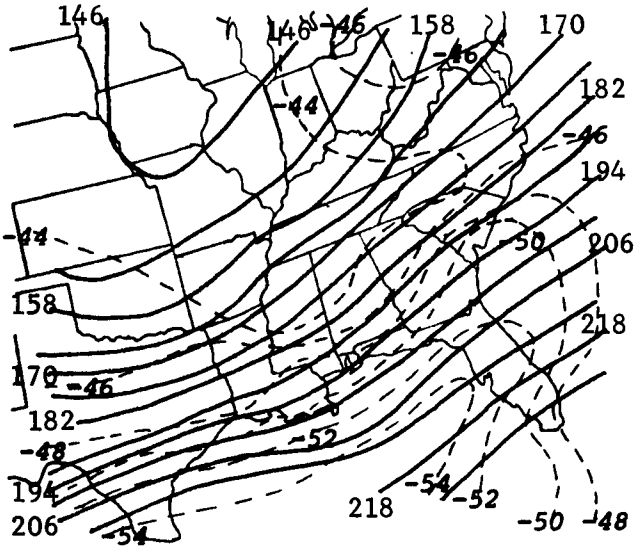

g) 200 mb

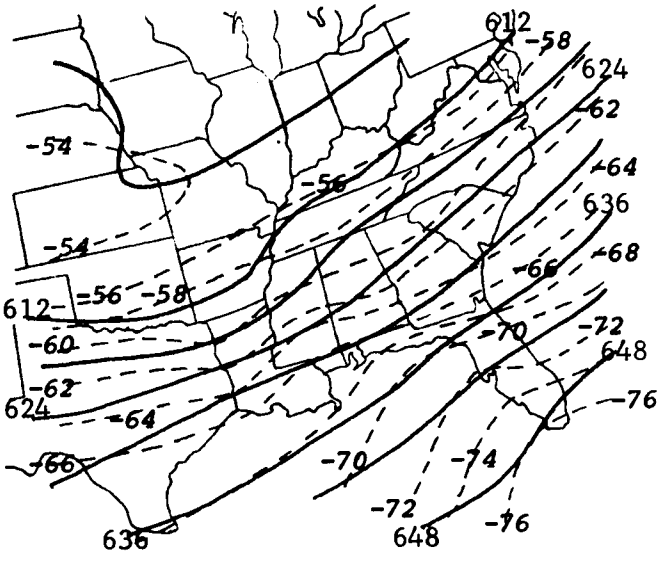

h) 100 mb

Fig. A-2. Synoptic charts for 03Z, February 19, 1964.

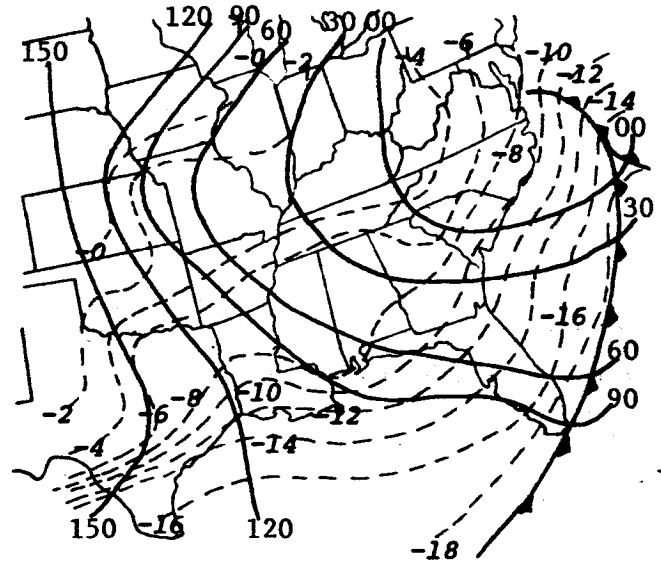

a) 1000 mb

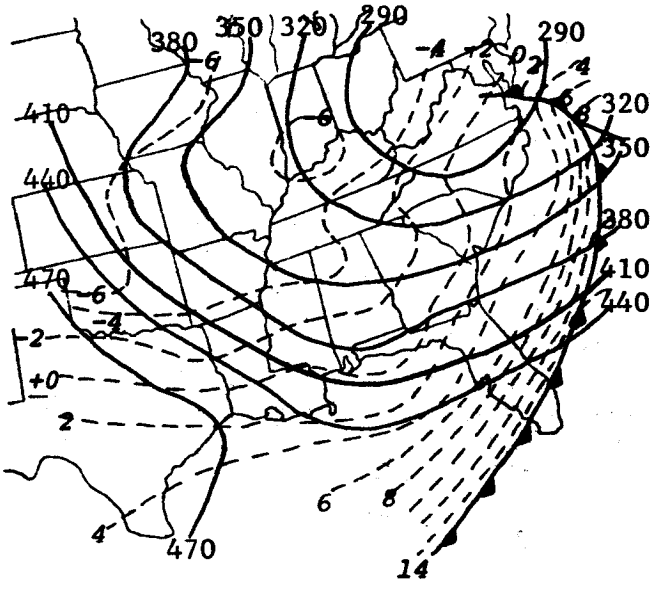

b) 850 mb

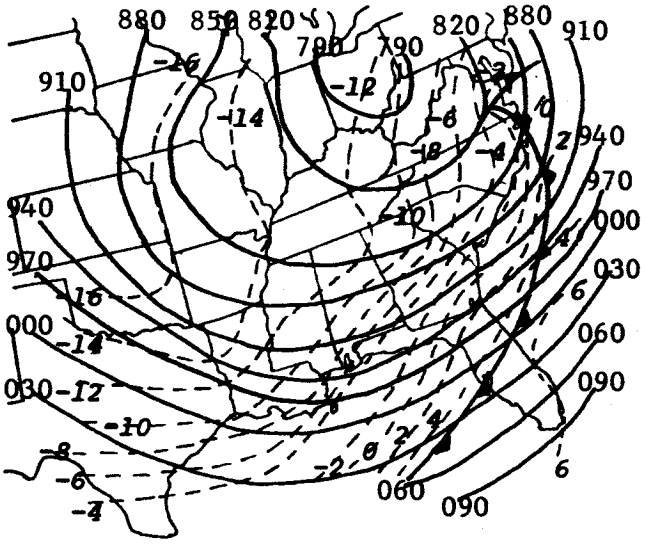

c) 700 mb

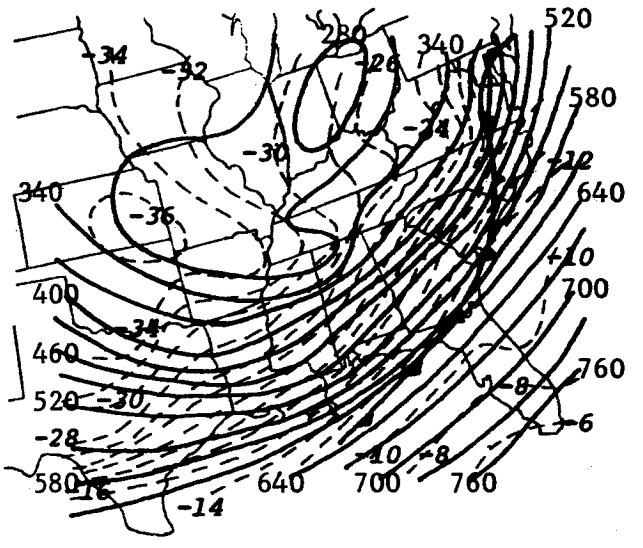

d) 500 mb

Fig. A-3. (Continued on following page)

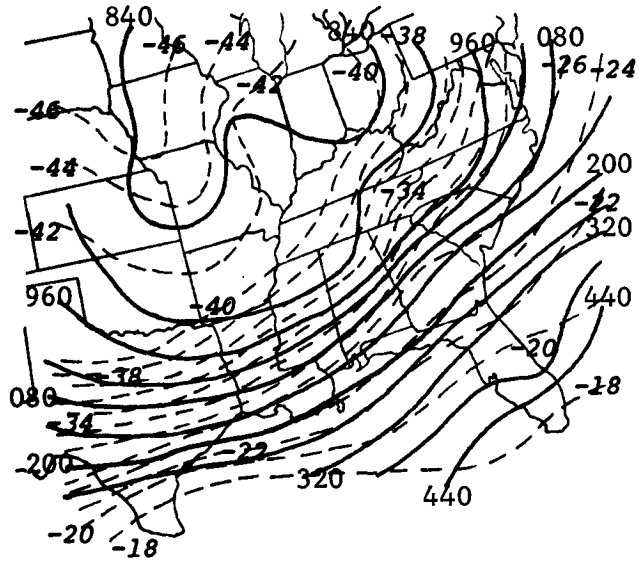

e) 400 mb

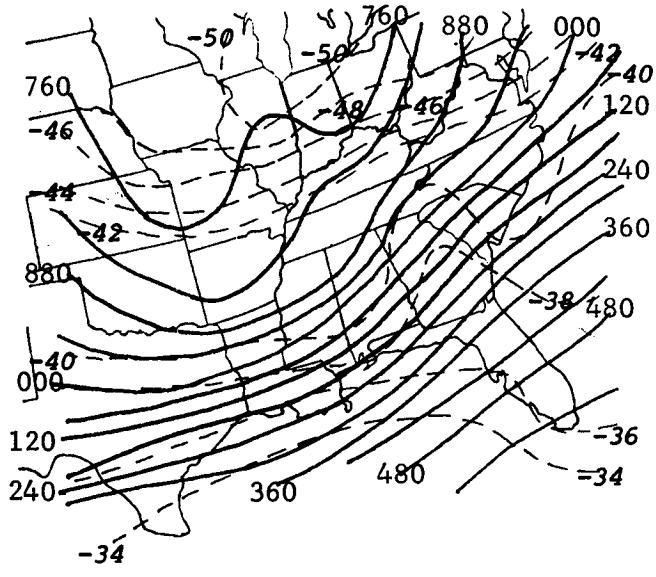

f) 300 mb

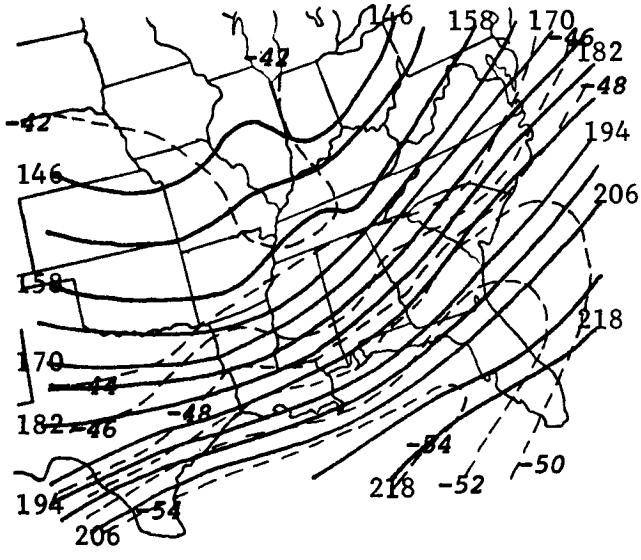

g) 200 mb

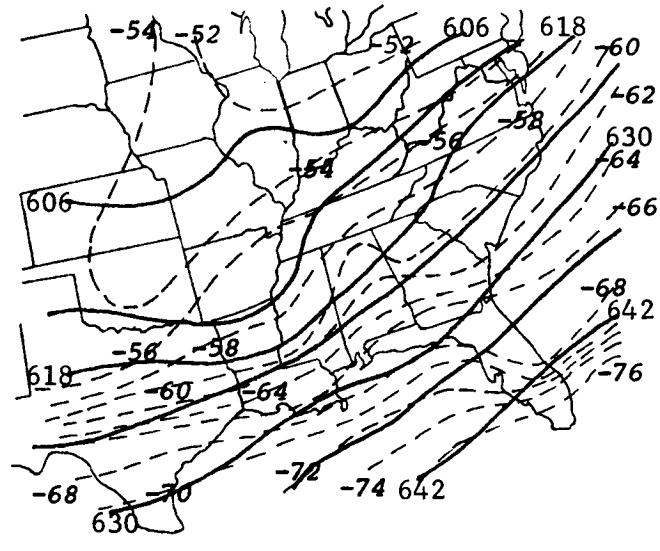

h) 100 mb

Fig. A-3. Synoptic charts for 06Z, February 19, 1964.

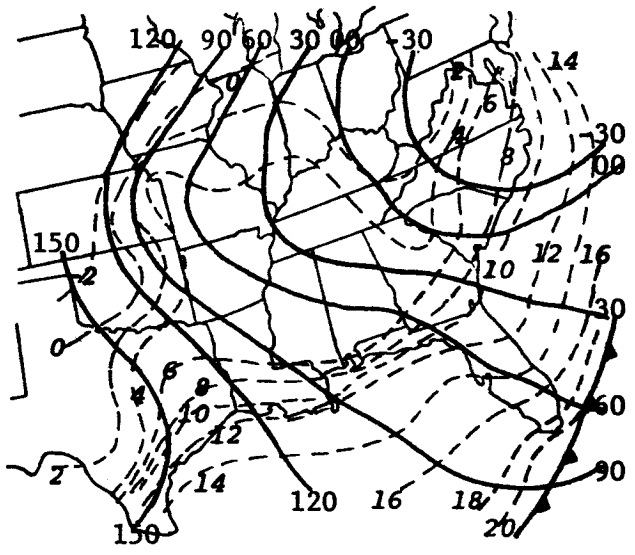

a) 1000 mb

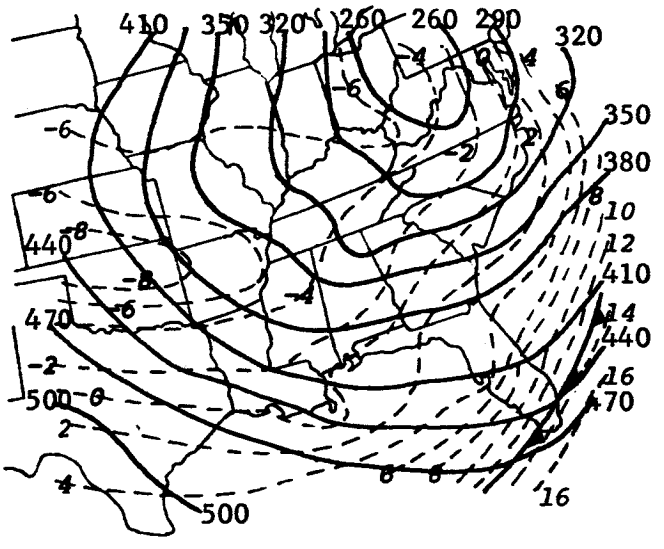

b) 850 mb

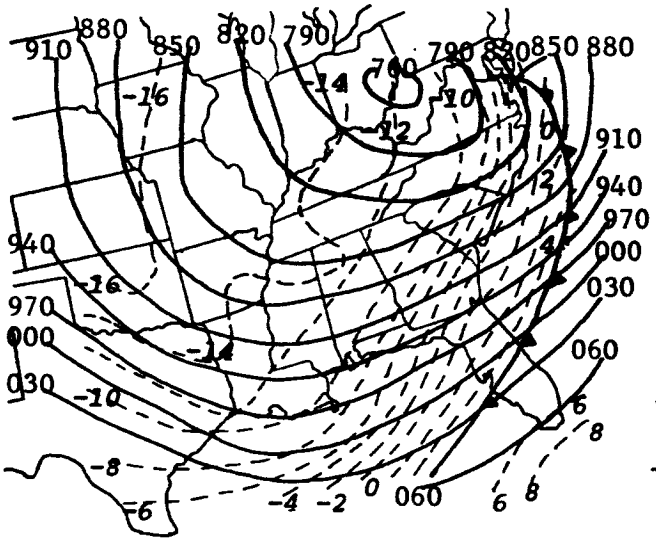

c) 700 mb

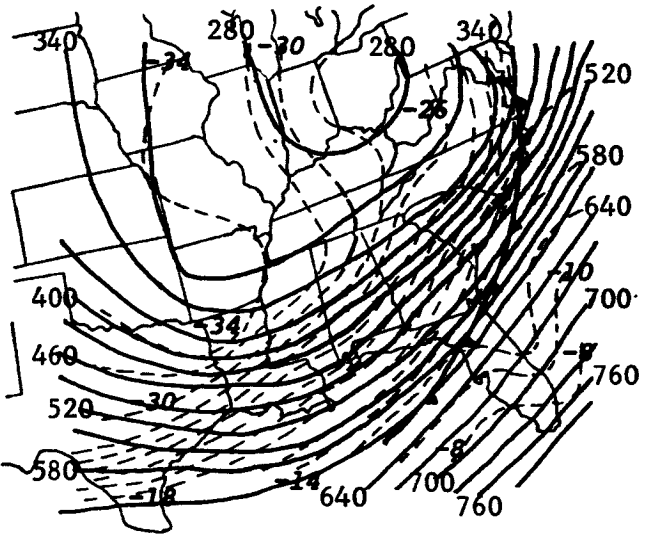

d) 500 mb

Fig. A-4. (Continued on following page)

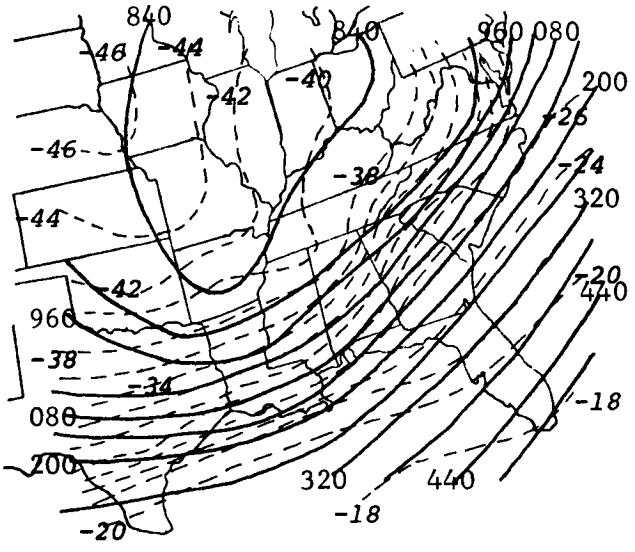

e) 400 mb

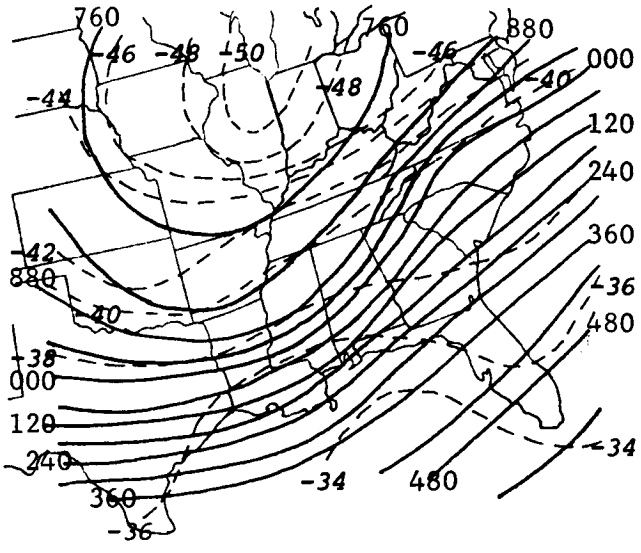

f) 300 mb

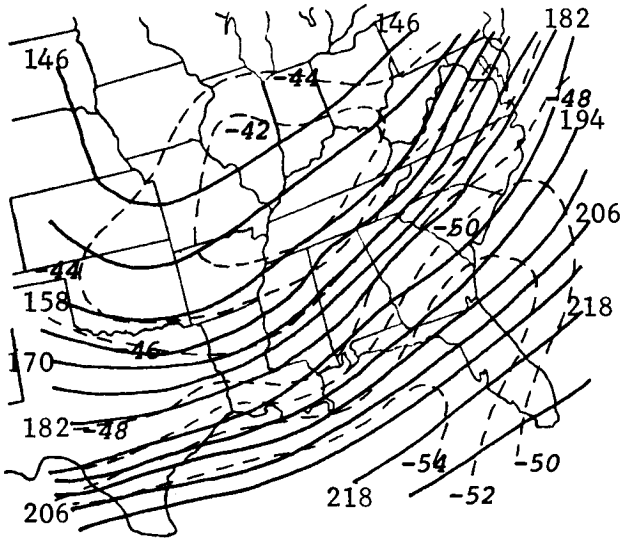

g) 200 mb

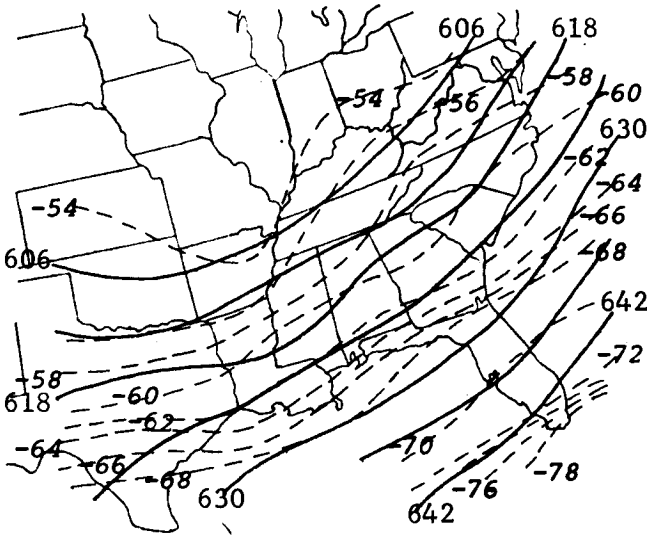

h) 100 mb

Fig. A-4. Synoptic charts for 09Z, February 19, 1964.

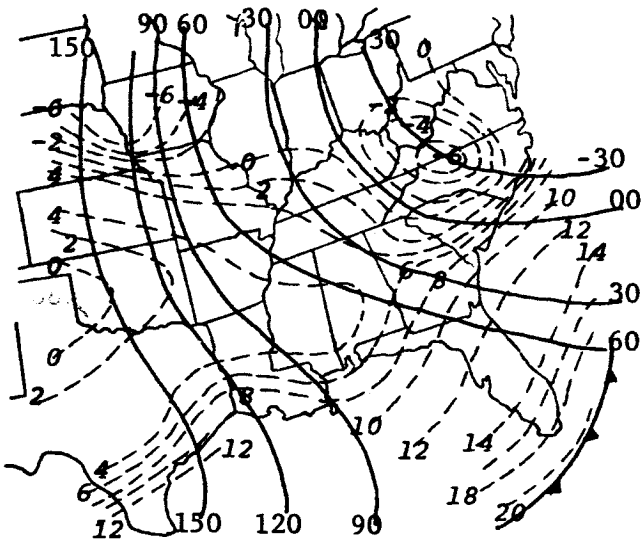

a) 1000 mb

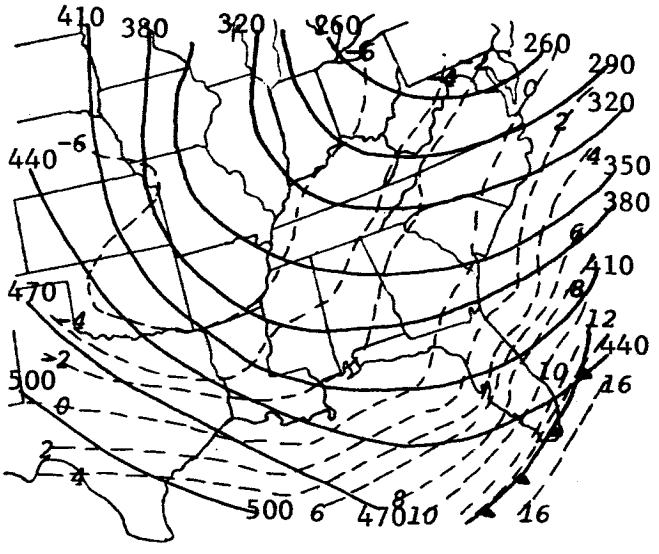

b) 850 mb

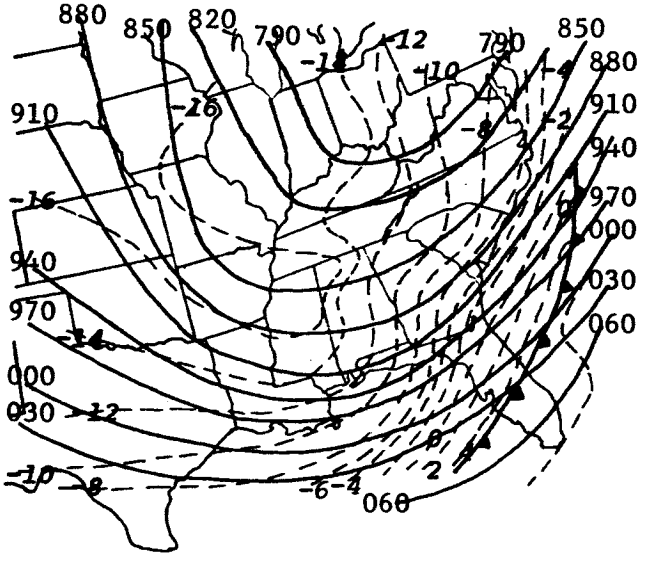

c) 700 mb

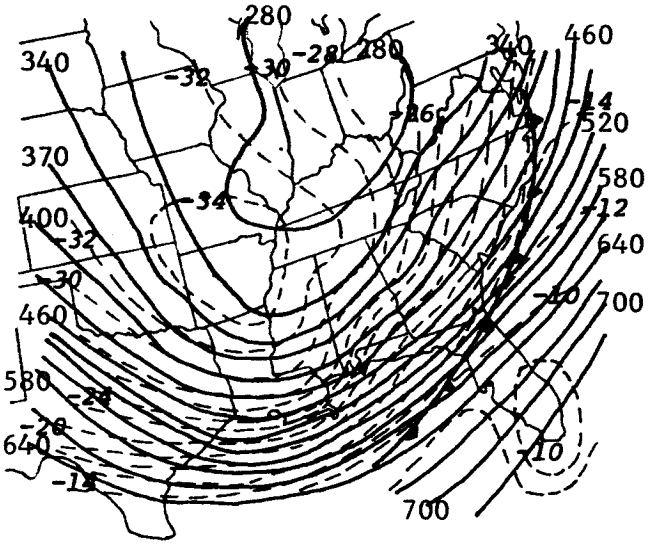

d) 500 mb

Fig. A-5. (Continued on following page)

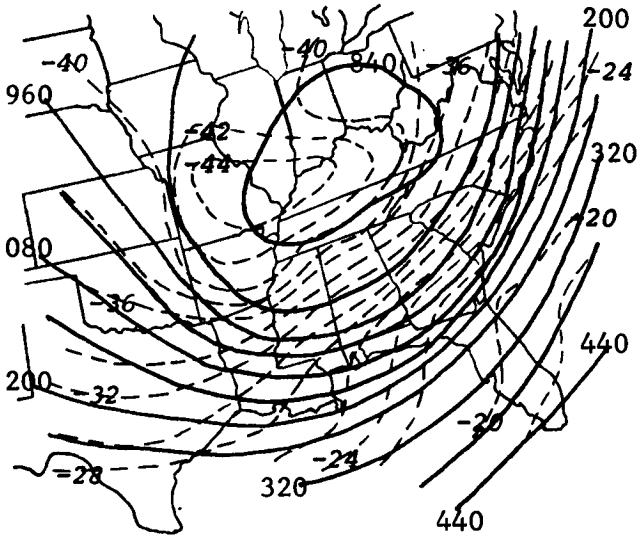

e) 400 mb

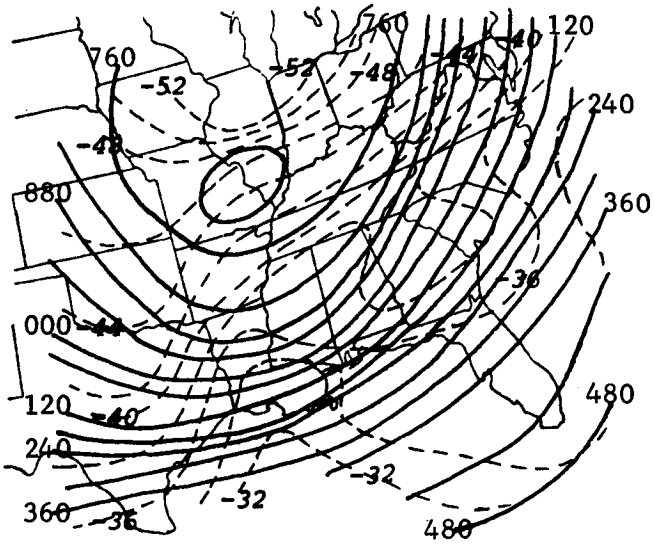

f) 300 mb

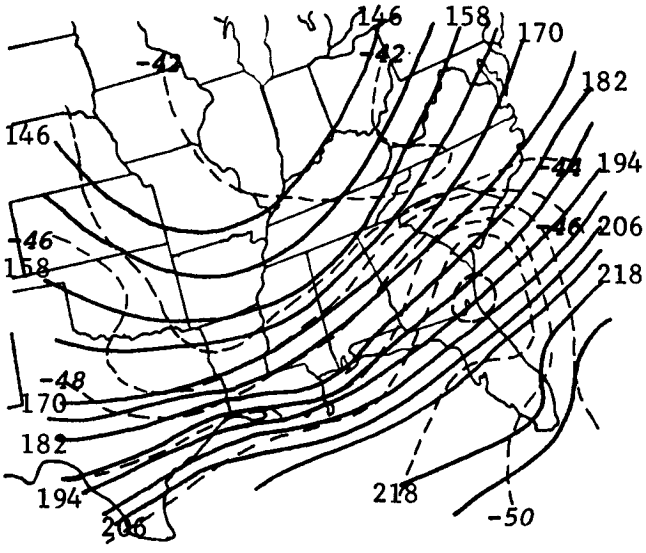

g) 200 mb

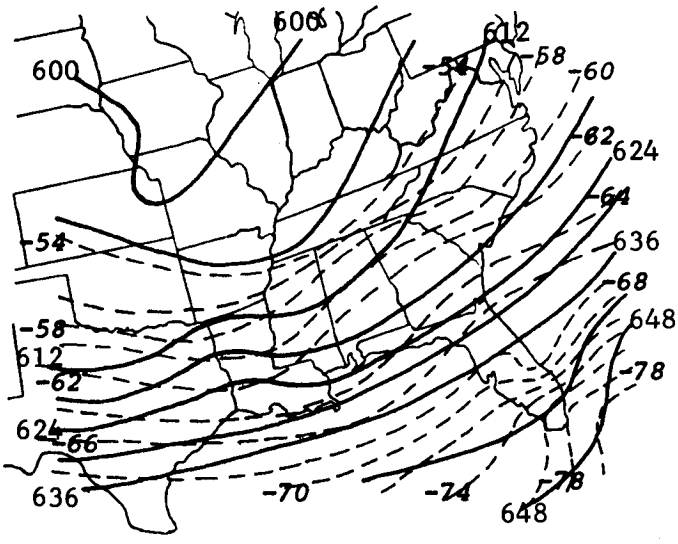

h) 100 mb

Fig. A-5. Synoptic charts for 12Z, February 19, 1964.

I. APPENDIX B

LIST OF STATION IDENTIFIERS

AHN	Athens, Georgia
BNA	Nashville, Tennessee
BRJ	Burrwood, Louisiana
CBI	Columbia, Missouri
CHS	Charleston, South Carolina
CRP	Corpus Christi, Texas
DAY	Dayton, Ohio
EYW	Key West, Florida
FTW	Fort Worth, Texas
GSO	Greensboro, North Carolina
HSV	Huntsville, Alabama
HTS	Huntington, West Virginia
JAN	Jackson, Mississippi
JAX	Jacksonville, Florida
KSC	Kennedy Space Center, Florida
LCH	Lake Charles, Louisiana
LIT	Little Rock, Arkansas
MIA	Miami, Florida
MGM	Montgomery, Alabama
MTF	Mississippi Test Facility
OKC	Oklahoma City, Oklahoma
OMA	Omaha, Nebraska
PIA	Peoria, Illinois
PIT	Pittsburgh, Pennsylvania

SAT	San Antonio, Texas
SHV	Shreveport, Louisiana
TOP	Topeka, Kansas
TPA	Tampa, Florida
VPS	Valpariso, Florida
063	Grand Bahama Island

☆U.S. GOVERNMENT PRINTING OFFICE: 1973-739-151/15